THÈSE

Université de Lille

Ecole Doctorale :

Sciences de la Matière, du Rayonnement et de l'Environnement

présentée par

Parnian PEYROVI

en vue de l'obtention du titre de

DOCTEUR EN CHIMIE
Spécialité Molécules et Matière Condensée

Sujet de thèse

Improved resistance to deactivation of coupled NH_3-SCR/ DPF catalyst for diesel exhaust emissions control

---

Soutenue le 25 octobre 2018

JURY

Xavier COURTOIS, Maître de Conférences, IC2MP, Université de Poitiers	**Rapporteur**
Patrick DA COSTA, Professeur, IJLRDA, Université Paris VI	**Rapporteur**
Pegie COOL, Professeur, Universiteit Antwerpen	**Examinateur**
Renaud COUSIN, Professeur, UCEIV, Université du Littoral – Côte d'Opale	**Examinateur**
Christophe DUJARDIN, Professeur, UCCS, ENSCL	**Directeur de thèse**
Pascal GRANGER, Professeur, UCCS, Université de Lille	**Co-Directeur de thèse**

Acknowledgments.

I would like to thank everyone who supported me during these years and without whom this thesis could not have been fulfilled.

I would like to thank Christophe DUJARDIN, my thesis director for giving me the opportunity to work with him and for everything he made for me. He was always ready to discuss (even small) problems and he was encouraging me in moments of doubt with the smile and good mood. I wish to thank as well my co-director, Pascal GRANGER for each very valuable discussion, precious remarks and for his constant motivation during this PhD period.

I would like to thank all jury members and particularly two referees Xavier COURTOIS and Patrick DA COSTA for having accepted to judge this thesis.

The financial help provided by AZMA CHIMIE, for pursuing my thesis is duly acknowledged.

I would like to gratefully acknowledge persons who have kindly made various catalysts analysis for me and/or trained me in doing it by my own, namely Olivier GARDOLL, Pardis SIMON, Martine TRENTESAUX, and Jean-Charles MORIN. I was lucky to be a part of such a group filled with learning experiences.

I also gratefully acknowledge the PhD student Sylvain GILLOT who I had the opportunity to work with through my thesis on this subject.

I would like to thank the UCCS members in general for the welcoming atmosphere and the good time I spent in the coffee room that made my days brighter. Thanks to Mickael, Olivier, Martine, Pardis, Anne-So, Jean-François, Jean- Charles, Elise, and Jean-Seb for the soirées de Trot and Belote. Merci!

Another big thanks goes to the colleagues at UCCS: Carmen, Guillaume R, Yash, Zhiping, Guillaume P, Dayane, Danilo, Bertrand, Shilpa, Grece, Juliana and Sarah for fruitful discussions on the subject and lots of memorable events. It is impossible to express my gratitude towards Tanushree in words for all her support and valuable time, trying her level best to lighten my mood and refresh me.

I would like to remember all the members of UCCS, for their presence, help and support, without which this thesis is impossible, every one of them stays close to my heart. A special thanks to all of you, guys.

Moreover, some very good friends persist spite of the distance, a very special thanks therefore goes to Marine and Adrien for making confidence in me and traveling with me to Iran and for just so many happy and intense moments we spent together. Mamnoon!

Acknowledgments.

I am grateful to all my friends: Fariba, Anahita, Hananeh, Soozan, Mehdi, and Avand for supporting me all that time. Special thanks goes to Noushine for being absolutely always there I am lucky to have you in my life.

I wish to express my thanks personally to Dr. Bahrami for his concern not only towards my academics but also to my personal life. I wish to remember the help and support provided by Mr. Choeib, and his lovely family during my tough times and also my very first days in Lille.

I would like to give a special thanks to Saideh joon, for her care and kindness towards me, seasoned with Iranian dishes and flavored with cups of tea at her home. I always felt at home.

I would like to express my deepest appreciation to my family in law; Audrey, Mathieu and Danaé for all their love, patience, encouragement, and unconditional support throughout my life including the years of PhD studying.

I wish to thank my cousin Paria, the one who was always there, no matter the distance. I consider myself so, so, lucky for having you. The geographical barriers were unnoticed and you were always present when I needed the most.

I would have achieved nothing without my family. I would like to thank my entire family, but especially my mom, dad, and sister have been nothing but supportive of me in my long absence from home, and I've been lucky to have their confidence, patience, pride, nurturing and love throughout my life. My sister has been my best friend all my life and I love her dearly and thank her for all her advice and support. Maman and baba joon, you are the ones who have made this thesis a reality by having faith in me and for instilling in me the courage to strive and achieve higher goals in life.

Finally, I would like to thanks Hélori. With your love, your smile, your everlasting patience, and your support even when you yourself were under loads of pressure and the wonderful times we spent together I am happy to know that we are able to surmount difficulties and accomplish great things together. You make my life complete Kutsi.

Acknowledgments.

List of abbreviations

a.u.	Arbitrary units
BET	Brunauer-Emmet-Teller
CO_2	Carbon dioxide
CFC	Cubic Face-Centered
CO	Carbon oxides
DOC	Diesel oxidation catalyst
DPF	Diesel particulate filter
EGR	Exhaust gas recirculation
EU	European Union
GHSV	Gas hourly space velocity
HC	Hydrocarbons
HC-SCR	Hydrocarbon-assisted Selective Catalytic Reduction
H_2-TPR	Hydrogen temperature-programmed reduction
ICP-OES	Inductively coupled plasma optical emission spectrometry
LNT	Lean NO_x trap
N_2O	Nitrous oxide
NH_3	Ammonia
NH_3^*	Ammonia adsorbed on catalyst walls
NH_3-SCR	Selective catalytic reduction of NO_x with NH_3
NMHC	Non-methane hydrocarbons
N_2	Nitrogen

List of abbreviations

NO	Nitric oxide
NO_2	Nitrogen dioxide
NO_x	Nitrogen oxides, includes NO and NO_2
O_2	Oxygen
PM	Particulate matter
RE	Rare earth
SCR	Selective Catalytic Reduction
SCR/DPF	Combined SCR and DPF
SSA	Specific surface area
SO_2	Sulphur dioxide
PM	Particulate matter
TCD	Thermal Conductivity Detector
TWC	Three-way catalyst
wt. %	Weight percentage
XPS	X-ray photoelectron spectroscopy
XRF	X-ray fluorescence
XRD	X-ray diffraction

List of abbreviations

Table of contents

Motivation and Objective……1

I Bibliography study……7

1 General introduction 10

1.1 Background 10

2 Pollutant formation and treatment 14

2.1 Sulphur dioxide 14

2.2 Hydrocarbon Compounds (HC) 15

2.3 Particulate matter (PM) 15

2.4 Carbon oxides (CO) 15

2.5 Nitrogen oxides (NO_x) 16

2.5.1 NO_x formation 16

3 Diesel and gasoline engine comparison 17

4 Nitrogen oxide removal techniques for diesel engines 18

4.1 Exhaust gas recirculation 19

4.2 Lean NO_x trap (LNT) 20

4.3 Selective catalytic reduction (SCR) 21

4.3.1 HC-SCR 22

4.3.2 NH_3-SCR 23

4.3.2.1 Inhabitation of the NH_3-SCR 27

5 The different techniques for removing hydrocarbons, CO and soot 28

5.1 Diesel Oxidation Catalyst (DOC) 28

5.2 Diesel particulate filters (DPF) 29

6 The active catalysts in urea-SCR 29

6.1 V_2O_5-WO_3/TiO_2 30

6.1.1 Proposed mechanisms 33

6.2 Zeolites 35

6.2.1 Cu-Zeolite SCR 36

6.2.1.1 Reaction mechanism 37

6.2.2 Fe-ZSM5 as SCR catalyst 38

6.2.2.1 Reaction mechanism 39

6.2.3 CuFe-ZSM-5 41

6.3 Cerium based catalyst 42

6.4 Rare earth 51

7 Conclusion 57

8 References 59

II Experimental protocols and techniques 69

1 Synthesis protocols 71

2 Chemical Characterization Techniques 72

2.1 X-ray diffraction (XRD) 72

2.2 Raman Spectroscopy 75

2.3 X-ray photoelectron spectroscopy (XPS) 76

2.4 Single point BET.....77

2.5 Pyridine adsorption-desorption.....79

2.6 Elemental analysis 79

2.6.1 ICP-OES 80

2.6.2 X-ray fluorescence (XRF).....81

2.7 Temperature programmed reduction by H_2 (H_2-TPR).....82

3 Catalytic performance measurements.....82

3.1 Experimental setup for catalytic test.....83

3.2 Catalytic performance test protocols 85

3.3 Quantitative analysis of the effluent gases composition…… …….86

4 References.....87

III The activity of $CeVO_4$-Based Catalysts for Ammonia-SCR Impact of surface cerium enrichment ……89

The activity of $CeVO_4$-Based Catalysts for Ammonia-SCR Impact of surface cerium enrichment.....91

Conclusion 117

Refrences.....117

IV Catalytic performances of $Ce_{1-X}RE_XV_{0.95}W_{0.05}O_4$ mixed oxides (RE=Pr, Gd, Tb, Er and X=0.1 and 0.5) ……..119

1 Catalytic performances of $Ce_{1-X}RE_XV_{0.95}W_{0.05}O_4$ mixed oxides (RE=Pr and Gd, X=0.1 and 0.5) for the selective catalytic reduction of NO_x by ammonia.....123

Table of contents.

1.1 Hydrothermal Synthesis of $Ce_{1-X}RE_XV_{0.95}W_{0.05}$ (RE= Pr and Gd, X=0.1 and 0.5) solids……...124

1.2 Bulk/Structural properties 125

1.2.1 X-ray diffraction 126

1.2.1.1 Unaged solids 126

1.2.1.2 Solids aged at 600°C 129

1.2.1.3 Solids aged at 850°C 130

1.2.2 Raman spectroscopy 133

1.2.3 Temperature-programmed reduction (H_2-TPR)..... 136

1.2.3.1 Unaged 136

1.2.3.2 Solids Aged at 600°C 137

1.2.3.3 Solids Aged at 850°C 139

1.3 Surface characterizations..... 141

1.3.1 Specific surface area 141

1.3.2 X-ray photo-electron spectroscopy (XPS) 143

1.4 Catalytic activity of $Ce_{1-X}RE_XV_{0.95}W_{0.05}O_4$ (RE=Pr and Gd, X=0.1 and 0.5) catalysts after hydrothermal aging at 600°C 153

1.4.1 Ammonia-selective catalytic reduction of NO_x to nitrogen in "Standard" condition: NO/NO_x =1..... 154

1.4.2 Ammonia-selective catalytic reduction of NO_x to nitrogen in "Fast" condition: NO/NO_x = 0.5 156

1.4.3 Ammonia-selective catalytic reduction of NO_x to nitrogen in "NO_2" condition: NO/NO_x =3/10 158

1.5 Catalytic activity of $Ce_{1-X}RE_XV_{0.95}W_{0.05}O_4$ (RE=Pr and Gd, X=0.1 and 0.5) catalysts after hydrothermal aging at 850°C 160

1.5.1 Ammonia-selective catalytic reduction of NO_x to nitrogen in "fast" condition: NO/NO_x = 0.5 160

1.6 Conclusion 161

2 Catalytic performances of mixed oxides $Ce_{0.5}RE_{0.5}V_{0.95}W_{0.05}O_4$ (RE= Pr, Gd, Tb, and Er) for selective catalytic reduction of NO_x by ammonia 163

2.1 Hydrothermal Synthesis of $Ce_{0.5}RE_{0.5}V_{0.95}W_{0.05}O_4$ (RE= Pr, Gd, Tb, and Er) solids. 163

2.2 Bulk/Structural properties 165

2.2.1 X-ray diffraction 165

2.2.1.1 Unaged solids 165

2.2.1.2 Solids Aged at 600°C 167

2.2.1.3 Solids Aged at 850°C 168

2.2.2 Raman spectroscopy 170

2.2.3 Temperature-programmed reduction (H_2-TPR) 172

2.2.3.1 Unaged 172

2.2.3.2 Solids Aged at 600°C 173

2.2.3.3 Solids Aged at 850°C 175

2.3 Surface characterizations 177

2.3.1 Specific surface area 177

2.3.2 X-ray photoelectron spectroscopy (XPS) 178

2.4 Catalytic activity of $Ce_{0.5}RE_{0.5}V_{0.95}W_{0.05}O_4$ (RE= Pr, Gd, Tb, and Er) catalysts after hydrothermal aging at 600°C 188

2.4.1 Ammonia-selective catalytic reduction of NO_x to nitrogen in "Standard" condition: NO/NO_x =1 188

2.4.2 Ammonia-selective catalytic reduction of NO_x to nitrogen in "fast" condition: NO/NO_x = 0.5 190

2.4.3 Ammonia-selective catalytic reduction of NO_x to nitrogen in "NO_2" condition: NO/NO_x =3/10 192

2.5 Catalytic activity of $Ce_{0.5}RE_{0.5}V_{0.95}W_{0.05}O_4$ (RE= Pr, Gd, Tb and Er) catalysts after hydrothermal aging at 850°C 193

2.5.1 Ammonia-selective catalytic reduction of NO_x to nitrogen in "Standard" condition: NO/NO_x =1 193

2.5.2 Ammonia-selective catalytic reduction of NO_x to nitrogen in "fast" condition: NO/NO_x = 0.5 194

2.5.3 Ammonia-selective catalytic reduction of NO_x to nitrogen in "NO_2" condition: NO/NO_x =3/10 195

2.6 Conclusion of section 197

3 References 199

V Catalytic performances of $Ce_{1-X}Er_XV_{0.95}W_{0.05}O_4$ (X= 0.2, 0.5, and 0.8) catalysts for the selective reduction of NO_x by ammonia……...204

1 Catalytic performances of $Ce_{1-X}Er_XV_{0.95}W_{0.05}O_4$ (X= 0.2, 0.5, and 0.8) catalysts for the selective reduction of NO_x by ammonia 207

1.1 Hydrothermal synthesis of $Ce_{1-X}Er_XV_{0.95}W_{0.05}O_4$ (X= 0.2, 0.5 and 0.8) solids 207

1.2 Bulk/Structural properties 209

1.2.1 X-ray fluorescence spectrometry……209

1.2.2 X-ray diffraction…….210

1.2.2.1 Unaged solids 210

1.2.2.2 Solids aged at 600°C 212

1.2.2.3 Solids aged at 850°C 212

1.2.3 Raman spectroscopy……...214

1.2.3.1 Unaged solids 214

1.2.3.2 Aged solids.....216

1.2.4 Temperature-programmed reduction (H_2-TPR)…….218

1.2.4.1 Reducibility of unaged solids.....218

1.2.4.2 Reducibility of aged samples 219

1.2.4.3 Determination of kinetic parameters for the low and high reduction process from H_2-temperature-programmed reduction experiments.....222

1.3 Surface characterizations.....226

1.3.1 Specific surface area……..…….226

1.3.2 X-ray photoelectron spectroscopy (XPS)……...227

1.4 Surface acidity from pyridine adsorption-desorption experiments 233

1.5 Catalytic activity of $Ce_{1-X}Er_XV_{0.95}W_{0.05}O_4$ (X=0, 0.2, 0.5, and 0.8) catalysts after hydrothermal aging at 600°C 235

1.5.1 Ammonia-selective catalytic reduction of NO_x to nitrogen in "Standard" condition: NO/NO_x=1…….235

1.5.2 Ammonia-selective catalytic reduction of NO_x to nitrogen in "fast" condition: NO/NO_x = 0.5…….236

1.5.3 Ammonia-selective catalytic reduction of NO_x to nitrogen in "NO_2" condition: NO/NO_x =3/10……238

1.6 Catalytic activity of $Ce_{1-X}Er_XV_{0.95}W_{0.05}O_4$ (X=0, 0.2, 0.5, and 0.8) catalysts after hydrothermal aging at 850°C 239

1.6.1 Ammonia-selective catalytic reduction of NO_x to nitrogen in "Standard" condition: NO/NO_x =1..... 239

1.6.2 Ammonia-selective catalytic reduction of NO_x to nitrogen in "fast" condition: NO/NO_x= 0.5……..240

1.6.3 Ammonia-selective catalytic reduction of NO_x to nitrogen in "NO_2" condition: NO/NO_x =3/10……242

1.7 Tentative comparison between physicochemical and catalytic properties..... 243

2 Conclusion 245

3 References 247

VI Catalytic performances of $Ce_{0.5}Er_{0.5}V_{0.95}X_{0.05}O_4$ mixed oxides (X=W, Mo, Sb, and Nb)……..250

1 Catalytic performances of $Ce_{0.5}Er_{0.5}V_{0.95}X_{0.05}O_4$ (X=W, Mo, Sb, and Nb) catalysts for the selective reduction of NO_x by ammonia 253

1.1 Hydrothermal synthesis of $Ce_{0.5}Er_{0.5}V_{0.95}X_{0.05}O_4$ (X=W, Mo, Sb, and Nb) solids. 253

1.2 Bulk/Structural properties 255

1.2.1 X-ray fluorescence spectrometry 255

1.2.2 X-ray diffraction 256

1.2.2.1 Unaged solids 256

1.2.2.2 Solids aged at 600°C 258

1.2.2.3 Solids aged at 850°C 259

1.2.3 Raman spectroscopy 261

1.2.4 Temperature-programmed reduction (H_2-TPR) 263

1.2.4.1 Solids Aged at 600°C 263

1.2.4.2 Solids Aged at 850°C 264

1.3 Surface characterizations 266

1.3.1 Specific surface area 266

1.3.2 X-ray photoelectron spectroscopy (XPS) 267

1.3.3 Surface acidity from pyridine adsorption-desorption experiments……275

1.4 Catalytic activity of $Ce_{0.5}Er_{0.5}V_{0.95}X_{0.05}O_4$ (X=W, Mo, Sb, and Nb) catalysts after hydrothermal aging at 600°C 277

1.4.1 Ammonia-selective catalytic reduction of NO_x to nitrogen in "Standard" condition: NO/NO_x=1 277

1.4.2 Ammonia-selective catalytic reduction of NO_x to nitrogen in "fast" condition: NO/NO_x= 0.5 278

1.4.3 Ammonia-selective catalytic reduction of NO_x to nitrogen in "NO_2" condition: NO/NO_x =3/10 279

1.5 Conclusion 282

2 References 282

General conclusions and outlook ……...286

Table of contents.

Motivation and objective

Motivation and objective

Motivation

The combustion of fossil fuels used in power plants, vehicles, and factories is one of the largest contributions to air pollution [1]. The exhaust air pollutants consist of Sulphur oxides, carbon monoxide, particulate matter, unburned hydrocarbons and nitrogen oxides (NO_x). Among them, NO_x is considered the primary pollutants causing a variety of environmental problems such as acid rain, photochemical smog, ozone depletion, fine particulate pollution and even accelerated global warming [1–3]. Increasing requirements for reducing NO_x emissions have stimulated interest in the improvement of currently used methods and development of new technologies for NO_x emission control. Depending on the type of NO_x emission source, three primary techniques for NO_x control are available: fuel control, combustion control, and post-combustion control. Selective catalytic reduction with NH_3 (NH_3-SCR), in which ammonia is used as the reducing agent of NO_x in the presence of a catalyst, is one of the most popular post-combustion techniques to control NO_x emission from combustion processes [4,5]. Furthermore, space limitations in the diesel engine, are forcing car manufacturers to seek for solutions that combine different functionalities into single converters. A possible solution is the embodiment of the NO_x selective catalytic reduction (SCR) functionality in the already present diesel particulate filter (DPF), and is achieved by depositing the SCR catalyst in the inner porosities of the filter walls, or on the top of them.

When soot accumulation generates pressure drop in the DFP, a periodic active regeneration mode is performed to prevent filter plugging and a decrease of engine performances. The heat released at high temperature ensures sufficient oxidation to remove soot. Accordingly, the SCR catalyst must withstand extreme temperatures to keep its intrinsic properties and its selective NO_x conversion. The thesis is focused on the design of a catalyst for the NH_3-SCR of NO_x that promotes NO to N_2 reduction that can withstand at the high temperature.

Commercial NH_3-SCR catalysts used for cleaning flue gases from power plants are based on V_2O_5-WO_3/TiO_2 oxides which, however, operate only in a rather high and narrow temperature range of 300-500°C. The temperature range of NO_x-containing exhaust gases from other sources such as diesel or lean-burn gasoline engines is much broader [6]. Therefore, the improvement of commercial vanadium-based catalysts and/or the development of new NH_3-SCR catalysts being sufficiently active and selective at low temperature are a scientific and technological need for NO_x emission control. Since vanadium-based catalysts have numerous advantages, for example, high conversion efficiency, high N_2 selectivity, excellent resistance to Sulphur, and low cost, these catalysts bear a significant potential for low-temperature NH_3-SCR if appropriate supports are used to extend the temperature working window. Furthermore, copper-exchanged zeolites are beginning to be used as promising catalysts for diesel vehicles; however, their limited hydrothermal stability and N_2 selectivity are disadvantages for practical applications [7,8].

CHA-type zeolite with smaller pores and stronger acidity, especially SSZ-13 zeolite upon exchange with Cu^{2+}, has been shown with better NH_3-SCR activity and selectivity than those of beta catalysts and ZSM-5 as well as higher hydrothermal stability. However, these zeolite-based catalysts still undergo deactivation above 550°C. In real applications, the temperature can reach beyond 800°C, which frequently degrades the durability of the catalyst. Therefore, it is desirable to develop catalysts which can be applied at a wider temperature window beyond 550°C or even higher.

Among the wide variety of catalysts tested in recent years, those based on (modified) ceria have proved to be the most promising ones [9–11]. With MnO_x as co-component, almost total NO conversion has been obtained at 100°C [12,13]. However, such catalysts suffer from undesired N_2O formation and deactivation by other flue gas components such as SO_2 or H_2O. CeO_2 reveals to be a useful catalyst component not only for SCR but also for other redox reactions since it

can store and release oxygen efficiently by a relatively facile reduction from Ce^{4+} to Ce^{3+} [14–16]. This property is promoted even more when cerium substituted by the rare earth with the smaller diameter such as Erbium or Terbium since doping with such kind of cations can create both short and long metal-oxygen bonds. Thus, the oxygen atoms bonded by long bonds to the metal become weaker and easier to remove. For this reason, SCR catalysts based on ceria-containing mixed oxide are almost always expected to be more active than those based on pure ceria.

Objective The objective of this study is the investigation of new thermally stable active phases that are able to maintain their catalytic performance presenting high N_2 selectivity after hydrothermal aging at high temperature.

Approach This thesis is divided into 6 chapters.

- First, a bibliography study (Chapter 1) on NH_3-SCR and conventional NH_3-SCR catalysts, as well as V_2O_5-WO_3/TiO_2 oxides is performed.
- In chapter 2, the synthesis protocol, employed conditions of the physico-chemical characterizations and the catalytic activity evaluation are presented.
- Chapter 3 focus on the catalytic activity of unsupported $CeVO_4$ with an excess of CeO_2 in standard and fast-SCR conditions. The choice of starting system, *i.e* Ce-based catalyst, as an alternative NH_3-SCR catalyst is justified. The result of physico-chemical characterization of solids prepared by the hydrothermal method as well as their catalytic performance is shown to illustrate the choice of Ce-based catalysts as a suitable alternative system.
- The first part of the chapter 4 discusses the catalytic performance of bulk $Ce_{1-X}RE_XV_{0.95}W_{0.05}O_4$ (RE= Pr and Gd, X=0.1 and 0.5) catalysts aimed at the conversion of NO_x by ammonia. At first, preparation procedures of all catalysts are described. This chapter also focuses on the characterization of the catalyst after synthesis and after the

hydrothermal aging at 600 and 850°C and correlating these measures with catalytic behavior. The second part of the chapter 4 deals with the catalytic system similar to those studied in the first part in which cerium substituted by the rare earth. In this section, we discussed the catalytic performance of $Ce_{0.5}RE_{0.5}V_{0.95}W_{0.05}O_4$ (RE= Pr, Gd, Tb, and Er) catalysts aimed to the conversion NO_x by ammonia, it seems that their properties depend on the nature of the element and in particular on their ionic radius.

- The Er species was found to be crucial for enhancing the NO_x conversion in chapter 4. The substitution of cerium by erbium increases NO conversion to nitrogen regardless of the operating conditions. Accordingly, in chapter 5 bulk $Ce_{1-X}Er_XV_{0.95}W_{0.05}O_4$ (X= 0.2, 0.5, and 0.8) catalysts prepared by the hydrothermal synthesis have been developed for the ammonia-selective catalytic reduction of NO_x to nitrogen.
- In the chapter 6, we investigate the replacement of W by Mo, Sb, and Nb in $Ce_{0.5}Er_{0.5}V_{0.95}W_{0.05}O_4$ catalyst structure should be beneficial for NH_3-SCR. A series of $Ce_{0.5}Er_{0.5}V_{0.95}X_{0.05}O_4$ (X=W, Mo, Sb, and Nb) catalysts was prepared by hydrothermal approach and was characterized by XRF, XRD, Raman, H_2-TPR, N_2 adsorption, XPS and Pyridine adsorption. The catalytic activity is then compared to the reference catalyst in Standard and fast-SCR conditions after hydrothermal aging at 600°C or 850°C. The conclusions and perspectives are reported in the last chapter of this study.

Chapter I

Bibliographic Study

Summary

1 General introduction 10

1.1 Background 10

2 Pollutant formation and treatment 14

2.1 Sulfur dioxide 14

2.2 Hydrocarbon Compounds (HC) 15

2.3 Particulate matter (PM) 15

2.4 Carbon oxides (CO) 15

2.5 Nitrogen oxides (NO_x) 16

2.5.1 NO_x formation 16

3 Diesel and gasoline engine comparison 17

4 Nitrogen oxide removal techniques for diesel engines 18

4.1 Exhaust gas recirculation 19

4.2 Lean NO_x trap (LNT) 20

4.3 Selective catalytic reduction (SCR) 21

4.3.1 HC-SCR 22

4.3.2 NH_3-SCR 23

4.3.2.1 Inhabitation of the NH_3-SCR 27

5 The different techniques for removing hydrocarbons, CO and soot 28

5.1 Diesel Oxidation Catalyst (DOC) 28

5.2 Diesel particulate filters (DPF) 29

6 The active catalysts in urea-SCR 29

6.1 V_2O_5-WO_3/TiO_2 30

6.1.1 Proposed mechanisms 33

6.2 Zeolites 35

6.2.1 Cu-Zeolite SCR 36

6.2.1.1 Reaction mechanism 37

6.2.2 Fe-ZSM5 as SCR catalyst 38

6.2.2.1 Reaction mechanism 39

6.2.3 CuFe-ZSM-5 41

6.3 Cerium based catalyst 42

6.4 Rare earth 51

7 Conclusion 57

7.1 References 59

1 General introduction

1.1 Background

Combustion of hydrocarbon fuels not only produces carbon dioxide (CO_2) and water (H_2O) as reaction products but also a wide range of other compounds. While the amount of the additional compounds is very small compared to the two main products, their effect on human health and/or the environment is significant. Environmental regulation has become stricter in order to reduce the impact of greenhouse gases and pollutants. A major reason for reducing these emissions is there harmful effects on human health and the environment [1–3].

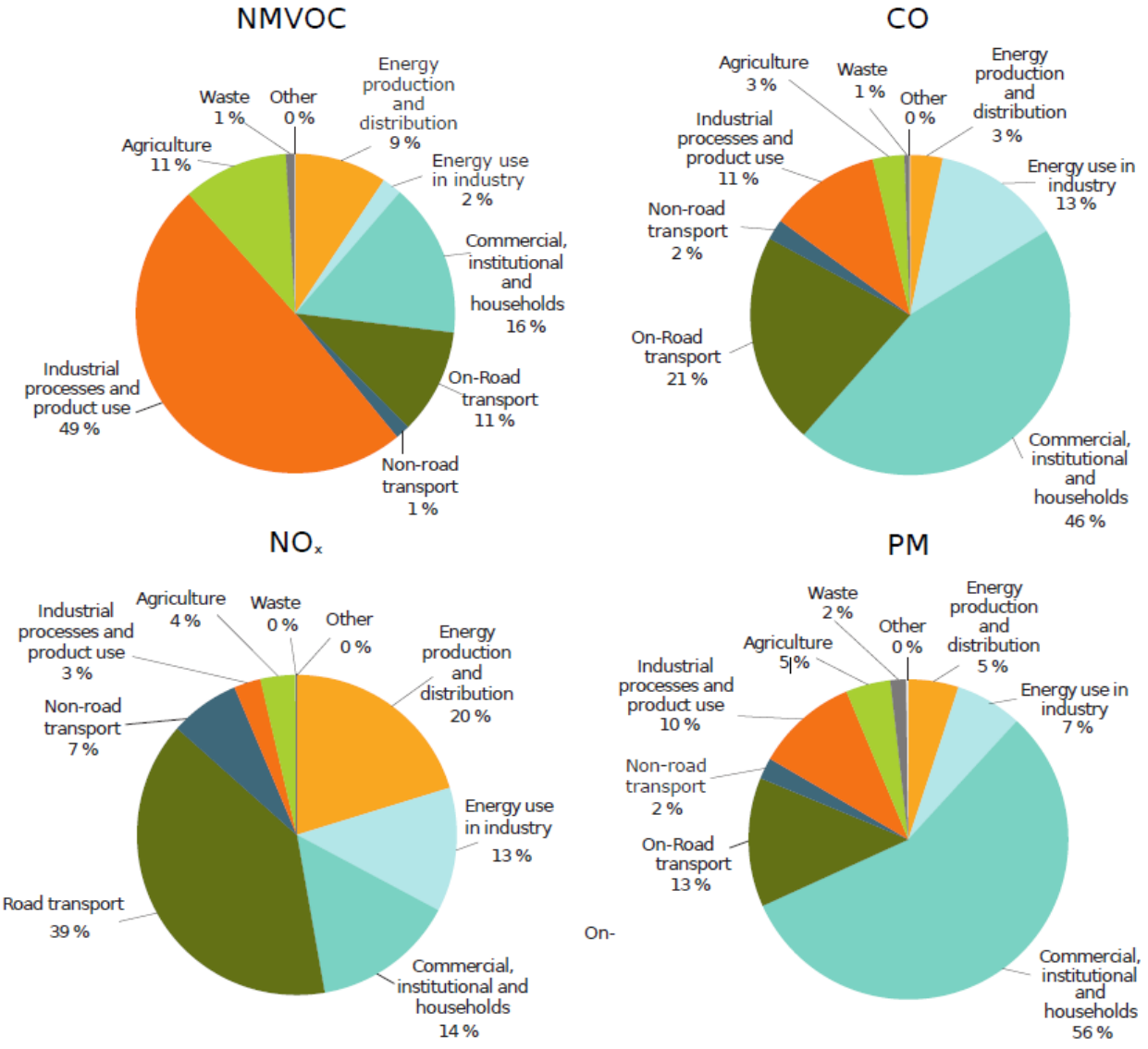

Figure 1.1 **– European emission inventory for NMVOC (includes HC), CO, NO_x, and PM. The data is collected and reported by the European Environment Agency** [19]

The use of automobiles and trucks generates more pollution than other human activity, and about 40% of NO_x emissions come from the mobile source [19]. Accordingly, reducing emissions from road transport is an important factor in order to the improvement of air quality. Nowadays, where fuel price has increased, the diesel engine has proven to be extremely efficient and cost-effective compared to the gasoline engine due to more energy density that can be extracted from diesel as compared with the same volume of the gasoline engine [20]. Therefore, the diesel engine provides higher mileage that makes it an evident choice for heavy duty transportation. Diesel engine offers the possibility of combining high thermal efficiency and low carbon dioxide emissions compared to the gasoline engine. Otherwise, the large draw of the diesel engines is emissions of nitrogen oxides (NO_x) and particulates. The high temperature in the combustion chamber of the diesel engine can help soot reduction but produce a huge number of nitric oxide [20].

In order to solve this problem standards more stringent enter into force. The first regulation dates back to the early 1990s with the introduction of the Euro 1 standard for light vehicles and Euro I for heavy vehicles. The latest Euro regulations have come into effect (1 September 2014 for Euro 6) (1 January 2014 for Euro VI) (Table 1.1 and Table 1.2). This law in 2014 requires a significant reduction in NO_x emissions for diesel vehicles. The recent regulations strongly insist on the limitation of NO_x emissions (50% and 80% fewer emissions required for light and heavy vehicles compared to Euro 5 and Euro V respectively) [5,6].

Table 1.1 – **Pollutant emissions limits from heavy-duty diesel engines** [5,6]**.**

Stage	Date	NO_x (g/kWh)	CO (g/kWh)	HC (g/kWh)	PM (g/kWh)
Euro I	**01-10-1993**	**9**	**4.90**	**1.23**	**0.36**
Euro II	**01-10-1996**	**7**	**4.00**	**1.10**	**0.15**
Euro III	**01-10-2001**	**5**	**2.10**	**0.66**	**0.13**
Euro IV	**01-10-2006**	**3.5**	**1.50**	**0.46**	**0.02**
Euro V	**01-10-2009**	**2**	**1.50**	**0.46**	**0.02**
Euro VI	**31-12-2013**	**0.4**	**1.50**	**0.13**	**0.01**

Table 1.2 – **Pollutant emissions limits from light diesel engines** [5,6]**.**

Stage	Date	NO_x (g/kWh)	CO (g/kWh)	$HC+NO_x$ (g/kWh)	PM (g/kWh)
Euro 1	**01-07-1992**	**-**	**2.72**	**0.97**	**0.140**
Euro 2	**01-01-1996**	**-**	**1.00**	**0.70**	**0.080**
Euro 3	**01-01-2000**	**0.50**	**0.64**	**0.56**	**0.050**
Euro 4	**01-01-2005**	**0.25**	**0.50**	**0.30**	**0.025**
Euro 5	**01-09-2009**	**0.18**	**0.50**	**0.23**	**0.005**
Euro 6	**01-09-2014**	**0.08**	**0.50**	**0.17**	**0.005**

Meet the legal standards demand on the industry to seek improvements in automotive emission control system like new engine concepts, fuel quality and in the design of exhaust catalysis.

For these systems, due to the high concentration of oxygen in the exhaust gas, it is impossible to reduce pollutants by a Three Way Catalysts (TWC). To overcome this problem a combination of two types of converters is used one for oxidation and the other one for reduction. The first one, called (DOC) is responsible for oxidizing of CO and HC, and the second one selective catalytic reduction unit (SCR) or a lean NO_x-trap (LNT) is used to convert NO and NO_2 to nitrogen by using a reducing agent. A diesel particulate filter (DPF) is placed after the DOC to trap soot.

Most of the vehicles that comply with Euro VI standard rely on the combination of SCR and DPF to remove NO_x and particulate matter from the exhaust gas [23]. This incorporation promises possible advantages for the after-treatment system like, significantly lowers after-treatment system volume, weight, and cost [8,9].

The combined SCR and DPF often abbreviated as SCR/DPF or SCR-DPF extend the wall-flow DPF filter with catalytic washcoat that promotes NO_x reduction. Catalysts that promote SCR reactions are washcoated mostly in the walls between channels or in the outlet channels [26]. Although, such incorporation allows mounting of both NO_x reduction and PM filtering technologies closer to the engine, thus minimizing the heat loss with improving overall NO_x conversion efficiency [25].

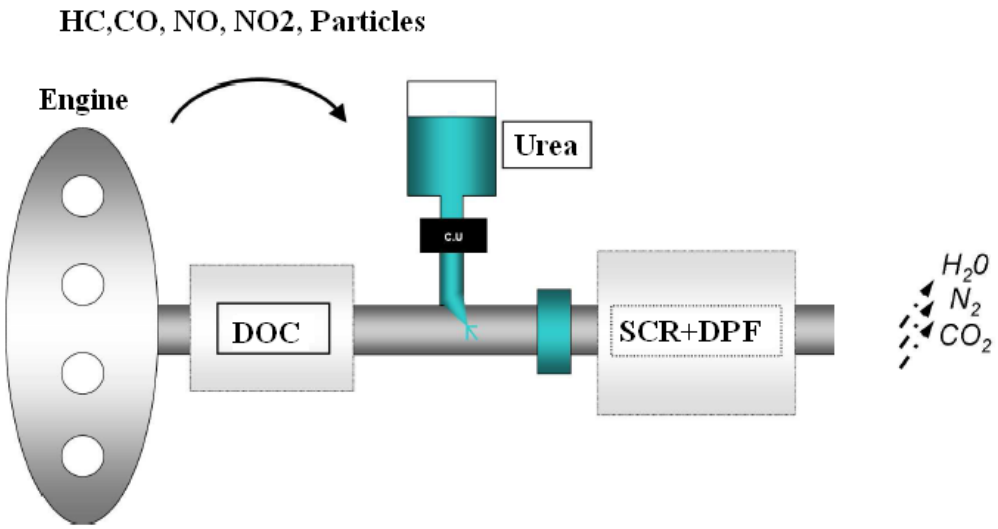

Figure 1.2 – **SCR/DPF incorporation** [26]

Fig 1.2 illustrates the incorporation of SCR and DPF, this incorporation still has some disadvantages. When soot accumulation exceeds soot oxidation, a periodic active regeneration mode is performed to prevent filter plugging. The heat released at high temperature ensures sufficient oxidation to remove soot. Accordingly, The SCR catalyst must withstand extreme temperatures to keep its intrinsic properties and its selective NO_x conversion [11,12].

2 Pollutant formation and treatment

Defining pollution is not simple. All man-made emissions into the air can be called air pollution because they alter the chemical composition of the natural atmosphere. The increase in the global concentrations of greenhouse gases can be called air pollution, even though concentrations not found to be toxic to humans and the ecosystem [29].

The emissions of internal combustion engines (ICE) can be classified as primary or secondary. Primary pollutants are substances are directly emitted into the atmosphere from sources. Secondary pollutants are not directly emitted from the source but instead form in the atmosphere from primary pollutants [30]. In Europe, the main air pollutants are defined as nitrogen oxides (NO_x), soot, sulfur dioxide (SO_2) and non-methane volatile organic compounds (NMVOCs). Other hazardous pollutants of exhaust gas can be particulate matter (PM), carbon monoxide (CO), hydrocarbons (HCs) and non-methane hydrocarbons (NMHCs). Soot, which is derived from combustion of diesel fuel, is a major air pollutant and the second largest cause of global warming. The impact of any pollutant on the atmosphere is dependent on its properties of water solubility, volatility, and reactivity. The less soluble, the more volatile, and the less reactive a species is, the more its effect becomes widespread and long-lasting. This section defines these pollutants and their sources of emission [29].

2.1 Sulfur dioxide

Sulfur dioxide (SO_2) is a gas formed when the sulfur is exposed to oxygen at elevated temperatures, during the combustion of fossil fuels, the petroleum refining, or the melting of metals. SO_2 is toxic to humans at high concentrations, but its main impact on air pollution is associated with the formation of rain and acid aerosols. In fact, the SO_2 dissolves in water droplets forming clouds and oxidizes to form sulfuric acid (H_2SO_4), which can then fall back to Earth as acid rain or snow, or form sulfate aerosol particles in the atmosphere.

2.2 Hydrocarbon Compounds (HC)

Hydrocarbon compounds consist of carbon and hydrogen molecules and include a variety of other volatile organic compounds (VOCs). Most HCs are not directly harmful to health at concentrations found in the ambient air. Hydrocarbon compounds play an important role in forming NO_2 and O_3, which are health and environmental hazards. Among various HC, non-methane hydrocarbons (NMHC) are reactive in the formation of secondary air pollutants [31].

2.3 Particulate matter (PM)

Particulate matter, also known as particle pollution or PM, is a complex mixture of small particles and liquid droplets. Particle pollution is made up of a number of components, including acids like sulfates and nitrates, organic chemicals, metals, and soil or particles. Size of particles is directly linked to their potential for causing the health problem. The fine particles irritate the respiratory tracts especially in children, and some particles containing polycyclic aromatic hydrocarbons (PAHs) are mutagenic and carcinogenic properties [32].

2.4 Carbon oxides (CO)

Carbon monoxide is colorless and odorless gases slightly denser than air. Residence time and turbulence in the combustion chamber, flame temperature, and excess O_2 affect CO formation. Hemoglobin carries oxygen to the cells, but when CO binds to it, hemoglobin is unable to bind with oxygen, thereby reducing the amount of oxygen delivered to all tissues of the body. Once CO has formed, it is slow to oxidize to CO_2. The exposure limit set by European instructions is set at 10 mg/m^3 for 8 hours [33] while this compound is evaluated as a mortal compound at 3680 mg/m^3 per hour [34]. Noteworthy, that carbon dioxide (CO_2), although the most commonly emitted combustion gas, is normally not considered as a pollutant since adverse health effects are not known. However, CO_2 should be regarded as a serious pollutant in terms of its global warming potential.

2.5 Nitrogen oxides (NO_x)

Nitrogen oxides (NO_x) are gaseous emissions that are formed when the air is heated to high temperatures. The general definition of NO_x today includes the compounds nitric oxide (NO) and nitrogen dioxide (NO_2). NO, and NO_2 are compounds that are of major concern in terms of air pollution as they are the only nitrogen oxides that are emitted in substantial quantities. Typically, the concentration of NO_x in untreated diesel exhausts ranges from 50 to 1000 ppm, depending on combustion temperature, engine load and fuel quality [35]. Approximately 90% of these oxides consist of NO and the rest NO_2 [36]. NO_x are involved in the formation of acid in the form of HNO_3 and contribute to the formation of tropospheric ozone. Nitrous oxide (N_2O) contributes to the greenhouse effect, a phenomenon caused by strong absorbance of infrared radiation in the atmosphere [37].

2.5.1 NO_x formation

Nitric oxide is formed when the nitrogen (N) in the air reacts with atmospheric oxygen (O) in combustion processes with high temperatures and pressure, as can be seen in the reaction formula [38]:

$$N_2 + O_2 \rightarrow 2NO \qquad \text{(Equation 1.1)}$$

Nitrogen dioxide, on the other hand, is formed when nitric oxide is oxidized by the oxygen in the surrounding air, as can be seen in the reaction formula:

$$2NO + O_2 \rightarrow 2NO_2 \qquad \text{(Equation 1.2)}$$

Nitrogen dioxide is not directly formed in the combustion process. Despite this, NO_x-gases are still considered to be directly emitted from a source, making them primary pollutants. Even though nitric oxide and nitrogen dioxide share many common attributes, they are not

equivalents in terms of environmental impact. Nitric oxide is odorless and only moderately toxic to humans and animals, while nitrogen dioxide is both toxic and carry a distinct and unpleasant odor [39].

As shown in Figure 1.3, the thermodynamic equilibrium in the presence of oxygen tends to the oxidation of NO to NO_2 at low temperature. Conversely, from 450°C, this trend reverses in favor of the predominance of NO. This graph explains the reason for which only NO is formed in the engine: from 700°C, NO is thermodynamically favored by more than 90%. In contrast, NO_2 is predominant at room temperature [1].

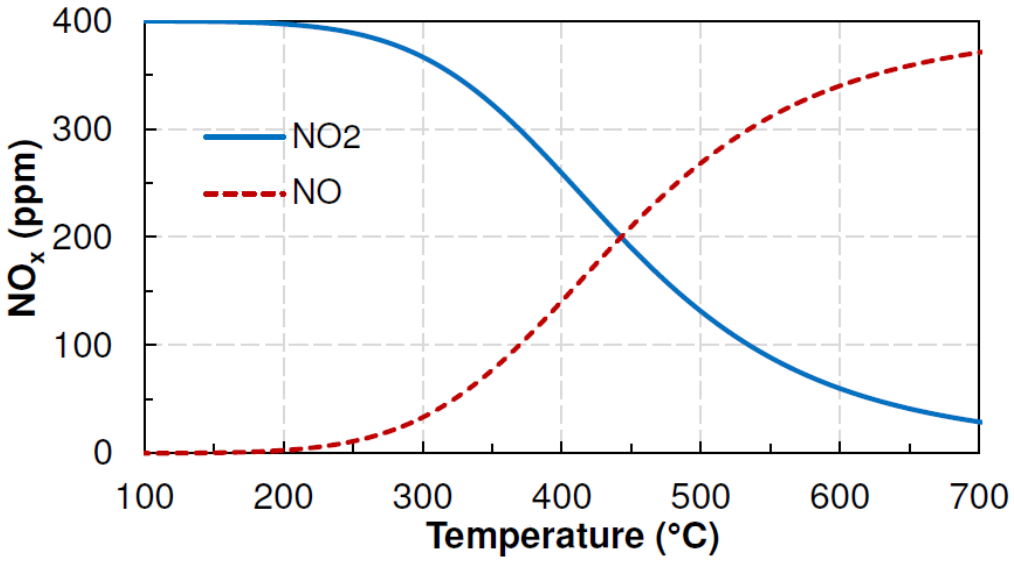

Figure 1.3 – **Thermodynamic equilibrium between NO and NO_2 for an initial mixture containing 400 ppm NO, 10% O_2, 10% CO_2 and 8% H_2O** [1]

3 Diesel and gasoline engine comparison

While gasoline and Diesel fuel are both based on mixture of hydrocarbons, their combustion is conducted in a significantly different manner, resulting in different compositions of the exhaust gas. The Diesel engine operating with a large excess of oxygen in contrast to the gasoline engine that works in stoichiometry condition. Note that the temperature exhaust gas of a diesel engine is between 150 to 250°C, while for an engine gasoline temperature range is higher (600 to 800°C). The essential difference between these two types of engine is the fuel ignition. In a

gasoline engine, fuel is mixed with air compressed by the piston and ignited by the spark. However, in a diesel engine, the air compressed first and then fuel is injected. In this type of engine, ignition happen by the high temperature which a gas achieves when greatly compressed. Auto-ignition is tuned by additives to ensure that diesel engine can be ignited just by compression [40]. Nowadays, the diesel engine is considered as an impressive success in many European countries for their durability, robustness, and especially for their best combustion efficiency which means lowers fuel consumption with less CO_2, CO, and HC production. However, as diesel engine works in the excess of oxygen that facilitates complete combustion, diesel engines emit NO_x and soot particle as major pollutants [41].

Table 1.3 **– The compositions of diesel exhaust gas** [41]

Compound	CO_2	H_2O	O_2	NO_x	HC	CO	SO_2	N_2O
Diesel	**2-12 %**	**2-12 %**	**3-17%**	**50-1000 ppm**	**200-300 ppm**	**10-500 ppm**	**10-30 ppm**	**~3 ppm**

4 Nitrogen oxide removal techniques for diesel engines

Emission control legislation has spread ever since to industrialized countries around the world. In the European Union, a compendium of emission control regulations was introduced for passenger cars and heavy-duty trucks, starting to be put into effect from 1992, with regular amendments for decreasing the number of permitted pollutants.

Thermodynamically, NO_x reduction reaction should proceed on its own at ambient conditions, since below about 700°C, N_2 and O_2 are favored over NO and NO_2 [42] (ΔH_f = +90 kJ/mol) [43]. However, the activation energy of this reaction is too large to occur naturally.

In order to reduce NO_x emissions from diesel engines, various techniques have been used, which can be classified into two categories: combustion control and post-combustion control. An example of combustion control is EGR that reduces the temperature of the engine cylinder and in this way reduces the amount of NO_x produced. Another example of combustion control

is HCCI which reduces NO_x formation by improving the homogeneity of the Fuel/Air mixture. The main objective of the post-combustion system is to reduce NO_x in the presence of the catalyst. The post-combustion systems like lean NO_x trap (LNT) and selective catalytic reduction (SCR) reduce NO_x catalytically by reducing agent. The focus of this thesis is the selective catalytic reduction (SCR) of NO_x by urea in the diesel engine.

4.1 Exhaust gas recirculation

To reduce NO_x emissions it is important to take measures to prevent them from forming. An effective way to do this is to lower the combustion temperature. A well-known and widely used method is Exhaust Gas Recirculation (EGR). In the EGR system, part of the exhaust gas is directed back into the engine by mixing it with the intake air of the engine. The increased heat capacity of the inert exhaust gas lowers the burning temperature in the cylinder. As the peak flame temperatures reduce, fewer NO_x emissions develop [44]. The EGR system lowers the NO_x emissions considerably, but in some cases, challenges are faced with the increased PM emissions and fuel consumption of the engine. Especially the use of a higher rate of EGR at the higher loads can cause problems. The use of EGR slows the combustion and moves the peak of the combustion towards retardation and this can affect the fuel consumption negatively. When the EGR system is used, the exhaust gas replaces some amount of oxygen in the cylinder which leads to the relatively incomplete combustion and raises the formation of PM emissions [44]. However in some cases, especially at lower loads, the use of the EGR can even improve specific brake consumption and PM emission as the effects of recirculation depend greatly on the characteristics of the basic engine and amount of EGR rates used.

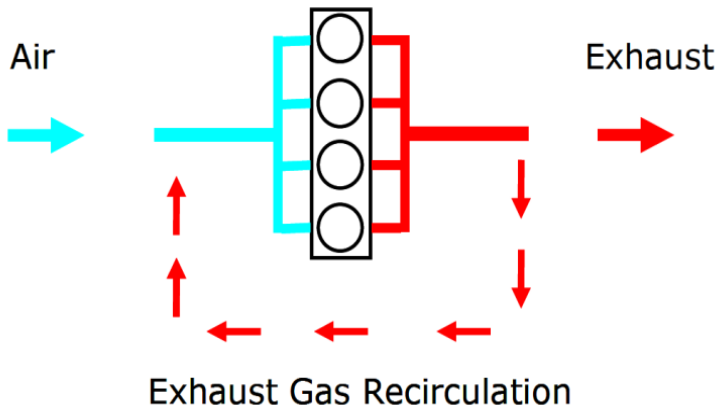

Figure 1.4 – **EGR - Exhaust Gas Recirculation** [45]

4.2 Lean NO_x trap (LNT)

This process, initially developed by Toyota in 1994 [46] relies on the nitrate storage capacities of catalysts. Lean NO_x technology has shown great performance in reducing NO_x in the oxygen-rich environment for lean burn application for high NO_x conversion efficiency and wider operating temperature window. LNT operates at two air/fuel (A/F) ratios corresponding to fuel-lean and fuel-rich phases for storing and reducing NO_x on the catalyst surface. Typical LNT catalyst consists of a cordierite substrate and γ-Al_2O_3 washcoat impregnated with noble metal (Pt, Pd or Rh) and a NO_x storage medium, an earth group such as barium or potassium oxide. During the fuel-lean phase, NO is oxidized to NO_2 on Pt nanoparticles which is stored in the form of nitrite and nitrate on the storage sites. During the rich phase NO_2 stored in the form of nitrites or nitrates is released from the storage sites and reduced to N_2.

Fuel lean-phase:

$$NO \xrightarrow[Pt]{O_2} NO_2 \xrightarrow[Ba]{O_2} Ba(NO_2)_2 \text{ and } Ba(NO_3)_2 \qquad \text{(Equation 1.3)}$$

Fuel rich-phase:

$$Ba(NO_2)_2 \text{ and } Ba(NO_3)_2 \xrightarrow{HC,H_2,CO} BaO+N_2 \xrightarrow{HC,H_2,CO} N_2+H_2O+CO_2 \qquad \text{(Equation 1.4)}$$

The NO_x conversion may be greater than 80% between 250 and 400°C [47]. For Pt-BaO/Al_2O_3 catalyst an order of reactivity is generally established between the different reducing agent, as follows [48], [49]:

$$H_2 > CO > C_3H_6$$

H_2 is therefore considered the most effective species for NO_x reduction, in particular at low temperature (200°C) [44]. On the other hand, its use favors the formation of ammonia as a reaction by-product. This ammonia can be used to reduce NO_x [50], a substantial formation of N_2O can also be observed. Other disadvantages such as the use of expensive noble metals, the overconsumption of fuel to reduce NO_x, low-temperature efficiency or fast deactivation materials (SO_x and temperature) make the SCR system often preferred over LNT system.

4.3 Selective catalytic reduction (SCR)

NO_x contained in the exhaust gas can be converted to N_2 when it reacts catalytically with a reductant (ammonia, urea, oxygenated hydrocarbon and hydrocarbon) in the presence of a catalyst. This process is called Selective Catalytic Reduction (SCR). Originally, ammonia was used as the reducing agent in this thesis. The removal of NO_x by SCR was first established for the thermal power plant in Japan in the late 1970s [51]. Later, SCR technology has been customized for automotive applications [51]. By the reason of safety, ammonia has been replaced by urea solution (AdBlue®). The reductants used in SCR of NO_x are presented in this section, while the information about catalyst materials applied is provided in next section. The adoption of a process involving the decomposition of NO, according to the reaction (Equation 1.5), is probably the most astute solution.

$$2NO\ (gas) \rightarrow N_2\ (gas) + O_2\ (gas) \qquad \text{(Equation 1.5)}$$

$\Delta G° = -86\ kJ.mol^{-1}$

$E_{(activation)} = 364\ kJ.mol^{-1}$

Indeed, this reaction is thermodynamically possible at the low temperature given the value of standard free enthalpy. On the other hand, the reaction rate is slow due to the high activation energy. Therefore, to have a sufficient reaction rate, it is necessary to work at high temperature or use a catalytic system. However, the strong adsorption of oxygen from the gas mixture or from the decomposition of NO_x on the active sites of the catalyst causes poisoning. In the presence of oxygen in the gaseous effluents, the reactions of oxidation of the reductant by O_2 and NO occur simultaneously. The catalytic reduction is said to be selective if this competition is in favor of the oxidation of the reducing agent by NO, on the other hand, this definition gives no indication on the selectivity in the transformation of NO to N_2 or N_2O.

4.3.1 HC-SCR

Hydrocarbon-SCR systems use hydrocarbons as the reductant. The reaction pathways depend on the hydrocarbon used. The reaction below describes the total reaction:

$$HC + NO_x \rightarrow N_2 + CO_2 + H_2O \qquad \text{(Equation 1.6)}$$

As the diesel fuel consists of the range of hydrocarbons, the investigation on the effect of different hydrocarbons on the SCR activities is essential. The researchers showed that, when the diesel fuel is employed as the reducing agent, the catalysts are expected to provide high efficiency by using long-chain hydrocarbons that are already contained in the diesel fuel. Burch *et al*. reported that, in general, SCR activity increases with the increase of the carbon number of hydrocarbons [52]. Shimizu *et al*. [53] investigated the effect of carbon number on water tolerance. After conducting some studies of HC-SCR on alumina-supported silver catalysts reported that the SCR reduction of NO_x by HC and water tolerance noticeably increased as the carbon number of alkane increases. Huge numbers of catalyst have been studied to discover a catalyst for HC-SCR with the best activity, selectivity, and durability.

Houel *et al.* [54] have investigated on ion-exchanged zeolite catalyst for HC-SCR technology. They mentioned that these catalysts show high performance on the reduction of NO_x by hydrocarbons in the presence of excess oxygen and they are highly tolerant to catalyst deactivation caused by sulfur-poisoning. Since the hydrothermal condition is always existent in after-treatment applications, Houel *et al.* showed that ion-exchanged zeolite is unsuitable for the realistic SCR for catalyst deactivation due to metal sintering or zeolite dealumination.

Comparing the activities of oxide-based catalysts it was found that alumina is the most active catalyst for HC-SCR. Several researchers report in the literature that the activity of alumina can be improved by the addition of transition metal such as Cu/Al_2O_3. Shimizu *et al*. [53] studied various transition metals as the catalyst substance. The $Cu\text{-}Al_2O_3$ with 16wt% Cu content exhibited higher activity than Cu-ZSM-5 at low temperature. Furthermore, the $Cu\text{-}Al_2O_3$ showed higher hydrothermal stability than Cu-ZSM-5. Further increase in temperature shows the decrease in the NO_x conversion. This decrease in activity is usually not related to deactivation of the catalyst but to decrease in availability of reductant due to unselective combustion with oxygen. Another problem with HC-SCR is that during increasing of reaction temperature maximum NO_x reduction is obtained almost simultaneously with maximum hydrocarbon conversion.

4.3.2 NH_3-SCR

To choose the best technology which is able to reduce NO_x, the researchers must take into account many aspects of cost, reliability and fuel consumption. The Selective Catalytic Reduction of NO_x, using NH_3 as a reductant, was chosen by the European vehicle manufacturers as the most promising technology able to comply with the strict emissions standards for heavy-duty diesel vehicles in July 2003 [55].

Selective catalytic reduction of NO_x by ammonia works in different steps. First of all, ammonia is obtained from the decomposition of urea according to the following reactions:

$$NH_2\text{-}CO\text{-}NH_2 \rightarrow NH_3 + HNCO \quad \text{(Equation 1.7)}$$

$$HNCO + H_2O \rightarrow NH_3 + CO_2 \quad \text{(Equation 1.8)}$$

After producing ammonia by urea hydrolysis, ammonia reacts with NO_x in the presence of O_2 to obtain N_2 and H_2O. There are three different reactions for NO_x reduction by ammonia:

The main SCR reaction is the reduction of NO with ammonia that can be called as standard SCR reaction:

$$4NH_3 + 4NO + O_2 \rightarrow 4N_2 + 6H_2O \quad \text{(Equation 1.9)}$$

However, the reaction between NO, NO_2, and NH_3 is much faster if the ratio between NO and NO_2 is equal. Under those conditions, the reaction called fast SCR:

$$2NH_3 + NO + NO_2 \rightarrow 2N_2 + 3H_2O \quad \text{(Equation 1.10)}$$

Usually, diesel oxidation catalyst (DOC) is used in the system to oxidize NO to NO_2:

There is a third reaction that occurs if the NO on NO_2 ratio is below 0.5 where NH_3-SCR with only NO_2 takes place, that called NO_2-SCR :

$$4NH_3 + 3NO_2 \rightarrow 3.5N_2 + 6H_2O \quad \text{(Equation 1.11)}$$

There are also several side reactions that occur and compete with the previous reactions. NO and NH_3 oxidation are two major reactions that may occur.

Oxidation of NO to NO_2 is considered to be the rate-determining step in NH_3-SCR, to improve the fast SCR reaction step:

$$NO + 1/2O_2 \rightarrow NO_2 \quad \text{(Equation 1.12)}$$

However, NH_3 oxidation is not a desirable reaction, thus less NH_3 will be available for NH_3-SCR and at the higher temperatures, and the oxidation of ammonia becomes more pronounced. NH_3 can be oxidized by the different reaction:

$$4NH_3 + 5O_2 \rightarrow 4NO + 6H_2O \quad \text{(Equation 1.13)}$$

$$4NH_3 + 3O_2 \rightarrow 2N_2 + 6H_2O \quad \text{(Equation 1.14)}$$

In the catalytic reaction, activated sites on the catalyst rapidly adsorb ammonia and gas-phase NO to form an activated complex [56]. The high temperature of the flue gas converts the ammonia to free radicals and provides the activation energy for the reaction [57]. NO_x reduction with ammonia is exothermic, resulting in the release of heat. However, because the NO_x concentration in the flue gas at the inlet of the SCR is typically 0.01–0.02% by volume, the amount of heat released is correspondingly small. Thermodynamic equilibrium is not a limiting factor in NO_x reduction if the flue gas is within the required temperature range [57]. A good description of ammonia storage and release over the catalyst surface is a crucial part of the overall SCR model. Therefore, a good model for the ammonia adsorption and desorption is important in order to get an accurate understanding of transient SCR activity. The reaction of ammonia oxidation takes place from the adsorbed NH_3 on the active sites, so the capability of oxidizing ammonia is dependent on the characteristics of ammonia storage and release. Therefore, the simulations of the kinetic parameters of NH_3 oxidation reaction must be considered together with taking into account the parameters for NH_3 adsorption and desorption [57].

The protocol developed by Wilken *et al*. [58] was applied, the focus of their work was to develop a kinetic model able to describe ammonia SCR mechanism over Cu-Beta catalyst. In step 1, NO and oxygen were passed over the catalyst and NO oxidation was investigated. This reaction can have a major effect on SCR rate since NO_2/NO mixtures are known to be more reactive than NO alone. Their experimental results showed that at lower temperatures the conversion is kinetically limited and the conversion of NO into NO_2 increases with temperature. At 400°C, an inhibition of NO conversion was observed, probably due to the blockage of the active sites by the NO_2 produced.

The oxidation of NH_3 has been studied by Wilken *et al*. [58]. For a realistic simulation of NH_3 oxidation, ammonia adsorption and desorption were considered together, as the ammonia-

oxidizing capability is dependent on its storage and release characteristics. The results reveal that ammonia oxidation rate increases as the temperature becomes higher. Wilken*et al*. [58] revealed that at the lowest temperature investigated (200˚C) there was no oxidation of ammonia. Luo *et al*. investigated the effect of the NO_2/NO_x ratio at different temperatures to NO_x conversion. NO_x conversion is very sensitive to the NO_2/NO_x ratio at temperatures between 250ºC and 300ºC, and a NO_2/NO_x ratio of 0.5, corresponding to an equimolar ratio of NO and NO_2, results in the highest conversion. This demonstrates that the fast SCR reaction has the highest rate at low temperatures. At higher temperatures (300–500°C), the dependence of NO_x conversion on NO/NO_2 ratio decreases, and very high NO_x conversion can be achieved regardless of the NO_x feed. At the highest temperature, 550°C, the NO_x conversion actually decreased slightly when increasing the NO_2 ratio from 0.5 to 1 [59].

Based on the inlet NO_x ratio, the different SCR reaction types have different dependencies on temperature. For the standard SCR (NO_2/NO_x=0), the conversion gradually increased with temperature from 250 to 400°C, and then remained about constant from 400 to 550°C. The fast SCR reaction (NO_2/NO_x=0.5) conversion was consistently high, even at low temperatures, but decreased slightly at 500°C or higher. The conversion for NO_2-SCR (NO_2/NO_x=1) first increased with increasing temperature until 300°C, and then decreased at higher temperatures.

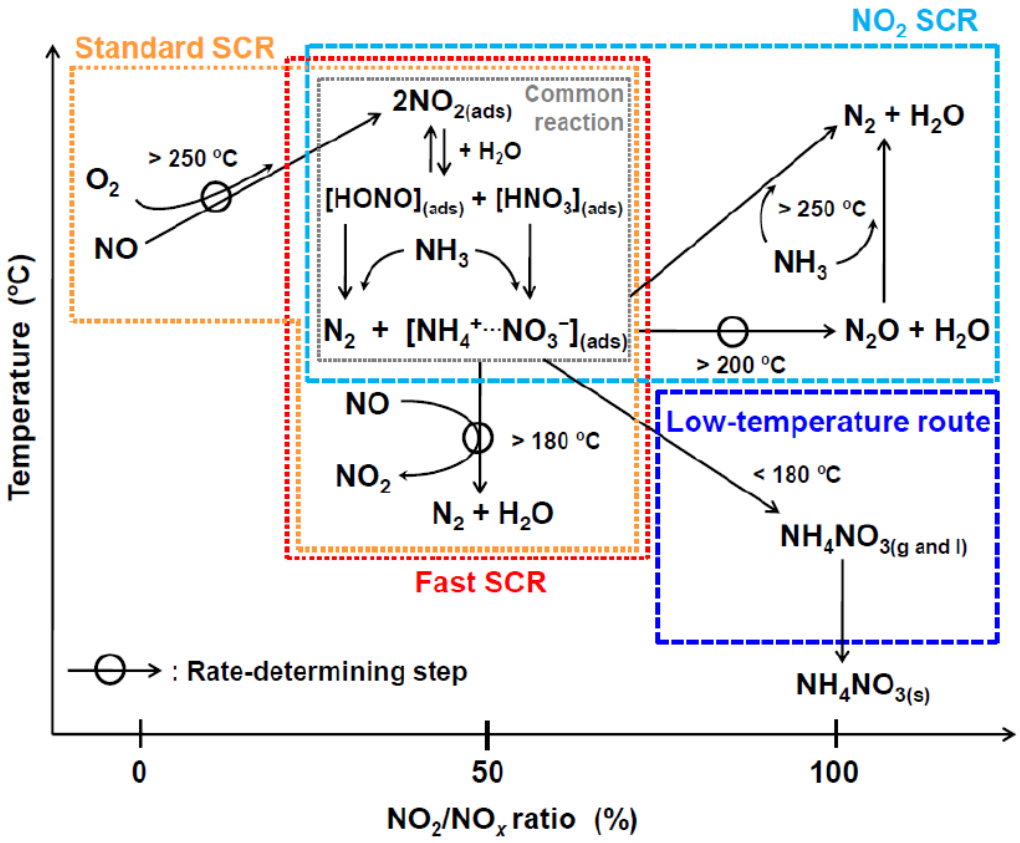

Figure 1.5 – **Generic SCR-reaction network over Fe-exchanged zeolites** [59]

Nowadays, in the new generation of diesel engines SCR incorporate with DPF (Diesel Particulate Filter). Ideally, the group of the soot abatement system and deNO$_x$ by impregnating the catalyst on the particulate filter (DPF) has many advantages. One of them is the reduction in the size of the various pollution control systems (oxidation catalyst for HC and CO, DPF for soot reduction for NO$_x$). This channel has some obstacles as the filter regeneration step to particle resulting in mounted in temperatures that can reach 900°C. The SCR catalyst will have to withstand extreme temperatures and keep its intrinsic properties of selective NO$_x$ conversion at a high level over time.

4.3.2.1 Inhabitation of the NH$_3$-SCR

Besides the reactions presented in the last section, undesired phenomena occur in parallel with the SCR process that limiting deNO$_x$ efficiency. Among them, the NH$_3$ oxidation provokes undesired over-consumption of the reducing agent, at the temperature higher than 420°C [60].

Low-temperature temporary catalyst deactivation due to the formation of NH_4NO_3 is another undesired phenomenon. When nitrates and ammonia ad-species interact at the temperature below 100°C, ammonium nitrate is formed and blocks the active sites for NH_3-SCR reaction. The formed NH_4NO_3 is stored on the active sites of the catalyst and leads to a reversible inhibition. However, at the higher temperature, the SCR catalyst is regenerated, since NH_4NO_3 undergoes thermal decomposition yielding thermal gaseous products, including N_2, H_2O, N_2O, and HNO_3. NH_4NO_3 is solid with a melting point of 170°C [61].

Finally, competitive adsorption between NH_3 and gaseous compounds in diesel engine exhaust constitutes a very important concern. Water, unburned hydrocarbons, carbon monoxide (CO), and sulfur oxide have been reported to be co-adsorb with ammonia [46,47].

5 The different techniques for removing hydrocarbons, CO and soot

5.1 Diesel Oxidation Catalyst (DOC)

The DOC primary function is oxidation of CO and unburned hydrocarbons to less harmful products like CO_2, H_2O, and NO to NO_2.

$$CO+1/2O_2 \rightarrow CO_2 \quad \text{(Equation 1.15)}$$

$$HC+O_2 \rightarrow CO_2+H_2O \quad \text{(Equation 1.16)}$$

$$NO+1/2O_2 \rightarrow NO_2 \quad \text{(Equation 1.17)}$$

DOCs generally consist of a precious metal coated flow-through honeycomb structure contained in the stainless steel housing. As hot diesel exhaust flows through the honeycomb structure, the precious metal coating causes a catalytic reaction that breaks down pollutants into less harmful components.

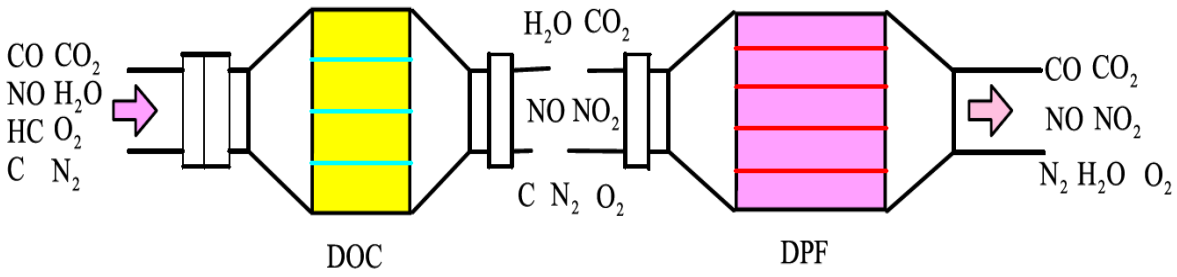

Figure 1.6 – **Diesel Oxidation Catalyst and Diesel Particulate Filter** [64]

5.2 Diesel particulate filters (DPF)

Today, application of Diesel particulate filters (DPF) is commonplace in automotive Diesel engines. The particulate filter is normally used in diesel engines to remove diesel particulate matter or soot from the exhaust of diesel engines. The particles are kept on the interior walls of the filter. Trapped particulates are burnt at normal exhaust temperatures using the powerful oxidative properties of NO_2 or at higher temperatures using O_2. In order to remove the particles from the filter walls, the filter must be periodically regenerated that need a high temperature.

6 The active catalysts in urea-SCR

The study of the NH_3-SCR and DPF incorporation is the focus of this thesis work. As mentioned above the incorporation of the NH_3-SCR catalyst in the pores of DPF has some obstacles as the DPF regeneration step which leads to a significant rise in temperature. Therefore, such catalysts have to exhibit both high N_2 selectivity and high-temperature stability over a broader operating temperature window. The important parameters influencing the activity of a catalyst are mainly defined by the acidity and the redox power [18]. Indeed, in NH_3-SCR, the mechanism is of Eley-Rideal type with strongly adsorbed ammonia and NO_x in gaseous form and weakly adsorbed [15, 16]. The first step is the adsorption of ammonia on an acidic site [21]. The adsorbed ammonia can then be activated on a redox site in a second step. It should be noted that, at the same time, part of the NO can oxidize to NO_2. The next step is the formation of one or more intermediate species and then desorption in the N_2 form [22]. The last step allows the

restoration of the redox site after its re-oxidation. This re-oxidation is carried out by NO_2 in fast-SCR and, where appropriate, by surface oxygen and gaseous oxygen. Deactivation of the catalysts is therefore often synonymous with a degradation of their acid or redox properties, in particular when they are dealing with the high temperature in the presence of water [23]. The last four decades of research yielded different classes of catalysts with a vast amount of diverse formulations.

6.1 V_2O_5-WO_3/TiO_2

The catalyst commonly used for the after-treatment of stationary sources is V_2O_5-WO_3/TiO_2 which is highly active for NH_3-SCR. In this catalyst the V_2O_5 is the active species, anatase titania (TiO_2) constitutes the support of the catalyst, while tungsten (WO_3) works as a physical and chemical promoter inhibiting a certain function of anatase phase of titania [65]. To their cost and performance advantages, these catalysts are considered good catalysts in terms of NO_x reduction and thermal stability. Various promoters, such as Mo, Fe, Ce or Mn oxides are occasionally implemented [21–23]. Despite the conventional V_2O_5 notation, vanadium is actually dispersed as VO_x species over the high surface area support due to the high interaction strength between V and Ti [69]. The formal oxidation state of supported vanadium oxide is either V^{5+} or V^{4+}, but catalysts generally contain both oxidized and reduced vanadium cations. The V^{5+}/V^{4+} redox couple is crucial for the SCR reaction, but also for oxidation catalysts or vanadium redox batteries. In aqueous solutions, V^{5+} ions form yellow complexes, while V^{4+} generates blue aqua-complexes [70]. For mobile applications where both DPF and SCR catalyst are required, DPF regeneration can severely deactivate the vanadium SCR catalyst. This phenomenon decreases the catalyst surface area and results in lower activity. On the other hand, the release of volatile vanadium compounds, such as V_2O_5, from these catalysts at high temperatures is a concern because of its toxic nature [71]. Among all supports, TiO_2 seems to

be the best choice for selective catalytic reduction of NO_x because of its thermal and chemical stability, acid-base properties and resistance to sulfur poisoning [72]. However, some oxide based systems can generate difficulties because of undesired phase transitions under operating conditions. A good example is TiO_2 because of its three polymorphs, anatase, rutile and brookite, which are all naturally occurring at atmospheric pressure [73].

WO_3 is proposed to have multiple promotional effects including the increase in the number of NH_3 adsorption sites [74] and the improvement of thermal stability of the thermodynamically unfavorable anatase phase [75]. Another important promoting effect is gained by increasing the surface acidity [76], which guarantees the NH_3 supply for the SCR reaction. One of the most important roles of tungsten is stopping the transformation of monomeric vanadyl to crystalline V_2O_5 [77]. Mainly monomeric vanadyl species are formed on the anatase surface at low V_2O_5 concentration, and then the monomeric species react to form polymeric vanadates with an increase in vanadium loading. When vanadium loading exceeds on the anatase surface, V_2O_5 crystallites are formed [77].

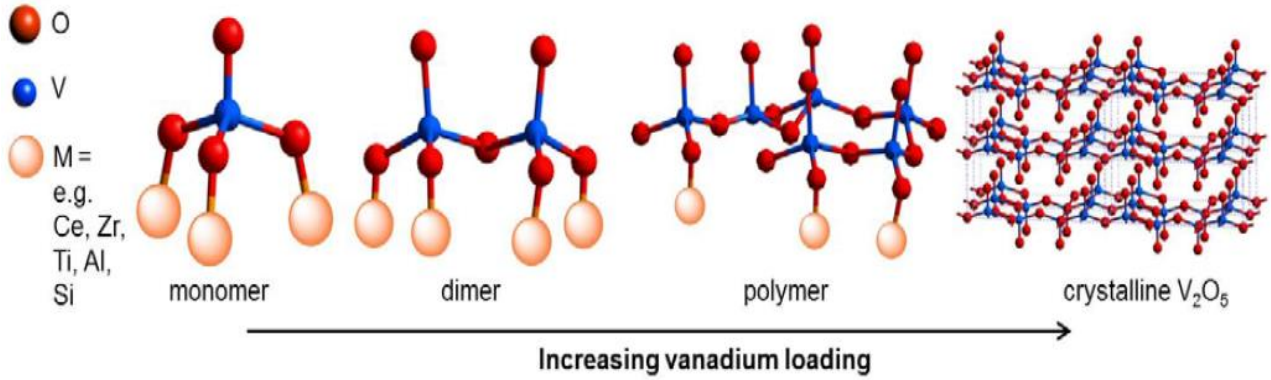

Figure 1.7 – **Possible structures of the VO_x species reported for supported vanadia catalysts depending on the vanadium loading** [77]

With the addition of WO_3, the weak basic sites of titania disappear and WO_3-TiO_2 becomes much more acidic. The type of acidity (Brönsted or Lewis sites) thereby depends on the loading as well as the surrounding atmosphere [78]. In the absence of water and with a moderate W-loading, surface tungstate species are present as Brönsted and Lewis acid sites [79], while in the presence of water, the Lewis acid sites can convert into Brönsted sites [79]. In order to improve the catalytic activity of V_2O_5-WO_3/TiO_2, many researchers investigated the effect of promoters adding on the catalytic activity. Promoters such as CeO_2 and MoO_3 create acid sites on the catalyst surface and the catalysts exhibit a higher catalytic activity [24,25]. Gao *et al*. investigated the effect of Mo adding on the structure of V_2O_5-WO_3/TiO_2. They proposed that, by dispersing molybdenum spices on the anatase titania the NO_x conversion improved by stopping the undesired transformation of anatase to rutile TiO_2 phase [80].

Ma *et al*. prepared Ce modified V_2O_5-WO_3/TiO_2 catalysts possessing comparable activity with commercial V_2O_5-WO_3/TiO_2 for the selective catalytic reduction of NO with NH_3 [82]. The synthesized catalysts are donated as V(x) Ti, V(x) WTi, V(x) CeTi andV(x) CeWTi with x representing the mass percentage of vanadium.

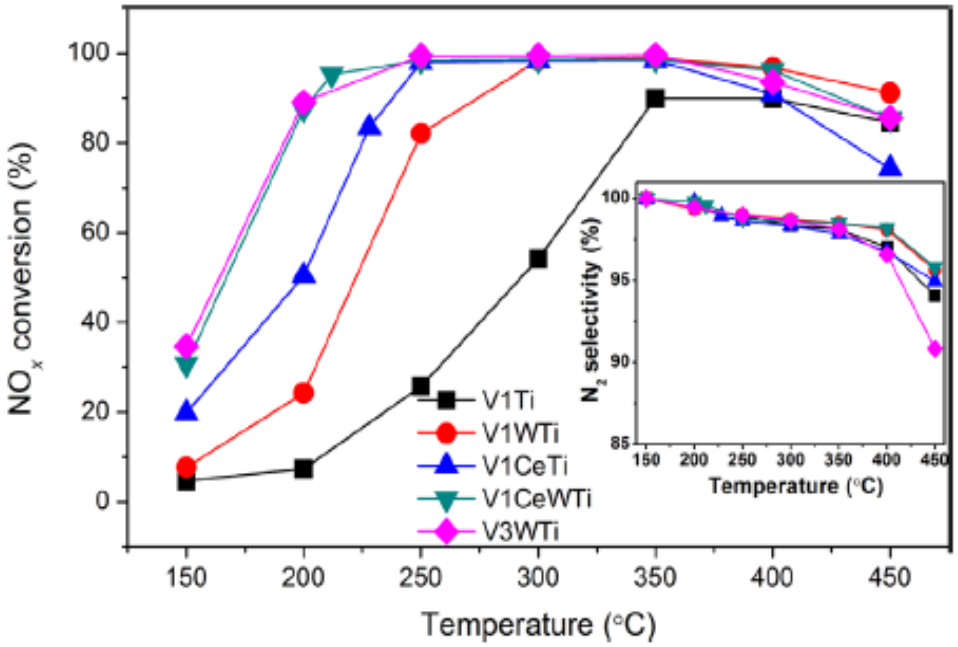

Figure 1.8 – **NO_x conversions and N_2 selectivity of the catalysts. Reaction conditions: [NO] = [NH_3] =500 ppm, [O_2] =5% and N_2 as balance. GHSV=150,000 h^{-1}** [82]

Figure 1.8 shows that the low-temperature SCR activity obviously enhanced by the V_2O_5–WO_3/TiO_2 modification with Ce. The V1CeWTi catalyst shows about 80% NO_x conversion and about 95% N_2 selectivity in the large temperature range between (190 to 450° C). They suggested that the high catalytic activity in low temperature can be the result of the synergistic effect between Ce and V by forming V–O–Ce bridges [82].

6.1.1 Proposed mechanisms

It is recognized that the active sites for NH_3-SCR on the V_2O_5-WO_3/TiO_2 catalyst are the vanadium oxide species. Some researchers believe that the increase of Brönsted acidity provided by WO_3 favors the reaction [83] while others state that the selective NO_x reduction reaction requires two active sites [84]. Accordingly, they believe WO_3 would offer a second active site [84]. The first popular proposal was an Eley-Rideal type mechanism, where gaseous NO reacted with adsorbed NH_4^+ to form N_2 and H_2O [85]. The ammonium ion is thereby adsorbed on a V-OH Brönsted acid site and an adjacent V^{5+}=O species acts as the redox active site [86].

Following the amide-nitrosamide SCR reaction mechanism (Fig 1.9) NH_3 absorbed on Lewis acid site instead of a Brönsted acid site and then splits into adsorbed NH_2 and hydrogen before it can react with NO. This mechanism was more detailed especially due to the introduction of the nitrosamide (H_2N-NO) intermediate which decomposes into N_2 and H_2O [87].

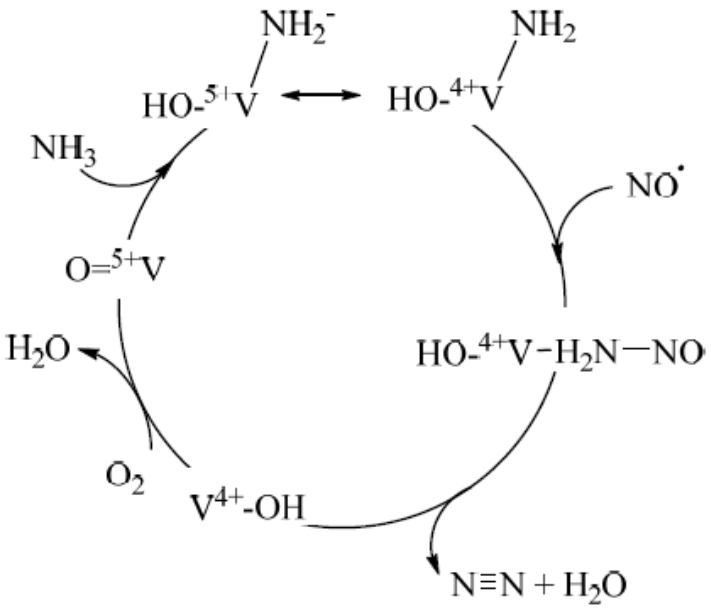

Figure 1.9 **– Proposed amide-nitrosamide reaction mechanism** [87]

A combination of the reaction including, the adjacent V species and the amide-nitrosamide mechanism was introduced by Topso *et al*. for standard SCR reaction. The mechanism proposed by Topso *et al*. [88, 89] for the standard-SCR requires the presence of a Brönsted V^{5+}-OH acid site on which the ammonia can be adsorbed. The proximity of a redox V^{5+}=O site is necessary to activate the -NH_4^+ species. NO can then incorporate to form an intermediate which is subsequently decomposed into N_2 and H_2O. The last step is the regeneration of redox site by re-oxidizing V^{4+}-OH to V^{5+}=O. This re-oxidation is completed by dioxygen (or NO_2). It is considered the limiting step in "Standard-SCR" for temperatures below 300°C. The rate constant of this step can be increased by the presence of NO_2 (better oxidizer than O_2) [41,42].

6.2 Zeolites

The zeolite material itself is a micro-porous, crystalline aluminosilicate with a crystalline structure similar to one of the examples: small, medium, and large-pore (Fig 1.10). The structure is composed of tetrahedral of an Al^{3+} or Si^{4+} ion surrounded by four O^{2-} ions. The Al and Si atoms are referred to by the term "T-atoms" because of their tetrahedral coordination [90].

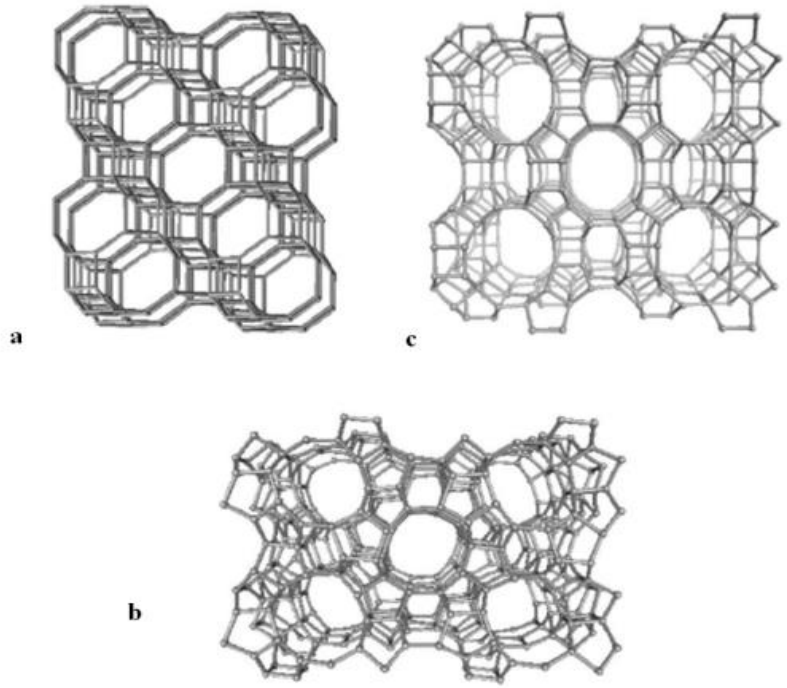

Figure 1.10 – **Structures of (a) small-pore CHA, (b) medium-pore MFI, and (c) Large-pore MOR zeolite structures** [90]

Zeolites are used for processes operating at higher temperatures where mixed oxides of vanadium and titanium deactivate quickly; these catalysts have the particularity of not promoting the oxidation of ammonia by O_2. The two key properties of zeolites are the high surface areas that provide a large number of active sites for NH_3-SCR to occur, and high acidity results in an increased number of the Brönsted acid sites that is important for NH_3 adsorption. Acidity is inversely proportional to the Si/Al ratio of the zeolite, which makes this an important factor in determining the catalytic properties of the zeolite [91]. Zeolites are not exceptionally

active for the ammonia SCR of NO_x by themselves, thus it is necessary to add an active cation such as Cu and Fe in order to improve the catalyst activity [92]. The high temperature operating range of zeolites, as well as their low thermal resistance in the presence of water and poisoning by sulfur dioxide, limits their commercial application [93]. The main drawback of zeolite SCR catalysts is their lack of hydrothermal stability. At high temperatures and in the presence of water vapor, the zeolite framework is compromised; combined effects of dealumination and undesired ion migration into the framework diminish the SCR capability [46,47].

The most recent SCR catalyst formulations contained copper exchanged into the chabazite (CHA) family of zeolites and were successfully developed for diesel vehicle applications. Cu-SSZ-13 and Cu-SAPO-34 catalysts attracted much attention for their utility in NH_3-SCR reactions for eliminating NO_x pollution. Both of the catalysts were found to be much more active, selective and hydrothermally stable for NH_3-SCR catalytic reactions. Among them, SSZ-13 and SAPO-34 are the main classes of zeolite of the CHA structure, and have a three dimensional zeolite with a small pore structure [49–51].

6.2.1 Cu-Zeolite SCR

Sultana *et al*. have investigated the effect of Cu ion exchange in SCR performance of the ZSM-5 zeolite (Fig 1.11). They found that Cu-exchanged Na-ZSM5 is significantly more active than H-ZSM. This effect is more noticeable in the range of 160 to 320°C. They attribute this high performance to an increase in the number of accessible Lewis and Brönsted acid sites and improving NO to NO_2 oxidation [92].

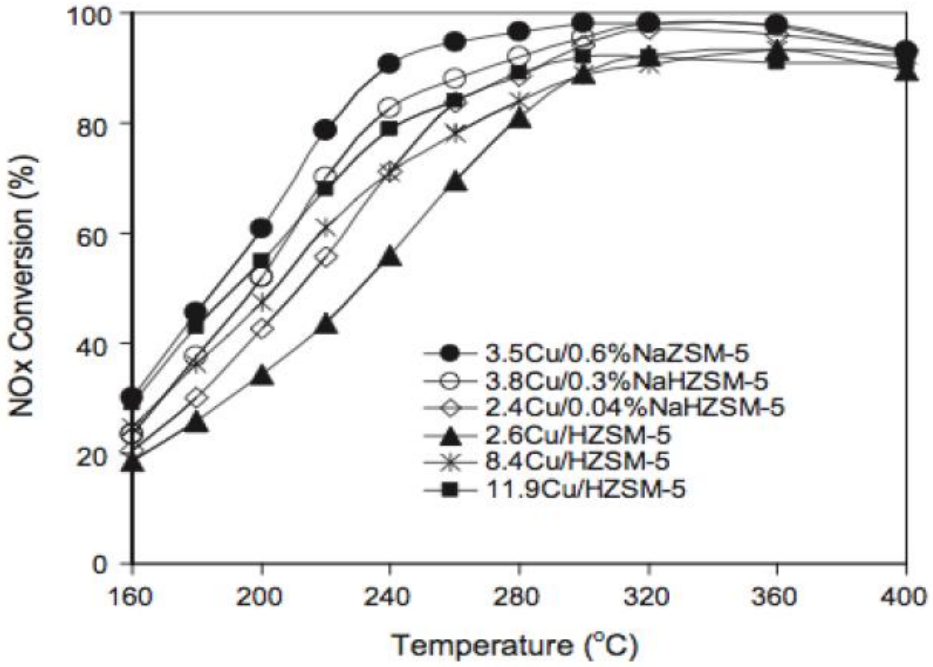

Figure 1.11 **– Selective catalytic reduction of NO by NH_3 over Cu-exchanged Na- and H-form ZSM-5 zeolites** [92]

6.2.1.1 Reaction mechanism

Janssens *et al.* [99] was proposed a mechanism for NH_3-SCR reaction over Cu-zeolite and is shown in Figure 1.12. According to this reaction mechanism, NO and O_2 (1) or NO_2 (8) first react with a Cu^+ site (A) to form a nitrate (B) or nitrite (C) species. The nitrate species is reduced by NO (2) to form a nitrite (C) species. The nitrite species react with ammonia to form nitrogen and water (4) and a Cu^{2+}-OH^- species (E), which then react with NO and ammonia to form water (6) and a Cu^+-$NONH_2$ species (G), which decompose to form nitrogen and water (7) and a Cu^+ site (A).

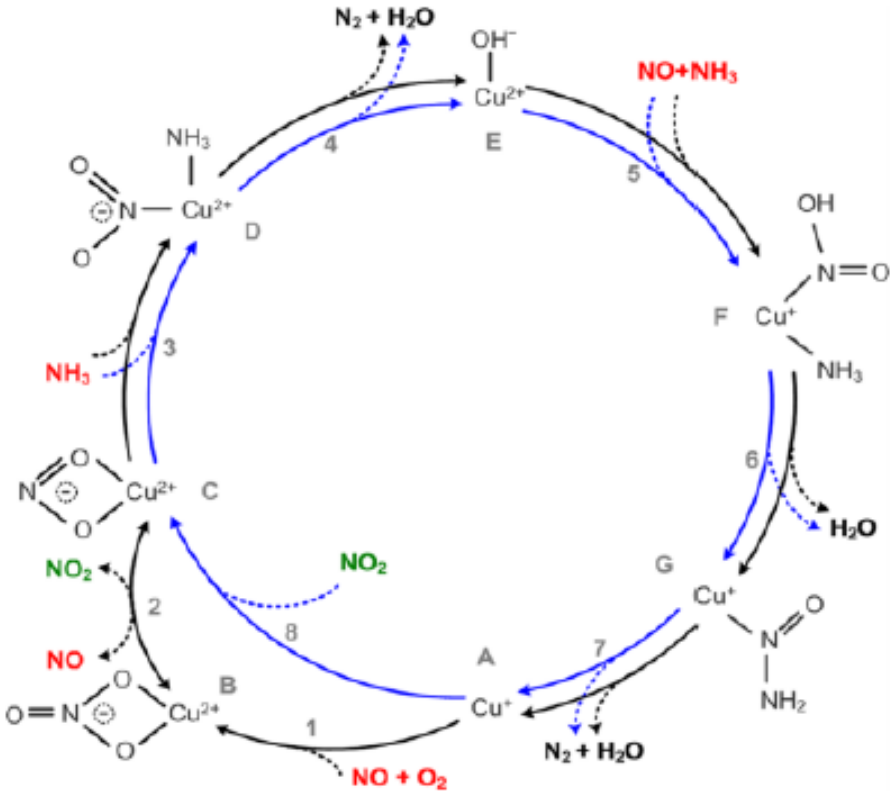

Figure 1.12 – **Catalytic cycle of NH_3-SCR on Cu-ZSM5** [99]

6.2.2 Fe-ZSM5 as SCR catalyst

In the last two decades, the modification of zeolites by incorporation of transition metals, especially with Fe has received much attention, their application in the NH_3-SCR reaction is of great importance for exhaust gas after-treatment [52,53].

Kustov *et al*. investigated the catalytic activity of different Fe-containing ZSM-5 catalysts (0.8–5wt %). At the highest temperature tested, 550°C, the NO_x conversion actually decreased slightly when increasing the NO_2 ratio from 0.5 to 1. Based on the inlet NO_x ratios, the different SCR reaction types have different dependencies on temperature. For the standard SCR (NO_2/NO_x=0), the conversion gradually increased with temperature from 250 to 400°C, and then remained about constant from 400 to 550°C. The fast SCR reaction (NO_2/NO_x=0.5) conversion was consistently high, even at low temperatures, but decreased slightly at 500°C or

higher. The conversion for NO_2-SCR (NO_2/NO_x=1) first increased with increasing temperature until 300°C, and then decreased at higher temperatures. For the conventional and the mesoporous catalyst with the same iron loading, mesoporous catalyst is more active in all temperatures. They suggested the high activity can be a result of the better diffusion of the reactant or/and product in the mesoporous. By increasing Fe content the catalytic activity increase for both conventional and mesoporous catalyst [102].

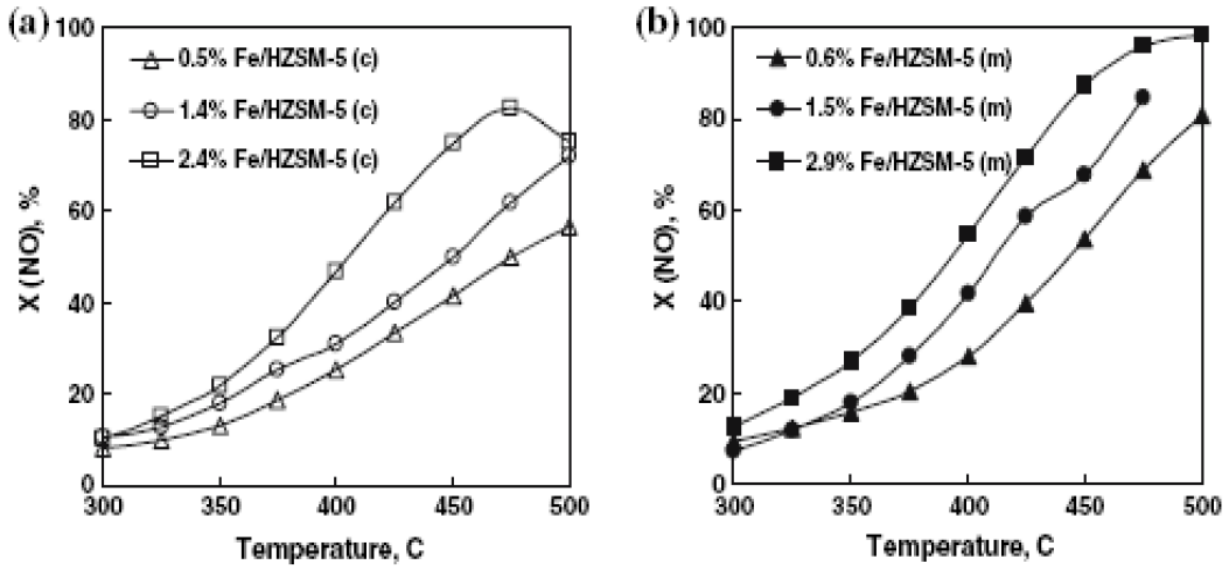

Figure 1.13 – **NO_x conversions in SCR with ammonia for conventional (a) and mesoporous (b) Fe/HZSM-5 catalysts. Reaction conditions: 50mg of the catalyst, 1000 ppm NO, 1100ppm NH_3, 3.5%O_2, 3H_2O balanced with N_2** [102]

6.2.2.1 Reaction mechanism

During the last years, all groups of Fe species have been proposed to be the active species in NH_3-SCR, but among the reported species the binuclear Fe-O-Fe species, were favored as the active species in the reduction of nitrogen oxides [103].

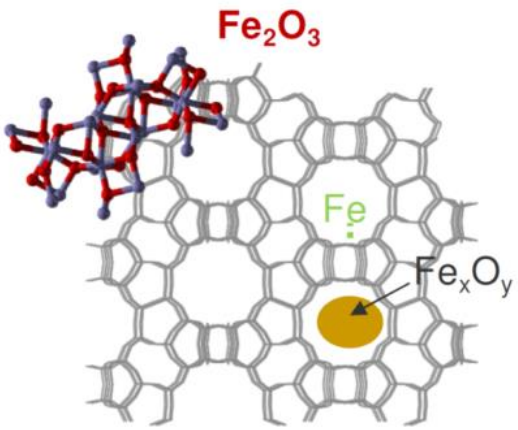

Figure 1.14 – **Overview of the different Fe species which can be present in Fe-zeolites**

The reason for the uncertainty about the active Fe species in the NH_3-SCR reaction is that Fe species can be present as Fe^{2+} and Fe^{3+} species, as the oxidation state of Fe can be changed easily. Delahay *et al*. [104] proposed a reaction mechanism for NO_x conversion by ammonia that is shown in Figure 1.15. In this cycle in the first step Fe^{2+} species is oxidized by O to an iron III oxo/hydroxo species. The extra framework oxygen then reacts with NO to form a nitrogen oxide intermediate bound to iron. Finally, this species reacts with ammonia to form water and nitrogen with reduction of Fe^{3+} to Fe^{2+}species [104].

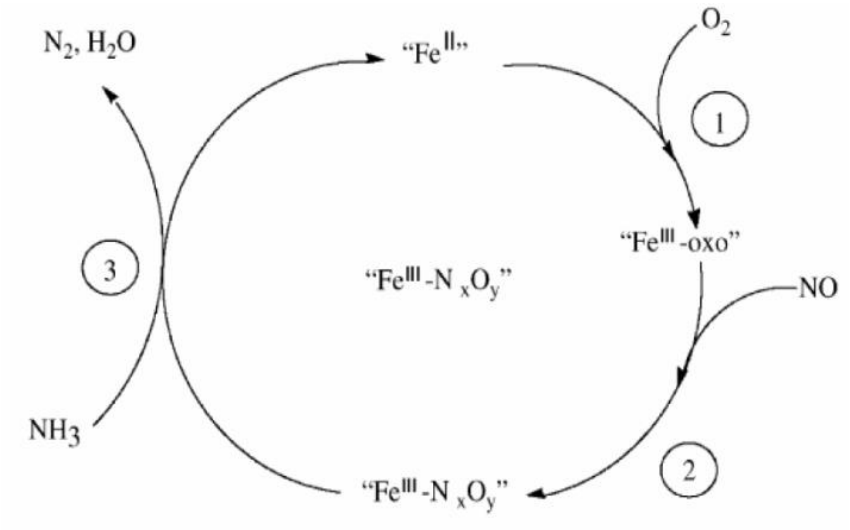

Figure 1.15 – **Catalytic cycle of NH_3-SCR on Fe-ZSM5** [104]

6.2.3 CuFe-ZSM-5

Narula *et al*. [105] investigated the catalytic activity of different ion exchanged ZSM5 catalyst. The CuFe-ZSM-5 catalyst exhibits about 80% NO_x conversion at 150°C and maintains at 90% conversion efficiency in the 200-450°C range which drops to 68% at 650°C. In comparison, the Cu-ZSM-5 powder shows only 30% NO_x conversion at 150°C which gradually increases to 90% at 250°C but starts to drop below 90% at 450°C and 58% at 625°C. The Fe-ZSM-5 powder exhibits 90% NO_x conversion efficiency in the 350-550°C range which drops to 80% at 650°C. The N_2O production (Figure 1.16.B) during SCR with CuFe-ZSM-5 reaches the maximum at 150°C and then is equal to that of Cu-ZSM-5 in the 200-650°C range. Fe-ZSM-5 does not produce N_2O at all during the SCR catalytic cycle. Thus, the low-temperature reactivity of CuFe-ZSM-5 can be attributed to a synergistic effect resulting from the incorporation of Fe^{3+} in close proximity to Cu^{2+} [105].

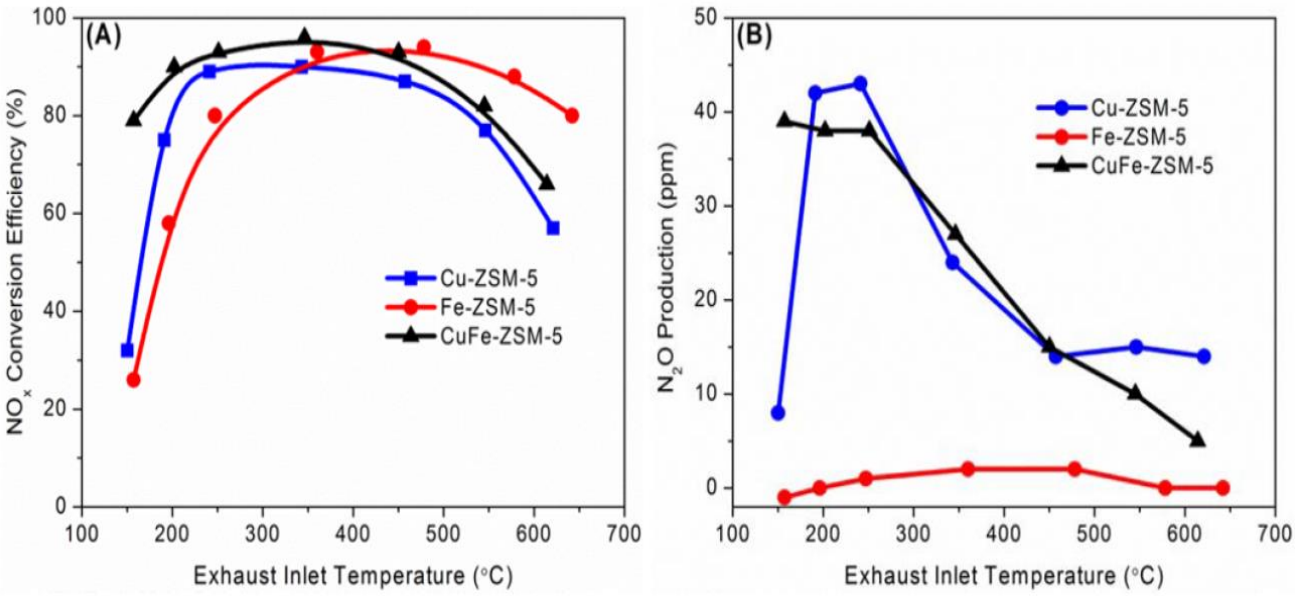

Figure 1.16 – **NO_x conversion (A) and N_2O production (B) of CuFe-ZSM5; 8.5% O_2, 8% CO_2, 7.25% H_2O, 250 ppm NO_2, 250 ppm NO, 500 ppmNH_3, space velocity of 50,000 h^{-1}** [105]

6.3 Cerium based catalyst

Cerium is a soft ductile metal which easily oxidizes in air and is abundantly available. It has a dual valence state: Ce^{4+} (CeO_2) and Ce^{3+} (Ce_2O_3). It is usually present in compounds in both the tetravalent (Ce^{4+}) and trivalent (Ce^{3+}) states. The crystallography of cerium oxide is cubic face-centered (CFC) structure [106]. In cerium oxide, cerium and oxide ions are arranged in a fluorite structure, oxygen atoms in the ceria are arranged in the plane with one another [107]. On account of, optimal textural properties and intense ability to interact with other components, cerium oxide can be used as the promoter [108], support [109] and active sites [110] for NH_3-SCR. Hence, many studies have focused on the Ce-based mixed oxide catalysts for the NH_3-SCR reaction; high NH_3-SCR activity could be attributed to considerable oxygen storage capacity [111], facility of changing oxidation state between Ce^{3+} and Ce^{4+} [112] and its stability to enhancing the oxidation of NO to NO_2 [110]. Moreover, ceria-based NH_3-SCR catalysts have attracted much attention due to their high non-toxic and relatively cheap characteristics [66,67]. NH_3 and NO_x were found to adsorb on the ceria simultaneously. Zhang *et al*. [115] proposed ceria with NO_x and NH_3 interaction. In the presence of NO_x, NH_3 reacted with adsorbed NO_x species along with forming N_2 at lower temperatures (250-450°C), and while at higher temperature, a significant portion of the NH_3 was oxidized to NO [115].

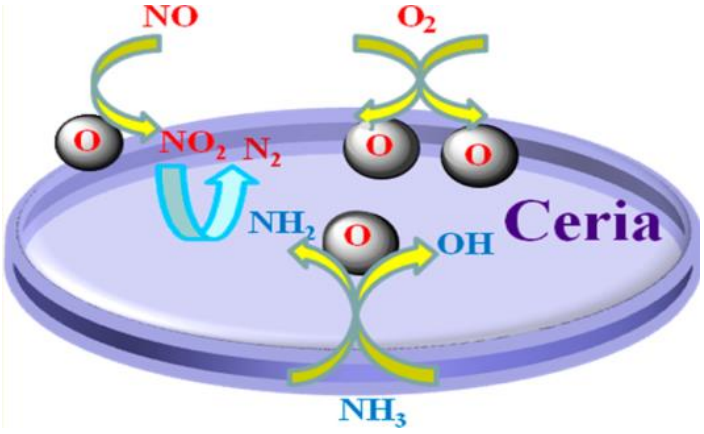

Figure 1.17 – **ceria interaction with NO_x and NH_3** [115]

It is generally accepted that NH_3 activation and ammonia adsorption are the key factors in the NH_3-SCR reaction. Therefore, various acidic components, such as VO_x, TiO_2, and MnO_2 and/or mix of two or more were used to improve the NH_3-SCR activity of ceria by improving ammonia adsorption.

Peng *et al*. [116] compared the NO_x conversion of V_xCe catalysts from 150 to 400°C with the activity of the commercial $V_2O_5WO_3/TiO_2$ catalyst in Standard-SCR condition. The catalysts are denoted as V_xCe, where x indicates the theoretical molar ratio of V to Ce. Only the $V_{0.75}Ce$ catalyst shows a higher NO_x conversion than the commercial $V_2O_5WO_3/TiO_2$ until 350°C, and after 350°C $V_2O_5WO_3/TiO_2$ exhibits higher activity. They suggested that Both Lewis (CeO_2 and polymeric VO_x) and Brönsted ($CeVO_4$) acid sites are reactive. At low temperature, adsorbed $N_2O_2^{2-}$ and dimer $(NO)_2$ are active to bond with adsorbed NH_3 species. At high temperature, surface nitrite or nitrate species can also be involved in the reaction [116].

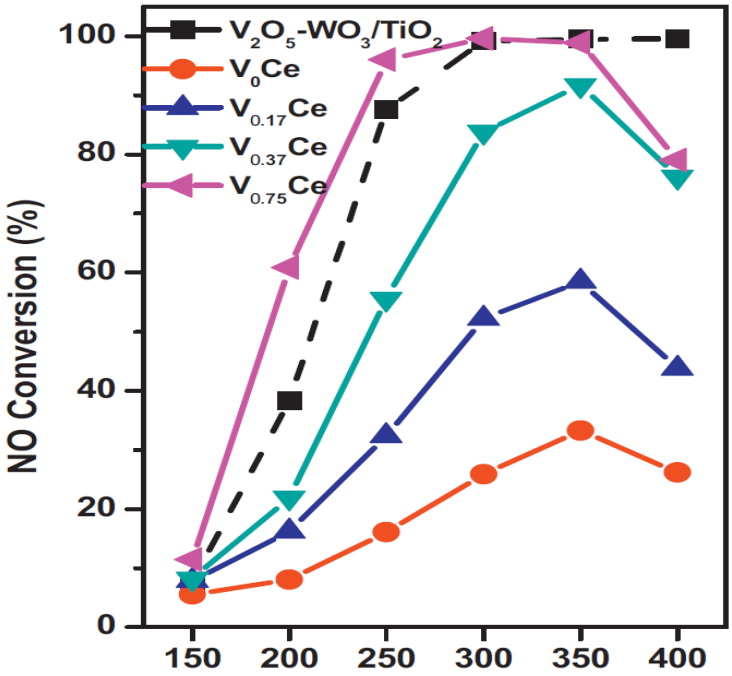

Figure 1.18 – **NO conversion NO = NH_3 = 500 ppm, O_2 = 3% and balanced by N_2, GHSV = 120.000 h^{-1}** [116]

In this context, catalysts based on manganese oxide (Mn) have been increasingly studied. The supported Mn oxides, such as MnO_x/TiO_2 [117] shows the NH_3-SCR activity at the low temperature in the presence of O_2. The oxides of manganese can also be used as a support, such as Fe-MnO_x/TiO_2 [118], Cu-MnO_x [119], Ni-MnO_x [120] or Nb-MnO_x [121] was reported to be active for NO_x reduction by ammonia at the low temperature. The use of manganese oxide that can be active at the high temperature has some disadvantages, namely significant formation of N_2O and low sulfur and water resistance [75–77]. However, the addition of Ce to Mn catalyst makes it possible to increase the NH_3-SCR activity.

Jiang *et al*. [124] prepared a series manganese-cerium oxide (MnO_x-CeO_2) with different Mn/(Mn+Ce) ratio. Figure 1.19 shows the SCR performance of MnO_x-CeO_2 with different Mn contents after catalyst calcination at 600°C. It can result from Figure 1.19, the MnO_x(0.32)-CeO_2 is the most active catalyst comparing to other catalysts in low temperature. They

suggested that higher surface area, better oxygen mobility, and richer active surface oxygen spices are the responsible for the good performance of this catalyst [124]. The MnO_x-CeO_2 catalysts have good properties, particularly due to the synergy between these two oxides. They are very active catalysts at low temperatures (150 to 250°C). However, their operating temperature range is too low. The thermal stability of these solids is limited to temperatures below 900°C [125].

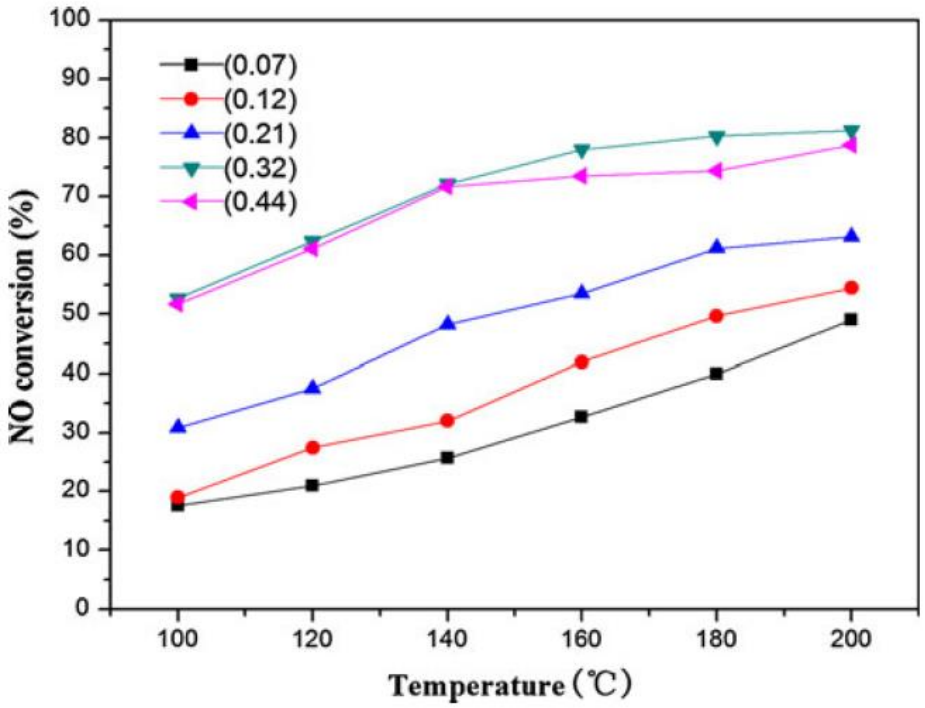

Figure 1.19 – **Performance of MnO_x(X)-CeO_2 (600°C) with different Mn contents** [124]

Chen *et al*. [126] investigated the ammonia SCR activity for series of cerium-tungsten oxide catalysts with different substitution level. Figure 1.20 shows that, while CeO_2 and WO_3 presented separately very low NO_x conversion achieved. However, the mix of two improved the catalytic activity incredibly. Among cerium-tungsten oxides, CeO_2–WO_3 with a Ce/W molar ratio of 3/2 exhibited the best activity. At about 200°C the NO_x conversion reaches 95%, and the activity could reach 100% at around 200–450°C. The strong interaction between Ce and W could be the main factor for the high activity of the CeO_2–WO_3 mixed oxide catalyst.

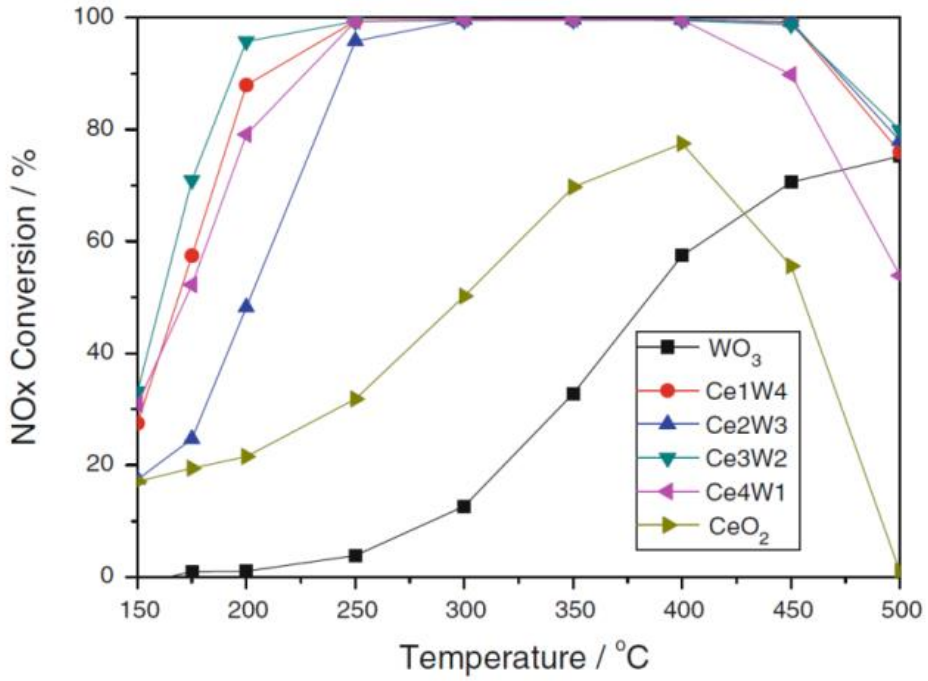

Figure 1.20 – **NO_x conversion, 500 ppm NO, 500 ppm NH_3, 3% O_2, N_2 as balance gas, GHSV: 47,000 h^{-1}** [126]

Peng *et al*. [127] proposed a reaction mechanism for WO_3-CeO_2 NH_3-SCR. In the first step, NH_3 bond to CeO_2 (on Ce^{3+}) or crystalline WO_3 as Lewis acids and strongly bonds to $Ce_2(WO_4)_3$ (on W–O–W or W=O) as Brönsted acids. Then NO or weakly absorbed spices like NO_2 react with NH_3 (Figure 1.21). However, the reducibility of the WO_x-CeO_2 catalysts was reported to be decreased by the strong interaction between ceria and tungsten oxide. The fresh catalyst is stable; however, after catalyst aging at about 760°C the catalyst activity lose incredibly [127].

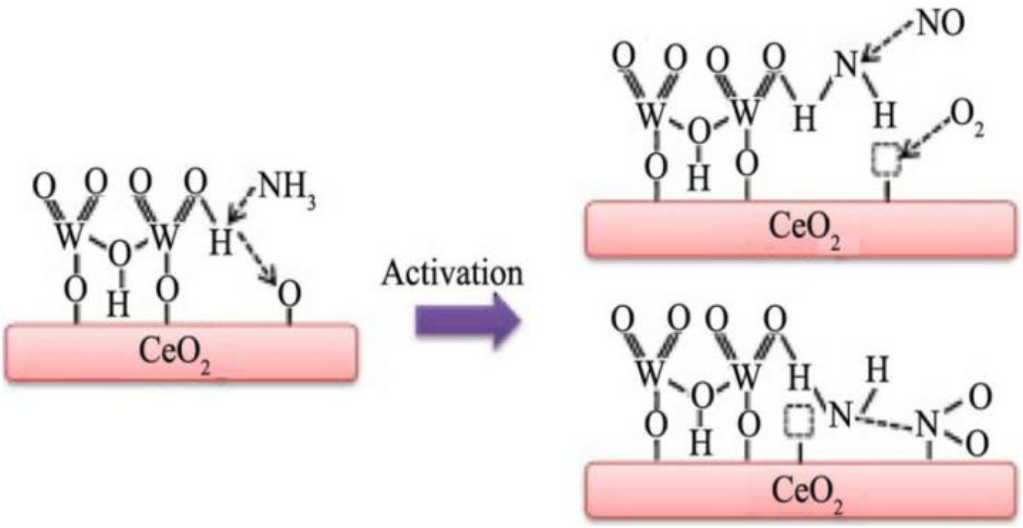

Figure 1.21 **– Reaction mechanism of CeO_2-WO_3 catalyst** [127]

Unlike the MnO_x oxide, zirconia does not have comparable redox properties. However, zirconia is known for its thermal stability. As an example, a preparation by the hydrothermal method of pure CeO_2 gives a specific surface area of 7m²/g after calcination at 900°C. While the incorporation of 35% atomic Zr improves the catalyst stability against sintering (35 m²/g) [128]. In addition, the chemical combination of these two oxides leads to a more significant pore volume and surface area than for pure solids. Another property of Zr is related to its ability to improve the oxygen storage capacity and the reducibility of cerium [129]. The Zr is incorporated in the cubic CeO_2 network for Ce/Zr greater than 0.8 atomic whatever the method of preparation [130]. In addition, the oxygen storage capacity increases considerably thanks to the incorporation of Zr [129]. Li *et al*. [131] studied the catalytic activity of WO_3/CeO_2-ZrO_2 catalyst. They obtained the NO_x conversion close to 100% between 300 and 500°C, in the presence of CO_2 and H_2O. They also suggest a synergistic effect between zirconia and ceria which promotes the NH_3-SCR activity. Lin *et al.* have shown that Mn and/or Fe catalyst supported on ZrO_2-TiO_2 had acidity, redox properties, and an oxygen storage capacity (OSC) greater than supported only on TiO_2. In addition, they tested mixed oxides ZrO_2-TiO_2-CeO_2 as a vanadium support that is normally supported on by TiO_2. The addition of ceria increases

further the OSC and the strong acidity of the catalyst, so the result is that the ZrO_2-TiO_2-CeO_2 support increases the NO_x conversion [78,79].

Niobium compound materials are of current interest as important catalysts for various reactions. Niobium oxides have been reported to be introduced into V_2O_5/TiO_2 catalysts, and the conversion of NO increased 2–4 times at low temperatures [134]. The addition of Nb to MnO_x–CeO_2 was found to be very effective in improving the activity and N_2 selectivity due to the significant increase of the surface acidity [75,78]. Qu *et al.* tried to combine the acidic properties of the Nb_2O_2 and the redox behavior of CeO_2 to improve the NH_3-SCR activity. Figure 1.22 shows the catalytic activity of the catalyst with different Ce/Nb ratio (0/1, 1/3, 1/1, 3/1, 1/0). The CeO_2 and Nb_2O_5 separately show the maximum conversion of 15% and 40% at 400°C respectively. The catalyst with Ce/Nb ratio of 1 is the most active catalyst at low temperature. With the Ce/Nb being 3/1, the catalyst is more active at high temperature [135].

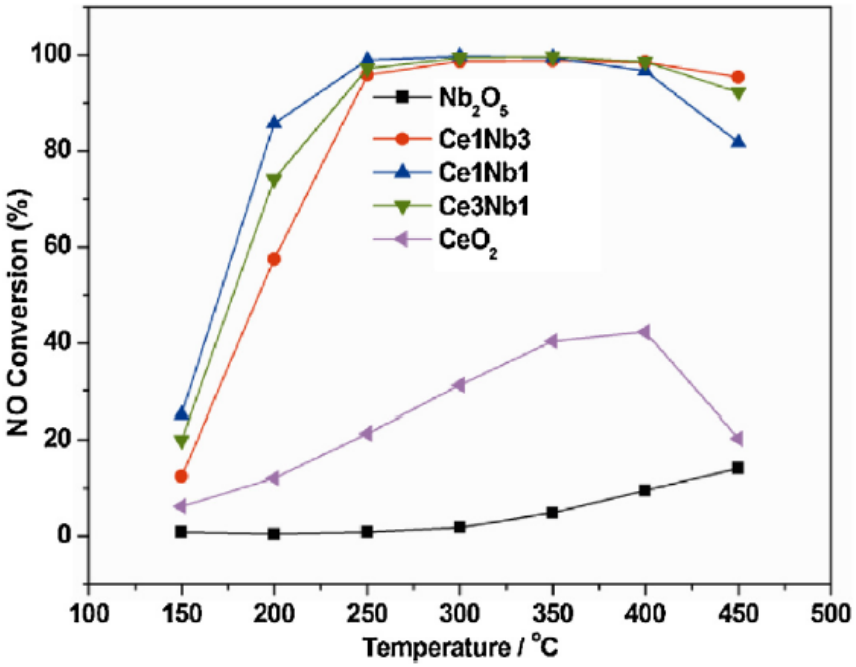

Figure 1.22 – **SCR performances over Ce_XNb_Y series of catalysts. Reaction condition: [NH_3] = [NO] =500ppm, O_2 =5%, total flow rate=200ml.min^{-1}, catalyst mass=0.1g, GHSV=120,000h^{-1}** [135]

It was believed that the catalyst redox ability and adsorption of NH_3 and NO_x play the important roles in the NH_3-SCR reaction. According to Ding *et al*. [136] study, the $CeNb_3Zr_2O_x$ catalyst exhibited higher redox ability than the $CeZr_2O_x$, indicating that the $CeNb_3Zr_2O_x$ possessed high oxidation ability of NO to NO_2, which was beneficial for the fast SCR. Furthermore, the addition of Nb promoted the adsorption and activation of NH_3, which were considered to be a key step in the NH_3-SCR process.

The NO_x conversion and N_2 selectivity in NH_3-SCR reaction over pure Nb_2O_5 and $CeNb_aZr_2O_x$ catalysts with different Nb contents presented in Figure 1.23. The addition of Nb resulted in a great enhancement of NO_x conversion both in low and high temperatures, high N_2 selectivity and a broad temperature window, which indicated that the coexistence of Nb and $CeZr_2O_x$ species was of essential importance for high NH_3-SCR performance. They suggested that the most active catalyst, $CeNb_3Zr_2O_x$ has also the highest specific surface area along with lowest crystallite diameter [136].

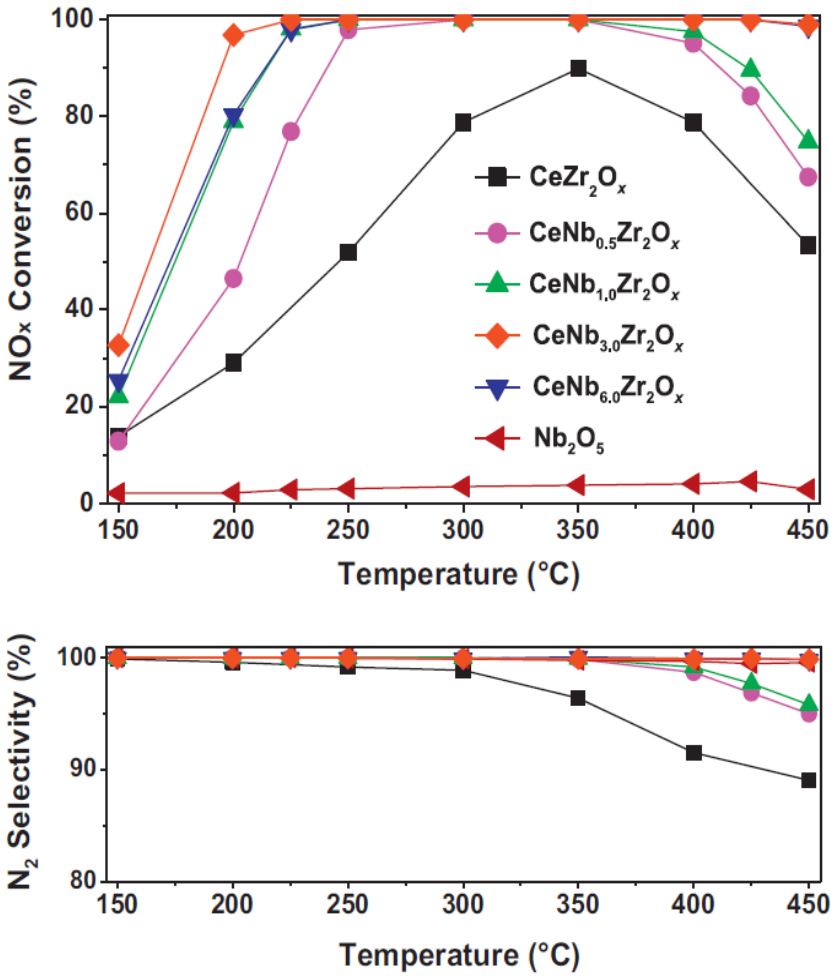

Figure 1.23 – **NO_x conversion and N_2 selectivity as a function of temperature over pure Nb_2O_5 and $CeNb_aZr_2O_X$ (a = 0, 0.5, 1.0, 3.0, 6.0) catalysts in NH_3-SCR reaction. Reaction conditions: [NO] = [NH_3] = 500 ppm, [O_2] = 5 vol. %, GHSV= 50,000 h^{-1}** [136]

Phil *et al*. [137] reported that the addition of Sb to V_2O_5/TiO_2 resulted in a higher SO_2 resistance than the addition of W because of the high electrical conductivity of Sb. The introduction of Sb to V_2O_5/TiO_2 catalysts contributed to enhancing the redox ability of the catalyst, thus leading to an improved NH_3-SCR activity of the V_2O_5/TiO_2 catalyst [138]. Xu *et al*. [139] proposed that doping Ce and Sb of V_2O_5/TiO_2 catalysts is a promising and efficient way to enhance its deNO_x performance. The redox property and surface acidity were the two crucial factors controlling the activity of NH_3-SCR catalyst [140]. The antimony promoted vanadia-ceria catalysts has been prepared by homogeneous precipitation method by Kumar *et al*. [141]. A fixed-bed reactor system was used for measuring the conversion of the NO_x at different

temperatures. With an introduction of Sb into vanadia-ceria, the catalysts show an improvement in the low-temperature NO_x conversion below 250°C as shown in Figure 1.24. Kumar *et al.* proposed that high activities of the Sb promoted catalysts were related to the increase of acid sites, redox properties and the increase of surface area with smaller, uniform-sized particles.

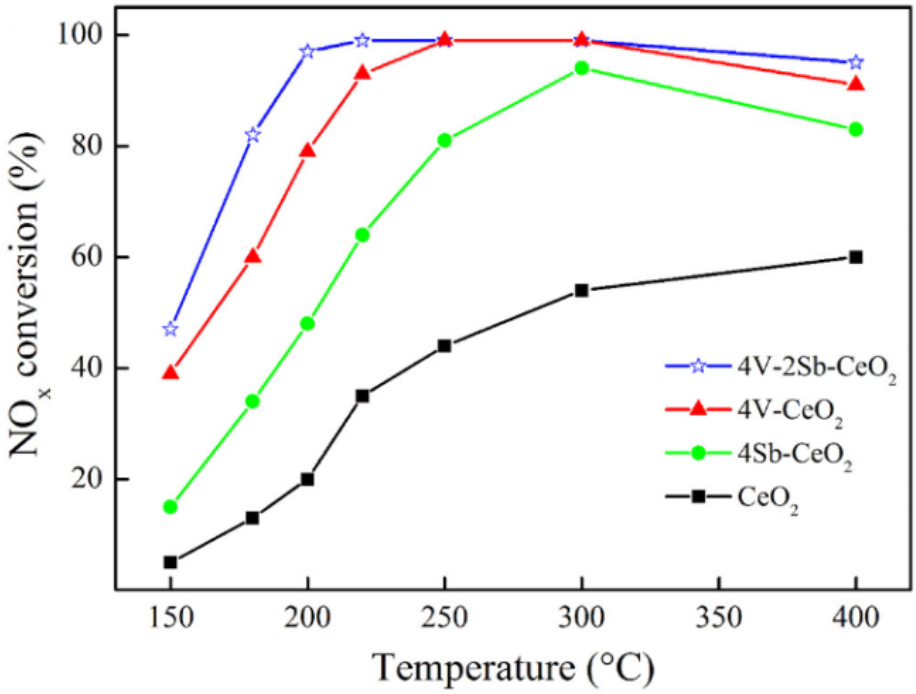

Figure 1.24 – **SCR performances over series of catalysts. Reaction condition: [NH_3] = [NO] =800ppm, O_2=3%, N_2 balance total, flow rate=500ml.min^{-1}, GHSV=60,000h^{-1}** [141]

6.4 Rare earth

Rare earth metal vanadates are potential active phases for the selective catalytic reduction (SCR) of nitric oxide by ammonia for exhaust gas emission control. Rare earth orthovanadates have been extensively studied and applied [125–128]. Recently significant research has been carried out in the field of zircon-type orthovanadate ($REVO_4$, RE = trivalent atom) due to their wide practical applications. The zircon structure can be described by CeO_8 dodecahedrons with eight similar Ce-O distances and isolated VO_4 tetrahedrons. This crystallographic structure promotes the stabilization of Ce^{3+} spices, even under oxidizing condition [146]. Vanadium sites

stabilized in the V^{5+} form are the sites of the redox reactions associating the oxide-reduction couples V^{5+}/V^{4+} and/or V^{4+}/V^{3+} [147].

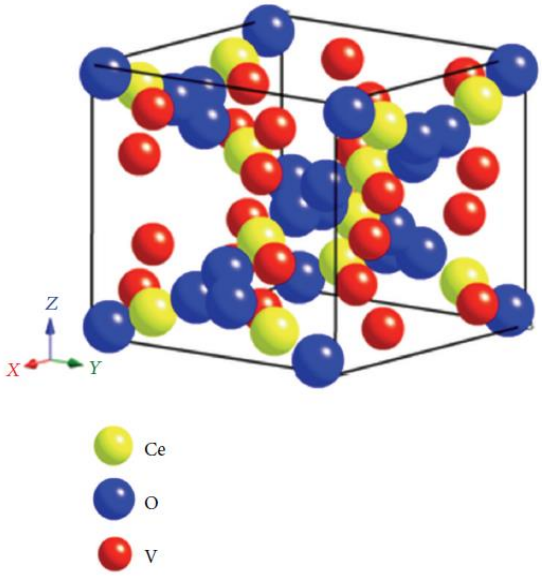

Figure 1.25 – **Zircon-type structure of $CeVO_4$** [146]

$CeVO_4$ has interesting physicochemical properties for the selective reduction of NO_x by ammonia, in particular, redox, and a remarkable thermal stability that have been used in various applications, for example, as a fuel cell electrode component [148] and oxidation catalyst [132,133]. Other applications have also been studied due to the $CeVO_4$ electronic properties [151], optical [152], luminescent [153].

Casanova *et al*. [154] interested in the effect of rare earth orthovanadate adding (so-called $REVO_4$) as stabilizers of the TiO_2-WO_3-SiO_2 formulation in order to improve the thermal stability of the catalyst for NH_3-SCR. The catalyst synthesis is carried out in 2 steps: first the precipitation of the lanthanide orthovanadate. The filtered washed and dried solid is then suspended in a solution of distilled water containing the commercial WO_3-SiO_2-TiO_2 support. The solid is recovered after evaporation of the solvent by heating to 80°C and then dried at 120°C. The first calcination at 650°C for 2 hours under air is carried out. Then the calcined solid is aged at 700°C and 750°C in air for 10 hours. They also highlight a dependence of

activity on the position of the element in the periodic table. The conditions for studying the catalytic reaction are as follows: NO = NH_3 = 200 ppm / O_2 = 2% / H_2O = 10% / GHSV = 180000h^{-1}. Although $CeVO_4$ / TiO_2-WO_3-SiO_2 has the best activity after calcination at 650°C and 700°C, its conversion to NO_x does not exceed 50% after calcination at 750°C. This is probably due to the transformation of the anatase phase TiO_2 into rutile phase, $CeVO_4$ does not stabilize the support. Consequently, the specific surface area of this catalyst decreases strongly after aging at 750°C (43 to 10 m^2/g) compared to other catalysts doped with $GdVO_4$, $TbVO_4$, $DyVO_4$ and, $ErVO_4$. The $ErVO_4$/TiO_2-WO_3-SiO_2 catalyst has the best activity after thermal treatment at 750°C. All the catalysts can be broadly divided in two groups: group A catalysts (comprising La, Ce, Pr and Nd) which suffer a slight deactivation after ageing and group B catalysts (comprising Sm, Gd, Tb, Dy, and Er) in which deactivation has no effect or even causes an improvement of overall efficiency.

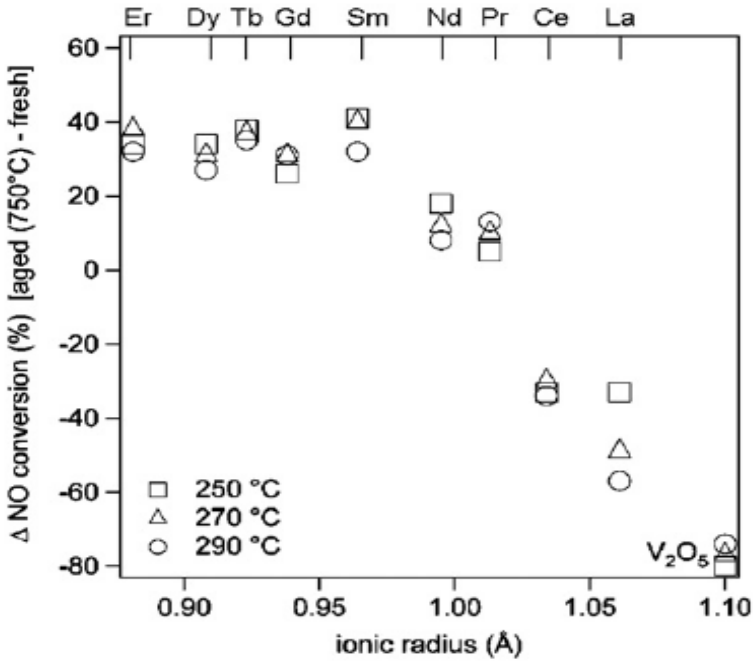

Figure 1.26 **– Difference in NO conversion obtained using fresh catalysts and catalysts aged at 750 °C as measured against ionic radius of the RE element** [154]

In a recent study, the same team tried to optimize the catalytic properties of the $ErVO_4$ solid by substituting the rare earth Er^{3+} with Fe^{3+}. The substitution of 8% of iron in $Fe_{1-x}Er_xVO_4/TiO_2$-WO_3-SiO_2 after calcination at 650°C increase NO_x conversion at low temperature in standard and fast-SCR. On the other hand, the formation of N_2O increases with the iron content in the solid, especially above 400°C. Calcination at 750°C deactivates the iron-rich catalysts; this deactivation is more noticeable in standard than fast-SCR. As Figure 1.27 shows, the best containing stability during high-temperature calcination (750°C), N_2 selectivity and low-temperature activity are obtained for the composition $Fe_{0.5}Er_{0.5}VO_4/TiO_2$-$WO_3$-$SiO_2$ [155].

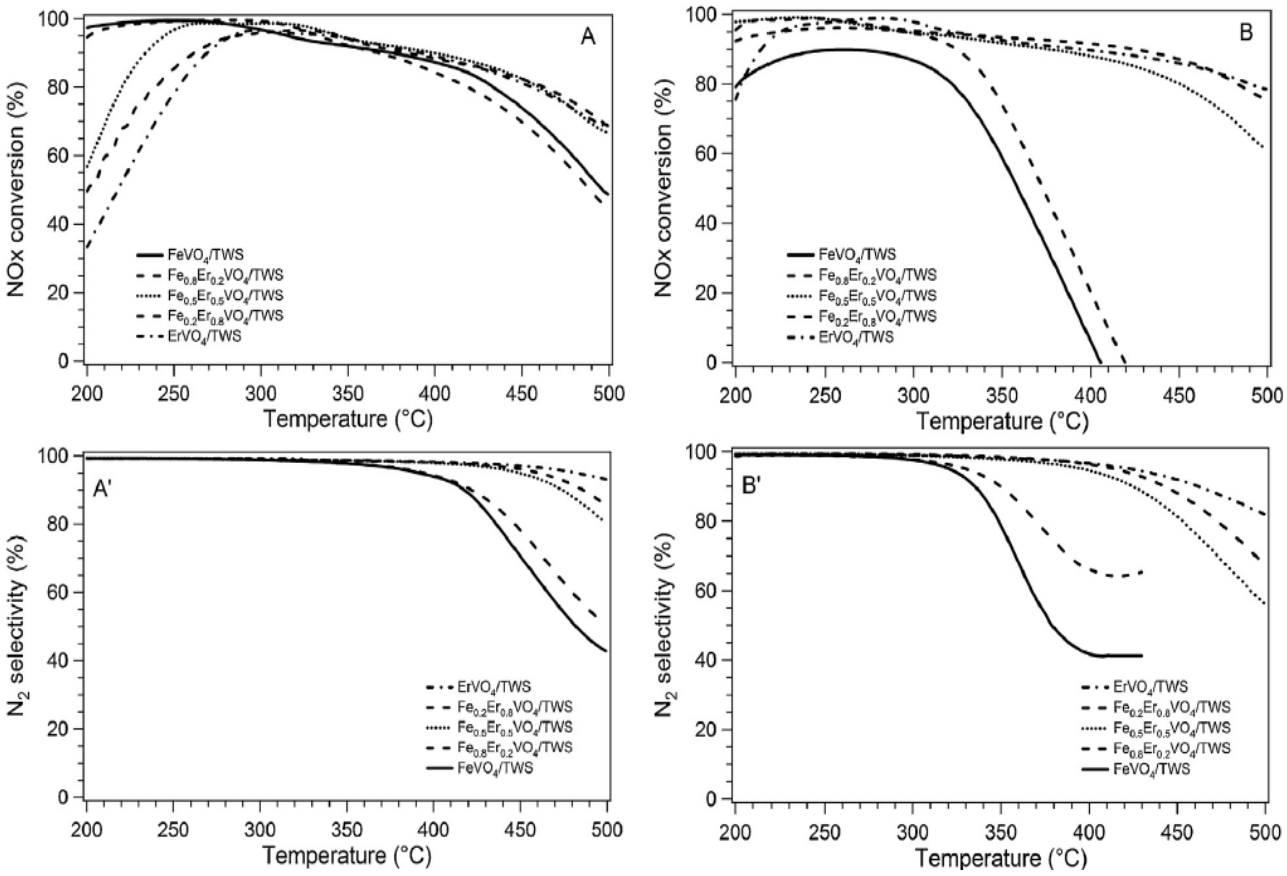

Figure 1.27 – **Standard SCR activity and selectivity of the fresh $Fe_xEr_{1-x}VO_4$/TWS catalysts aged at 650°C for 2h (A and A') and the catalysts after aging at 750°C for 10 h (B and B'). Experimental conditions: 200 ppm NO/ 220 ppm NH_3/ 2% O_2/ 10% H_2O/ GHSV=180000h^{-1}** [155]

Gillot *et al.* [156] underlined the potential of unsupported $CeVO_4$ solid prepared by the hydrothermal method in NH_3-SCR reaction. They focused on the influence of the final pH (2.0, 3.3, and 5.5) and aging (600°C) on the catalytic activity on mixtures of different composition corresponding to molar ratios NO/NO_x = 1/2, 1 respectively associated with Fast- and Standard-SCR conditions. Temperature-programmed experiments were performed with a constant heating rate of 3°C/min. The total flow rate was 333 mL/min insuring a gas hourly space velocity of 250 000 $mLh^{-1}g^{-1}$. The reaction mixture was composed of 400 ppm NH_3, 400 ppm NO_x, 8 vol.% O_2, 10 vol.% CO_2 and 10 % H_2O diluted in He.

They showed that the solid is predominantly composed of tetragonal $CeVO_4$ phase with a slight segregation of cubic CeO_2 phase [156]. The presence of segregated ceria was found to promote significantly the catalytic performances at low temperature. The formation of ceria was observed for pH values above 3 [156]. The loss of conversion at low temperature can also be related to the loss of specific surface area after aging and in the whole temperature conversion to less reducible vanadium sites. The specific interaction between cerium and vanadium through V^{5+}–O^{2-}–Ce^{3+} bonds in $CeVO_4$ can limit the formation of active oxygen species for ammonia oxidative reaction. The best catalytic performances were obtained on 3.3-CeV in Fast-SCR conditions with the selective conversion of NO_x into nitrogen between 200 and 450°C [156].

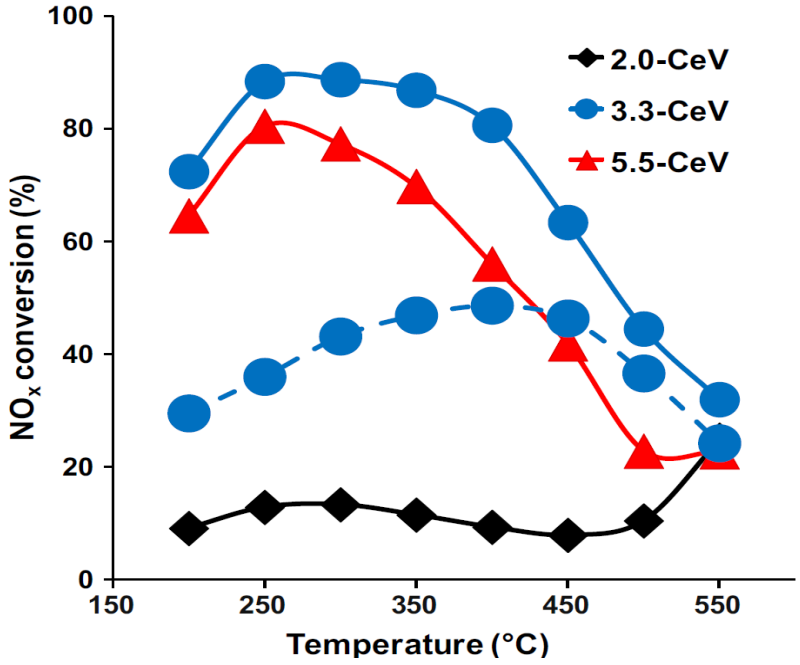

Figure 1.28 – **NO_x conversion during the Fast-SCR (solid lines) and during the Standard-SCR (dotted line) from $CeVO_4$ solids aged in wet atmosphere at 600°C [156]**

Up to now, only one study of Peng *et al.* [157] has discussed reaction mechanisms over VO_x/CeO_2 catalysts during NH_3-SCR. Two different mechanisms depending on temperature have been proposed based on in-situ-DRIFTS and operando Raman results. At low temperature (150°C), both Lewis (from CeO_2 and polymeric VO_x) and Brönsted ($CeVO_4$) acid sites were involved. Adsorbed NO_2 and cis-$N_2O_2^{2-}$ formed during purging in $NO+O_2$ flow, reacted with adsorbed NH_3. However, at high temperature (250-350°C), a part of the Lewis acid sites was converted to Brönsted acid sites. Instead of adsorbed NO_2 and cis-$N2O_2^{2-}$, surface nitrite or nitrate species were postulated as being involved in the reaction with adsorbed NH_3. Since the complicated mechanism of NH_3-SCR over vanadia-containing catalysts depends on a variety of factors, for example, on the type of active VO_x and acid sites, on the kind of the support and the reaction conditions, further investigations are still needed to get the better understanding of these materials for NH_3-SCR.

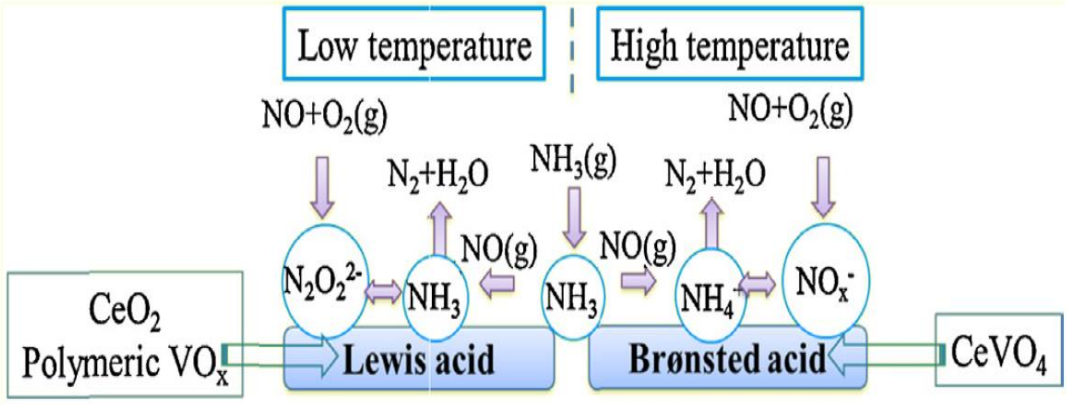

Figure 1.29 – **Structure–activity relationship and reaction mechanism of the vanadia supported on ceria catalysts** [157]

7 Conclusion

Restrictions on nitric oxide (NO_x) emissions are becoming continuously more stringent to mitigate the associated problems of among others acid rain and photochemical smog. The main sources of NO_x emission are diesel exhaust streams from mobile applications and hence a lot of research is conducted on this topic. One way of reducing the residual NO_x content in the exhaust stream is by the Selective Catalytic Reduction (SCR) with ammonia (NH_3) as a reducing agent. This method, in which NO_x and NH_3 are converted into N_2 and H_2O, is already used in practice, even though many questions concerning the detailed reaction mechanism remain unanswered. A thorough understanding of this mechanism is however crucial in order to find structure-activity relations of the involved catalyst material. Only then an intelligent catalyst design is achievable to uphold the upcoming restrictions. A complete SCR control study is presented in this dissertation. Starting from the diesel engine and after-treatment system, several practical problems related to SCR control were addressed. Areas for future work include the improvement of the NO_x reduction performance, the demonstration of the SCR catalyst durability improvements, the development of the aging protocol, and the emissions control during a DPF regeneration event, etc. Moreover, in the context of the increasingly more and

more stringent and comprehensive exhaust emission standards; it is a great trend to implement a better understanding and improvement of the unregulated emissions such as N_2O that has a greater contribution to the global warming effect. Selective catalytic reduction (SCR) of nitrogen oxides by ammonia over V_2O_5-WO_3/TiO_2 catalysts is a critical and established technology for the purification of exhaust gases from stationary sources. This process requires a high temperature (300-500°C). On the other hand, the nitrogen oxide-containing exhaust gases of diesel engines have a significantly lower temperature. Earlier studies have shown that metal-exchanged zeolites provide a catalytic system with excellent properties in terms of activity and selectivity. It has been proven that the metal exchange greatly enhances the performance of the catalyst; however, the nature of these metal catalytic centers remains a point of discussion. Recently, the lot of attention has been given to Cu-SSZ-13, which has a chabazite topology consisting of chabazite cages surrounded by double 6 membered ring (d6r) subunits. These subunits and small pore windows greatly enhance the hydrothermal stability of the catalyst, which is essential since the SCR reaction takes place in the close vicinity of the Diesel Particulate Filter which is oxidized frequently at elevated temperatures. When supported on a TiO_2-based material, the SCR activity of various $REVO_4$ such as $FeVO_4$, $ErVO_4$ or $TbVO_4$ can be greatly enhanced. The stability is proposed to originate from the ability of the rare earth metals to suppress the undesired anatase to rutile phase transition of the support. As explained above, there is an urgent need to improve the activity of NH_3-SCR deNO_x catalysts. The aim of this thesis is to develop the newly modified catalysts that are capable of converting NO_x and NH_3 to N_2 after hydrothermal aging. The first step will be to study the physico-chemical properties and the catalytic performances of bulk $CeVO_4$. In a second step, the impact of cerium substitution by RE (Rare Earth) is conducted. Finally, after combining the most promising results, the addition of low amounts of (W, Mo, Sb, and Nb) may be considered.

8 References

[1] K. Skalska, J. S. Miller, and S. Ledakowicz, "Trends in NO_x abatement: A review," Sci. Total Environ., vol. 408, no. 19, pp. 3976–3989, 2010.

[2] C. J. Pereira and M. D. Amiridis, "NO_x Control from Stationary Sources," no. x, 1995.

[3] V. Aneja, "Atmospheric nitrogen compounds II: emissions, transport, transformation, deposition and assessment," Atmos. Environ., vol. 35, no. 11, pp. 1903–1911, 2001.

[4] G. Busca, L. Lietti, G. Ramis, and F. Berti, "Chemical and mechanistic aspects of the selective catalytic reduction of NO_x by ammonia over oxide catalysts: A review," Appl. Catal. B Environ., vol. 18, no. 2, pp. 1–36, 1998.

[5] D. Cobb, L. Glatch, J. Ruud, and S. Snyder, "Application of selective catalytic reduction (SCR) technology for NO_x reduction from refinery combustion sources," Environ. Prog., vol. 10, no. 1, pp. 49–59, 1991.

[6] J. Li, H. Chang, L. Ma, J. Hao, and R. T. Yang, "Low-temperature selective catalytic reduction of NO_x with NH_3 over metal oxide and zeolite catalysts-A review," Catal. Today, vol. 175, no. 1, pp. 147–156, 2011.

[7] X. Liu, X. Wu, D. Weng, and Z. Si, "Durability of Cu/SAPO-34 catalyst for NOxreduction by ammonia: Potassium and sulfur poisoning," Catal. Commun., vol. 59, pp. 35–39, 2015.

[8] J. Wang, T. Yu, X. Wang, G. Qi, J. Xue, M. Shen, and W. Li, "The influence of silicon on the catalytic properties of Cu/SAPO-34 for NO_x reduction by ammonia-SCR," Appl. Catal. B Environ., vol. 127, no. x, pp. 137–147, 2012.

[9] L. Vicari, "in other materials that electrostriction by light intensity gradients can generate," vol. 3749, no. August 1999, pp. 524–525.

[10] Z. Lian, F. Liu, and H. He, "Effect of preparation methods on the activity of VO_x/CeO_2 catalysts for the selective catalytic reduction of NO_x with NH_3," Catal. Sci. Technol., vol. 5, no. 1, pp. 389–396, 2015.

[11] Y. Peng, C. Wang, and J. Li, "Structure-activity relationship of VO_x/CeO_2 nanorod for NO removal with ammonia," Appl. Catal. B Environ., vol. 144, pp. 538–546, 2014.

[12] Z. Liu, Y. Yi, S. Zhang, T. Zhu, J. Zhu, and J. Wang, "Selective catalytic reduction of NO_x with NH_3 over Mn-Ce mixed oxide catalyst at low temperatures," Catal. Today, vol. 216, no. x, pp. 76–81, 2013.

[13] C. Liu, J. W. Shi, C. Gao, and C. Niu, "Manganese oxide-based catalysts for low-temperature selective catalytic reduction of NO_x with NH_3: A review," Appl. Catal. A Gen., vol. 522, pp. 54–69, 2016.

[14] A. Trovarelli, "Catalytic properties of ceria and CeO_2-Containing materials," Catal. Rev. - Sci. Eng., vol. 38, no. 4, pp. 439–520, 1996.

[15] J. Beckers and G. Rothenberg, "Sustainable selective oxidations using ceria-based materials," Green Chem., vol. 12, no. 6, pp. 939–948, 2010.

[16] L. Vivier and D. Duprez, "Ceria-based solid catalysts for organic chemistry," ChemSusChem, vol. 3, no. 6, pp. 654–678, 2010.

[17] R. J. Laumbach and H. M. Kipen, "Respiratory health effects of air pollution: Update on biomass smoke and traffic pollution," J. Allergy Clin. Immunol., vol. 129, no. 1, pp. 3–11, 2012.

[18] R. N. Colvile, E. J. Hutchinson, J. S. Mindell, and R. F. Warren, "The Transport secotor as a source of air pollution," Atmos. Environ., vol. 35, no. 2001, pp. 1537–1565, 2001.

[19] European Environment Agency, European Union emission inventory report 1990–2014 under the UNECE Convention on Long-range Transboundary Air Pollution (LRTAP), no. 16. 2016.

[20] N. C. Surawski, Z. D. Ristovski, R. J. Brown, and R. Situ, “Gaseous and particle emissions from an ethanol fumigated compression ignition engine,” Energy Convers. Manag., vol. 54, no. 1, pp. 145–151, 2012.
[21] G. J. M. Velders, “The Euro emission standards for cars and trucks in relation to NO_2 limit value exceedances in the Netherlands,” no. 2, 2013.
[22] RSA, “Euro IV , Euro V and VI Emissions Regulations for Heavy Duty Vehicle,” vol. 2009, no. September 2015, pp. 1–10, 2015.
[23] R. Cloudt, R. Baert, and F. Willems, “SCR-only Concept for Heavy-duty Euro VI Applications,” Mtz, vol. 70, no. x, pp. 58–63, 2009.
[24] “SINCHEM doctoral research subject Coupling of soot oxidation and ammonia-mediated selective catalytic reduction of nitrogen oxides .,” no. 2, p. 3.
[25] T. C. Watling, Å. Johansson, and G. John, “Computer Simulation of Automotive Emission Control Systems are highlighted,” no. 2, pp. 152–165, 2015.
[26] J. Lee, M. Paratore, and D. Brown, “Evaluation of Cu-Based SCR / DPF Technology for Diesel Exhaust Emission Control,” SAE Int. J. Fuels Lubr., vol. 1, no. 1, pp. 96–101, 2008.
[27] J. Rodríguez-Fernández, M. Lapuerta, and J. Sánchez-Valdepeñas, “Regeneration of diesel particulate filters: Effect of renewable fuels,” Renew. Energy, vol. 104, pp. 30–39, 2017.
[28] C. Beatrice, S. Di Iorio, C. Guido, and P. Napolitano, “Detailed characterization of particulate emissions of an automotive catalyzed DPF using actual regeneration strategies,” Exp. Therm. Fluid Sci., vol. 39, pp. 45–53, 2012.
[29] “https://iasmania.com/environment-pollution-air-pollutants/.” .
[30] N. Hickey, I. Boscarato, and J. Kaspar, “Current Environmental Issues and Challenges,” 2014.
[31] S. Bhandarkar, “Vehicular Pollution , Their Effect on Human Heatlh and Mitigation Measures,” Veh. Eng., vol. 1, no. 2, pp. 33–40, 2013.
[32] J. O. Anderson, J. G. Thundiyil, and A. Stolbach, “Clearing the Air: A Review of the Effects of Particulate Matter Air Pollution on Human Health,” J. Med. Toxicol., vol. 8, no. 2, pp. 166–175, 2012.
[33] European Environment Agency, Air quality in Europe, no. 9. 2013.
[34] A. Paca, “Monoxyde de carbone,” Ars Sante, p. 6, 2012.
[35] J. Harkins and J. K. Goodwine, “Oxides of nitrogen in diesel exhaust,” J. Air Pollut. Control Assoc., vol. 14, no. 1, pp. 34–38, 1964.
[36] A. S. Ayodhya, V. T. Lamani, M. Thirumoorthy, and G. N. Kumar, “NO_x reduction studies on a diesel engine operating on waste plastic oil blend using selective catalytic reduction technique,” J. Energy Inst., pp. 1–10, 2018.
[37] Environmental Protection Agency (EPA), “Nitrogen oxides (NO_x), why and how they are controlled,” Epa-456/F-99-006R, no. November, p. 48, 1999.
[38] A. Holmqvist, “Implementation of an NH_3 Storage Model Based SCR-Simulation Algorithm,” 2016.
[39] S. Natit and S. Universio, “MECHANISM A N D MODELING OF NITROGEN CHEMISTRY IN COMBUSTION (x),” vol. 15, pp. 287–338, 1989.
[40] M. Tunér, “Combustion of Alternative Vehicle Fuels in Internal Combustion Engines A report on engine performance from combustion of alternative fuels based on literature review,” no. March, 2015.
[41] I. A. Reşitolu, K. Altinişik, and A. Keskin, “The pollutant emissions from diesel-engine vehicles and exhaust aftertreatment systems,” Clean Technol. Environ. Policy, vol. 17, no. 1, pp. 15–27, 2015.
[42] Y. Traa, B. Burger, and J. Weitkamp, “Zeolite-based materials for the selective catalytic

reduction of NO_x with hydrocarbons," Microporous Mesoporous Mater., vol. 30, pp. 3–41, 1999.
[43] M. V. Twigg, "Progress and future challenges in controlling automotive exhaust gas emissions," Appl. Catal. B Environ., vol. 70, no. 1–4, pp. 2–15, 2007.
[44] M. Božić, A. Vučetić, M. Sjerić, D. Kozarac, and Z. Lulić, "Experimental study on knock sources in spark ignition engine with exhaust gas recirculation," Energy Convers. Manag., vol. 165, pp. 35–44, 2018.
[45] S. Reifarth, Efficiency and Mixing Analysis of EGR-Systems for Diesel Engines, no. 2014:01. 2014.
[46] R. M. Heck, "Catalytic abatement of nitrogen oxides–stationary applications," Catal. Today, vol. 53, no. 4, pp. 519–523, 1999.
[47] S. Alain, R. Emmanuel, and B. Gérard, "Post-traitement des émissions polluantes des moteurs thermiques à combustion interne Moteurs à allumage commandé," Tech. l'ingénieur, vol. 33, no. BM 2508, 2011.
[48] T. Szailer, J. H. Kwak, D. H. Kim, J. C. Hanson, C. H. F. Peden, and J. Szanyi, "Reduction of stored NO_x on Pt/Al_2O_3 and $Pt/BaO/Al_2O_3$ catalysts with H_2 and CO," J. Catal., vol. 239, no. 1, pp. 51–64, 2006.
[49] P. Kočí, F. Plát, J. Štěpánek, Š. Bártová, M. Marek, M. Kubíček, V. Schmeißer, D. Chatterjee, and M. Weibel, "Global kinetic model for the regeneration of NO_x storage catalyst with CO, H_2 and C_3H_6 in the presence of CO_2 and H_2O," Catal. Today, vol. 147, no. SUPPL., 2009.
[50] N. Le Phuc, X. Courtois, F. Can, S. Royer, P. Marecot, and D. Duprez, "NO_x removal efficiency and ammonia selectivity during the NO_x storage-reduction process over $Pt/BaO(Fe, Mn, Ce)/Al_2O_3$ model catalysts. Part I: Influence of Fe and Mn addition," Appl. Catal. B Environ., vol. 102, no. 3–4, pp. 353–361, 2011.
[51] I. Nova, A. Beretta, G. Groppi, L. Lietti, E. Tronconi, and P. Forzatti, "Monolithic Catalysts for NO," no. x, pp. 171–214, 2006.
[52] R. Burch and P. . Millington, "Selective reduction of nitrogen oxides by hydrocarbons under lean-burn conditions using supported platinum group metal catalysts," Catal. Today, vol. 26, pp. 185–206, 1995.
[53] H. He, C. Zhang, and Y. Yu, "A comparative study of Ag/Al_2O_3 and Cu/Al_2O_3 catalysts for the selective catalytic reduction of NO by C_3H_6," vol. 90, no. 1995, pp. 191–197, 2004.
[54] V. Houel, D. James, P. Millington, S. Pollington, S. Poulston, R. Rajaram, and R. Torbati, "A comparison of the activity and deactivation of Ag/Al_2O_3 and Cu/ZSM-5 for HC-SCR under simulated diesel exhaust emission conditions," J. Catal., vol. 230, no. 1, pp. 150–157, 2005.
[55] S. Fischer, K. Rusch, B. Amon, and S. E. Control, "SCR Technology to Meet Future Diesel Emission Regulations in Europe General Drivers for Emissions Control Technology Advantages of SCR Technology Technical Description of SCR Technology Technical Performance of SCR Systems Boundary Conditions for Using SC."
[56] E. Richter, H. J Schmidt, and H. G Schecker, "Adsorption and catalytic reactions of NO and NH_3 on activated carbon," Chem. Eng. Technol., vol. 13, no. 1, pp. 332–340, 1990.
[57] M. Tsitsiriki, O. Bereketidou, H. Latsios, and M. A. Goula, "SYSTEM DESIGN AND COST ESTIMATIONS FOR NO_x SELECTIVE CATALYTIC REDUCTION (SCR) ON COAL- FIRED BOILERS," no. X, pp. 5–7, 2007.
[58] N. Wilken, K. Kamasamudram, N. W. Currier, J. Li, A. Yezerets, and L. Olsson, "Heat of adsorption for NH_3, NO_2 and NO on Cu-Beta zeolite using microcalorimeter for NH_3 SCR applications," Catal. Today, vol. 151, no. 3–4, pp. 237–243, 2010.
[59] J. Y. Luo, X. Hou, P. Wijayakoon, S. J. Schmieg, W. Li, and W. S. Epling, "Spatially

resolving SCR reactions over a Fe/zeolite catalyst," Appl. Catal. B Environ., vol. 102, no. 1–2, pp. 110–119, 2011.
[60] G. Qi, J. E. Gatt, and R. T. Yang, "Selective catalytic oxidation (SCO) of ammonia to nitrogen over Fe-exchanged zeolites prepared by sublimation of $FeCl_3$," J. Catal., vol. 226, no. 1, pp. 120–128, 2004.
[61] W. M. Chien, D. Chandra, K. H. Lau, D. L. Hildenbrand, and A. M. Helmy, "The vaporization of NH_4NO_3," J. Chem. Thermodyn., vol. 42, no. 7, pp. 846–851, 2010.
[62] V. Bolis, C. Busco, and P. Ugliengo, "Thermodynamic study of water adsorption in high-silica zeolites.," J. Phys. Chem. B, vol. 110, no. 30, pp. 14849–59, 2006.
[63] I. Malpartida, O. Marie, P. Bazin, M. Daturi, and X. Jeandel, "An operando IR study of the unburnt HC effect on the activity of a commercial automotive catalyst for NH_3-SCR," Appl. Catal. B Environ., vol. 102, no. 1–2, pp. 190–200, 2011.
[64] Y. Deng, W. Zheng, E. Jiaqiang, B. Zhang, X. Zhao, Q. Zuo, Z. Zhang, and D. Han, "Influence of geometric characteristics of a diesel particulate filter on its behavior in equilibrium state," Appl. Therm. Eng., vol. 123, pp. 61–73, 2017.
[65] Q. Zhang, C. Song, G. Lv, F. Bin, H. Pang, and J. Song, "Journal of Industrial and Engineering Chemistry Effect of metal oxide partial substitution of V_2O_5 in $V_2O_5 – WO_3 / TiO_2$ on selective catalytic reduction of NO with NH_3," J. Ind. Eng. Chem., vol. 19, no. 1, pp. 160–166, 2014.
[66] Z. Liu, Y. Li, T. Zhu, H. Su, and J. Zhu, "Selective Catalytic Reduction of NO_x by NH_3 over Mn-Promoted V_2O_5 / TiO_2 Catalyst," no. x, 2014.
[67] M. Twigg, "Urea-SCR Technology for deNO_x After Treatment of Diesel Exhausts," 2014.
[68] L. Lietti, G. Ramis, F. Berti, G. Toledo, D. Robba, G. Busca, and P. Forzatti, "Chemical, structural and mechanistic aspects on NO_x SCR over commercial and model oxide catalysts," Catal. Today, vol. 42, no. 1–2, pp. 101–116, 1998.
[69] D. M. Chapman, "Behavior of titania-supported vanadia and tungsta SCR catalysts at high temperatures in reactant streams: Tungsten and vanadium oxide and hydroxide vapor pressure reduction by surficial stabilization," Appl. Catal. A Gen., vol. 392, no. 1–2, pp. 143–150, 2011.
[70] P. Alotto, M. Guarnieri, and F. Moro, "Redox flow batteries for the storage of renewable energy: A review," Renew. Sustain. Energy Rev., vol. 29, pp. 325–335, 2014.
[71] P. Moreau, P. Valero, V. Tschamber, A. Brillard, J.-F. Brilhac, Y. Hohl, and R. Vonarb, "Investigation of vanadium sublimation from SCR catalysts," no. October, pp. 1–6, 2015.
[72] S. Bagheri, N. Muhd Julkapli, and S. Bee Abd Hamid, "Titanium dioxide as a catalyst support in heterogeneous catalysis," ScientificWorldJournal, vol. 2014, p. 727496, 2014.
[73] D. A. H. Hanaor and C. C. Sorrell, "Review of the anatase to rutile phase transformation," J. Mater. Sci., vol. 46, no. 4, pp. 855–874, 2011.
[74] M. D. Amiridis, R. V Duevel, and I. E. Wachs, "The effect of metal oxide additives on the activity of V_2O_5/TiO_2 catalysts for the selective catalytic reduction of nitric oxide by ammonia," Appl. Catal. B Environ., vol. 20, pp. 111–122, 1999.
[75] P. Forzatti, "Present status and perspectives in de-NO_x SCR catalysis," Appl. Catal. A Gen., vol. 222, no. 1–2, pp. 221–236, 2001.
[76] T. Yamaguchi, Y. Tanaka, and K. Tanabe, "Isomerization and disproportionation of olefins over tungsten oxides supported on various oxides," J. Catal., vol. 65, no. 2, pp. 442–447, 1980.
[77] D. Keller, "X-ray absorption spectroscopy of supported vanadium oxide catalysts."
[78] G. Busca, "Acid Catalysts in Industrial Hydrocarbon Chemistry," pp. 5366–5410, 2007.
[79] I. Chimica, F. Ingegneria, U. P. J. F. Kennedy, and I.- Genova, "Characterization of

tungsta-titania catalysts," vol. 8, no. 8, pp. 1744–1749, 1992.
[80] Y. Gao, T. Luan, T. Lü, K. Cheng, and H. Xu, "Performance of V_2O_5-WO_3-MoO_3/TiO_2 catalyst for selective catalytic reduction of NO_x by NH_3," Chinese J. Chem. Eng., vol. 21, no. 1, pp. 1–7, 2013.
[81] D. W. Kwon, K. H. Park, and S. C. Hong, "Enhancement of SCR activity and SO_2 resistance on VO_x/TiO_2 catalyst by addition of molybdenum," Chem. Eng. J., vol. 284, pp. 315–324, 2016.
[82] Z. Ma, X. Wu, Y. Feng, Z. Si, D. Weng, and L. Shi, "Low-temperature SCR activity and SO_2 deactivation mechanism of Ce-modified V_2O_5-WO_3/TiO_2 catalyst," Prog. Nat. Sci. Mater. Int., vol. 25, no. 4, pp. 342–352, 2015.
[83] S. G. Chen and R. T. Yang, "Unified Mechanism of Alkali and Alkaline Earth Catalyzed Gasification Reactions of Carbon by CO_2 and H_2O," Energy & Fuels, vol. 11, no. 21, pp. 421–427, 1997.
[84] H. Eckert and I. E. Wachs, "J.P. Chen, R.T. Yang, Appl. Catal. 80 (1992) 1356.," J. Phys. Chem., vol. 93, no. 18, pp. 6796–6805, 1989.
[85] M. Inomata and A. Miyamoto, "Mechanism of the Reaction of NO and NH, on Vanadium Oxide Catalyst in the Presence of Oxygen under the Dilute Gas Condition," J. Catal., vol. 148, pp. 140–148, 1980.
[86] F. J. J. G. Janssen, F. M. G. Van Den Kerkhof, H. Bosch, and J. R. H. Ross, "Mechanism of the reaction of nitric oxide, ammonia, and oxygen over vanadia catalysts. 2. Isotopic transient studies with oxygen-18 and nitrogen-15," J. Phys. Chem., vol. 91, no. 27, pp. 6633–6638, 1987.
[87] G. RAMIS, G. BUSCA, V. LORENZELLI, and P. FORZATTI, "Fourier Transform-Infrared Study of the Adsorption and Coadsorption of Nitric Oxide , Nitrogen Dioxide and Ammonia on and Mechanism of Selective Catalytic Reduction," Appl. Catal., vol. 64, no. 2, pp. 243–257, 1990.
[88] H. Kamata, K. Takahashi, and C. U. I. Odenbrand, "The role of K_2O in the selective reduction of NO with NH_3 over a V_2O5WO_3/TiO_2 commercial selective catalytic reduction catalyst," pp. 189–198, 1999.
[89] H. Kamata, K. Takahashi, and C. U. I. Odenbrand, "Kinetics of the Selective Reduction of NO with NH_3 over a $V_2O_5(WO_3)$/TiO_2 Commercial SCR Catalyst," J. Catal., vol. 113, pp. 106–113, 1999.
[90] T. C. Bowen, R. D. Noble, and J. L. Falconer, "Fundamentals and applications of pervaporation through zeolite membranes," J. Memb. Sci., vol. 245, no. 1–2, pp. 1–33, 2004.
[91] H. Sjövall, L. Olsson, E. Fridell, and R. J. Blint, "Selective catalytic reduction of NO_x with NH_3 over Cu-ZSM-5-The effect of changing the gas composition," Appl. Catal. B Environ., vol. 64, no. 3–4, pp. 180–188, 2006.
[92] A. Sultana, T. Nanba, M. Haneda, M. Sasaki, and H. Hamada, "Influence of co-cations on the formation of Cu^+ species in Cu/ZSM-5 and its effect on selective catalytic reduction of NO_x with NH_3," Appl. Catal. B Environ., vol. 101, no. 1–2, pp. 61–67, 2010.
[93] S. Shwan, Metal-exchanged zeolites for NH_3-SCR applications - Activity and Deactivation studies, vol. Ph.D. 2014.
[94] H.-Y. Chen and W. M. . Sachtler, "Activity and durability of Fe/ZSM-5 catalysts for lean burn NO_x reduction in the presence of water vapor," Catal. Today, vol. 42, no. 1–2, pp. 73–83, 1998.
[95] O. Kröcher, M. Devadas, M. Elsener, A. Wokaun, N. Söger, M. Pfeifer, Y. Demel, and L. Mussmann, "Investigation of the selective catalytic reduction of NO by NH_3 on Fe-ZSM5 monolith catalysts," Appl. Catal. B Environ., vol. 66, no. 3–4, pp. 208–216, 2006.
[96] C. Paolucci, J. R. Di Iorio, F. H. Ribeiro, R. Gounder, and W. F. Schneider, Catalysis

Science of NO_x Selective Catalytic Reduction With Ammonia Over Cu-SSZ-13 and Cu-SAPO-34, 1st ed., vol. 59, no. x. Elsevier Inc., 2016.
[97] J. H. Kwak, R. G. Tonkyn, D. H. Kim, J. Szanyi, and C. H. F. Peden, "Excellent activity and selectivity of Cu-SSZ-13 in the selective catalytic reduction of NO_x with NH_3," J. Catal., vol. 275, no. 2, pp. 187–190, 2010.
[98] P. G. Blakeman, E. M. Burkholder, H. Y. Chen, J. E. Collier, J. M. Fedeyko, H. Jobson, and R. R. Rajaram, "The role of pore size on the thermal stability of zeolite supported Cu SCR catalysts," Catal. Today, vol. 231, no. x, pp. 56–63, 2014.
[99] T. V. W. Janssens, H. Falsig, L. F. Lundegaard, P. N. R. Vennestrøm, S. B. Rasmussen, P. G. Moses, F. Giordanino, E. Borfecchia, K. A. Lomachenko, C. Lamberti, S. Bordiga, A. Godiksen, S. Mossin, and P. Beato, "A consistent reaction scheme for the selective catalytic reduction of nitrogen oxides with ammonia," ACS Catal., vol. 5, no. 5, pp. 2832–2845, 2015.
[100] A. Grossale, I. Nova, and E. Tronconi, "Study of a Fe-zeolite-based system as NH_3-SCR catalyst for diesel exhaust aftertreatment," Catal. Today, vol. 136, no. 1–2, pp. 18–27, 2008.
[101] S. Brandenberger, O. Kröcher, A. Tissler, and R. Althoff, "Effect of structural and preparation parameters on the activity and hydrothermal stability of metal-exchanged ZSM-5 in the selective catalytic reduction of NO by NH_3," Ind. Eng. Chem. Res., vol. 50, no. 8, pp. 4308–4319, 2011.
[102] A. L. Kustov, K. Egeblad, M. Kustova, T. W. Hansen, and C. H. Christensen, "Mesoporous Fe-containing ZSM-5 zeolite single crystal catalysts for selective catalytic reduction of nitric oxide by ammonia," Top. Catal., vol. 45, no. 1–4, pp. 159–163, 2007.
[103] M. Schwidder, M. S. Kumar, K. Klementiev, M. M. Pohl, A. Brückner, and W. Grünert, "Selective reduction of NO with Fe-ZSM-5 catalysts of low Fe content: I. Relations between active site structure and catalytic performance," J. Catal., vol. 231, no. 2, pp. 314–330, 2005.
[104] G. Delahay, D. Valade, A. Guzmán-Vargas, and B. Coq, "Selective catalytic reduction of nitric oxide with ammonia on Fe-ZSM-5 catalysts prepared by different methods," Appl. Catal. B Environ., vol. 55, no. 2, pp. 149–155, 2005.
[105] C. K. Narula, X. Yang, M. Moses-debusk, D. R. Mullins, S. M. Mahurin, and Z. Wu, Final Report Nano Catalysts for Diesel Engine Emission Remediation, no. April. 2012.
[106] P. Min, S. Zhang, Y. Xu, and R. Li, "Enhanced oxygen storage capacity of CeO_2 with doping-induced unstable crystal structure," Appl. Surf. Sci., 2018.
[107] J. J. Peña Leal and R. A. Barrio, "Modelling the structure of disordered cerium oxide thin films," Phys. A Stat. Mech. its Appl., vol. 483, pp. 259–265, 2017.
[108] X. Wang, A. Shi, Y. Duan, J. Wang, and M. Shen, "Catalytic performance and hydrothermal durability of CeO_2–V_2O_5–ZrO_2/WO_3–TiO_2 based NH_3-SCR catalysts," Catal. Sci. Technol., vol. 2, no. 7, p. 1386, 2012.
[109] L. Xu, X. S. Li, M. Crocker, Z. S. Zhang, A. M. Zhu, and C. Shi, "A study of the mechanism of low-temperature SCR of NO with NH_3 on MnO_x/CeO_2," J. Mol. Catal. A Chem., vol. 378, no. 2, pp. 82–90, 2013.
[110] K. Krishna, G. B. F. Seijger, C. M. Van Den Bleek, and H. P. A. Calis, "Very active CeO_2-zeolite catalysts for NO_x reduction with NH_3," ChemComm, vol. 2, no. 2, pp. 2030–2031, 2002.
[111] C. Tang, H. Zhang, and L. Dong, "Ceria-based catalysts for low-temperature selective catalytic reduction of NO with NH_3," Catal. Sci. Technol., vol. 6, no. 5, pp. 1248–1264, 2016.
[112] W. Shan, F. Liu, Y. Yu, and H. He, "The use of ceria for the selective catalytic reduction of NO_x with NH_3," Cuihua Xuebao/Chinese J. Catal., vol. 35, no. 8, pp. 1251–1259,

2014.
[113] X. Gao, Y. Jiang, Y. Fu, Y. Zhong, Z. Luo, and K. Cen, "Preparation and characterization of CeO_2/TiO_2 catalysts for selective catalytic reduction of NO with NH_3," Catal. Commun., vol. 11, no. 5, pp. 465–469, 2010.
[114] Y. Shen, S. Zhu, T. Qiu, and S. Shen, "A novel catalyst of CeO_2/Al_2O_3 for selective catalytic reduction of NO by NH_3," Catal. Commun., vol. 11, no. 1, pp. 20–23, 2009.
[115] L. Zhang, J. Pierce, V. L. Leung, D. Wang, and W. S. Epling, "Characterization of ceria's interaction with NO_x and NH_3," J. Phys. Chem. C, vol. 117, no. 16, pp. 8282–8289, 2013.
[116] Y. Peng, C. Wang, and J. Li, "Applied Catalysis B: Environmental Structure – activity relationship of VO_x/CeO_2 nanorod for NO removal with ammonia," vol. 144, pp. 538–546, 2014.
[117] P. R. Ettireddy, N. Ettireddy, S. Mamedov, P. Boolchand, and P. G. Smirniotis, "Surface characterization studies of TiO_2 supported manganese oxide catalysts for low temperature SCR of NO with NH_3," Appl. Catal. B Environ., vol. 76, no. 1–2, pp. 123–134, 2007.
[118] G. Qi and R. T. Yang, "Low-temperature selective catalytic reduction of NO with NH_3 over iron and manganese oxides supported on titania," Appl. Catal. B Environ., vol. 44, no. 3, pp. 217–225, 2003.
[119] M. Kang, E. D. Park, J. M. Kim, and J. E. Yie, "Cu-Mn mixed oxides for low temperature NO reduction with NH_3," Catal. Today, vol. 111, no. 3–4, pp. 236–241, 2006.
[120] Y. Wan, W. Zhao, Y. Tang, L. Li, H. Wang, Y. Cui, J. Gu, Y. Li, and J. Shi, "Ni-Mn bi-metal oxide catalysts for the low temperature SCR removal of NO with NH_3," Appl. Catal. B Environ., vol. 148–149, pp. 114–122, 2014.
[121] Z. Lian, F. Liu, H. He, X. Shi, J. Mo, and Z. Wu, "Manganese-niobium mixed oxide catalyst for the selective catalytic reduction of NO_x with NH_3 at low temperatures," Chem. Eng. J., vol. 250, no. x, pp. 390–398, 2014.
[122] Y. Jiang, C. Bao, Q. Liu, G. Liang, M. Lu, and S. Ma, "A novel CeO_2 -MoO_3 -WO_3 /TiO_2 catalyst for selective catalytic reduction of NO with NH_3," Catal. Commun., vol. 103, pp. 96–100, 2018.
[123] W. S. Kijlstra, J. C. M. L. Daamen, J. M. van de Graaf, B. van der Linden, E. K. Poels, and A. Bliek, "Inhibiting and deactivating effects of water on the selective catalytic reduction of nitric oxide with ammonia over MnO_x/Al_2O_3," Appl. Catal. B Environ., vol. 7, no. 3–4, pp. 337–357, 1996.
[124] H. Jiang, J. Zhao, D. Jiang, and M. Zhang, "Hollow MnO_x-CeO_2 nanospheres prepared by a green route: A novel low-temperature NH_3-SCR catalyst," Catal. Letters, vol. 144, no. 2, pp. 325–332, 2014.
[125] M. Casapu, O. Kröcher, and M. Elsener, "Screening of doped MnO_x-CeO_2 catalysts for low-temperature NO-SCR," Appl. Catal. B Environ., vol. 88, no. 3–4, pp. 413–419, 2009.
[126] L. Chen, J. Li, W. Ablikim, J. Wang, H. Chang, L. Ma, J. Xu, M. Ge, and H. Arandiyan, "CeO_2–WO_3 Mixed Oxides for the Selective Catalytic Reduction of NO_x by NH3 Over a Wide Temperature Range," Catal. Letters, vol. 141, no. 12, pp. 1859–1864, 2011.
[127] Y. Peng, K. Li, and J. Li, "Identification of the active sites on CeO_2-WO_3 catalysts for SCR of NOx with NH_3: An in situ IR and Raman spectroscopy study," Appl. Catal. B Environ., vol. 140–141, no. x, pp. 483–492, 2013.
[128] R. Si, Y. W. Zhang, S. J. Li, B. X. Lin, and C. H. Yan, "Urea-based hydrothermally derived homogeneous nanostructured $Ce_{1-x}Zr_xO_2$ (x=0-0.8) solid solutions: A strong correlation between oxygen storage capacity and lattice strain," J. Phys. Chem. B, vol. 108, no. 33, pp. 12481–12488, 2004.
[129] A. Trovarelli, F. Zamar, J. Llorca, C. De Leitenburg, G. Dolcetti, and J. T. Kiss,

"Nanophase Fluorite-Structured CeO_2–ZrO_2 Catalysts Prepared by High-Energy Mechanical Milling Analysis of Low-Temperature Redox Activity and Oxygen Storage Capacity," J Catal, vol. 169, pp. 490–502, 1997.

[130] S. Rossignol, Y. Madier, and D. Duprez, "Preparation of zirconia–ceria materials by soft chemistry," Catal. Today, vol. 50, no. 2, pp. 261–270, 1999.

[131] J. Li, Z. Song, P. Ning, Q. Zhang, X. Liu, H. Li, and Z. Huang, "Influence of calcination temperature on selective catalytic reduction of NOxwith NH_3 over CeO_2-ZrO_2-WO_3 catalyst," J. Rare Earths, vol. 33, no. 7, pp. 726–735, 2015.

[132] K. Jug, T. Homann, and T. Bredow, "Reaction Mechanism of the Selective Catalytic Reduction of NO with NH_3 and O_2 to N_2 and," Molecules, vol. 23, no. 12, pp. 2966–2971, 2004.

[133] L. I. N. Tao and Z. Qiu, Monolith Manganese Based Catalyst Supported on $ZrOTiO_2$ for NH_3 SCR Reaction at Low Temperature," vol. 24, no. 7, pp. 1127–1131, 2008.

[134] V. Pârvulescu, "Selective catalytic reduction of NO with NH_3 over mesoporous V_2O_5–TiO_2–SiO_2 catalysts," J. Catal., vol. 25, pp. 49–54, 2003.

[135] R. Qu, X. Gao, K. Cen, and J. Li, "Relationship between structure and performance of a novel cerium-niobium binary oxide catalyst for selective catalytic reduction of NO with NH_3," Appl. Catal. B Environ., vol. 142–143, no. x, pp. 290–297, 2013.

[136] S. Ding, F. Liu, X. Shi, and H. He, "Promotional effect of Nb additive on the activity and hydrothermal stability for the selective catalytic reduction of NO_x with NH_3 over $CeZrO_x$ catalyst," Appl. Catal. B Environ., vol. 180, pp. 766–774, 2016.

[137] H. H. Phil, M. P. Reddy, P. A. Kumar, L. K. Ju, and J. S. Hyo, "SO_2 resistant antimony promoted V_2O_5/TiO_2 catalyst for NH_3-SCR of NO_x at low temperatures," Appl. Catal. B Environ., vol. 78, no. 3–4, pp. 301–308, 2008.

[138] X. Du, X. Gao, Y. Fu, F. Gao, Z. Luo, and K. Cen, "The co-effect of Sb and Nb on the SCR performance of the V_2O_5/TiO_2 catalyst," J. Colloid Interface Sci., vol. 368, no. 1, pp. 406–412, 2012.

[139] C. Xu, J. Liu, Z. Zhao, F. Yu, K. Cheng, Y. Wei, A. Duan, and G. Jiang, "NH_3-SCR denitration catalyst performance over vanadium-titanium with the addition of Ce and Sb," J. Environ. Sci. (China), vol. 31, no. x, pp. 74–80, 2015.

[140] P. A. Kumar, Y. E. Jeong, S. Gautam, H. P. Ha, K. J. Lee, and K. H. Chae, "XANES and DRIFTS study of sulfated Sb/V/Ce/TiO_2 catalysts for NH_3-SCR," Chem. Eng. J., vol. 275, no. x, pp. 142–151, 2015.

[141] P. A. Kumar, Y. E. Jeong, and H. P. Ha, "Low temperature NH_3-SCR activity enhancement of antimony promoted vanadia-ceria catalyst," Catal. Today, vol. 293–294, no. x, pp. 61–72, 2017.

[142] L. Chen, J. Li, and M. Ge, "Promotional Effect of Ce-doped V_2O_5-WO_3/TiO_2 with Low Vanadium Loadings for Selective Catalytic Reduction of NO_x by NH_3," J. Phys. Chem. C, vol. 113, no. x, pp. 21177–21184, 2009.

[143] M. Casanova, E. Rocchini, A. Trovarelli, K. Schermanz, and I. Begsteiger, "High-temperature stability of V_2O_5/TiO_2-WO_3-SiO_2 SCR catalysts modified with rare-earths," J. Alloys Compd., vol. 408–412, no. x, pp. 1108–1112, 2006.

[144] M. A. L. Vargas, M. Casanova, A. Trovarelli, and G. Busca, "An IR study of thermally stable V_2O_5-WO_3-TiO_2 SCR catalysts modified with silica and rare-earths (Ce, Tb, Er)," Appl. Catal. B Environ., vol. 75, no. 3–4, pp. 303–311, 2007.

[145] N. Bion, J. Saussey, M. Haneda, and M. Daturi, "Study by in situ FTIR spectroscopy of the SCR of NO_x by ethanol on Ag/Al_2O_3 — Evidence of the role of isocyanate species," J. Catal., vol. 217, no. x, pp. 47–58, 2003.

[146] A. Watanabe, "Highly conductive oxides, CeVO4, $Ce_{(1-x)}M_{(x)}VO_{(4-0.5x)}$ (M = Ca, Sr, Pb) and $Ce_{(1-y)}Bi_{(y)}VO_4$, with zircon-type structure prepared by solid-state reaction in air," J.

Solid State Chem., vol. 153, no. 1, pp. 174–179, 2000.
[147] C. T. Au, W. D. Zhang, and H. L. Wan, "Preparation and characterization of rare earth orthovanadates for propane oxidative dehydrogenation," Catal. Letters, vol. 37, no. 3–4, pp. 241–246, 1996.
[148] C. T. G. Petit, R. Lan, P. I. Cowin, J. T. S. Irvine, and S. Tao, "Novel redox reversible oxide, Sr-doped cerium orthovanadate to metavanadate," J. Mater. Chem., vol. 21, no. 2, pp. 525–531, 2011.
[149] F. Luo, C. J. Jia, R. Liu, L. D. Sun, and C. H. Yan, "Nanorods-assembled $CeVO_4$ hollow spheres as active catalyst for oxidative dehydrogenation of propane," Mater. Res. Bull., vol. 48, no. 3, pp. 1122–1127, 2013.
[150] N. Ekthammathat, T. Thongtem, A. Phuruangrat, and S. Thongtem, "Synthesis and characterization of $CeVO_4$ by microwave radiation method and its photocatalytic activity," J. Nanomater., vol. 2013, pp. 1–7, 2013.
[151] R. Jindal, M. M. Sinha, and H. C. Gupta, "Lattice vibrations of AVO_4 crystals (A = Lu, Yb, Dy, Tb, Ce)," Spectrochim. Acta - Part A Mol. Biomol. Spectrosc., vol. 113, pp. 286–290, 2013.
[152] A. B. Garg, K. V. Shanavas, B. N. Wani, and S. M. Sharma, "Phase transition and possible metallization in $CeVO_4$ under pressure," J. Solid State Chem., vol. 203, pp. 273–280, 2013.
[153] L. Zhu, Q. Li, J. Li, X. Liu, J. Meng, and X. Cao, "Selective synthesis of mesoporous and nanorod $CeVO_4$ without template," J. Nanoparticle Res., vol. 9, no. 2, pp. 261–268, 2007.
[154] M. Casanova, K. Schermanz, J. Llorca, and A. Trovarelli, "Improved high temperature stability of NH_3-SCR catalysts based on rare earth vanadates supported on $TiO_2WO_3SiO_2$," Catal. Today, vol. 184, no. 1, pp. 227–236, 2012.
[155] M. Casanova, J. Llorca, A. Sagar, K. Schermanz, and A. Trovarelli, "Mixed iron-erbium vanadate NH_3-SCR catalysts," Catal. Today, vol. 241, no. PA, pp. 159–168, 2015.
[156] S. Gillot, J. P. Dacquin, C. Dujardin, and P. Granger, "High Intrinsic Catalytic Activity of $CeVO_4$-Based Catalysts for Ammonia-SCR: Influence of pH During Hydrothermal Synthesis," Top. Catal., vol. 59, no. 10–12, pp. 987–995, 2016.
[157] Y. Peng, C. Wang, and J. Li, "Structure-activity relationship of VO_x/CeO_2 nanorod for NO removal with ammonia," Appl. Catal. B Environ., vol. 144, pp. 538–546, 2014.

Chapter II

Experimental protocols and techniques

Summary

1 Synthesis protocols 71

2 Chemical Characterization Techniques 72

2.1 X-ray diffraction (XRD) 72

2.2 Raman Spectroscopy 75

2.3 X-ray photoelectron spectroscopy (XPS) 76

2.4 Single point BET 77

2.5 Pyridine adsorption-desorption 79

2.6 Elemental analysis 79

2.6.1 Inductively Coupled Plasma – Optical Emission Spectrometry (ICP-OES) 80

2.6.2 X-ray fluorescence (XRF) 81

2.7 Temperature programmed reduction by H_2 (H_2-TPR) 82

3 Catalytic performance measurements 82

3.1 Experimental setup for catalytic test 83

3.2 Catalytic performance test protocols 85

3.3 Quantitative analysis of the effluent gases composition 85

4 References 87

1 Synthesis protocols

All synthesis protocols are based on the hydrothermal route from nitrate precursors. In spite of the fact that the hydrothermal technique has made great progress, there is no unanimity about its definition. The term hydrothermal usually refers to any heterogeneous reaction in the presence of aqueous solvents or mineralizers under high pressure and temperature conditions to dissolve and recrystallize materials that are relatively insoluble under ordinary conditions. Hydrothermal synthesis is a technique that involves the growth of materials from aqueous solutions at elevated temperature and pressures. Temperature, pressure, and mineralizers are used in this process to increase precursor solubility and to change solution conditions to favor formation of the desired phase. Mineralizers are complexing agents that act to increase the solubility of the starting precursors by forming soluble complexes. This route has several advantages including simplicity, low processing temperatures, low cost, high product purity, and the ability to control the particle size. Depending on the compound to be formed the precursors need to be well-chosen because they influence greatly the synthesis condition. Indeed, different precursor solubilities may make necessary to change the synthesis parameters such as the pH and in some case may lead to the impossibility of forming a desired mixed oxide. All solids were synthesized via a hydrothermal route reported in the following chapters. Na_3VO_4 (99.98 wt% from Sigma-Aldrich) was added to 50 mL of distilled water under vigorous stirring until complete dissolution. An aqueous solution of nitric acid (3 M) was further added drop by drop until the stabilization to pH =1.8. Once stabilized, the solution of all other precursors together was poured into the vanadium solution. A sodium hydroxide solution (1 M) was added dropwise. The suspension was subsequently treated in a Teflon-lined hydrothermal synthesis autoclave at 180°C for 24h. Solids were separated from the aqueous solution by centrifugation, washed abundantly with distilled water and finally with ethanol. Solids were then dried in air at 80°C for 24 h and solids were denoted as ‘‘unaged’’ solids. The solids (150–

300 μm) were aged at 600 and 850°C for 5 h (denoted as ‘‘Aged’’ solids) in a gas mixture composed of air and 10 vol. % H_2O with a gas hourly space velocity of 42 000 $mL.h^{-1}.g^{-1}$.

2 Chemical Characterization Techniques

The catalysts prepared were characterized in order to determine their physical properties such as the specific surface area, the particles size and, on the other hand, their surface and bulk properties such as the composition, the crystallite size, the structure, etc. In the present work, the techniques used to characterize the catalysts are divided in two groups corresponding to the determination of morphological and textural properties (i) surface properties by X-ray photo-electron spectroscopy (XPS), nitrogen adsorption and pyridine adsorption (ii) bulk properties by ICP-OES, X-ray fluorescence (XRF), X-ray diffraction (XRD), temperature programmed reduction of hydrogen (H_2-TPR) and Raman spectroscopy.

2.1 X-ray diffraction (XRD)

X-ray diffraction is a non-destructive technique that is widely used for structure determination of crystalline materials. This technique was carried out using D8 Advance Bruker X-ray diffractometer with monochromatized Cu (K_α=1.5418Å). Measurements were accomplished at room temperature in the 2θ range 5–80° using a step size of 0.05° with an acquisition time equal to 0.5s. The treatment of the results was made with the software EVA and the diffraction patterns have been indexed by comparison with the Joint Committee on Powder Diffraction Standards (JCPDS) files.

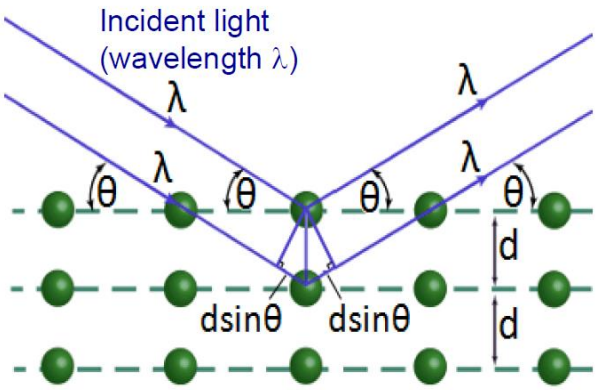

Figure 2.1 – **Visualization of Bragg diffraction**

Most crystals can have many sets of planes passed through their atoms. Each plane has a particular interplanar distance and will give rise to a characteristic angle of diffracted x-rays. The relationship between wavelength, atomic spacing and diffraction is known as the Bragg equation, in which n is an integer (reflection order), λ is the wavelength of the incident X-ray beam, d is the distance between parallel lattice planes, and θ is the angle of diffraction (E.q. 2.1).

$$n \cdot \lambda = 2d \cdot \sin\theta \qquad \text{(Equation 2.1)}$$

The interplanar distance can be calculated from the Bragg equation when the wavelength is known (based on the type of X-ray tube applied and if using monochromator) and the angle can be measured (with a diffractometer). With a single compound, a set of d-spaces is obtained, which can be used for comparison with sets of d-spaces obtained from standard compounds and/or from a database. In general, six parameters are required to define the shape and size of a unit cell, these being three cell edge lengths (conventionally, defined as a, b, and c), and three angles (conventionally, defined as α, β, and γ). In the mathematical sense, a, b, and c are vectors since they specify both length and direction. α is the angle between b and c, β is the angle between a and c, γ is the angle between a and b [1].

Table 2.1 – **Unit cell types and the seven crystal systems**

Crystal System	Bravais Lattices	Symmetry	Axis System
Cubic	**P,I,F**	**m3m**	**a=b=c, α=β=γ=90**
Tetragonal	**P,I**	**4/mmm**	**a=b≠c, α=β=γ=90**
Hexagonal	**P,R**	**6/mmm**	**a=b≠c, α=β=90 γ=120**
Rhombohedral	**R**	**3m**	**a=b=c, α=β=γ≠90**
Orthorhombic	**P,C,I,F**	**mmm**	**a≠b≠c, α=β=γ=90**
Monoclinic	**P,C**	**2/m**	**a≠b≠c, α=γ=90 β≠90**
Triclinic	**P**	**1**	**a≠b≠c, α≠β≠γ≠90**

In addition to phase determination, powder XRD patterns can be used to estimate the crystal size in a powder material. As the particle size decreases, the reflections in the XRD pattern will be broadened. This correlation is used in Scherrer's equation to calculate the particle size (D):

$$D = \frac{K\lambda}{\beta\cos\theta} \qquad \text{(Equation 2.2)}$$

Where K is the shape factor (K=1 for spherical particles), λ is the X-ray wavelength (1.5418Å in the case of Cu Ka radiation), β is the full width at half maximum of the reflection peak that has the same maximum intensity in the diffraction pattern, and θ is the Bragg angle [2].

Heat treatment causes particles to form larger grains, thereby increasing the degree of crystallinity of the sample. This effect is often seen as increased peak intensity in the diffraction data and change in width. Heat treatment of samples provides an opportunity to compare how the shape and intensity of peaks change between samples of various particle sizes [3].

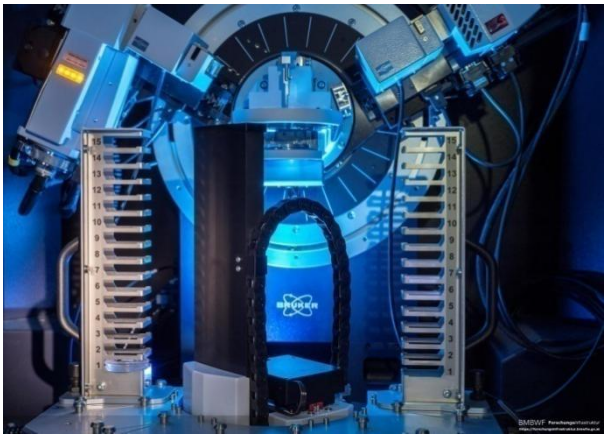

Figure 2.2 **– Laboratory X-ray diffractometer**

2.2 Raman Spectroscopy

Raman scattering spectroscopy is a technique for observing vibrational and rotational (in the case of gas phase) states of molecules and crystals. The fundamental process of the Raman Effect is the transfer of energy between light and matter. Raman spectroscopy employs this effect by measuring the scattering of the light from molecules in different vibrational states of the material and the consequent energy exchange between the incoming light and the molecule. Raman stokes and anti-stokes effects correspond to diffusion phenomena inelastic photons following their interaction with the specimen. The loss (stokes diffusion) or the gain (anti-stokes diffusion) of energy during these phenomena give direct access to the vibrational states of the specimen [4].

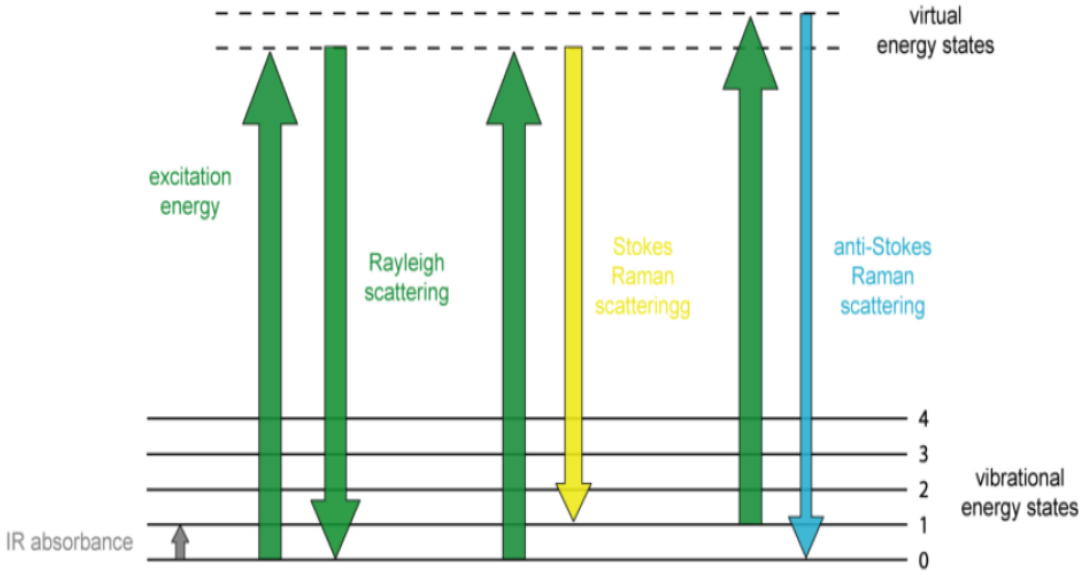

Figure 2.3 – **The absorbance and scattering of light from matter**

Experimentally, a Raman spectrum is made with a monochromatic excitation source (laser) whose wavelength can be from UV to near IR. Analyze were carried out using a confocal Raman microscope (Xplora, Horiba Jobin Yvon). The 638nm diode laser with a power of 25mW was used to excite the sample through a 50X objective (LWD: long working distance; NA: 0.50) (MPlan N, Olympus). The RAMAN signal collected in the backscattering mode was dispersed in the built-in spectrograph by a 600 gr/mm grating and detected by an Open-Electrode CCD (Syncerity, Horiba Jobin Yvon). The total data acquisition time was 5s using the LabSpec 6 software.

2.3 X-ray photoelectron spectroscopy (XPS)

X-ray photoelectron spectroscopy allows the chemical composition of a material to be determined nondestructively. In this technique, a sample is illuminated with X-rays to excite electrons from bound states and eject them into the vacuum. Analysis of the energy spectrum of the emitted electrons enables the chemical identification of the surface. To generate an XPS spectrum, a monochromatic X-ray beam with a photon energy of hν incident upon a sample surface causes the photoemission of electrons from energy levels with a binding energy E_b <

hν. A simple model suggests that the kinetic energy, E_k, of the photoelectron is simply the difference between the photon energy and electron binding energy [5]:

$$E_k = h\nu - E_b \text{ (Koopman's theorem)} \qquad \text{(Equation 2.3)}$$

The X-ray photoelectron spectroscopy (XPS) experiments were carried out in a Kratos AXIS Ultra DLD spectrometer using a monochromatic Al K_α radiation (1486.6 eV) operating at 225 W (15 mA, 15kV). High-resolution spectra were collected using an analysis area of ≈300µm×700µm and a 40 eV pass energy. Instrument base pressure was 4×10−10 Torr. The Kratos charge neutralizer system was used for all analyses and the binding energies were corrected taking C 1s peak corresponding to C-C/C-H type bonding at 285 eV as reference. The C 1s, O 1s, V 2p,W 4f, Ce 3d, Pr 3d, Gd 4d, Tb 4d, Er 4d, Sb 3d, Mo 3d and Nb 3d spectra were analyzed using the CasaXPS software (version 2.3.16, Casa Software Ltd.). Spectra decomposition and quantification was performed after a Shirley type background subtraction and Gaussian–Lorentzian profiles with 30/70 Gaussian/Lorentzian proportion were used.

2.4 Single point BET

Specific surface is one of the most important textural proprieties and can be used for correlating the physical chemical properties of the catalyst with its reactivity. The specific surface area of powder is determined by physical adsorption of nitrogen, on the surface of the solid and calculating the amount of the solid of adsorbate gas corresponding to a monomolecular layer on the surface applying Brunauer, Emett and Teller (BET) method [6].

The resultant equation of BET adsorption isotherm in the linear form is:

$$\frac{P}{n^a.(P^0-P)} = \frac{C-1}{n_m^a.C}\frac{P}{P^0} + \frac{C-1}{n_m^a.C} \qquad \text{(Equation 2.4)}$$

In which n^a is the amount adsorbed gas at the relative pressure P/P^o, n_m^a is the monolayer capacity, P is the measured pressure of the gas, P^o is the saturated vapor pressure of the gas at the temperature of adsorption, and C is a constant.

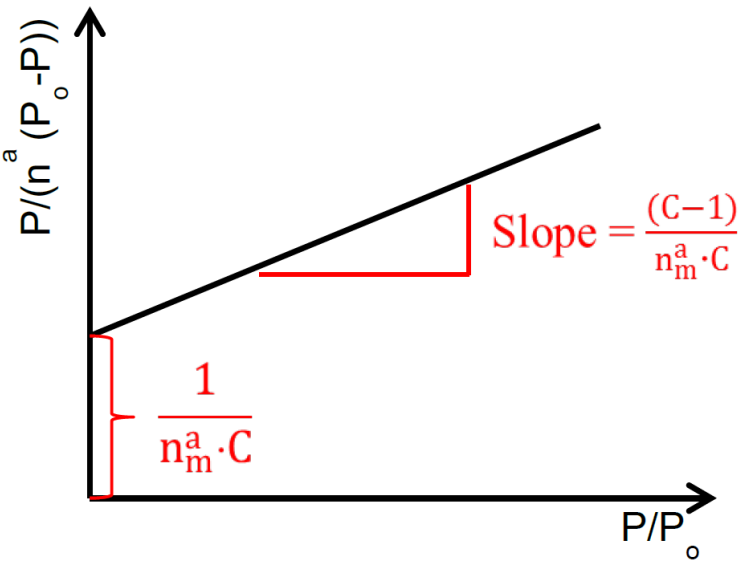

Figure 2.4 – **Visualization of BET**

Hence, the specific surface area (SBET) can be determined from Eq:

$$S_{BET} = \frac{n_m^a . L . a_m}{m} \qquad \text{(Equation 2.5)}$$

In which a_m is molecular cross-sectional area, m is the mass of adsorbent, and $L = 6.023 \cdot 10^{23}$ is the Avogadro constant.

The specific areas of the solids are determined using a FlowSorb III apparatus (Micromeritics) equipment after heating under vacuum at 100°C for 45 minutes to remove adsorbed residual impurities.



Figure 2.5 – **B.E.T. FlowSorb III machine of the laboratory**

2.5 Pyridine adsorption-desorption

The use of pyridine as a selective probe molecule to characterize both qualitative and quantitative aspects of surface acidity is widespread. The assignments of the IR bands are related to the band positions and the type of interaction between pyridine and the sites on which it is adsorbed [7–9]. The nature of the acid sites in the aged catalysts at 600°C was investigated by pyridine adsorption and the strength of acid sites was determined via desorption at 150°C, 250°C, 350°C and 450°C. Infrared spectroscopic measurements during pyridine adsorption-desorption experiments were carried out on a Nicolet Protégé 460 infrared spectrometer. Prior to pyridine adsorption at room temperature, samples were outgassed under vacuum (10^{-5} mbar) at 450°C. First of all, a standardized pellet at 201mm² is loaded. IR spectra were recorded after evacuation at different temperatures in the range of 150–450°C. The values of the absorption coefficients used for the quantification of Lewis and Brönsted acid sites after integration of infrared bands were respectively 2.22 cm/µmol and 1.67 cm/µmol as reported in the literature [10]. The quantification of acid sites can be obtained as followed:

$$n = (A*S)/(\varepsilon*m) \qquad \text{(Equation 2.6)}$$

A: area of the band (absorbance)

S: surface of the pellet (2.01cm^2)

ε: molar extinction coefficient (cm/μmol)

n: number of acidic sites (μmol/g)

m: mass of the pellet (g)

2.6 Elemental analysis

The elemental analysis allows determining the weigh composition of every spice present in the solid. The elemental composition of the catalyst has been obtained by Inductivity Coupled Plasma optical emission spectroscopy (ICP-OES) and X-Ray Fluorescence (XRF).

2.6.1 Inductively Coupled Plasma – Optical Emission Spectrometry (ICP-OES)

The elemental analyzes were performed using an optical emission spectrometer (ICP-OES, Varian Vista Pro axial view). The principle of the ICP-OES measurement is based on the nebulization then the atomization of the liquid sample in argon plasma (6000-8000°C). The electrons of the outer layers of the sample are then excited to a higher energy level. Their return to the ground state is accompanied by the emission of a series of electromagnetic waves characteristic of each element in the range of the UV-visible spectrum. The different wavelengths are separated by a spectrometer containing a network and a prism and then detected simultaneously by a CCD detector (Coupled Charge Device). The intensity of the radiation is proportional to the concentration of the element.

2.6.2 X-ray fluorescence (XRF)

The relative content of oxide was determined with the use of an energy dispersive X-Ray Fluorescence spectrometer M4 TORNADO (Bruker). This instrument is equipped with 2 anodes a Rhodium X-ray tube 50 kV/600 µA (30 W) and a Tungsten X-Ray tube 50 kV/700 µA (35 W). For sample characterization, the X-rays Rhodium with a polycapillary lens enabling excitation of an area of 200 µm was used. The detector used was a Silicon-Drift-Detector Si (Li) with <145 eV resolution at 100000 cps (Mn Kα) and cooled with a Peltier cooling (253°K). The measurement was done under vacuum (20 mbar). The elements, that can be measured by this instrument unit range from sodium (Na) to uranium (U). Quantitative analysis was done using the fundamental parameter (FP) (standardless). As elements are present in stoichiometric compounds, its formula was used for quantification of the weight percent of each element.

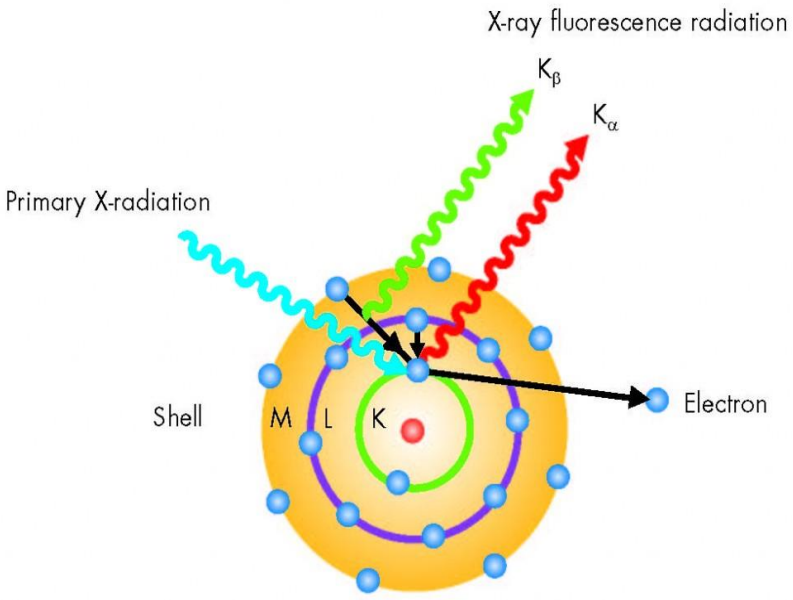

Figure 2.6 – **principle of XRF**

2.7 Temperature programmed reduction by H_2 (H_2-TPR)

The redox properties play a significant role in catalysis. The reducibility of catalysts can be characterized by H_2-TPR. Based on H_2-TPR profiles, reduction peaks of different species were obtained at temperatures needed for their reduction. The hydrogen consumption can be used for the quantification of the reduction capacity of active species. Temperature-programmed reduction with hydrogen (H_2-TPR) of the catalysts was performed in Micromeritics Autochem 2920 equipment, and a temperature ramp from 20 to 1000 °C with ramping of 10°C/min under a mixture consisting of 5% hydrogen diluted in argon (total flow rate of 3L.h^{-1}). The effluent gas was analyzed with a Thermal Conductivity Detector (TCD).



Figure 2.7 – **Micromeritics Autochem 2920 machine**

3 Catalytic performance measurements

Catalytic performance tests were conducted in lab-scale condition experiments with feed gas composition representative of the exhaust gas. The diesel engines exhaust gas compositions are generally complex with atmospheric pollutants present in very low concentrations (a few 1000 ppm) with the majority gases including CO_2, H_2O, and O_2 (5 to 15%). The reaction mixture depends on numerous conditions, for example, it depends on engine conditions, and the location of the different pollution control systems. In this thesis, the catalytic reaction condition adapted

to operating conditions comparable to the real conditions, in particular with a fluctuating NO/NO_x ratio.

Table 2.2 **– Feed compositions for catalytic tests**

Gas	NO_x	NH_3	O_2	CO_2	H_2O
Content (% volume)	**0.04**	**0.04**	**8.00**	**10.00**	**10.00**

The NO/NO_x ratio depends on many factors: the amount of O_2, temperature, the presence of an upstream DOC (Diesel Oxidation Catalyst) and etc. In order to investigate the fluctuation of NO/NO_x ratio in the NH_3-SCR lines, 3 different NO/NO_x ratio were chosen:

NO/NO_x = 1/2 or 200 ppm NO and 200 ppm NO_2. The Fast-SCR reaction predominates:

$$2NH_3+NO+NO_2=2N_2+3H_2O \qquad \text{(Equation 2.7)}$$

NO/NO_x = 3/10 or 120 ppm NO and 280 ppm NO_2. The "NO_2-SCR" reaction predominates:

$$8NH_3+ 6NO_2=7N_2+12H_2O \qquad \text{(Equation 2.8)}$$

NO/NO_x = 1/1 or 400 ppm NO. The Standard-SCR reaction predominates:

$$4NH_3+ 4NO+O_2=4N_2+6H_2O \qquad \text{(Equation 2.9)}$$

3.1 Experimental setup for catalytic test

Catalytic measurements were performed with a setup according to the scheme in Fig 2.8. The reactants were supplied into the reactor by gas tubes and the follow rates were fixed by Brooks 5850S, 5850SE and 5850TR mass flow regulators. This allowed conducting the tests with a space velocity (Eq. 2.10 with Q_0 standing for the total flow rate, $m_{catalyst}$ for the mass of the catalyst) of 250 000 $mL.h^{-1}.g^{-1}$ in all conditions. All gases are passed at a 3 bars pressure before introduction to the reactor. The different gas streams (except NH_3) are homogenized in a mixer before being introduced into the reactor. The diluted ammonia is sent out of the mixer to the evaporator to avoid the ammonium nitrate formation in the presence of NO_2. An excess of helium is sent to the evaporator in order to obtain a sufficient flow rate to carry the water vapor constantly. The NH_3+H_2O+He mixture is added to the reaction stream at the reactor inlet.

$$\text{Space velocity} = \frac{\boldsymbol{Q_0}}{\boldsymbol{m_{catalyst}}} \qquad [\text{Space velocity}] = \frac{\mathbf{ml.h^{-1}}}{\mathbf{g}} \quad \text{(Eq 2.10)}$$

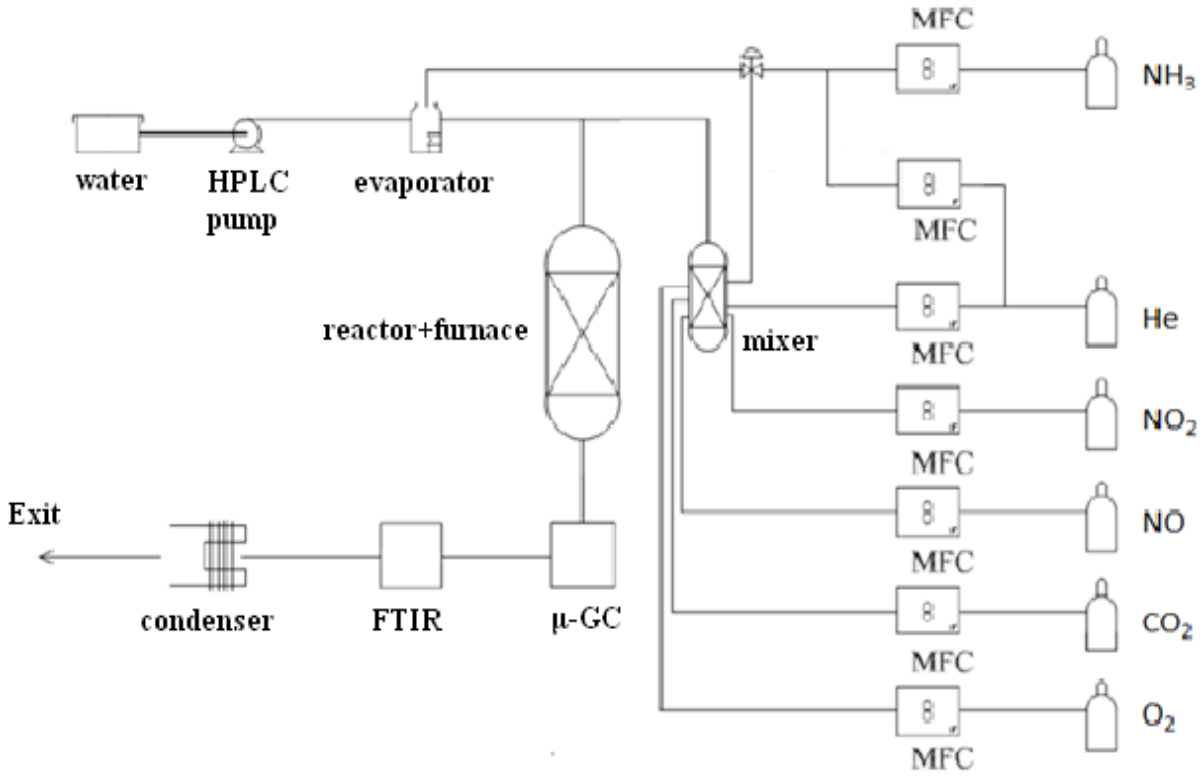

Figure 2.8 – **catalytic test setup scheme**

Selective catalytic reduction of NO_x by ammonia was performed at atmospheric pressure. In our study, the test was carried out using a quartz fixed bed flow reactor (inner diameter (*d*) of 8mm). A constant heating rate of 3°C/min was maintained up to the final temperature. The tests were measured at a total flow rate (F_0) of 20 $L.h^{-1}$ corresponds to a residence time (W/F_0) of 4 $\times 10^{-3}$ $g.h.L^{-1}$. The temperature is measured by a thermocouple inserted directly in the catalytic bed and the reactor is heated by means of an electric furnace. For each test, 80 mg of given samples were sieved in the granulometry of 150-300 µm and mixed with 1 g of SiC in order to improve the thermal diffusion in the catalytic bed. The inlet and output of the reactor are maintained at 180°C to prevent the formation of ammonium nitrate. Downstream of these devices, the water is removed after µGC using a Peltier condenser maintained at 5°C.

3.2 Catalytic performance test protocols

After each aging step (10% H_2O + air, 5h), the catalytic performances are evaluated in three reaction mixtures corresponding to the NO/NO_x molar ratios (1/2, 3/10 and 1/1) from 200°C to 500°C (GHSV = 250 000mL.h^{-1}.g^{-1}).

The outlet gas concentration (N_2 and N_2O) was analyzed with a µGC for the substituted solids for all substituted solids. It is not possible to detect the impact of ammonia oxidation to NO. The experimental protocol is illustrated in Figure 2.9.

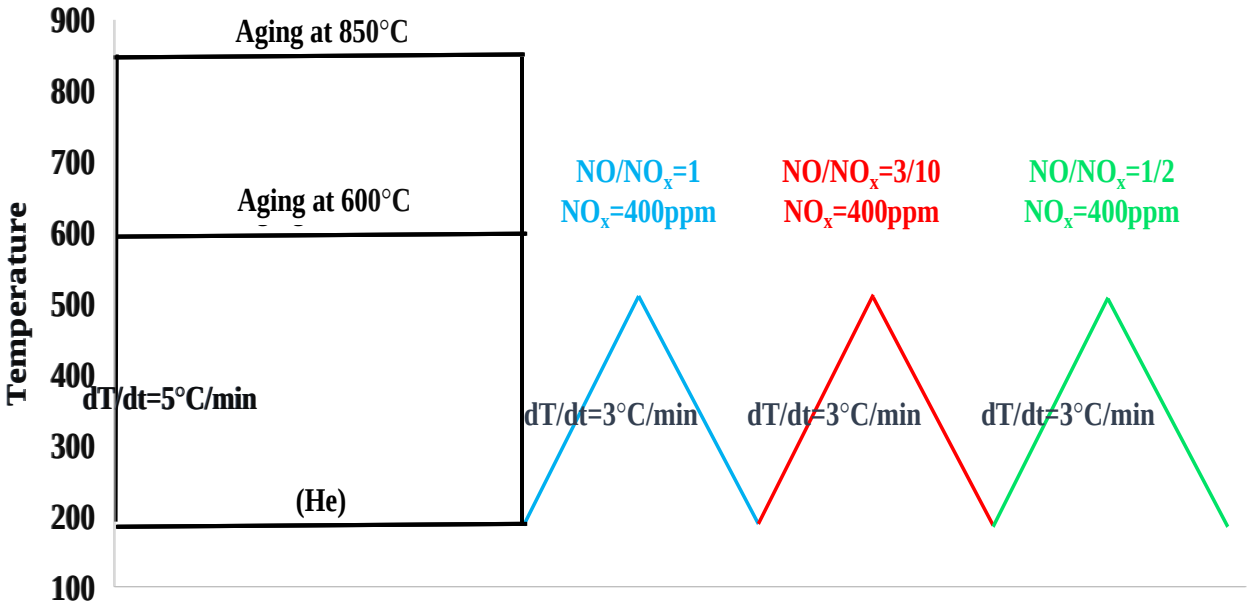

Figure 2.9 – **Catalytic cycle used to study the performance of NH_3-SCR catalysts**

3.3 Quantitative analysis of the effluent gases composition

The chromatography analysis performed on the effluents directly at the outlet of the reactor with a Varian CP4900 µGC equipped with a "Genie Filter" membrane filter. The lines and injectors of µGC are heated to 160°C. The µGC is equipped with two columns, each one is equipped with a thermal conductivity detector (micro TCD). Helium is used as a carrier gas. N_2, O_2 and NO are separated by a 5Å molecular sieve (MS5A). Another column Porapak (PPQ)

separates CO_2, N_2O and H_2O. Due to a slow elution of NO and the thermodynamic equilibrium between NO/NO_2, its accurate quantification cannot be obtained from µGC.

µGC quantification performed by an calibration of peak areas and due to the response coefficients from the calibration lines. The NO_x conversion is calculated from the N_2 and N_2O concentration according to Equation 2.11:

$$NO_{x\ conversion} = \frac{2*(C_{N_2}+C_{N_2O})}{C_{NO_x\ inlet}} * 100 \qquad \text{(Equation 2.11)}$$

The N_2O selectivity determined from Equation 2.12:

$$N_2O_{\ selectivity} = \frac{C_{N_2O}}{(C_{N_2}+C_{N_2O})} * 100 \qquad \text{(Equation 2.12)}$$

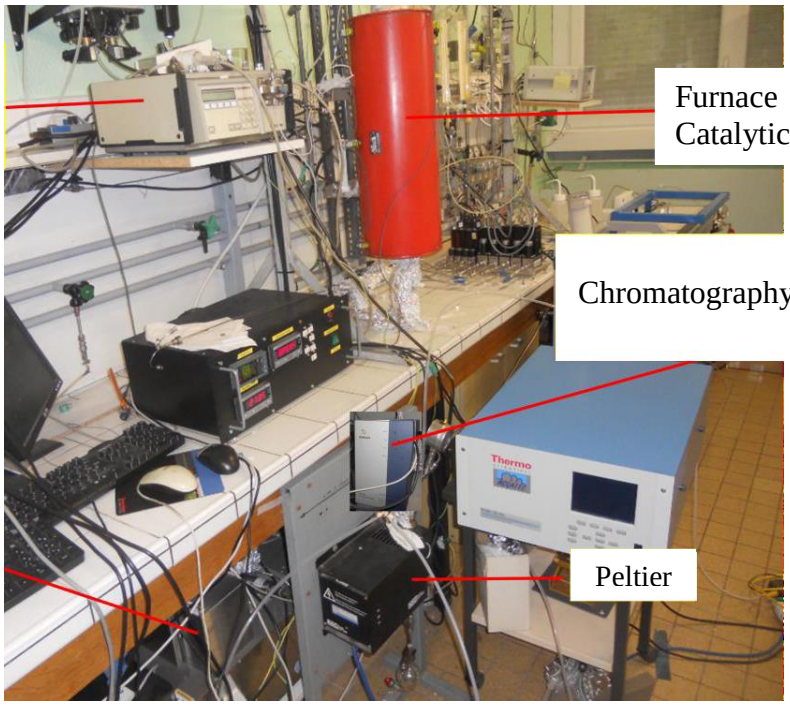

Figure 2.10 – **Set-up used for the NH_3-SCR**

4 References

[1] R. Asahi, Y. Taga, W. Mannstadt, and A. J. Freeman, “Electronic and optical properties of anatase TiO_2,” vol. 61, no. 11, pp. 7459–7465, 2000.

[2] A. Monshi, M. R. Foroughi, and M. R. Monshi, “Modified Scherrer Equation to Estimate More Accurately Nano-Crystallite Size Using XRD,” vol. 2012, no. September, pp. 154–160, 2012.

[3] R. Sharma, D. P. Bisen, U. Shukla, and B. G. Sharma, “X-ray diffraction : a powerful method of characterizing nanomaterials,” vol. 4, no. 8, pp. 77–79, 2012.

[4] R. H. Atalla, U. P. Agarwal, and J. S. Bond, “Raman Spectroscopy,” *Methods in Lignin Chemistry*. pp. 162–176, 1992.

[5] C. R. Brundle and A. D. Baker, “Electron Spectroscopy : Theory , Techniques and Applications Basic Concepts of X-ray Photoelectron Spectroscopy,” vol. 2.

[6] P. H. Emmett, “Gases i n Multimolecular Layers,” vol. 407, no. 1, 1936.

[7] F. Hatayama and T. Ohno, “Structure and Acidity of Vanadium Oxide layered on Titania (Anatase and Rutile),” vol. 87, no. 16, pp. 2629–2633, 1991.

[8] T. Barzetti, E. Selli, D. Moscotti, L. Forni, C. Fisica, U. Milano, and V. C. Golgi, “Pyridine and ammonia as probes for FTIR analysis of solid acid catalysts,” vol. 92, no. ii, pp. 1401–1407, 1996.

[9] J. Goscianska, M. Ziolek, E. Gibson, and M. Daturi, “Meso – macroporous zirconia modified with niobia as support for platinum — Acidic and basic properties,” *Catal. Today*, vol. 152, no. 1–4, pp. 33–41, 2010.

[10] Z. Tvaru and Z. Sobalı, “Determination and properties of acid sites in H-ferrierite A comparison of ferrierite and MFI structures,” vol. 24, pp. 223–233, 1998.

Chapter III

The activity of $CeVO_4$-Based Catalysts for Ammonia-SCR: Impact of surface cerium enrichment

The activity of $CeVO_4$-Based Catalysts for Ammonia-SCR: Impact of surface cerium enrichment

Though cerium is known to promote NH_3-SCR reaction over catalysts, the effect of its loading in the system investigated in this chapter. This section addresses this point, in order to further understand its role in NH_3-SCR reaction. CeO_2 with high oxygen storage capacity, non-toxicity and facile cycling between Ce^{+3} and Ce^{+4} has been extensively applied in redox reactions [1]. However, it is generally known that pure CeO_2 only shows poor SCR performance [2–7]. Bulk $CeVO_4$ catalysts with an excess of CeO_2 prepared by hydrothermal synthesis have been developed for the ammonia-selective catalytic reduction of NO_x to nitrogen. The catalytic properties were evaluated in standard-and fast-SCR conditions for stationary and mobile applications. The coexistence of Ce^{4+} species stabilized as CeO_2 with bulk $CeVO_4$ was found to be crucial for enhancing the intermediate formation of NO_2 from NO oxidation. Such cooperative effects impact on the NO conversion to nitrogen regardless of the operating conditions. Aging processes under the wet atmosphere at 600°C and 850°C did not destabilize the bulk zircon-type structure of $CeVO_4$. No loss of vanadium was observed due to significant sublimation of vanadium. Aged $CeVO_4$ catalyst with 11% CeO_2 in excess exhibits better catalytic properties in terms of NO conversion and selectivity. This opens new perspectives for vanadium-based catalysts in mobile sources applications. This higher catalytic activity of 11Ce-CeV catalyst can be attributed to the lattice labile oxygen and high surface area compared to that of Ce-CeV and 13Ce-CeV catalysts.

The activity of $CeVO_4$-Based Catalysts for Ammonia-SCR: Impact of surface cerium enrichment

Parnian Peyrovi, Sylvain Gillot, Jean-Philippe Dacquin, Pascal Granger, Christophe Dujardin*

Univ. Lille, CNRS, ENSCL, Centrale Lille, Univ. Artois, UMR 8181, UCCS - Unité de Catalyse et Chimie du Solide, 59650 Villeneuve d'Ascq, France

Abstract

The ammonia-SCR catalytic activity of unsupported $CeVO_4$ with an excess of CeO_2 was investigated in standard and fast-SCR conditions. Solids were obtained from a hydrothermal synthesis route under a mild condition and then stabilized after aging in a wet atmosphere at 600 and 850°C. Particular attention was paid to the role of the excess of CeO_2 and the consequences of hydrothermal aging on physical-chemical properties and catalytic activity. The XRD patterns put into evidence the formation of the zircon-type structure of $CeVO_4$ in agreement with a segregation of cubic face-centered structure of ceria (CeO_2). Along with adding the excess of CeO_2, high specific surface area (102 m^2/g) for the 11wt. % CeO_2 /$CeVO_4$ catalyst was obtained. The presence of CeO_2 nanoparticles in addition to $CeVO_4$ nanoparticles has limited the decrease in the specific surface area after aging at 600 and 850°C. The catalyst with 11wt. % CeO_2 /$CeVO_4$ exhibited the best catalytic performances in standard and fast SCR conditions.

Keywords: ammonia-SCR, nitrogen oxides, nitrous oxide, vanadium, $CeVO_4$

*Christophe Dujardin
christophe.dujardin@ensc-lille.

1 Introduction

Nitrogen oxides (NO_x) emitted from diesel engines would be harmful to human health and the environment. SCR of NO_x with NH_3 is considered to be the most efficient technology for reducing NO_x emission in the presence of excess oxygen [1]. However, even though this technology has been available for decades, the improvement of the operating temperature window and hydrothermal stability of the SCR catalysts is a challenge to meet the emission standards of NO_x from the mobile source. Complex systems for the simultaneous treatment of NO_x, hydrocarbon, and soot have been introduced, which are generally expensive and can lead to the reduction of engine efficiency [2,3]. The engine space limitation forced manufacturers to seek an alternative solution with the combination of different aftertreatment components. The incorporation of SCR catalyst directly into the porosity of the diesel particle filter (DPF) would save space, money and simplify the post-processing vehicles equipped with a diesel engine. Such implementation requires the improved thermal resistance of the SCR catalyst due to the exotherms related to the periodic regeneration of DPF [4]. Existing urea SCR active catalysts can serve as a starting point for a catalyst that is both active and stable under these new conditions. Important parameters influencing the activity of a catalyst are defined mainly by acidity and redox properties [5]. Therefore, deactivation of the catalysts is synonymous with degradation of their acid and/or redox properties, in particular when they are exposed to high temperature in the presence of water [6]. The aim of this study is focused on the development of new thermally stable active phases which are capable of maintaining their catalytic performances after hydrothermal aging at the high-temperature corresponding to intense conditions and maintain its selectivity toward N_2.

For the past several years copper-exchanged zeolite chabazite was commercialized for selective catalytic reduction of NO_x with ammonia [7]. Zeolite stability depends on the nature of the

structure, as for Cu-SSZ-13 and Cu-SAPO-34 zeolites catalysts for which the small pores and their chabazite-type structure limit the dealumination and segregation of large particles of Cu_xO_y [8]. Kwak *et al*. studied the activity and selectivity of Cu-SSZ-13 toward N_2 in comparison with Cu-beta and Cu-ZSM-5 zeolite in standard SCR condition. They confirmed that Cu-SSZ-13 catalyst shows higher NO_x conversion with the lower N_2O formation (<5 ppm) over the entire temperature range [9]. The NO_x conversion of commercial Cu-SSZ-13 and Cu-SAPO-34 catalysts deposited onto a monolith was investigated by Ma *et al*. in standard SCR condition and after aging at 600, 750 and 850°C [10]. They illustrate that the hydrothermal treatment of catalysts caused the decrease of SCR performance due to zeolite structure destruction and/or copper agglomeration. Their results indicate that Cu-SAPO-34 is much more resistant to high-temperature hydrothermal treatment than Cu-SSZ-13. It was observed that Cu-SSZ-13 yielded more N_2O formation than the Cu-SAPO-34 catalyst, especially at high temperature. Cu-SAPO-34 catalyst presents lower than 5% N_2O selectivity in a whole range of temperature after aging at 850°C [10].

The current benchmark catalyst used for the aftertreatment of stationary sources is V_2O_5-WO_3/TiO_2 which is highly active for NH_3-SCR especially at standard SCR condition. The SCR catalyst mostly including anatase TiO_2 as support material, WO_3 as a promoter of activity and stability and V_2O_5 as the active redox species [11]. The mechanism of NH_3-SCR over vanadia-containing catalysts reported in the literature usually assumes that acidic sites are needed for facilitating ammonia adsorption [12,13]. Otherwise, there are still some problems with the utilization of this catalyst, such as a limited operating temperature window and low N_2 selectivity at high temperature which reduce its further application in the deNO_x process for mobile sources [14]. The main drawback is associated with the toxicity of V_2O_5 oxide and its volatilization above the sublimation temperature (670°C) [15].

Among the wide variety of catalysts tested in recent years, those based on (modified) ceria

attracts considerable attention in NH_3-SCR [16,17]. On account of, optimal textural properties and intense ability to interact with other components, cerium oxide can be used as the promoter [18], support [19] and active sites [20] for NH_3-SCR catalysts.

Ceria is considered as a very active oxide in the SCR reaction, owing to considerable oxygen storage capacity [21], facility of changing oxidation state between Ce^{3+} and Ce^{4+} [22] and its stability to enhancing the oxidation of NO to NO_2 [23,24]. Moreover, ceria-based NH_3-SCR catalysts have attracted much attention due to their high non-toxic and relatively cheap characteristics [25–27]. In spite of that, there are still large numbers of problems, such as the sulfur resisting capacity [28] aging resistance [29] and low selectivity to N_2 [30] to be solved. Hydrothermal aging of the catalyst is well known as a negative impact on catalytic activity that significantly decreases the NO_x conversion capability of an SCR system [31,32]. However, limited information is available in the literature with regard to the effect of hydrothermal aging on NH_3-SCR NO_x conversion of CeO_2 modified catalysts [29,33]. $CeVO_4$ based materials have received recent attention in view of their potential applications in NH_3-SCR [34–36]. Gillot *et al*. underlined the potential of unsupported $CeVO_4$ catalyst prepared by the hydrothermal method in NH_3-SCR reaction. They showed that the catalyst is predominantly composed of tetragonal $CeVO_4$ phase but a slight segregation of cubic CeO_2 phase is also put into evidence [37].

The aim of this study is to highlight the role played by CeO_2 in the catalytic activity of $CeVO_4$ in the NH_3-SCR reaction. The segregation of CeO_2 during the synthesis will be investigated through the physicochemical characterization. It will show that the excess of CeO_2 in the catalyst formulation leads to improved catalytic activity after aging at 600 and 850°C.

2 Experimental

2.1 Catalyst Preparation and Physicochemical Characterization

The samples were prepared by hydrothermal method (Fig 1). Appropriate amounts of vanadium salt Na_3VO_4 (99.98 wt. % Sigma-Aldrich) were dissolved in 50mL of distilled water at room temperature. The solution was acidified to a pH close value to 1.8 with the nitric acid solution at room temperature. The excess of $Ce(NO_3)_3 \cdot 6H_2O$ was added to the vanadium solution under stirring. Sodium hydroxide solution (1M) was added dropwise into the above solution to adjust the pH to 7. pH values during precipitation decrease sharply that can be explained by the following set of Equations (1) – (2) hence leading to the formation of $CeVO_4$.

$$VO_2^+ + 2OH^- = VO_4^{3-} + 2H^+ \quad (1)$$

$$Ce^{3+} + VO_4^{3-} = CeVO_4 \quad (2)$$

The resulting mixture suspension was transferred into a 50 ml Teflon-lined stainless steel autoclave and sealed tightly. Hydrothermal synthesis was carried out at 180°C for 24 h in an oven without shaking or stirring. After cooling to room temperature, the precipitates were collected, washed with distilled water and absolute ethanol several times, and then dried in air at 80°C for 24 h. The reference $CeVO_4$ materials and modified with an excess of 11 and 13 wt. % CeO_2 were respectively labeled Ce-CeV, 11Ce-CeV and 13Ce-CeV.

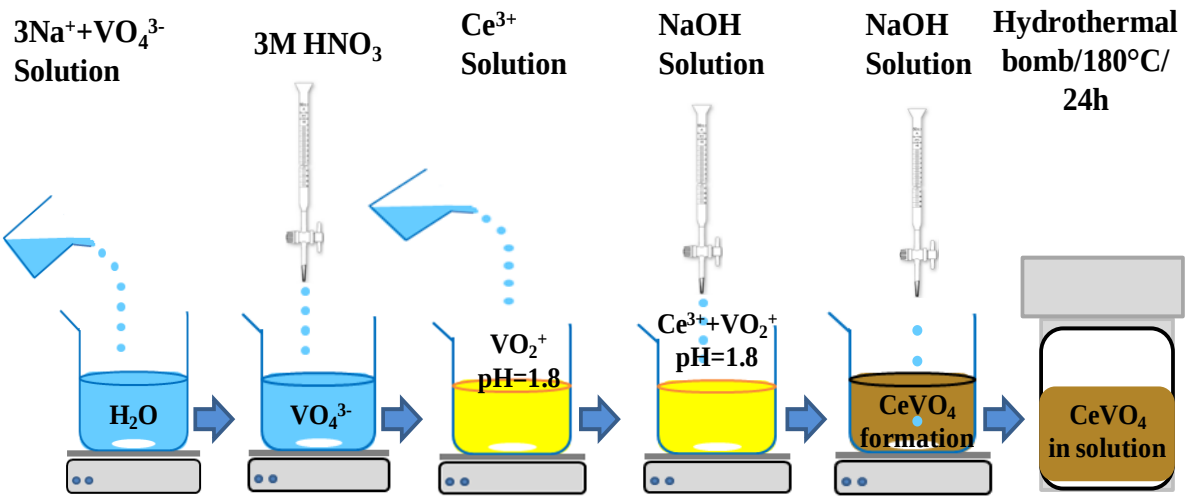

Fig 1 Steps involved during the hydrothermal synthesis of $CeVO_4$

Elementary analyses were performed by using inductively coupled plasma atomic emission spectroscopy (ICP-OES) Varian Vista Pro. A charge-coupled device (CCD) covering a broad spectral range (from 167 to 765 nm) was used as a detector.

Specific surface area of mixed oxides was measured by adsorption of N_2 at -196°C according to BET method. The specific areas were determined using a FlowSorb III apparatus (Micromeritics) equipment after heating under vacuum at 100°C for 45 minutes to remove adsorbed residual impurities.

All the samples were characterized by powder X-ray diffraction (XRD) on a D8 Advance Bruker X-ray diffractometer. XRD patterns were recorded from 5 to 80° (2θ) with a scanning step of 0.02° and an acquisition time of 0.5s.

The surface composition of samples over a thickness between 5 and 10 nm was determined by X-Ray Photoelectron Spectroscopy (XPS). XPS measurements were carried out using an AXIS Ultra DLD Kratos spectrometer. The system included a monochromatic X-ray source and an Al-Mg double anode. A spectral decomposition of the experimental photopeaks was analyzed using the CasaXPS software.

Temperature-programmed reduction with hydrogen (H_2-TPR) of the catalysts(70 mg) was performed in Micromeritics Autochem 2920 equipment, and with a temperature ramp from 20 to 1000°C (10°C/min) under 5% H_2/Ar (total flow rate of 3L.h^{-1}).

Raman spectra were acquired using a confocal Raman microscope (Xplora, Horiba Jobin Yvon). The 638 nm diode laser was used to excite the sample through a 50X objective (MPlan N, Olympus). The Raman signal collected in the backscattering mode was dispersed in the built-in spectrograph by a 600 gr/mm grating and detected by an Open-Electrode CCD (Syncerity, Horiba Jobin Yvon). The total data acquisition time was 5s.

2.2 Catalytic measurements

Catalytic performances were evaluated on catalyst powder (150–300 μm, 80 mg) in 1 g SiC (210 μm) tested in a plug-flow reactor. The catalytic performances are estimated in two reaction mixtures corresponding to the NO/NO_x molar ratios =1/2 and 1 (with NO_x = NH_3 = 400ppm, 10% CO_2, 10% H_2O and 8% O_2 diluted in He) from 200°C to 500°C with a heating rate of 5°C/min (GHSV = 250 000 mL.h^{-1}.g^{-1}). Before the activity test, the catalyst is aged at 600 and 850°C for 5 hours in the wet atmosphere (10% H_2O in air) with an hourly space velocity (GHSV) of 42000mL.h^{-1}.g^{-1}. The outlet gas concentration (N_2 and N_2O) was analyzed with a μGC equipped with two distinct columns (molecular sieve 5Å and porapak Q). The NO_x conversion is calculated from the N_2 and N_2O concentrations according to Eq. (3) and N_2O selectivity determined from Eq. (4):

$$X_{N_2O+N_2} = \frac{2 * (C_{N_2} + C_{N_2O})}{C_{NO_x\,inlet}} * 100 \qquad (3)$$

$$S_{N_2O} = \frac{C_{N_2O}}{(C_{N_2} + C_{N_2O})} * 100 \qquad (4)$$

3 Results and Discussion

The series of $CeVO_4$ catalysts with 0, 11 and 13wt. % CeO_2 in excess that denoted as Ce-CeV, 11Ce-CeV and 13Ce-CeV respectively were synthesized through the hydrothermal method. The chemical analysis was done by ICP-OES method to identify and quantify the elements present in the sample (Table 1). As a general trend, the cerium sub-stoichiometry associated with V/Ce = 0.83 and 0.81 corresponds to 11Ce-CeV and 13Ce-CeV respectively (Table 1).

3.1 Catalytic properties of cerium doped $CeVO_4$ catalysts in ammonia SCR

The NO_x conversion for different NO/NO_x ratio on Ce-CeV, 11Ce-CeV, and 13Ce-CeV catalysts after an ex-situ hydrothermal aging at 600°C or 850°C was investigated. NO_x concentration in diesel exhaust is usually composed of more than 90% NO [38]. On one hand, the main reaction of SCR with ammonia with NO/NO_x ratio equal to 1 so-called standard SCR will be:

$$2NO + 2NH_3 + 1/2O_2 \rightarrow 2N_2 + 3H_2O \qquad (5)$$

On the other hand, the NO_x conversion with equimolar amounts of NO and NO_2 (NO/NO_x=0.5) so-called fast-SCR has a higher reaction rate than that of standard SCR and is the following:

$$NO + NO_2 + 2NH_3 \rightarrow 2N_2 + 3H_2O \qquad (6)$$

Fast-SCR reaction is usually proposed as a practical possibility to increase the performance of diesel engine $DeNO_x$ systems [39,40].

Standard SCR

The NO_x conversion profiles during standard-SCR condition versus temperature are collected in Fig 2.A on the Ce-CeV catalysts aged in the presence of steam in the air at 600°C. All catalysts possessed of the high N_2 selectivity (100%) in the whole temperature range. The NO_x conversion increases with temperature at the low-temperature range (200–300°C). The reference Ce-CeV catalyst leads to an increase of NO_x conversion from 30% conversion at 200°C with a maximum NO_x conversion of 50% at 400°C. At high temperature, the oxidation

of NH_3 with oxygen leads to the lower NO_x conversion. The NO_x conversion declined when the temperature rises to 400°C on Ce-CeV catalyst likely due to the occurrence of undesired oxidation of NH_3 with oxygen as discussed elsewhere [37]. The NO_x conversion decreases to 35% at 500°C due to the competitive oxidation of NH_3 with oxygen that leads to lower NO_x conversion. Interestingly, significant changes in NO_x conversion are observable with regard to the amount of CeO_2 in excess. Previous investigations showed that CeO_2 itself can catalyze the ammonia-SCR reaction above 250°C [41]. 11Ce-CeV catalyst has a much higher NO_x conversion. The remarkable promotion effect of CeO_2 with the doping amount of 11% in standard-SCR condition is observed at medium temperature with a maximum conversion of 80% between 300–350°C. The capacity of CeO_2 to oxidize NO to NO_2 has been already pointed out [5, 42] and could be the driving force in the overall SCR process leading to a closer NO/NO_x ratio encountered in fast-SCR conditions. On the other hand, a NO_x conversion drop appears above 450°C likely related to the competitive oxidation of NH_3. It is worthwhile to note that 11Ce-CeV is more prone to more to oxidize NH_3 to NO than Ce-CeV in standard SCR-conditions. Surprisingly, 13Ce-CeV catalyst behave differently with a lower NO_x conversion capability with a maximum NO_x conversion of 45% at 300°C, while limited conversion enhancement achieves compared to Ce-CeV catalyst. The undesirable ammonia oxidation by oxygen is the predominant side reaction that results in decreasing NO_x conversion above 350°C.

Fast SCR

Under Fast-SCR conditions, an equimolar mixture of NO and NO_2 is introduced into the reactor (Fig 2.B). Catalytic measurements in fast SCR conditions on Ce-CeV catalyst lead to a higher NO_x conversion of approximately 89 versus 36 % for standard SCR conditions at 250°C. On the other hand, the conversion curves converge at high temperature irrespective of the operating conditions. Kobel *et al*. [40] found that the reaction involving an equimolar NO and NO_2 feed mixture (fast-SCR), is significantly faster than the standard-SCR reaction. They recommended,

in fast-SCR condition gaseous NO_2 replace oxygen as a more effective oxidizing agent, hence allowing faster reoxidation of the vanadium sites. In the same way, Topsoe *et al*. suggested that the rate determining step in NH_3-SCR reaction over vanadium-containing catalysts is the reoxidation of V^{4+}–OH to V^{5+}=O species.

NO_x conversion increases from 65% at 200°C to a maximum of 89% at 250°C on Ce-CeV catalyst and then starts to decreases. The NO_x conversion decreases from 80% to 30% between 300 to 500°C. The addition of CeO_2 on 11Ce-CeV leads to an increase of NO_x conversion between 250–400°C, with maximum NO_x conversion of 95% at 250°C. The NO_x conversion of 11Ce-CeV catalyst is much higher than that of the reference Ce-CeV catalyst, but its NO_x conversion is quite limited in the low (<250°C) and in high (>450°C) temperature range. Further addition of CeO_2 on 13Ce-CeV has a detrimental effect on NO_x conversion, which doesn't exceed 60% in the whole temperature range.

Ce-CeV catalyst is 100% selective toward N_2 (200–450°C) in fast SCR whereas at 500°C the N_2 selectivity declines to 90%. The 11Ce-CeV catalyst has the highest N_2 selectivity among the investigated catalysts in fast SCR. Moreover, a lower N_2 selectivity of 13Ce-CeV can be observed suggesting that the oxidative function on the 13Ce-CeV catalyst promote the non-selective oxidation of NH_3 at the expense of NH_3-SCR.

Impact of thermal aging

The NO_x conversion in fast-SCR condition versus temperature is reported for the catalysts aged at 850°C in Fig 2.C. It is obvious that hydrothermal aging at 850°C results in the decrease of NO_x conversion, which might be due to the sintering of active component. The NO_x conversion reaches 15% at 200°C on Ce-CeV catalyst, a maximum of 40% is recorded near 300°C and NO_x conversion decreases to 5% at 500°C. The NO_x conversions of catalysts with the excess of cerium remain below 40% underlining the detrimental effect of thermal aging at 850°C. NO_x conversion of 35–39% on 11Ce-CeV catalyst is significantly enhanced in a wide range of

temperature (250–450°C). Further temperature increase results in a lower NO_x conversion (25% at 500°C). The 11Ce-CeV catalyst has the higher NO_x conversion in fast-SCR compared to the reference Ce-CeV and 13Ce-CeV catalysts but a lower selectivity towards nitrogen formation, all selectivities decrease monotonically as a function of the temperature. The N_2 selectivity of the 13Ce-CeV catalyst decreases noticeably at 300–350°C with quite a large amount of N_2O being formed.

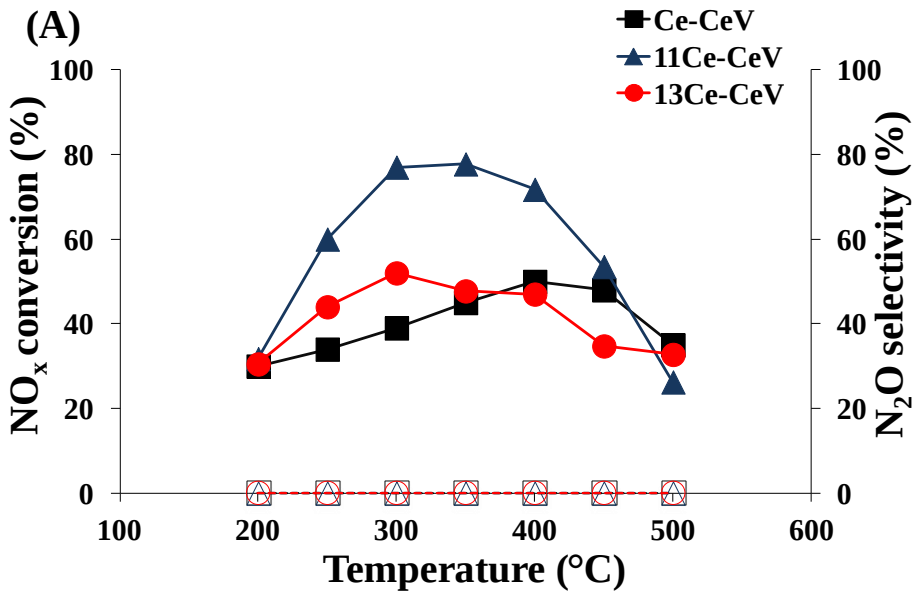

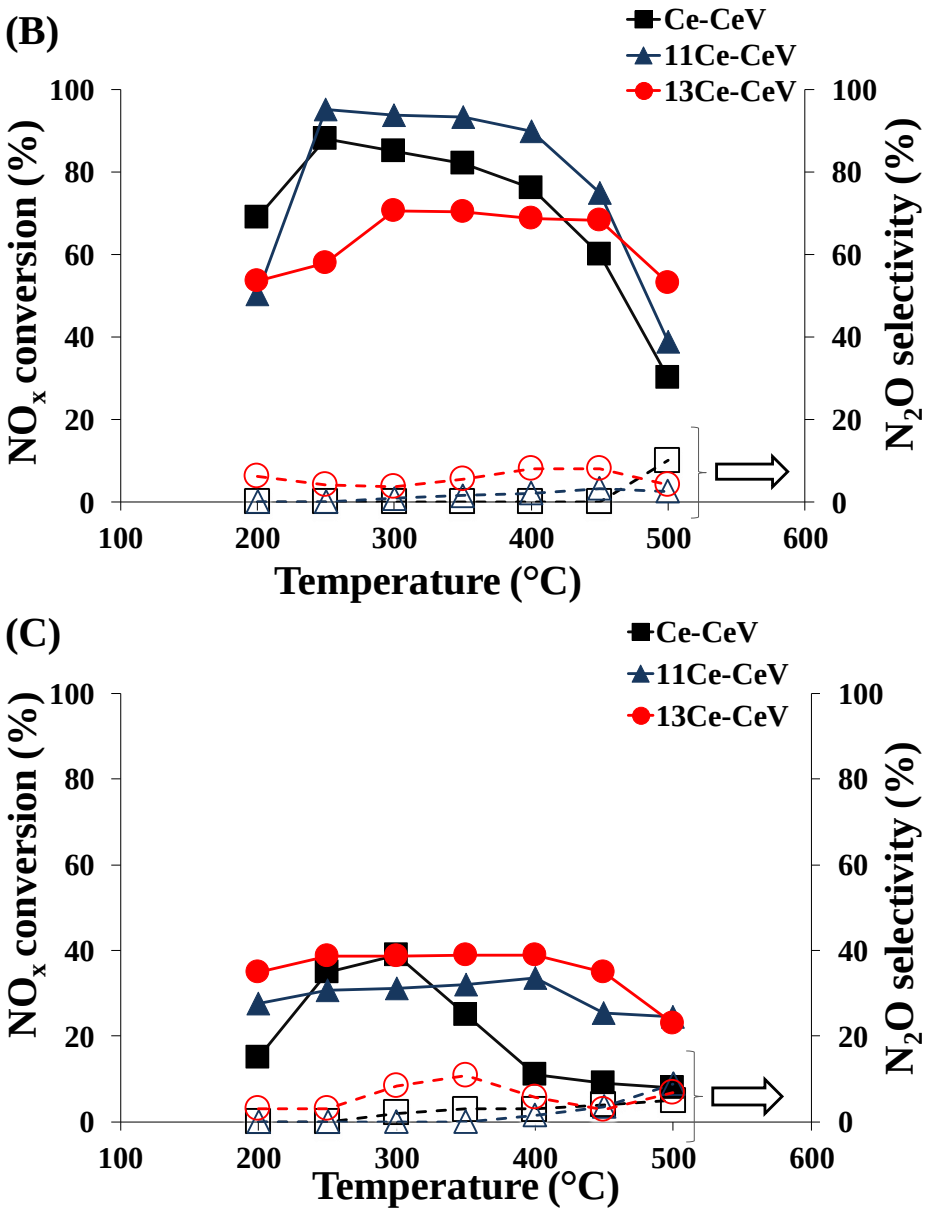

Fig 2 NO_x conversion (solid lines) and N_2O selectivity (dotted line) during the standard-SCR (A) and fast-SCR (B) reaction after aging at 600°C; fast-SCR (C) after aging at 850°C

3.2 Characterization of Bulk and Surface properties

3.2.1 Bulk Properties

The powder diffractograms recorded for the catalysts obtained after aging at 600 and 850°C in a wet atmosphere are displayed in Fig 3. The tetragonal zircon structure of $CeVO_4$ is detected for all catalysts with characteristic lines located at 2θ = 18, 24, 32 and 48°. Additional X-ray lines appear at 2θ = 28.5, 33 and 47.5° ascribed to the cubic face-centered fluorite structure of

CeO_2 on all Ce-CeV samples. The formation of ceria could be explained by the dehydration of $Ce(OH)_3$ during the hydrothermal synthesis and following oxidation with air into CeO_2 [43].

Table 1 lists the crystallite size that has been estimated using the Scherrer equation from the reflections corresponding to the (200) plane of $CeVO_4$ and (111) planes of CeO_2 at $2\theta = 24°$ and 28.5° respectively. The fresh catalysts generally have a $CeVO_4$ crystallite diameter from 15 to 27 nm.

The specific surface area is presented in Table 1. The high specific surface areas between 46 to 102 m^2/g of fresh catalysts can be explained by the relatively low temperature (180°C) during the hydrothermal synthesis. These values are in agreement with the crystallite diameter evolution.

Impact of aging

Hydrothermal aging at 600°C and 850°C lead to crystallographic changes mainly associated with the appearance of a phase assigned to rhombohedric Ce_7O_{12} for all catalysts except for the catalyst with the lower Ce loading (Ce-CeV catalyst) (Fig 3.B). The segregation of Ce_7O_{12} phase is not necessarily useful in NH_3-SCR since Ce_7O_{12} oxide possesses pairs of anionic oxygen vacancies on the axis [41]. The catalysts with cerium in excess have the smaller crystallite size in comparison with the reference Ce-CeV after aging at 600°C. Along with increasing the excess of cerium from 11 to 13wt. % CeO_2, the crystallite diameter increases (44 to 61 nm). The comparison of crystallite diameter after aging at 600 and 850°C illustrates the higher sensitivity of $CeVO_4$ than CeO_2 phase to the sintering. By increasing cerium content on Ce-CeV catalyst, the CeO_2 phase is slightly less sensitive to the sintering in comparison to the other phase.

The theoretical values of the specific surface area (S_{th}) calculated from the crystallites diameter of $CeVO_4$ obtained by XRD analysis are presented in Table 1. The comparison of experimental and theoretical values (S_{exp} and S_{th} respectively) can be used to distinguish if the sintering

process is driven either by agglomeration and/or crystal growth phenomena. It should be noticed that a good agreement is obtained with S_{th}/S_{exp} close to 1 for the fresh catalysts. The addition of 11wt. % CeO_2 increases the specific surface area of the fresh catalyst. After aging at 600°C, a beneficial effect of CeO_2 addition is clearly observed, the modified catalysts with 11% of CeO_2 in excess preserving a specific surface area approximately five times higher than that of the Ce-CeV reference catalyst. The presence of CeO_2 nanoparticles can limit the $CeVO_4$ sintering by acting as a diluent for $CeVO_4$ nanoparticles thus limiting the loss of specific surface area. Indeed, an aging temperature of 850°C decreases the specific surface area of all catalysts. However, the S_{th}/S_{exp} values increase after aging at 850°C suggesting that the loss of specific surface area is a combination of both crystal growth and agglomeration processes for all catalysts.

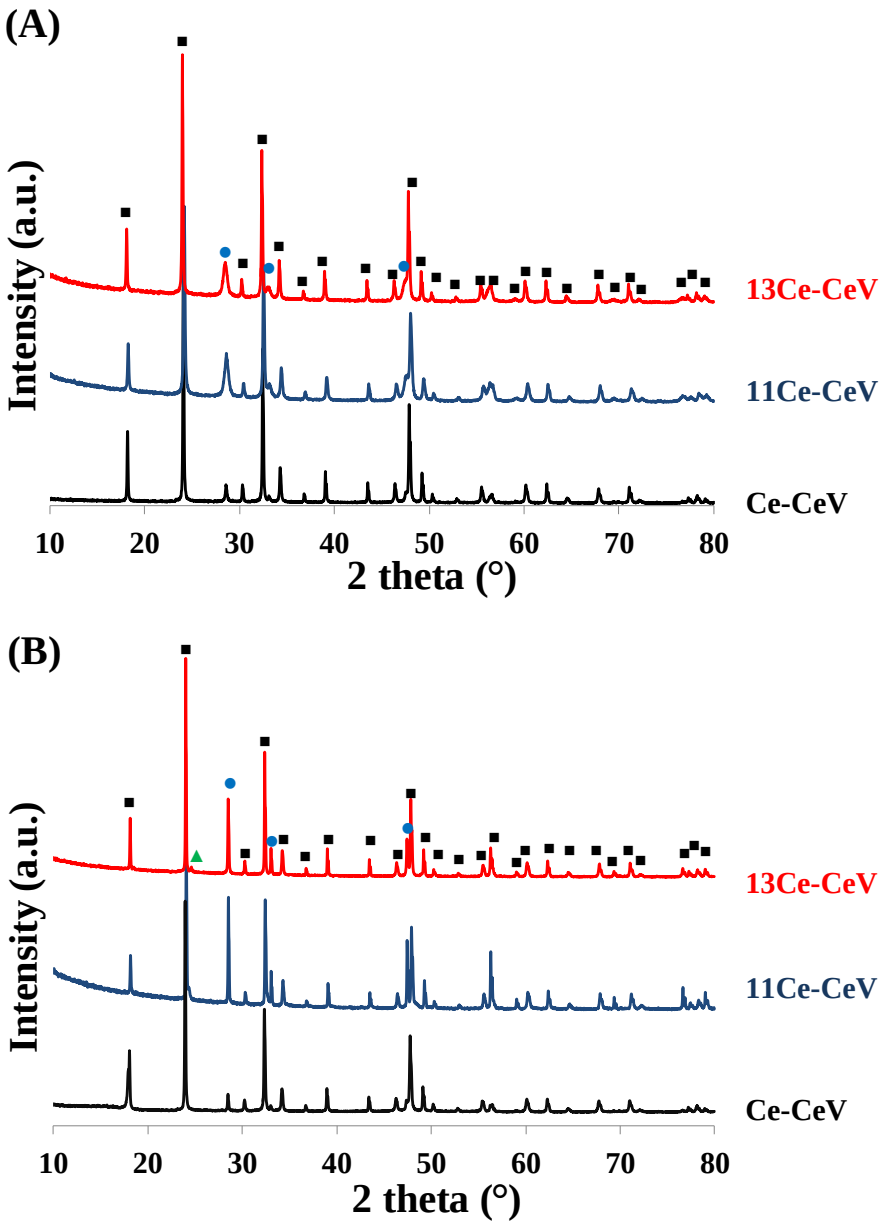

Fig 3 XRD patterns recorded on catalysts aged at 600°C (A) and aged at 850°C (B)—(■) tetragonal phase of $CeVO_4$, (●) cubic structure of CeO_2 (▲) rhombohedric phase of Ce_7O_{12}

The redox property of catalysts is involved in the catalytic cycle of NH_3-SCR reactions and is investigated through H_2-temperature-programmed reduction. Two peaks were clearly observed in the whole reduction process as shown in Fig 4 for the series of Ce-CeV catalysts. The peak above 700°C is associated with the bulk reduction of $CeV^{+5}O_4 \rightarrow CeV^{+3}O_3$ [44]. This peak shifts to lower temperature (from 786 to 770°C) with the increase of CeO_2 loading, implying that the 11Ce-CeV and 13Ce-CeV catalysts have better redox properties than that of Ce-CeV catalyst. The less intense reduction peak observed at low temperature could reflect the reduction of

surface Ce^{4+} species to Ce^{3+} both in CeO_2 and $CeVO_4$. Those observations could also contribute to the reduction of V^{5+} of the surface, which is difficult to be distinguished due to the similar reduction temperature [45]. This reduction peak shifts to the higher temperature by increasing CeO_2 loading whereas the H_2 consumption progressively increases from 0.07 to 0.12 mmol H_2/g. The surface V^{5+} reduction peak of the Ce-CeV catalyst was very weak indicating that the number of surface vanadium species was very small and hard to be reduced over Ce-CeV. The evolution of vanadium species on the surface would explain the change of NO_x conversion and the N_2 selectivity. The catalyst with 11 wt. % of cerium in excess (11Ce-CeV) causes the exposure of more vanadium species on the surface, thus promoting the NH_3-SCR reactions performances. However, when the amount of Ce increase to the 13%, the phase separation occurs and extra surface vanadium species expose, which cause the unexpected NH_3 oxidation and hence decrease both the NO conversion and the N_2 selectivity [46].

Fig 5 compares the Raman spectrum of catalysts after aging at 600°C. Strong Raman lines at 760 and 840 cm^{-1} correspond to the anti-symmetric (B_{1g}) and symmetric (A_{1g}) stretching of VO_4^{3-} tetrahedrons. The bending modes of B_{1g} and A_{1g} are detected at 447 and 361 cm^{-1}, respectively. The Raman line at 247 cm^{-1} is characteristic of the B_{2g} bending mode of the VO_4 tetrahedrons. The external mode of $CeVO_4$ vibration appears at 214cm^{-1}. The proximity of the CeO_2 line (F_{2g} mode to 460cm^{-1}) and the combination line E_g + B_{2g} of VO_4^{3-} at 460 cm^{-1} (corresponding to $CeVO_4$) prevents a clear identification of the CeO_2 phase by Raman spectroscopy [44,45]. The absence of Raman band in the region 800–1000 cm^{-1} characterizing V_2O_5 is remarkable emphasizing the structural stability of $CeVO_4$.

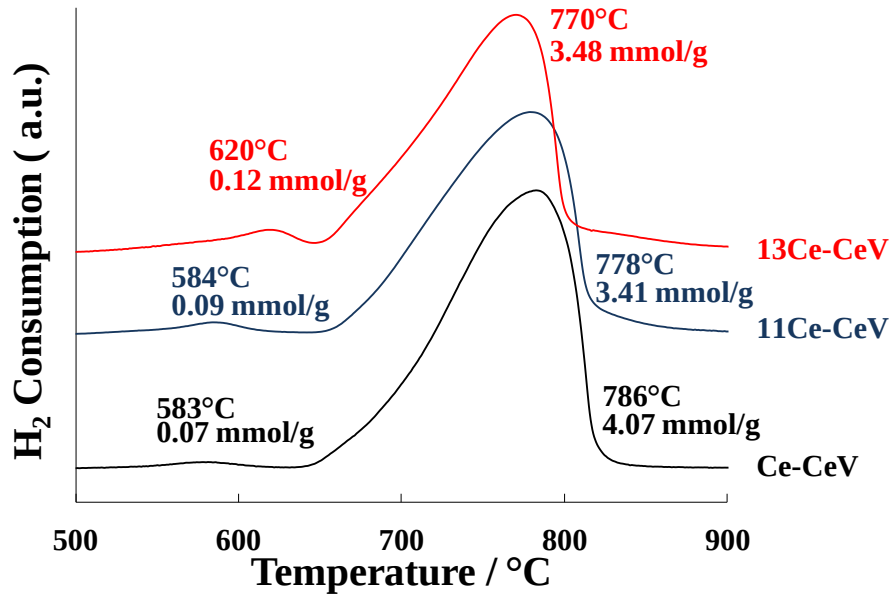

Fig 4 H_2 consumption during H_2-temperature-programmed reduction profiles on Ce-CeV catalysts aged at 600°C

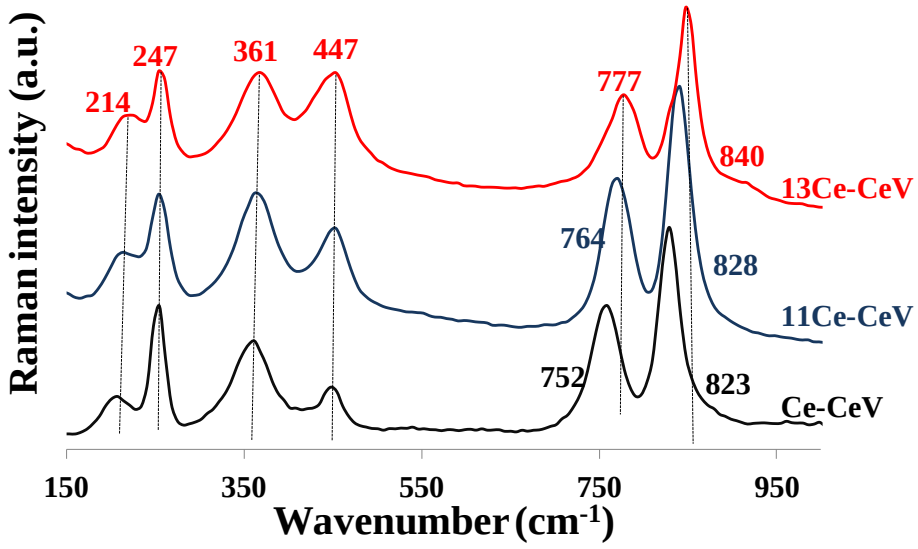

Fig 5 Comparison of Raman spectra of Ce-CeV catalysts aged at 600°C

Table 1 Physicochemical properties of catalysts prepared via the hydrothermal method and aged at 600 and 850°C in Air + 10 %H_2O

Catalysts	Thermal treatment	Bulk atomic ratio V/Ce[a]	Na content [a] wt.%	Crystallite size (nm) [b]		SSA ($m^2\ g^{-1}$)		S_{th}/S_{exp}
				$CeVO_4$	CeO_2	Experimental	Theoretical[c]	
Ce-CeV	Fresh	0.94	0.50	27	46	46	47	1.0
	Aged 600°C	0.94		85	57	6	15	2.5
	Aged 850°C	1.20		96	82	0.5	13	26
11Ce-CeV	Fresh	0.83	0.42	15	8	102	80	0.7
	Aged 600°C	0.83		44	20	32	29	0.9
	Aged 850°C	1.10		81	71	3	15	5.0
13Ce-CeV	Frseh	0.81	0.07	21	9	60	60	1.0
	Aged 600°C	0.81		61	19	20	20	1.0
	Aged 850°C	1.06		77	68	2.5	16	6.4

[a] From ICP-OES analysis
[b] From XRD analysis
[c] Calculated from the crystallite size of $CeVO_4$ obtained from XRD with $S_{th} = 6/(\rho.d_{crystallite})$

The oxidation state and the surface atomic concentrations of cerium, vanadium, and oxygen are investigated through the characterization of Ce 3d, O 1s and V 2p core levels. Results are presented in Table 2. The Ce 3d spectra are complex and can be deconvoluted into $3d_{5/2}$ and $3d_{3/2}$ spin-orbit components (labeled as v and u, respectively) describing the $Ce^{4+}\leftrightarrow Ce^{3+}$ electronic transitions (Fig 6). The peaks v^0, v', u^0, and u' are characteristic of Ce^{3+} that are indicative of the $3d^{10}4f^1$ initial electronic configuration while v, v'', v''', u, u'', and u''' are attributed to Ce^{4+}, representative of the $3d^{10}4f^0$ electronic configuration. The four intense components v (BE ~ 882.5 eV), u (BE ~ 900.9 eV), v''' (BE ~ 898.2 eV), u''' (BE ~ 917.1 eV) as well as the two weaker components v'' (BE ~ 889.4 eV) and u'' (BE ~ 908.2 eV) can be assigned to Ce^{4+} cations. The four other intense components v' (BE ~ 885.6 eV), u' (BE ~ 903.7 eV), v^0 (BE ~ 881.3 eV) and u^0 (BE ~ 899.0 eV) that is overlapped by v''' and u' components corresponds to Ce^{3+} [49, 50]. Hence both Ce^{3+} and Ce^{4+} cations coexist in the Ce-CeV catalysts. The evolution of Ce^{4+}/Ce^{3+} surface atomic ratio is reported in Table 2. The Ce^{4+}/Ce^{3+} ratio increases by adding CeO_2 and by aging at 600°C. After aging at 850°C, Ce^{4+}/Ce^{3+} ratio increases over Ce-13CeV and 11Ce-CeV catalysts and this ratio decreases for Ce-CeV catalyst.

The O 1s photopeak characterized by two contributions at 530.5 eV and 532.0 eV referring the distribution at the surface of lattice oxygen O^{2-} (O_β) and adsorbed oxygen species (O_α) that are O^{2-}, O^-or OH groups. It is widely accepted that O_α species are more active than O_β species due to their higher mobility [51], surface oxygen vacancies and defect sites [52]. In addition, O_α species enhance the fast-SCR reaction (equation 6) owing to the prior oxidation of NO to NO_2 [5]. The O_α/O_β ratio in Ce-CeV reference sample is calculated as 0.34 while that of Ce-11CeV and Ce-13CeV catalysts increased up to 0.49 and 0.41, respectively. These results suggest that a high activity for NO oxidation to NO_2 can enhance the fast-SCR activity with the high concentration of chemisorbed oxygen species towards low temperature. For the V 2p photopeak, the binding energy separation between the core levels V $2p_{1/2}$ (524.9 eV) and V $2p_{3/2}$ (517.6 eV) is 7.3 eV, corresponding to the oxidation states of V^{5+} [53]. The binding energies for the photopeak V $2p_{3/2}$ remain almost unchanged for the series whatever the amount of CeO_2 or the hydrothermal aging. The estimates of V/Ce, V/O and Ce/O surface atomic ratio is presented in Table 2. The evolution of V/Ce surface atomic ratio reveals an increase in vanadium surface concentration after aging especially at 850°C except for Ce-CeV catalyst. The Ce/O and V/O surface atomic ratios vary slightly with aging.

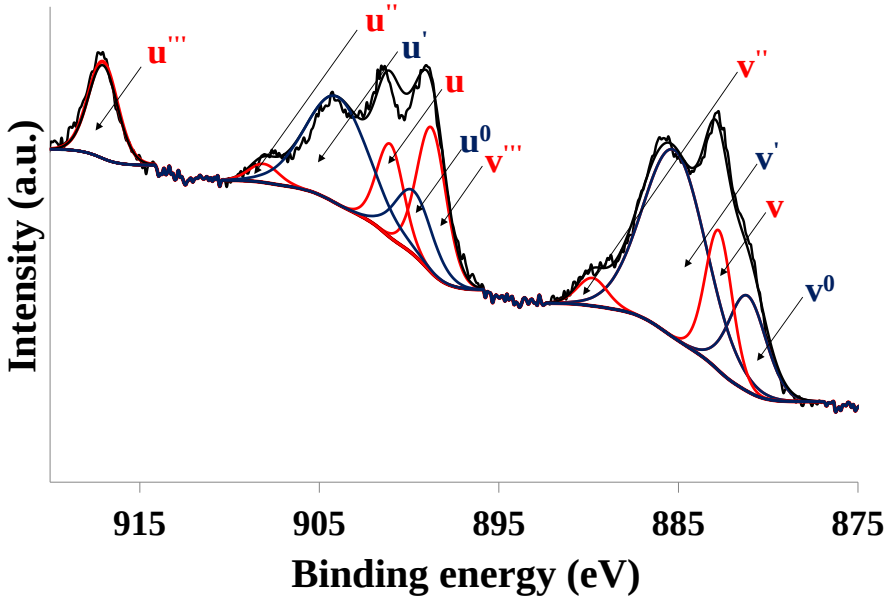

Fig 6 Deconvolution of the Ce 3d core level on 11Ce-CeV catalyst after thermal aging at 600°C

Table 2 XPS analysis of samples aged at 600 and 850°C for 5 h in air and 10 vol. % H_2O

Catalyst	Thermal treatment	B.E. (eV)		Surface atomic ratio				
		$Ce3d_{5/2}$	$V2p_{3/2}$	Ce/O	V/O	V/Ce	Ce^{4+}/Ce^{3+}	O_α/O_β
Ce-CeV	Unaged	883.7	517.6	0.31	0.24	0.78	0.12	0.34
	Aged 600°C	883.5	517.7	0.26	0.25	0.94	0.23	0.27
	Aged 850°C	883.4	517.7	0.29	0.24	0.82	0.12	0.33
11Ce-CeV	Unaged	883.3	517.5	0.26	0.20	0.77	0.30	0.49
	Aged 600°C	883.2	517.6	0.25	0.20	0.83	0.56	0.57
	Aged 850°C	883.1	517.6	0.18	0.18	1.00	0.70	0.69
13Ce-CeV	Unaged	883.4	517.4	0.30	0.20	0.67	0.34	0.41
	Aged 600°C	883.3	517.4	0.30	0.22	0.73	0.43	0.30
	Aged 850°C	883.1	517.5	0.23	0.20	0.85	0.80	0.52

3.3 General Discussion

A series of $CeVO_4$ with an excess of CeO_2 (11 and 13 wt. %) was synthesized by hydrothermal synthesis. The catalysts were ex-situ aged at 600 and 850°C in 10% H_2O in the air. The zircon-type structure of $CeVO_4$ is obtained after hydrothermal synthesis without additional calcination step and preserved after aging. The presence of segregated ceria revealed in XRD pattern is in agreement with the surface Ce^{4+} that confirms the presence of CeO_2 at the surface of the catalyst. A greater sensibility of $CeVO_4$ phase towards sintering is put into evidence from the evolution of the specific surface area and XRD measurements after thermal aging. In fact, the thermal sintering of CeO_2 is more visible after aging at 850°C. As a matter of fact, the lower specific surface area and the larger crystallite size of Ce-CeV comparing to 11Ce-CeV and 13Ce-CeV can be partly explained by the presence of CeO_2. Yeh *et al*. reported that a wide size distribution of particle size slows significantly the sintering process at high temperature [54]. Therefore, the coexistence of two different crystalline phases with different crystalline sizes can slow the agglomeration process. The coexistence of CeO_2 was found as a key parameter for samples with cooperative effects on the NO_x conversion to nitrogen regardless to the operating conditions. The formation of more reducible VO_x species at the surface is also consistent with H_2-TPR. In this sense, H_2-TPR measurements underline that 11Ce-CeV and 13Ce-CeV

catalysts have better redox properties than that of Ce-CeV catalyst. CeO_2 can enhance the redox properties of the $CeVO_4$ catalyst due to its redox shift between Ce^{4+} and Ce^{3+} [5]. Accordingly, The higher Ce^{4+}/Ce^{3+} ratio may result in the higher SCR activity due to the intensified oxygen storage between Ce^{4+} and Ce^{3+} via the following equations $2CeO_2 \rightarrow Ce_2O_3 + O^*$ and $Ce_2O_3 + 1/2\ O_2 \rightarrow 2CeO_2$, which can promote the oxidation of NO to NO_2 [5]. Peng *et al*. proposed that CeO_2 create the new Lewis acid sites and $CeVO_4$ could be served as the Brönsted acid sites [55]. They concluded that at 150 and 250°C the cis-$(N_2O)_2^{2-}$ and $(NO)_2$ species are responsible for the activity, these species react with the adsorbed NH_3 species (Lewis and Brönsted acid sites). At high temperature (350°C), the nitrate and nitrite species are involved in the reaction mechanism [55].

4 Conclusions

This study was devoted to the catalytic properties of bulk $CeVO_4$ catalysts with the excess of CeO_2 (11 and 13 wt. %) prepared by hydrothermal synthesis and further aged at 600°C or 850°C in the presence of steam. The physicochemical properties were studied using ICP, XRD, Raman, BET, H_2-TPR and XPS analysis before and after aging. The XRD patterns put into evidence the coexistence of the zircon-type structure of $CeVO_4$ and the segregation of CeO_2 after aging at 600°C and Ce_7O_{12} after aging at 850°C. It is worthy to be mentioned that the loss of vanadium in the elemental analysis was not observed after aging, which suggested the strong stabilization of V^{5+} species in $CeVO_4$ structure. High specific surface area (up to 102 m^2/g) was obtained for solid with 11 wt. % of CeO_2 in excess. The presence of segregated ceria was found to promote the catalytic performances of the catalyst. The best catalytic performances were obtained on 11Ce-CeV with the selective conversion of NO_x into nitrogen between 250 and 450°C. The change of oxidation properties led to the promotion of NH_3 oxidation when CeO_2 content was above the optimal loading. Basically, such enhancement could be related to an

increased density of sites provided by CeO_2 for oxidizing NO to NO_2 and then ensuring a faster re-oxidation of V (IV) to V (V) compared to O_2 in standard conditions.

Acknowledgements

This work has achieved within a research project supported by Azma Chimie Company. We would like to thank Olivier Gardoll, Laurence Burylo, Pardis Simon, and Martin Trentesaux, for their technical support for Thermal analysis, XRD, and XPS measurements respectively.

References

[1] O. V. Ogidiama and T. Shamim, "Performance analysis of industrial selective catalytic reduction (SCR) systems," *Energy Procedia*, vol. 61, pp. 2154–2157, 2014.

[2] H. L. Zhang, Y. Zhu, S. D. Wang, M. Zhao, M. C. Gong, and Y. Q. Chen, "Activity and thermal stability of $Pt/Ce_{0.64}Mn_{0.16}R_{0.2}O_x$ (R = Al, Zr, La, or Y) for soot and NO oxidation," *Fuel Process. Technol.*, vol. 137, no. 2, pp. 38–47, 2015.

[3] S. Liu, X. Wu, D. Weng, M. Li, and H. R. Lee, "Combined promoting effects of platinum and MnO_x-CeO_2 supported on alumina on NO_x-assisted soot oxidation: Thermal stability and sulfur resistance," *Chem. Eng. J.*, vol. 203, pp. 25–35, 2012.

[4] F. Millo, M. Rafigh, D. Fino, and P. Miceli, "Application of a global kinetic model on an SCR coated on Filter (SCR-F) catalyst for automotive applications," *Fuel*, vol. 198, pp. 183–192, 2017.

[5] F. Gao, X. Tang, H. Yi, S. Zhao, C. Li, J. Li, Y. Shi, and X. Meng, *A Review on Selective Catalytic Reduction of NO_x by NH_3 over Mn–Based Catalysts at Low Temperatures: Catalysts, Mechanisms, Kinetics and DFT Calculations*, vol. 7, no. 7. 2017.

[6] X. Xie, J. Lu, E. Hums, Q. Huang, and Z. Lu, "Study on the Deactivation of V_2O_5–WO_3/TiO_2 Selective Catalytic Reduction Catalysts through Transient Kinetics," *Energy Fuels*, vol. 29, no. 6, pp. 3890–3896, 2015.

[7] C. Paolucci, J. R. Di Iorio, F. H. Ribeiro, R. Gounder, and W. F. Schneider, *Catalysis Science of NO_x Selective Catalytic Reduction With Ammonia Over Cu-SSZ-13 and Cu-SAPO-34*, 1st ed., vol. 59, no. x. Elsevier Inc., 2016.

[8] P. G. Blakeman, E. M. Burkholder, H. Y. Chen, J. E. Collier, J. M. Fedeyko, H. Jobson, and R. R. Rajaram, "The role of pore size on the thermal stability of zeolite supported Cu SCR catalysts," *Catal. Today*, vol. 231, no. x, pp. 56–63, 2014.

[9] J. H. Kwak, R. G. Tonkyn, D. H. Kim, J. Szanyi, and C. H. F. Peden, "Excellent activity and selectivity of Cu-SSZ-13 in the selective catalytic reduction of NOxwith NH3," *J. Catal.*, vol. 275, no. 2, pp. 187–190, 2010.

[10] L. Ma, Y. Cheng, G. Cavataio, R. W. McCabe, L. Fu, and J. Li, "Characterization of commercial Cu-SSZ-13 and Cu-SAPO-34 catalysts with hydrothermal treatment for

NH_3-SCR of NOxin diesel exhaust," *Chem. Eng. J.*, vol. 225, no. x, pp. 323–330, 2013.

[11] Q. Zhang, C. Song, G. Lv, F. Bin, H. Pang, and J. Song, "Journal of Industrial and Engineering Chemistry Effect of metal oxide partial substitution of V_2O_5 in V_2O – WO_3/TiO_2 on selective catalytic reduction of NO with NH3," *J. Ind. Eng. Chem.*, vol. 19, no. 1, pp. 160–166, 2014.

[12] M. Gruber and K. Hermann, "Elementary steps of the catalytic NO_x reduction with NH_3: Cluster studies on reactant adsorption at vanadium oxide substrate," *J. Chem. Phys.*, vol. 138, no. 9, 2013.

[13] Q. Liu, Z. Liu, and C. Li, "Adsorption and Activation of \ce{NH_3} during Selective Catalytic Reduction of NO by \ce{NH_3}," *Chinese J. Catal.*, vol. 27, no. 7, pp. 636–646, 2006.

[14] X. Yao, R. Zhao, L. Chen, J. Du, C. Tao, F. Yang, and L. Dong, "Selective catalytic reduction of NO_x by NH_3 over CeO_2 supported on TiO_2: Comparison of anatase, brookite, and rutile," *Appl. Catal. B Environ.*, vol. 208, pp. 82–93, 2017.

[15] P. Moreau, P. Valero, V. Tschamber, A. Brillard, J.-F. Brilhac, Y. Hohl, and R. Vonarb, "Investigation of vanadium sublimation from SCR catalysts, October, pp. 1–6, 2015.

[16] Z. Lian, F. Liu, and H. He, "Effect of preparation methods on the activity of VO_x /CeO_2 catalysts for the selective catalytic reduction of NO_x with NH_3," *Catal. Sci. Technol.*, vol. 5, no. 1, pp. 389–396, 2015.

[17] Y. Peng, J. Li, L. Chen, J. Chen, J. Han, H. Zhang, and W. Han, "Alkali Metal Poisoning of a CeO_2 –WO_3 Catalyst Used in the Selective Catalytic Reduction of NO_x with NH_3 : an Experimental and Theoretical Study," *Environ. Sci. Technol.*, vol. 46, no. 5, pp. 2864–2869, 2012.

[18] X. Wang, A. Shi, Y. Duan, J. Wang, and M. Shen, "Catalytic performance and hydrothermal durability of CeO_2–V_2O_5–ZrO_2/WO_3–TiO_2 based NH_3-SCR catalysts," *Catal. Sci. Technol.*, vol. 2, no. 7, p. 1386, 2012.

[19] L. Xu, X. S. Li, M. Crocker, Z. S. Zhang, A. M. Zhu, and C. Shi, "A study of the mechanism of low-temperature SCR of NO with NH3on MnO_x/CeO_2," *J. Mol. Catal. A Chem.*, vol. 378, no. 2, pp. 82–90, 2013.

[20] K. Krishna, G. B. F. Seijger, C. M. Van Den Bleek, and H. P. A. Calis, "Very active CeO_2 -zeolite catalysts for NO_x reduction with NH_3," *ChemComm*, vol. 2, no. 2, pp. 2030–2031, 2002.

[21] C. Tang, H. Zhang, and L. Dong, "Ceria-based catalysts for low-temperature selective catalytic reduction of NO with NH_3," *Catal. Sci. Technol.*, vol. 6, no. 5, pp. 1248–1264, 2016.

[22] W. Shan, F. Liu, Y. Yu, and H. He, "The use of ceria for the selective catalytic reduction of NO_x with NH_3," *Cuihua Xuebao/Chinese J. Catal.*, vol. 35, no. 8, pp. 1251–1259, 2014.

[23] G. Qi, R. T. Yang, and R. Chang, "MnO_x-CeO_2 mixed oxides prepared by co-precipitation for selective catalytic reduction of NO with NH_3 at low temperatures," *Appl. Catal. B Environ.*, vol. 51, no. 2, pp. 93–106, 2004.

[24] X. Zhao, L. Huang, H. Li, H. Hu, X. Hu, L. Shi, and D. Zhang, "Promotional effects of zirconium doped $CeVO_4$ for the low-temperature selective catalytic reduction of NO_x with NH_3," *Appl. Catal. B Environ.*, vol. 183, no. x, pp. 269–281, 2016.

[25] Y. Shen, S. Zhu, T. Qiu, and S. Shen, "A novel catalyst of CeO_2/Al_2O_3 for selective catalytic reduction of NO by NH_3," *Catal. Commun.*, vol. 11, no. 1, pp. 20–23, 2009.

[26] X. Gao, Y. Jiang, Y. Fu, Y. Zhong, Z. Luo, and K. Cen, "Preparation and characterization of CeO_2/TiO_2 catalysts for selective catalytic reduction of NO with NH_3," *Catal. Commun.*, vol. 11, no. 5, pp. 465–469, 2010.

[27] M. Adamowska, A. Krztoń, M. Najbar, P. Da Costa, and G. Djéga-Mariadassou, "DRIFT study of the interaction of NO and O_2 with the surface of $Ce_{0.62}Zr_{0.38}O_2$ as deNOxcatalyst," *Catal. Today*, vol. 137, no. 2–4, pp. 288–291, 2008.

[28] Y. Zeng, S. Zhang, Y. Wang, and Q. Zhong, "CeO_2 supported on reduced TiO_2 for selective catalytic reduction of NO by NH_3," *J. Colloid Interface Sci.*, vol. 496, no. x, pp. 487–495, 2017.

[29] J. Yu, Z. Si, M. Zhu, X. Wu, L. Chen, D. Weng, and J. Zou, "NH_3 -SCR activity, hydrothermal stability and poison resistance of a zirconium phosphate/$Ce_{0.5}Zr_{0.5}O_2$ catalyst in simulated diesel exhaust," *RSC Adv.*, vol. 5, no. 102, pp. 83594–83599, 2015.

[30] G. Qi and R. T. Yang, "Performance and kinetics study for low-temperature SCR of NO with NH_3 over MnO_x-CeO_2 catalyst," *J. Catal.*, vol. 217, no. 2, pp. 434–441, 2003.

[31] D. Wang, Y. Jangjou, Y. Liu, M. K. Sharma, J. Luo, J. Li, K. Kamasamudram, and W. S. Epling, "A comparison of hydrothermal aging effects on NH_3-SCR of NO_x over Cu-SSZ-13 and Cu-SAPO-34 catalysts," *Appl. Catal. B Environ.*, vol. 165, no. x, pp. 438–445, 2015.

[32] M. Valdez Lancinha Pereira, A. Nicolle, and D. Berthout, "Hydrothermal aging effects on Cu-zeolite NH_3-SCR catalyst," *Catal. Today*, vol. 258, pp. 424–431, 2015.

[33] S. Gillot, G. Tricot, H. Vezin, J.-P. Dacquin, C. Dujardin, and P. Granger, "Development of stable and efficient $CeVO_4$ systems for the selective reduction of NO x by ammonia: Structure-activity relationship," *Appl. Catal. B Environ.*, vol. 218, no. 2, pp. 338–348, 2017.

[34] M. Casanova, K. Schermanz, J. Llorca, and A. Trovarelli, "Improved high temperature stability of NH_3-SCR catalysts based on rare earth vanadates supported on $TiO_2WO_3SiO_2$," *Catal. Today*, vol. 184, no. 1, pp. 227–236, 2012.

[35] M. Casanova, J. Llorca, A. Sagar, K. Schermanz, and A. Trovarelli, "Mixed iron-erbium vanadate NH_3-SCR catalysts," *Catal. Today*, vol. 241, no. PA, pp. 159–168, 2015.

[36] M. B. Bellakki, T. Baidya, C. Shivakumara, N. Y. Vasanthacharya, M. S. Hegde, and G. Madras, "Synthesis, characterization, redox and photocatalytic properties of $Ce_{1-x}Pd_xVO_4$ $(0 \leq x \leq 0.1)$," *Appl. Catal. B Environ.*, vol. 84, no. 3–4, pp. 474–481, 2008.

[37] S. Gillot, J. P. Dacquin, C. Dujardin, and P. Granger, "High Intrinsic Catalytic Activity of $CeVO_4$-Based Catalysts for Ammonia-SCR: Influence of pH During Hydrothermal Synthesis," *Top. Catal.*, vol. 59, no. 10–12, pp. 987–995, 2016.

[38] A. S. Ayodhya, V. T. Lamani, M. Thirumoorthy, and G. N. Kumar, "NO_x reduction studies on a diesel engine operating on waste plastic oil blend using selective catalytic reduction technique," *J. Energy Inst.*, pp. 1–10, 2018.

[39] G. Tuenter, W. F. van Leeuwen, and L. J. M. Snepvangers, "Kinetics and Mechanism of the NO_x Reduction with NH_3 on V_2O_5-WO_3-TiO_2 Catalyst," *Ind. Eng. Chem. - Prod. Res. Dev.*, vol. 25, no. 4, pp. 633–636, 1986.

[40] A. Kato, S. Matsuda, T. Kamo, F. Nakajima, H. Kuroda, and T. Narita, "Reaction

between nitrogen oxide (NO_x) and ammonia on iron oxide-titanium oxide catalyst," *J. Phys. Chem.*, vol. 85, no. 26, pp. 4099–4102, 1981.

[41] P. Anil, Y. Eun, and H. Phil, "Low temperature NH_3-SCR activity enhancement of antimony promoted vanadia-ceria catalyst," *Catal. Today*, vol. 293–294, pp. 61–72, 2017.

[42] H. Chang, X. Chen, J. Li, L. Ma, C. Wang, C. Liu, J. W. Schwank, and J. Hao, "Improvement of activity and SO_2 tolerance of Sn-modified MnO_x -CeO_2 catalysts for NH_3-SCR at low temperatures," *Environ. Sci. Technol.*, vol. 47, no. 10, pp. 5294–5301, 2013.

[43] L. Chen, "Hydrothermal synthesis and ethanol sensing properties of $CeVO_4$ and $CeVO_4$-CeO_2 powders," *Mater. Lett.*, vol. 60, no. 15, pp. 1859–1862, 2006.

[44] B. Agula, T. Ren, X. Zhao, B. Zhaorigetu, and Z. Yuan, "Relationship between the reducibility and selectivity of $CeMo_xV_{1-x}O_4$ catalysts by kinetic parameters of TPR," *J. Nat. Gas Chem.*, vol. 20, no. 3, pp. 232–236, 2011.

[45] M. Shen, L. Xu, J. Wang, C. Li, W. Wang, J. Wang, and Y. Zhai, "Effect of synthesis methods on activity of $V_2O_5/CeO_2/WO_3$-TiO_2 catalyst for selective catalytic reduction of NO_x with NH_3," *J. Rare Earths*, vol. 34, no. 3, pp. 259–267, 2016.

[46] X. Zhao, L. Huang, H. Li, H. Hu, X. Hu, L. Shi, and D. Zhang, "Promotional effects of zirconium doped $CeVO_4$ for the low-temperature selective catalytic reduction of NO_x with NH_3," *Appl. Catal. B Environ.*, vol. 183, no. x, pp. 269–281, 2016.

[47] H. Yang, J. Zha, P. Zhang, Y. Qin, T. Chen, and F. Ye, "Fabrication of $CeVO_4$ as nanozyme for facile colorimetric discrimination of hydroquinone from resorcinol and catechol," *Sensors Actuators, B Chem.*, vol. 247, pp. 469–478, 2017.

[48] M. V. Bosco, M. A. Bañares, M. V. Martínez-Huerta, A. L. Bonivardi, and S. E. Collins, "In situ FTIR and Raman study on the distribution and reactivity of surface vanadia species in V_2O_5/CeO_2 catalysts," *J. Mol. Catal. A Chem.*, vol. 408, pp. 75–84, 2015.

[49] C. Anandan and P. Bera, "Growth, characterization and interfacial reaction of magnetron sputtered Pt/CeO_2 thin films on Si and Si_3N_4 substrates," *Surf. Interface Anal.*, vol. 47, no. 7, pp. 777–784, 2015.

[50] R. Cousin, M. Dourdin, E. Abi-aad, D. Courcot, S. Capelle, M. Guelton, and A. Abouka, "Formation of $CeVO_4$ phase during the preparation of CuVCe oxide catalysts," vol. 93, no. 21, pp. 3863–3867, 1997.

[51] L. Liu, J. Shi, H. Cao, R. Wang, and Z. Liu, "Fabrication of CeO_2 –MO_x (M = Cu, Co, Ni) composite yolk–shell nanospheres with enhanced catalytic properties for CO oxidation," *Beilstein J. Nanotechnol.*, vol. 8, pp. 2425–2437, 2017.

[52] H. Huang, Y. Gu, J. Zhao, and X. Wang, "Catalytic combustion of chlorobenzene over VO_x/CeO_2 catalysts," *J. Catal.*, vol. 326, no. 3, pp. 54–68, 2015.

[53] J. Światowska-Mrowiecka, V. Maurice, S. Zanna, L. Klein, and P. Marcus, "XPS study of Li ion intercalation in V_2O_5 thin films prepared by thermal oxidation of vanadium metal," *Electrochim. Acta*, vol. 52, no. 18, pp. 5644–5653, 2007.

[54] C. Division, "Effect of Particle Size Distribution on the Sintering of Alumina," vol. 487, no. December, pp. 484–487, 1988.

[55] Y. Peng, C. Wang, and J. Li, "Structure-activity relationship of VO_x/CeO_2 nanorod for NO removal with ammonia," *Appl. Catal. B Environ.*, vol. 144, pp. 538–546, 2014.

Conclusion

This study was devoted to the catalytic properties of bulk $CeVO_4$ catalysts at a constant CeO_2 loading in excess (11 and 13 wt. % CeO_2) prepared by hydrothermal synthesis and further aged at 600 and 850°C in the presence of steam. The aging study on NH_3-SCR shows that thermal aging significantly affects the overall NO_x reduction of the catalysts. In present work, it was found that the excess of CeO_2 was an effective way to improve the SCR activity of $CeVO_4$. Characterization results proved that the excess of CeO_2 could decrease the crystallite size of $CeVO_4$ phase and increase its specific surface area, accompanied with the generation of more surface adsorbed oxygen species and more Ce^{4+}, especially over 11Ce-CeV catalyst. The qualities mentioned above contributed to the enhancement of the SCR activity of 11Ce-CeV compared to the other investigated catalysts.

References

[1] P. Anil, Y. Eun, and H. Phil, "Low temperature NH_3-SCR activity enhancement of antimony promoted vanadia-ceria catalyst," Catal. Today, vol. 293–294, no. x, pp. 61–72, 2017.

[2] S. Zhan, H. Zhang, Y. Zhang, Q. Shi, Y. Li, and X. Li, "Applied Catalysis B: Environmental Efficient NH_3-SCR removal of NO_x with highly ordered mesoporous," vol. 203, no. x, pp. 199–209, 2017.

[3] H. Lv, X. Hua, W. Xie, Q. Hu, J. Wu, and R. Guo, "Promotion effect of H_2 pretreatment on CeO_2 catalyst for NH_3-SCR reaction," J. Rare Earths, 2018.

[4] X. Yao, Z. Wang, S. Yu, F. Yang, and L. Dong, "Applied Catalysis A , General Acid pretreatment e ff ect on the physicochemical property and catalytic performance of CeO_2 for NH_3-SCR," vol. 542, no. February, pp. 282–288, 2017.

[5] R. Qu, X. Gao, K. Cen, and J. Li, "Relationship between structure and performance of a novel cerium-niobium binary oxide catalyst for selective catalytic reduction of NO with NH_3," Appl. Catal. B Environ., vol. 142–143, pp. 290–297, 2013.

[6] P. A. Kumar, Y. E. Jeong, and H. P. Ha, "Low temperature NH_3-SCR activity enhancement of antimony promoted vanadia-ceria catalyst," Catal. Today, vol. 293–294, no. x, pp. 61–72, 2017.

[7] L. Chen, J. Li, W. Ablikim, J. Wang, H. Chang, L. Ma, J. Xu, M. Ge, and H. Arandiyan, "CeO_2–WO_3 Mixed Oxides for the Selective Catalytic Reduction of NO_x by NH_3 Over a Wide Temperature Range," Catal. Letters, vol. 141, no. 12, pp. 1859–1864, 2011.

Chapter IV

Catalytic performances of $Ce_{1-X}RE_XV_{0.95}W_{0.05}O_4$ mixed oxides (RE=Pr, Gd, Tb, Er and X=0.1 and 0.5)

Summary

1 Catalytic performances of $Ce_{1-X}RE_XV_{0.95}W_{0.05}O_4$ mixed oxides (RE=Pr and Gd, X=0.1 and 0.5) for the selective catalytic reduction of NO_x by ammonia 123

1.1 Hydrothermal Synthesis of $Ce_{1-X}RE_XV_{0.95}W_{0.05}$ (RE=Pr and Gd, X=0.1 and 0.5) solids..... 124

1.2 Bulk/Structural properties..... 125

1.2.1 X-ray diffraction..... 126

1.2.1.1 Unaged solids 126

1.2.1.2 Solids aged at 600°C..... 129

1.2.1.3 Solids aged at 850°C..... 130

1.2.2 Raman spectroscopy..... 133

1.2.3 Temperature-programmed reduction (H_2-TPR) 136

1.2.3.1 Unaged..... 136

1.2.3.2 Solids Aged at 600°C 137

1.2.3.3 Solids Aged at 850°C 139

1.3 Surface characterizations..... 141

1.3.1 Specific surface area..... 141

1.3.2 X-ray photo-electron spectroscopy (XPS) 143

1.4 Catalytic activity of $Ce_{1-X}RE_XV_{0.95}W_{0.05}O_4$ (RE=Pr and Gd, X=0.1 and 0.5) catalysts after hydrothermal aging at 600°C 153

1.4.1 Ammonia-selective catalytic reduction of NO_x to nitrogen in "Standard" condition: NO/NO_x =1 154

1.4.2 Ammonia-selective catalytic reduction of NO_x to nitrogen in "Fast" condition: NO/NO_x = 0.5 156

1.4.3 Ammonia-selective catalytic reduction of NO_x to nitrogen in "NO_2" condition: NO/NO_x =3/10 158

1.5 Catalytic activity of $Ce_{1-X}RE_XV_{0.95}W_{0.05}O_4$ (RE=Pr and Gd, X=0.1 and 0.5) catalysts after hydrothermal aging at 850°C 160

1.5.1 Ammonia-selective catalytic reduction of NO_x to nitrogen in "fast" condition: NO/NO_x = 0.5 160

1.6 Conclusion 161

2 Catalytic performances of mixed oxides $Ce_{0.5}RE_{0.5}V_{0.95}W_{0.05}O_4$ (RE= Pr, Gd, Tb, and Er) for selective catalytic reduction of NO_x by ammonia 163

2.1 Hydrothermal Synthesis of $Ce_{0.5}RE_{0.5}V_{0.95}W_{0.05}O_4$ (RE= Pr, Gd, Tb, and Er) solids 163

2.2 Bulk/Structural properties 165

2.2.1 X-ray diffraction 165

2.2.1.1 Unaged solids 165

2.2.1.2 Solids Aged at 600°C 167

2.2.1.3 Solids Aged at 850°C 168

2.2.2 Raman spectroscopy 170

2.2.3 Temperature-programmed reduction (H_2-TPR) 172

2.2.3.1 Unaged 172

2.2.3.2 Solids Aged at 600°C 173

2.2.3.3 Solids Aged at 850°C 175

2.3 Surface characterizations 177

2.3.1 Specific surface area 177

2.3.2 X-ray photoelectron spectroscopy (XPS) 178

2.4 Catalytic activity of $Ce_{0.5}RE_{0.5}V_{0.95}W_{0.05}O_4$ (RE= Pr, Gd, Tb, and Er) catalysts after hydrothermal aging at 600°C 188

2.4.1 Ammonia-selective catalytic reduction of NO_x to nitrogen in "Standard" condition: NO/NO_x =1 188

2.4.2 Ammonia-selective catalytic reduction of NO_x to nitrogen in "fast" condition: NO/NO_x = 0.5 190

2.4.3 Ammonia-selective catalytic reduction of NO_x to nitrogen in "NO_2" condition: NO/NO_x =3/10 192

2.5 Catalytic activity of $Ce_{0.5}RE_{0.5}V_{0.95}W_{0.05}O_4$ (RE= Pr, Gd, Tb and Er) catalysts after hydrothermal aging at 850°C 193

2.5.1 Ammonia-selective catalytic reduction of NO_x to nitrogen in "Standard" condition: NO/NO_x =1 193

2.5.2 Ammonia-selective catalytic reduction of NO_x to nitrogen in "fast" condition: NO/NO_x = 0.5 194

2.5.3 Ammonia-selective catalytic reduction of NO_x to nitrogen in "NO_2" condition: NO/NO_x =3/10 195

2.6 Conclusion of section 197

3 References 199

1 Catalytic performances of $Ce_{1-X}RE_XV_{0.95}W_{0.05}O_4$ mixed oxides (RE=Pr and Gd, X=0.1 and 0.5) for the selective catalytic reduction of NO_x by ammonia

Introduction of rare earth elements (RE) in an oxide-based SCR catalyst formulation has been the subject of a few investigations [1–6]. A modification of the acid character of the catalyst was also observed upon introduction of lanthanides (La, Sm, Ce) in low and high loading V_2O_5/Al_2O_3 SCR catalysts [2]. In this study, an enhancement of SCR reaction performances was observed by Ce doping with the rare earth, and this was correlated to the ionicity of the V–O bond in surface vanadium species, altered by the presence of the rare earth element.

In this section, we discuss the influence of the partial substitution of cerium by different Rare Earth elements $Ce_{1-X}RE_XV_{0.95}W_{0.05}O_4$ (RE= Pr and Gd, X=0.1 and 0.5) on the conversion of NO_x by ammonia. At first, preparation procedures of all catalysts are described. This chapter also focuses on the characterization of the catalysts after synthesis and after hydrothermal aging at 600 and 850°C. Characterization techniques (XRF, XRD, BET (Brunauer-Emmett-Teller), RAMAN, H_2-TPR, and XPS) have been performed in order to physicochemical features with catalytic behavior. The resulting formulations were tested in the NH_3-SCR reaction. The replacement of cerium by other trivalent ions with a smaller diameter, such as Pr and Gd may strongly enhance oxygen mobility and storage capacity. The reference catalyst ($CeV_{0.95}W_{0.05}O_4$) was studied for later comparison. The influence of Ce/RE ratio, as well as the effect of aging conditions on their activity in ammonia SCR reaction, was investigated. SCR activity at medium/low temperature was found to correlate directly with the RE (Pr and Gd) loading of the catalysts. This was the result of a beneficial interaction between the rare earth element and the vanadium species ascribed to the formation of RE vanadates.

1.1 Hydrothermal Synthesis of $Ce_{1-X}RE_XV_{0.95}W_{0.05}$ (RE= Pr and Gd, X=0.1 and 0.5) solids

The hydrothermal method has attracted the extensive attention because it is comparatively simple and easy to prepare narrowly sized particles. To study the impact of smaller isovalent cations (Pr and Gd) into the tetragonal structure of $CeVO_4$, $Ce_{1-X}RE_XV_{0.95}W_{0.05}O_4$ catalysts with X= 0, 0.1, and 0.5 were synthesized. The samples were prepared by the hydrothermal method; various stages of preparation of the $Ce_{1-X}RE_XV_{0.95}W_{0.05}O_4$ (RE=Pr and Gd) are shown in Fig 4.1. The appropriate amount of precursor salt Na_3VO_4 (99.98wt% Sigma-Aldrich) was dissolved in 50 mL of distilled water at room temperature. The solution was acidified and mixed under vigorous stirring until reaching a pH value close to 1.8. Previous studies have shown the sensitivity of vanadium species to pH changing that can be found in oligomeric form $V_{10}O_{28}^{6-}$ or $V_3O_9^{3-}$ [7]. Under this pH condition, vanadium is stabilized as VO_2^+ ions. The appropriate amounts of $Ce(NO_3)_3{\cdot}6H_2O$, $(NH_4)_6H_2W_{12}O_{40}.xH_2O$ (meta) 99.99%, RE $(NO_3)_3$. $5H_2O$ (RE=Pr and Gd) were added and solubilized into the vanadium solution under stirring. Sodium hydroxide solution (1M) was added dropwise to the above solution to adjust the pH to 7. pH values during precipitation decrease sharply. The resulting suspension was transferred into a 50 mL Teflon-lined stainless steel autoclave and sealed tightly. Hydrothermal synthesis was carried out at 180°C for 24h in an oven without shaking or stirring. After cooling to room temperature, the precipitates were collected, washed with distilled water and absolute ethanol several times, and then dried in air at 80°C for 24 h.

Two temperatures (600 and 850°C) were chosen for the aging thermal treatment. The samples were hydrothermally aged in a fixed bed flow reactor under the wet atmosphere (10% H_2O in air) with a GHSV of 41666 $mL.h^{-1}.g^{-1}$, and a temperature rise of 5°C/min. The catalysts were maintained at steady-state at the final temperature for 5h.

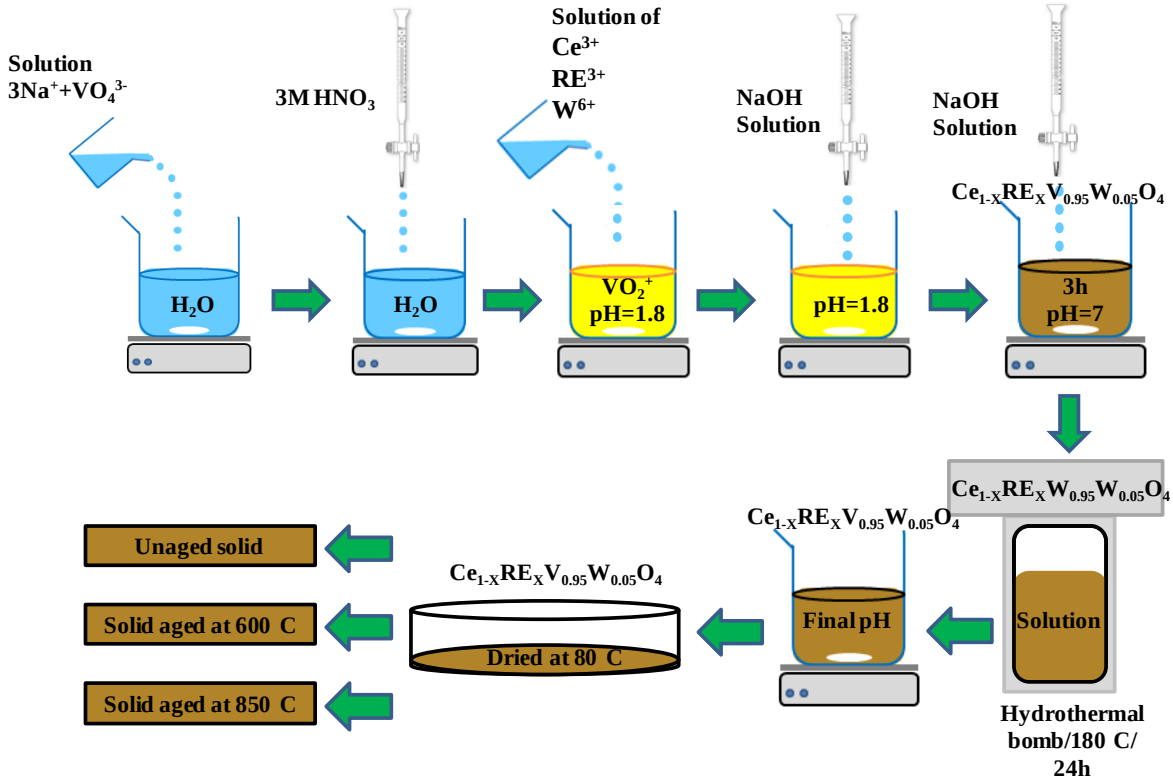

Figure 4.1 – **Steps involved during the hydrothermal synthesis of $Ce_{1-X}RE_XV_{0.95}W_{0.05}O_4$ (RE= Pr and Gd, X=0.1 and 0.5) catalysts**

1.2 Bulk/Structural properties

The elemental analysis allows determining the weight composition of every element present in the catalyst. The chemical analysis was done by X-ray fluorescence spectrometry method to determine the bulk composition of selected $Ce_{1-X}RE_XV_{0.95}W_{0.05}O_4$ (Table 4.1). The value presented in the brackets corresponds to the expected values. An excess of cerium and tungsten is discernible while a slight V and RE (Pr and Gd) deficiency are observable. $Ce_{0.5}Pr_{0.5}V_{0.95}W_{0.05}O_4$ catalyst exhibits an XRF composition of Pr lower than the nominal values. The compositions of the catalysts are not affected intensely by hydrothermal aging. The measured values are close to the theoretical values and the observed variations are not significant (except for tungsten) compared to global composition, which indicates the successful preparation of $Ce_{1-X}RE_XV_{0.95}W_{0.05}O_4$ by hydrothermal method and the absence of volatilization of oxide during the high-temperature thermal aging.

Table 4.1 – **Elemental analysis of $Ce_{1-X}RE_XV_{0.95}W_{0.05}O_4$ catalysts by X-ray fluorescence**

Catalyst	Aging temperature (°C)	Chemical composition expressed as oxide			
		V_2O_5 (wt.%)	Ce_2O_3 (wt.%)	WO_3 (wt.%)	RE_2O_3 (wt.%)
$Ce_{0.9}Pr_{0.1}V_{0.95}W_{0.05}O_4$	unaged	32.7 (32.2)	58.0 (57.0)	4.2 (2.2)	6.50 (7.0)
	600	32.6 (32.2)	58.1 (57.0)	4.2 (2.2)	6.70 (7.0)
	850	30.0 (32.2)	58.0 (57.0)	4.3 (2.2)	6.80 (7.0)
$Ce_{0.5}Pr_{0.5}V_{0.95}W_{0.05}O_4$	unaged	32.1 (32.2)	34.1 (30.7)	4.0 (2.2)	29.20 (35.0)
	600	32.0 (32.2)	34.2 (30.7)	4.1 (2.2)	29.00 (35.0)
	850	32.0 (32.2)	34.4 (30.7)	4.2 (2.2)	28.70 (35.0)
$Ce_{0.9}Gd_{0.1}V_{0.95}W_{0.05}O_4$	unaged	30.5 (32.2)	59.0 (57.0)	4.1 (2.2)	6.20 (7.0)
	600	30.1 (32.2)	59.1 (57.0)	4.2 (2.2)	6.10 (7.0)
	850	30.0 (32.2)	59.1 (57.0)	4.3 (2.2)	6.20 (7.0)
$Ce_{0.5}Gd_{0.5}V_{0.95}W_{0.05}O_4$	unaged	29.9 (32.2)	33.0 (30.7)	4.0 (2.2)	32.70 (35.0)
	600	29.9 (32.2)	33.1 (30.7)	4.2 (2.2)	32.60 (35.0)
	850	29.8 (32.2)	33.4 (30.7)	4.3 (2.2)	32.10 (35.0)

1.2.1 X-ray diffraction

The X-ray diffraction analysis technique allows detecting the crystallized phases after hydrothermal synthesis and hydrothermal treatment at 600°C and 850°C. In addition to phase determination, powder XRD patterns can be used to estimate the crystal size in a powder sample.

1.2.1.1 Unaged solids

The XRD patterns of series of unaged $Ce_{1-X}RE_XV_{0.95}W_{0.05}$ catalysts are displayed in Fig 4.2. For the catalysts, the predominance crystallographic phase is tetragonal $REVO_4$ (RE= Ce, Pr, and Gd). For all phases, the most intense line is located at $2\theta = 24.0°$.

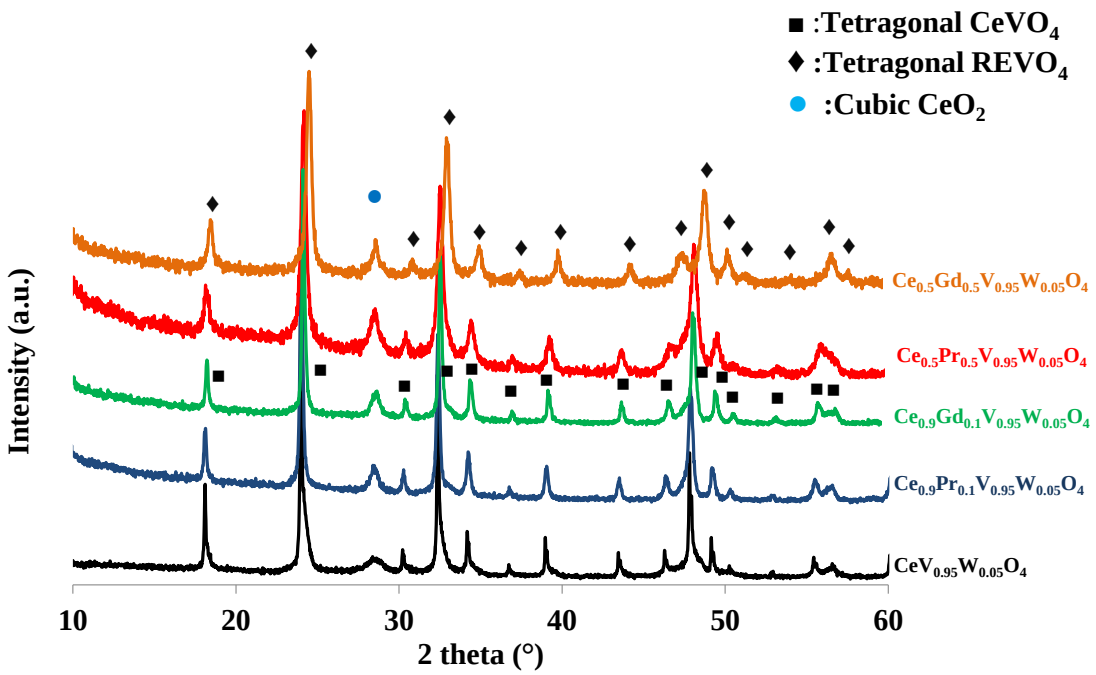

Figure 4.2 – **Crystallographic structure of unaged $Ce_{1-x}RE_xV_{0.95}W_{0.05}O_4$ (RE=Pr and Gd, X=0, 0.1 and 0.5) catalysts**

Additional X-ray lines appear at 2θ= 28.5, 33 and 47.5° ascribed to the face-centered fluorite structure of CeO_2 on all samples. The formation of ceria could be explained by the dehydration of $Ce(OH)_3$ during the hydrothermal synthesis and subsequent oxidation with air into CeO_2 [8]. The crystal structure of cubic CeO_2 is presented in Fig 4.3. Ceria has a face-centered cubic (fcc) unit cell with space group Fm3m. The Ce cations are bonded to eight O nearest neighbors while the O anions are tetrahedrally bonded to four Ce nearest neighbors [2].

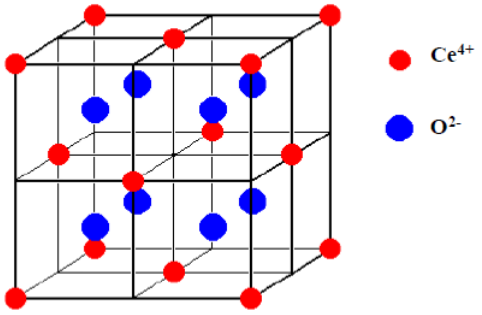

Figure 4.3 – **The crystal structure of cubic CeO_2** [9]

The high oxidation power of Ce (IV) enables pure ceria to catalyze total oxidation reactions. Its selectivity, however, can be tuned to a variety of selective heterogeneous catalytic redox reactions by modification with other metal ions that modify both redox and acid-base properties of ceria. In catalytic applications, ceria is frequently doped with rare earth elements in order to modify its electronic and/or structural properties. Incorporation of trivalent cations into the ceria lattice creates lattice oxygen anion vacancies by a charge-compensating effect of doped cations. This increases the oxygen mobility [10]. These vacancies are associated with the dopant cations and are randomly distributed on anion sites within the fluorite lattice [11]. If the dopant has a variable oxidation state, as is the case with praseodymium, the resulting vacancies are extremely mobile. This strongly influences the redox properties of the ceria by increasing both total and kinetic oxygen storage [11].

A correlation can be established between the 2θ values of $CeVO_4$ crystalline structure and the rare earth atomic fraction and nature (Fig 4.7). This displacement could be the result of the partial substitution of Ce by rare earth element and it is more important for $Ce_{0.5}RE_{0.5}V_{0.95}W_{0.05}O_4$ catalysts. This displacement is higher for the catalyst doped with Gadolinium in agreement with the lower ionic radius (Gd^{3+}). All reflections of these mixed oxides were gradually shifted to the higher 2θ angles with increasing the cerium substitution by the rare earth. These results indicate a decrease in the lattice parameter due to the replacement of cerium by smaller rare earth ions.

No reflections of a vanadium- and tungsten-containing phase were detected, suggesting that no segregated V_2O_5 or WO_3 oxides were formed during synthesis or aging. These species have an amorphous character or have the crystallite sizes below the XRD detection limit.

1.2.1.2 Solids aged at 600°C

The powder diffractograms recorded for the catalysts obtained after aging at 600°C in a wet atmosphere (10% H_2O diluted in air) are displayed in Fig 4.4. After aging at 600°C no additional diffraction lines are observed for recorded patterns. The crystallite sizes for $REVO_4$ and CeO_2 were calculated from the Debye-Scherrer relationship taking the most intense reflection into account. The values reported in Table 4.2. show that a significant crystallite growth for $REVO_4$ is discernible emphasizing the fact that sintering occurs even at moderate aging temperature. On the other hand, CeO_2 seems to be much more resistant to thermal sintering at 600°C.

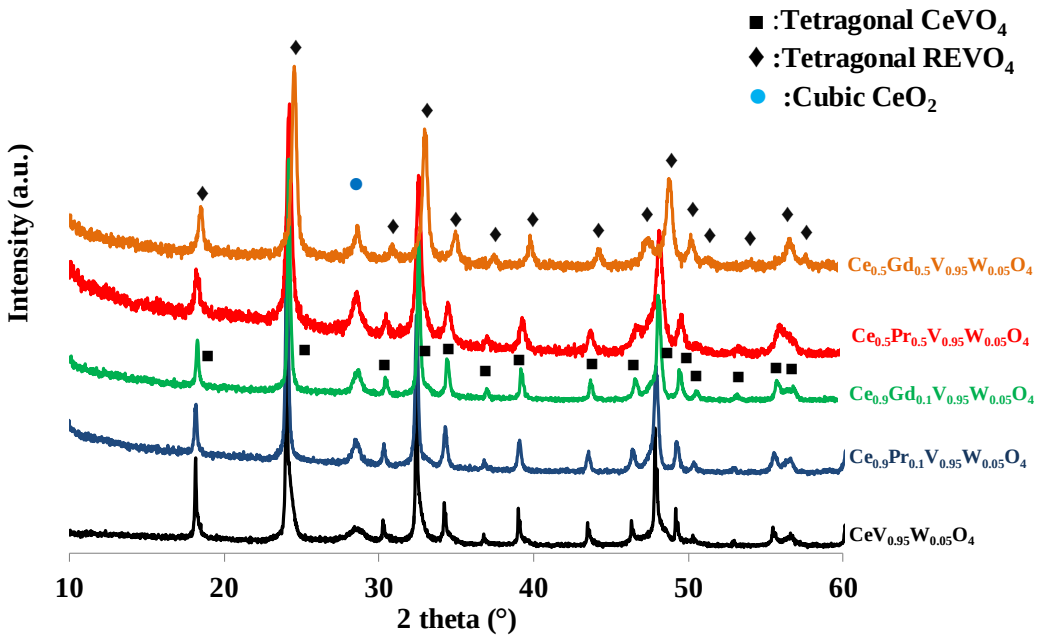

Figure 4.4 – **Crystallographic structure of $Ce_{1-X}RE_XV_{0.95}W_{0.05}O_4$ (RE=Pr and Gd, X=0, 0.1 and 0.5) catalysts aged at 600°C**

1.2.1.3 Solids aged at 850°C

Hydrothermal aging at 850°C induces significant crystallographic changes. For all substituted catalysts, an additional crystalline phase attributed to rhombohedric Ce_7O_{12} is detected after aging at 850°C (Fig 4.5). The characteristic diffraction lines of V_2O_5 do not appear on the spectra recorded on unaged and after hydrothermal aging.

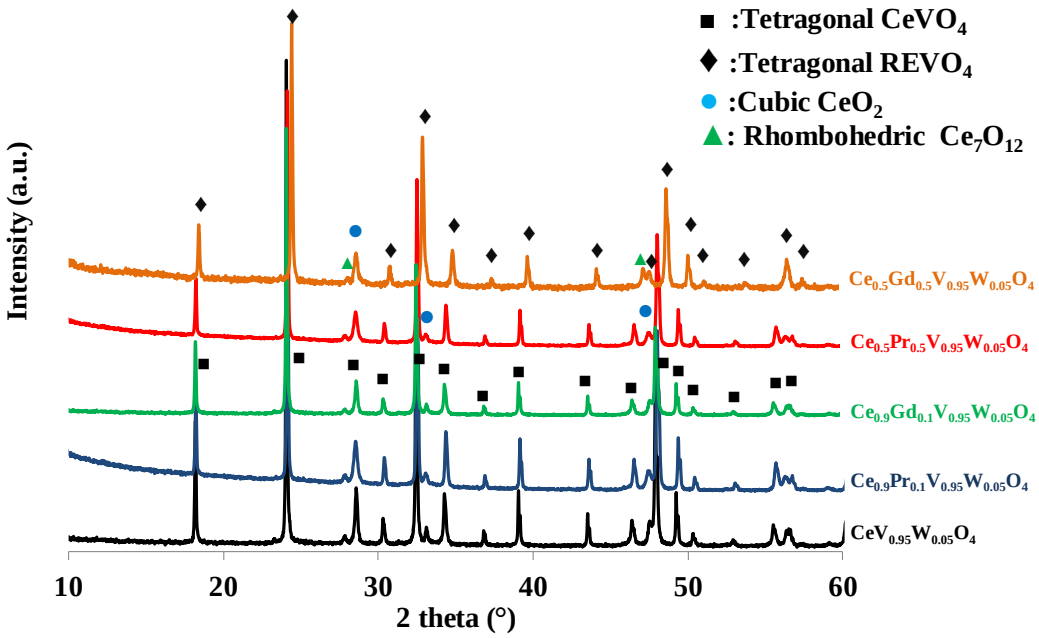

Figure 4.5 – **Crystallographic structure of $Ce_{1-X}RE_XV_{0.95}W_{0.05}O_4$ (RE=Pr and Gd, X=0, 0.1 and 0.5) catalysts aged at 850°C**

Fig 4.6 summarized the unit cell of Ce_7O_{12} that shows the two distinct Ce sites: Ce (1) in black and Ce (2) in dark grey. The O (1) sites are shown in grey (teal) with the O (2) light grey (orange). The O vacancy sites are shown in white [12].

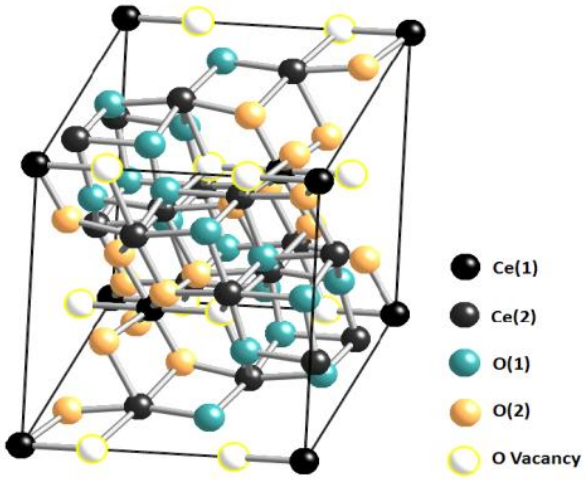

Figure 4.6 – **Crystallographic representation of Ce_7O_{12}** [12]

The segregation of Ce_7O_{12} phase is not necessarily helpful in NH_3-SCR since Ce_7O_{12} oxide has pairs of anionic oxygen vacancies on the axis [13]. Researchers generally noticed that anionic vacancy improves the mobility of the oxygen on the surface. Normally, O^- and O^{2-} species are favorable oxidants that allow a gain of activity in standard-SCR conditions owing to their capacity to oxidize NO to NO_2 and to re-oxidize the redox sites [3,4].

The influence of the degree of cerium substitution and the nature of the rare earth on the crystallite diameter of $REVO_4$ (RE=Ce, Pr, and Gd) and CeO_2 phases are shown in Table 4.2. The crystallite diameter of $REVO_4$ was calculated from the Scherrer formula by considering the diffraction lines at $2\theta = 24.0°$ corresponding to the crystallographic plane of (200). The plane (001) at $2\theta = 28.5°$ was considered for calculating the crystallite diameter of CeO_2. In addition, the diffraction peaks become sharper with increasing aging temperature, which reveals the change in crystallite size with aging. It is revealed that with increasing the aging temperature crystallite diameter increases. The unaged catalysts generally have the same $REVO_4$ crystallite diameter (17 to 22 nm). The impact of the nature of rare earth and the degree of cerium substitution by rare earth (Pr and Gd) on the crystallite diameter is more visible after thermal aging. The more cerium substituted by rare earth, the smaller the crystallite size is, and the

catalyst with the smaller ionic radius (gadolinium) possessed of the lower crystallite diameter. The comparison of crystallite diameter before and after aging shows the more sensitivity of $REVO_4$ to sintering than the CeO_2 phase. The CeO_2 crystallite diameter is between 20 and 54 nm after aging at 600°C and between 40 and 122 nm after aging at 850°C. This sensitivity to sintering affects more the unsubstituted catalysts $CeV_{0.95}W_{0.05}O_4$ and affects less $Ce_{0.5}Gd_{0.5}V_{0.95}W_{0.05}O_4$ catalyst with higher substitution degree and lower ionic radius. The XRD result also reveals that CeO_2 crystallites have a good sintering resistance after aging at 600°C.

Table 4.2 – **Influence of cerium substitution by rare on the average crystallite size of $REVO_4$ and CeO_2**

Catalyst	Aging temperature (°C)	$REVO_4$ crystallite diameter (nm)	CeO_2 crystallite diameter (nm)
$CeV_{0.95}W_{0.05}O_4$	unaged	22	10
	600	54	14
	850	112	40
$Ce_{0.9}Pr_{0.1}V_{0.95}W_{0.05}O_4$	unaged	17	15
	600	32	16
	850	75	40
$Ce_{0.5}Pr_{0.5}V_{0.95}W_{0.05}O_4$	unaged	20	19
	600	21	17
	850	50	36
$Ce_{0.9}Gd_{0.1}V_{0.95}W_{0.05}O_4$	unaged	18	17
	600	33	16
	850	76	33
$Ce_{0.5}Gd_{0.5}V_{0.95}W_{0.05}O_4$	unaged	18	20
	600	20	22
	850	40	37

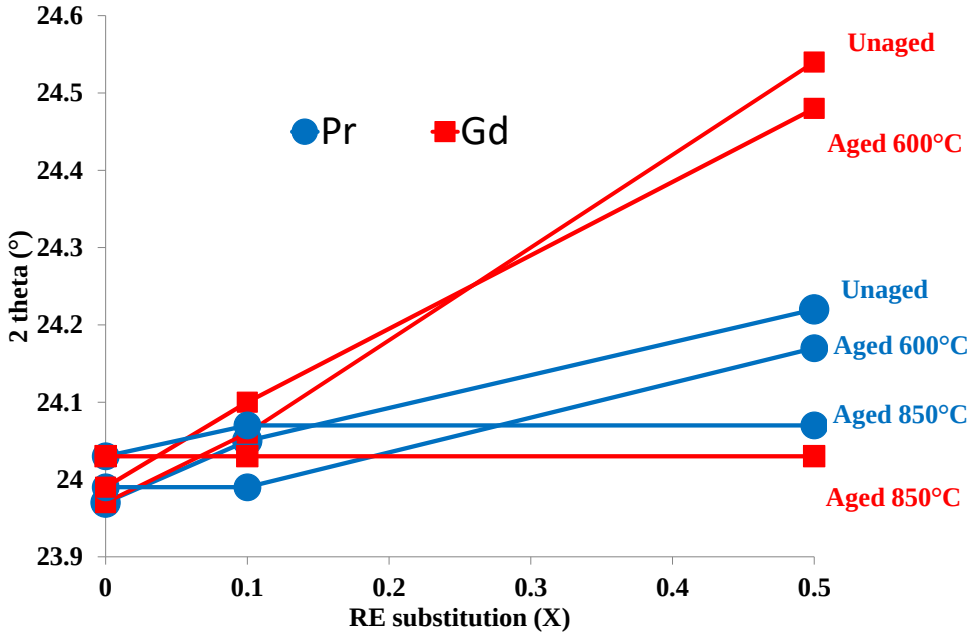

Figure 4.7 – **2theta (°) evolution according to the substitution degree of unaged and aged catalysts**

1.2.2 Raman spectroscopy

The structural information of $Ce_{1-X}RE_XV_{0.95}W_{0.05}O_4$ mixed oxides (RE=Pr and Gd, X=0.1 and 0.5) catalysts were further studied by Raman spectroscopy. In order to collect the RAMAN signal, the 638nm diode laser was used to excite the sample that is not conducive to the detailed study including a low resolution. Figs 4. (8)–(10) correspond to Raman spectra recorded on fresh catalysts and then on catalysts aged at 600°C or 850°C. The typical bands for $REVO_4$ (RE=Pr, Gd, Ce) were located at 220, 254, 367, 460, 774 and 840 cm^{-1}. The Raman band at 840 cm^{-1} confirms the tetrahedral environment of vanadium in the zircon-type structure of $REVO_4$. The Raman band at 840 cm^{-1} was assigned to A_{1g} vanadate symmetric stretching (ν_1), at 774 cm^{-1} to the B_{2g} antisymmetric stretching of vanadates (ν_3), at 460 and 367 cm^{-1} to B_{2g} and B_{1g} deformations (ν_4 and ν_3, respectively). The $Ce_{1-X}RE_XV_{0.95}W_{0.05}O_4$ mixed oxides (RE=Pr and Gd, X=0.1 and 0.5) catalysts displayed the similar Raman bands of $REVO_4$, indicating that the crystalline structure of catalysts was kept the same with $CeVO_4$. However,

the Raman band at 840 cm^{-1} obviously shifts to higher wavenumbers, which is probably due to the doping of rare earth into the crystalline structure. As seen, CeO_2 exhibits an intense and narrow band at 460 cm^{-1} previously ascribed to the F_{2g} vibration of the characteristic cubic fluorite structure of CeO_2. The absence of Raman band in the region 800–1000 cm^{-1} characterizing V_2O_5 is remarkable emphasizing the structural stability of $REVO_4$.

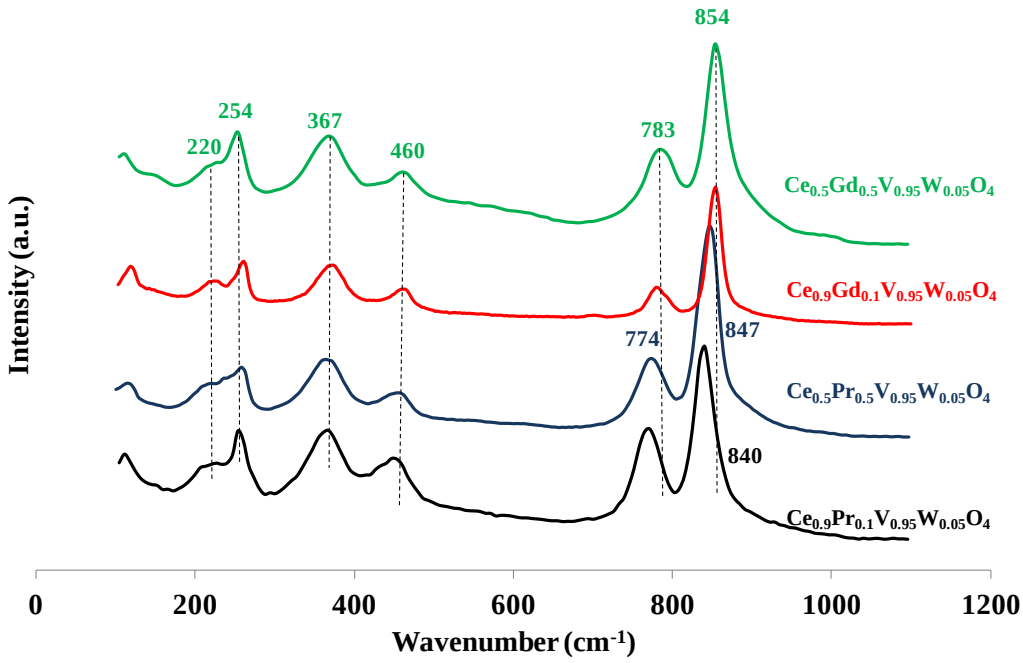

Figure 4.8 – **Raman structure of unaged $Ce_{1-x}RE_xV_{0.95}W_{0.05}O_4$ (RE=Pr and Gd, X=0.1 and 0.5) mixed oxides catalysts**

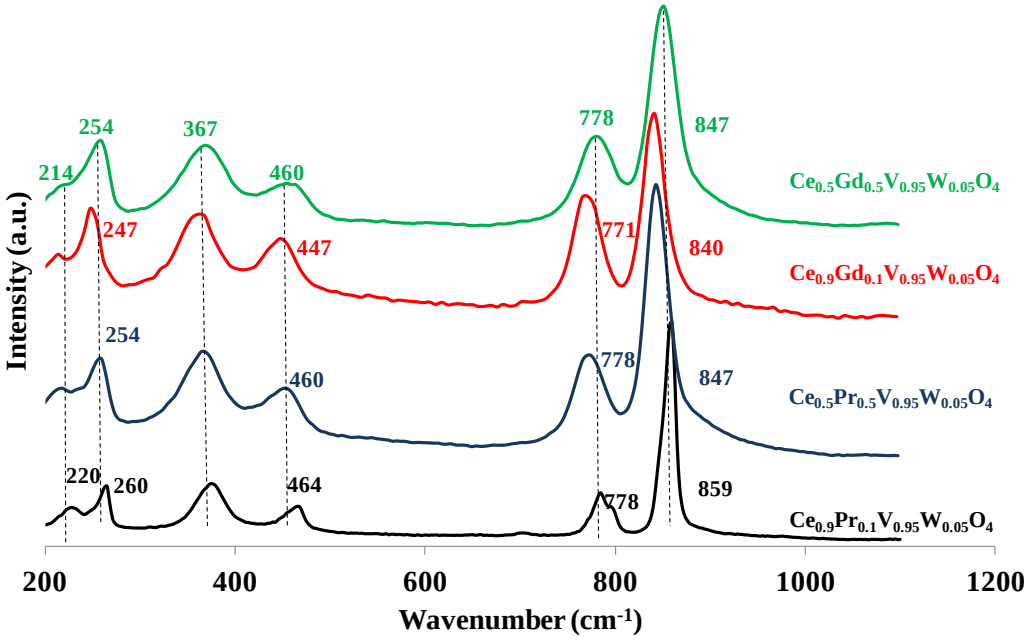

Figure 4.9 – **Raman structure of $Ce_{1-X}RE_XV_{0.95}W_{0.05}O_4$ (RE=Pr and Gd, X=0.1 and 0.5) mixed oxides catalysts aged at 600°C**

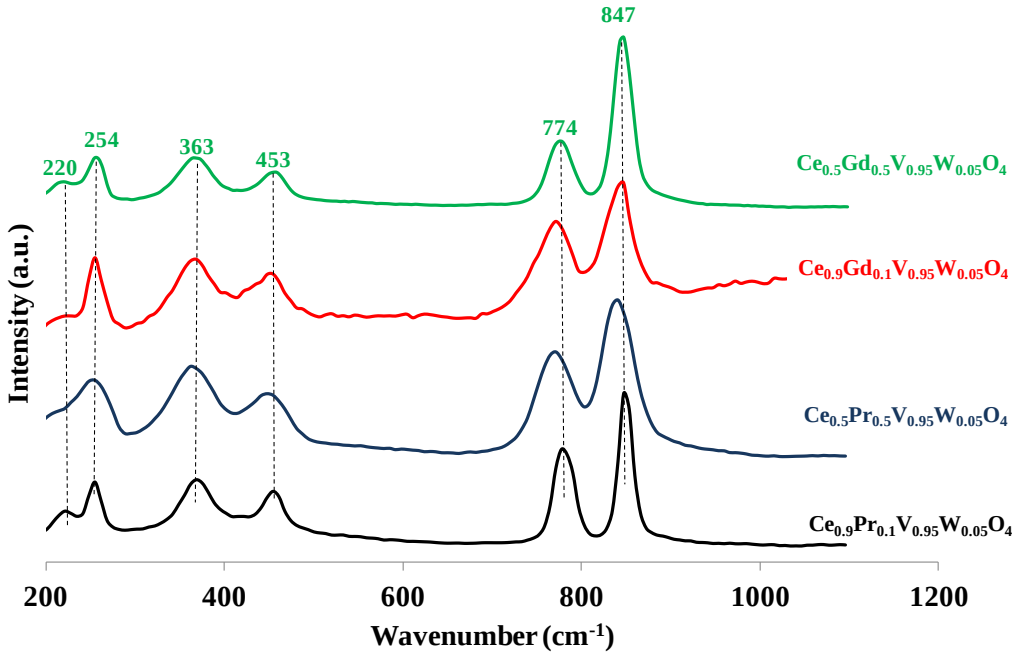

Figure 4.10 – **Raman structure of $Ce_{1-X}RE_XV_{0.95}W_{0.05}O_4$ (RE=Pr and Gd, X=0.1 and 0.5) mixed oxides catalysts aged at 850°C**

1.2.3 Temperature-programmed reduction (H_2-TPR)

1.2.3.1 Unaged

It is recognized that the redox property of catalysts is significant in the catalytic cycle of NH_3-SCR reactions. The Fig 4.11 shows the H_2-TPR profile of the unaged catalysts doped with praseodymium or gadolinium. Reduction proceeded in two stages. The prominent reduction peak around 800°C corresponds to the bulk reduction of V^{5+} to V^{3+}:

$$CeVO_4 + H_2 = CeVO_3 + H_2O \qquad \text{(Equation 4.1)}$$

Integration of this peak yielded an H/V atomic ratio of 2 (Table 4.3), which correspond to the theoretical value for Eq. 4.1. The weak and broad peak around 557–580°C would correspond to surface processes mainly related to the reduction of V^{5+}. On the other hand, one cannot rule out the reduction of surface Ce^{4+} species to Ce^{3+}, which is difficult to be distinguished due to the similar reduction temperature. With considering the small peak to the surface V^{5+} reduction, this reduction peak moves to the lower temperature by increasing rare earth content. The surface V^{5+} reduction peak of the catalysts was very weak indicating that the number of surface vanadium species was very small and more reducible than $CeVO_4$. However, the H_2 consumption of surface V^{5+} reduction peak increase by increasing the degree of cerium substitution by rare earth from 0.1 to 0.5.

Integration of the signal indicates the H_2 consumption of first reduction peak (V^{5+} to V^{3+}) is approximately the same for the different degree of cerium substitution. The Fig 4.11 also shows that by increasing substitution degree and replacing praseodymium by gadolinium the T_{max} slightly shifts to the high temperature. Unaged catalysts have the $REVO_4$ crystallites diameter which does not differ significantly by changing the degree of cerium substitution. Table 4.2 shows the crystallite diameter of $REVO_4$ that was calculated from the Scherrer formula. According to the crystallite diameter results, the crystallite diameter of unaged substituted

catalysts is still approximately the same. Therefore, the reduction temperature is not affected a lot by increasing the degree of cerium substitution.

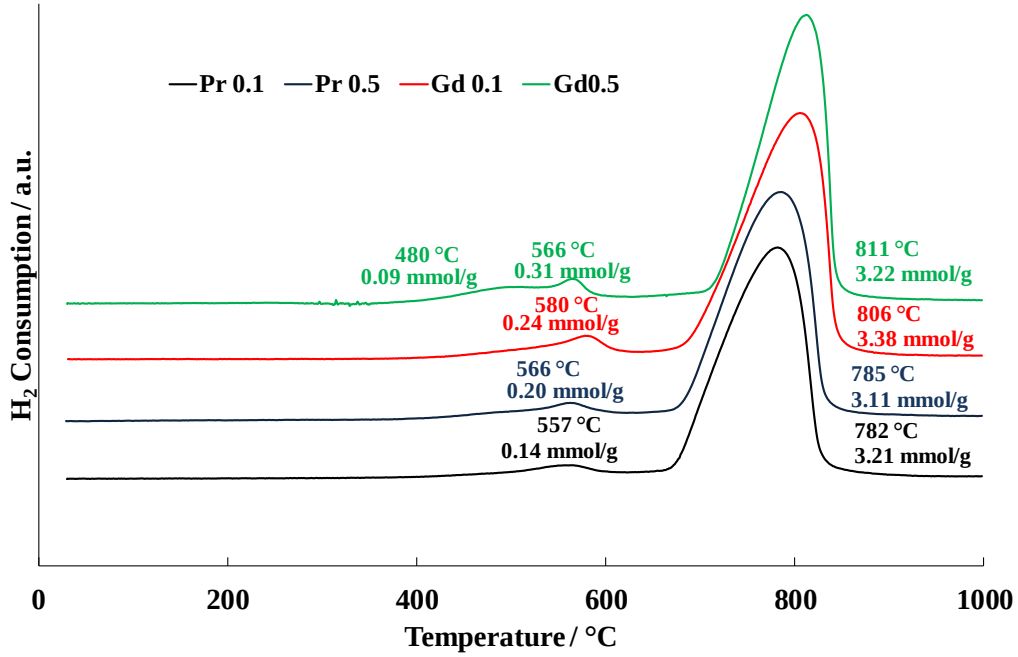

Figure 4.11 – **H_2-TPR of unaged $Ce_{1-X}RE_XV_{0.95}W_{0.05}O_4$ (RE=Pr and Gd, X=0.1 and 0.5) catalysts**

1.2.3.2 Solids Aged at 600°C

The reducibility behavior of the substituted catalysts after aging at 600°C was investigated with H_2-TPR profiles as shown in Fig 4.12. Two main reduction peaks appeared in all the curves, the reduction peak around 800°C corresponding to the reduction of V^{5+} to V^{3+}. In addition, the small broad peak can attribute to the reduction of V^{5+} of the surface and/or the reduction of surface Ce^{4+} species to Ce^{3+}.

In comparison with unaged catalysts, the reduction peaks showed different behavior. It is possible to make a relationship between the reduction temperature and $REVO_4$ crystallite size, these facts suggest that by increasing the substitution degree (X=0.1 to 0.5) of cerium by rare earth the crystallite diameter and the temperature of $CeVO_4$ to $CeVO_3$ reduction peak decrease. The H_2-consumption of the praseodymium-containing catalyst remains unchanged whatever

the degree of substitution. The evolution of vanadium species on the surface would explain the change of NO_x conversion and the N_2 selectivity. The $Ce_{0.5}RE_{0.5}V_{0.95}W_{0.05}O_4$ (RE=Pr and Gd) catalysts cause the exposure of more vanadium species on the surface which are put into evidence by the increase of low-temperature peak. It should be noted that tungsten oxides are reduced in the same temperature range as $CeVO_4$ [16, 17]. Over $Ce_{0.9}RE_{0.1}V_{0.95}W_{0.05}O_4$ (RE=Pr and Gd) and $Ce_{0.9}Pr_{0.5}V_{0.95}W_{0.05}O_4$ catalysts the estimated values for the H/V atomic ratios (Table 4.3), greater than 2 (assuming that W^{6+} is reduced to W^{4+}); confirm an additional consumption of hydrogen linked to the reduction of species WO_x.

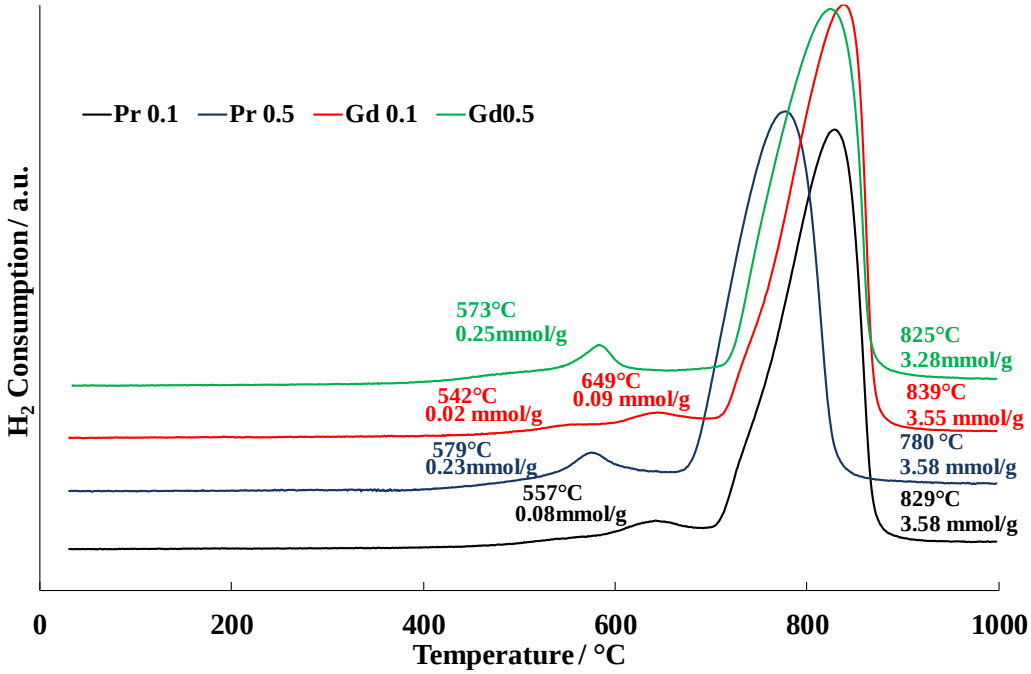

Figure 4.12 – **H_2-TPR of $Ce_{1-X}RE_XV_{0.95}W_{0.05}O_4$ (RE=Pr and Gd, X=0.1 and 0.5) catalysts aged at 600°C**

1.2.3.3 Solids Aged at 850°C

Figure 4.13 presents the TPR profiles of the $Ce_{1-X}RE_XV_{0.95}W_{0.05}O_4$ catalysts after aging at 850°C. The high-temperature reduction peak is assigned to the reduction of vanadium species from $CeVO_4$ into $CeVO_3$ with H_2 consumption setting close to theoretical value. On the other hand, the reduction peaks observed at low temperature completely disappeared after aging at 850°C. The lack of observation of this reduction peak over aged catalysts at 850°C could be associated with the conjunction of several factors. It can be due to the low specific surface area ($<4 m^2/g$) of catalysts after aging, the agglomeration of monomeric vanadium species by getting large V_2O_5 clusters and a loss of active element by volatilization at high temperature.

The modifications of the particle size can be related to the significant alteration of reducibility. By increasing the aging temperature, the crystallite diameter (Table 4.3) increase and accordingly reduction peaks shift to the higher temperature for all catalysts. As exemplified in Figure 4.14 one can observe that a linear relationship can be established by plotting T_{Max} vs. the crystallite size which suggests that the reducibility of $Ce_{1-X}RE_XV_{0.95}W_{0.05}$ is mostly altered by thermal sintering.

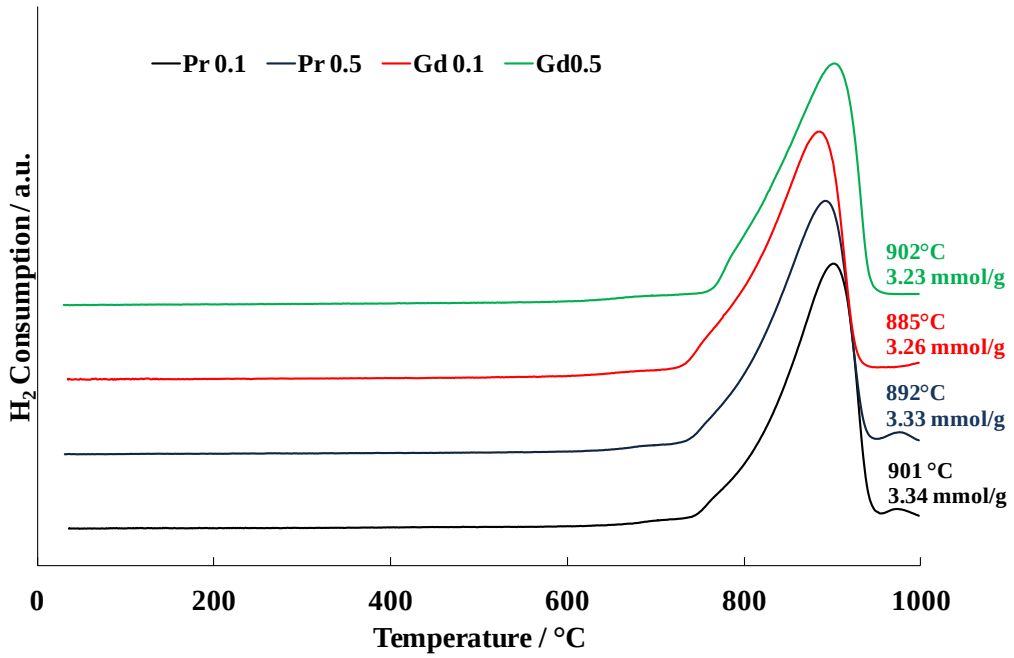

Figure 4.13 – **H_2-TPR of $Ce_{1-X}RE_XV_{0.95}W_{0.05}O_4$ (RE=Pr and Gd, X=0.1 and 0.5) catalysts aged at 850°C**

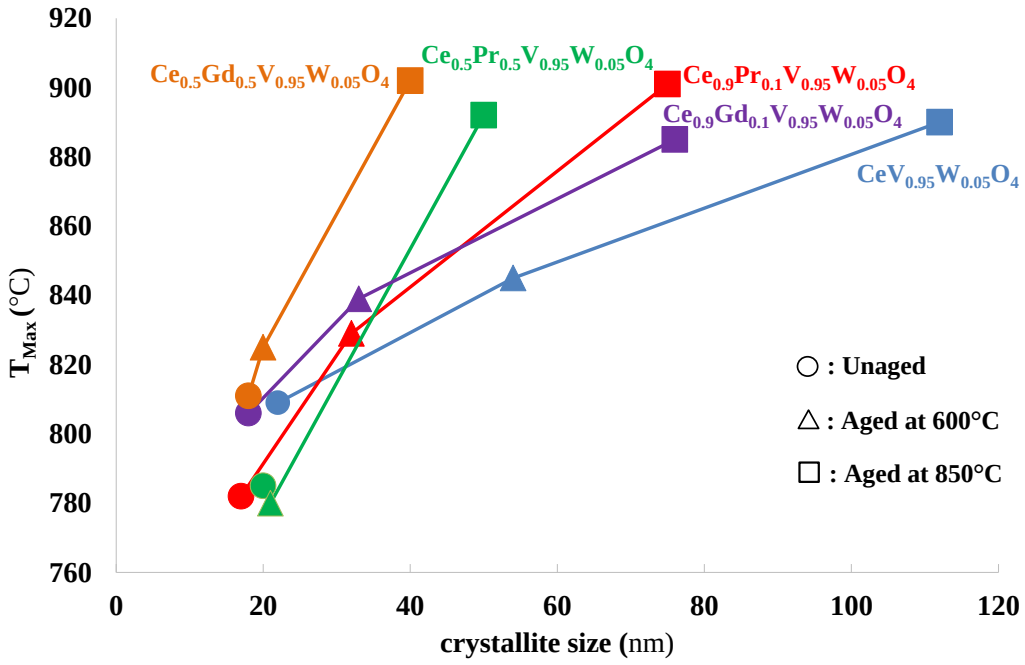

Figure 4.14 – **Correlation between the maximum reduction temperatures (T_{Max}) vs. the crystallite size over $Ce_{1-X}RE_XV_{0.95}W_{0.05}$ catalysts**

Table 4.3 – **H_2-TPR results of $Ce_{1-X}RE_XV_{0.95}W_{0.05}O_4$ (X=0.1 and 0.5; RE=Pr and Gd); (70mg, 50ml min^{-1})**

Catalyst	Aging temperature (°C)	H_2 consumption [a] (mmol g^{-1})	H/V	T_{max} reduction peaks
$CeV_{0.95}W_{0.05}O_4$	unaged	3.32	1.90	809
	600	3.54	2.00	845
	850	3.78	2.00	890
$Ce_{0.9}Pr_{0.1}V_{0.95}W_{0.05}O_4$	unaged	3.21	2.00	782
	600	3.58	2.10	829
	850	3.34	2.00	901
$Ce_{0.5}Pr_{0.5}V_{0.95}W_{0.05}O_4$	unaged	3.11	1.90	785
	600	3.58	2.10	780
	850	3.33	2.00	892
$Ce_{0.9}Gd_{0.1}V_{0.95}W_{0.05}O_4$	unaged	3.38	2.00	806
	600	3.55	2.10	839
	850	3.26	2.00	885
$Ce_{0.5}Gd_{0.5}V_{0.95}W_{0.05}O_4$	unaged	3.22	1.90	811
	600	3.28	1.90	825
	850	3.23	1.90	902

[a] Consumption integrated in the temperature range of 700-1000°C

1.3 Surface characterizations

1.3.1 Specific surface area

It is already realized in heterogeneous catalysis that better comprehension of catalytic behavior requires the knowledge of the surface area. The specific surface area of the powder is determined by physical adsorption of nitrogen on the surface of the catalyst and by calculating the amount of adsorbate gas corresponding to a monomolecular layer on the surface. The results of the specific surface area are reported in Table 4.4.

Table 4.4 – **Influence of cerium substitution by rare earth and hydrothermal aging on the specific surface area**

Catalyst	Aging temperature (°C)	Experimental specific surface area S_{exp} ($m^2.g^{-1}$)	Theoretical specific surface area S_{th} ($m^2.g^{-1}$)
$CeV_{0.95}W_{0.05}O_4$	Unaged	56	60
	600°C	18	23
	850°C	2	12
$Ce_{0.9}Pr_{0.1}V_{0.95}W_{0.05}O_4$	Unaged	62	74
	600°C	19	39
	850°C	2.8	16
$Ce_{0.5}Pr_{0.5}V_{0.95}W_{0.05}O_4$	Unaged	64	63
	600°C	38	60
	850°C	3	25
$Ce_{0.9}Gd_{0.1}V_{0.95}W_{0.05}O_4$	Unaged	60	70
	600°C	20	38
	850°C	2.6	17
$Ce_{0.5}Gd_{0.5}V_{0.95}W_{0.05}O_4$	Unaged	61	70
	600°C	41	63
	850°C	3.5	32

S_{th} specific surface area calculated from the size of cubic crystallites $S_{th} = 6/\rho D_\rho$

Incorporation of RE (PR and Gd) enhanced the BET (Brunauer-Emmett-Teller) surface area. The experimental and theoretical values of the specific surface area calculated from the crystallites diameter of $REVO_4$ and obtained by XRD analysis, S_{exp} and S_{th} respectively, are presented in Table 4.4. These values can be used to distinguish if the sintering process is driven either by agglomeration and/or crystal growth phenomena. Rare earth incorporation in $CeV_{0.95}W_{0.05}O_4$ structure slightly improves the texture of the unaged catalysts. After aging at 600°C, a beneficial effect of rare earth is clearly observed; the modified catalysts with a substitution degree of 0.5 possessed of a specific surface area approximately two times greater than that of the $CeV_{0.95}W_{0.05}O_4$ reference catalyst. The insertion of rare earth into the $CeV_{0.95}W_{0.05}O_4$ structure improves the sintering resistance of the $REVO_4$ particles (XRD part) thus limiting the loss of specific surface area. Indeed, an aging temperature of 850°C, decrease the specific surface area of all catalysts. The observed variations on the S_{exp} values below the theoretical S_{th} values can be explained by the increase in $REVO_4$ crystallite size due to agglomeration after aging.

1.3.2 X-ray photo-electron spectroscopy (XPS)

The chemical composition of the surface was investigated by XPS. In the case of the bulk catalysts, we can consider that the extracted information is depictive of the surface of the catalyst. The core levels of Ce 3d, Pr 3d, Gd 4d, V 2p, W 4f and O 1s characteristics of cerium, vanadium, praseodymium, gadolinium, and oxygen have been studied by X-ray photoelectron spectroscopy. The samples were analyzed without in-situ pre-treatment, all samples are directly introduced into the analysis chamber and analyzed under ultra-vacuum. Fitting the Ce 3d spectra is often used to characterize the oxidation state of the elements in the solid. The measured spectra are decomposed into individual peaks or doublets according to their origin. The corresponding XPS spectra over as-synthesized and aged catalysts are shown in Fig 4.15–25. Fig 4.15 shows the spectra of Ce 3d, the XP spectra of Ce 3d splits into ten peaks denoted as v^0 (881.3 eV), v (882.5 eV), v′ (885.5 eV), v″ (888 eV), v‴ (898.5 eV), u^0 (899.0 eV), u (900.8 eV), u′ (903.8 eV), u″ (906.9 eV), u‴ (916.6 eV) [18]. The red curves labeled v, v″, v‴ and u, u″, u‴ are characteristic of the Ce^{4+} species, whereas the blue curves for Ce^{3+} are indicated at positions labeled v^0, v′ and u^0, u′. The XPS spectrum of Ce 3d can be also denoted as two sets which can be ascribed to the $3d_{3/2}$ and $3d_{5/2}$ spin-orbital multiples. In Fig 4.15, the Ce $3d_{5/2}$ peaks denoted as v″ and Ce $3d_{3/2}$ peaks as u″. The relative intensity of the satellites u‴ at 917 eV is representative of the presence of Ce^{4+}. The Ce3d photopeaks do not show any remarkable change in shape depending on the rare earth substitution. By the integration of the different components, it is possible to estimate the ratio of Ce^{4+}/Ce^{3+} (Table 4.5). Regardless of the substitution degree, the cerium photo-peaks envelope and the obtained values of the Ce^{4+}/Ce^{3+} ratio shows the predominance of Ce^{3+} over substituted samples. Furthermore, the hydrothermal aging causes an increase of the relative concentration of Ce^{4+}.

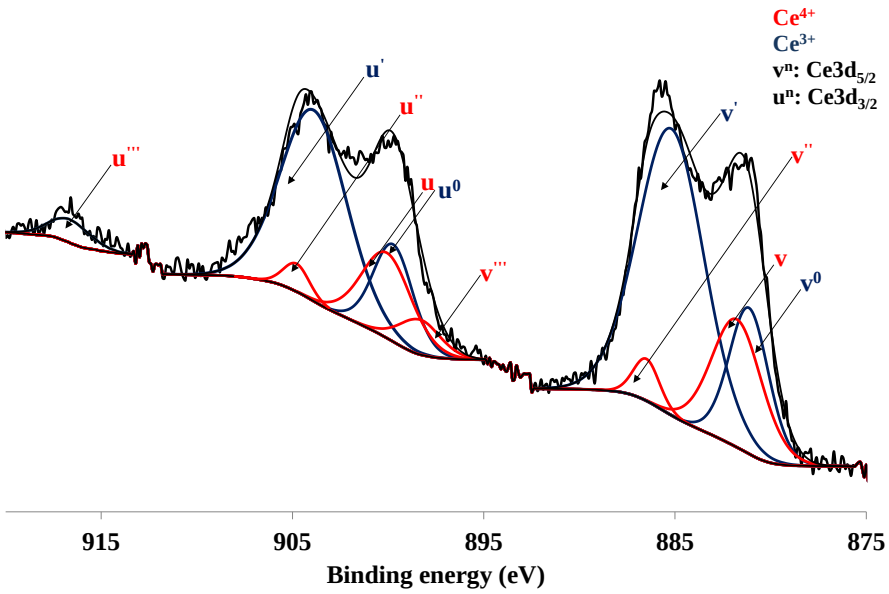

Figure 4.15 – **Fitted Ce 3d XP spectrum of fresh $Ce_{0.5}Pr_{0.5}V_{0.95}W_{0.05}O_4$ catalyst**

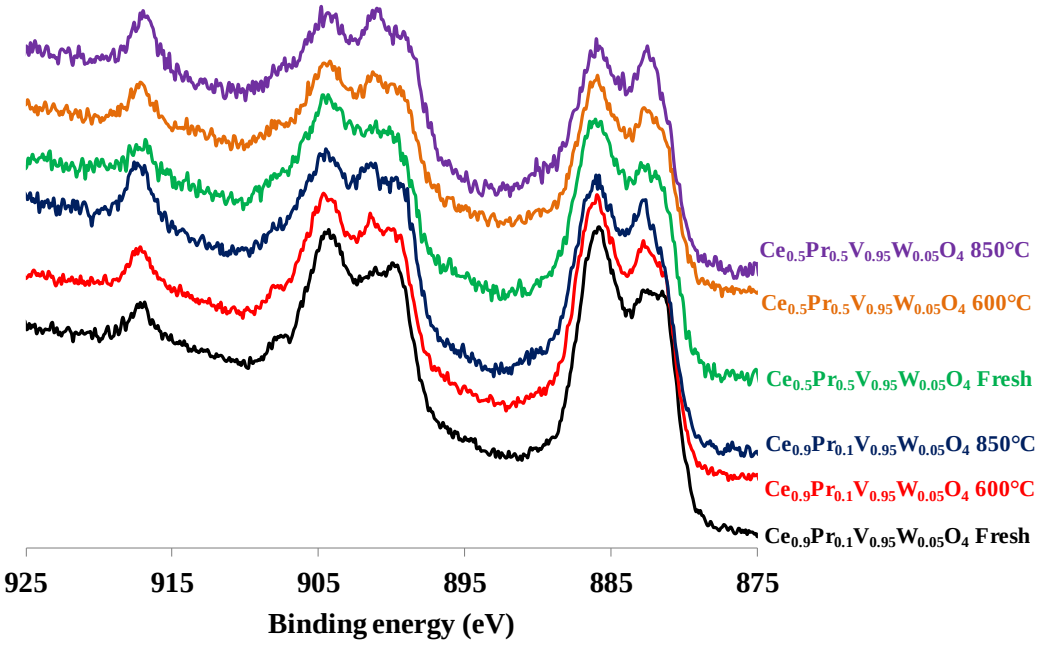

Figure 4.16 – **XPS Spectra of Ce 3d core level of the $Ce_{1-x}Pr_xV_{0.95}W_{0.05}O_4$ (X=0.1 and 0.5) catalysts**

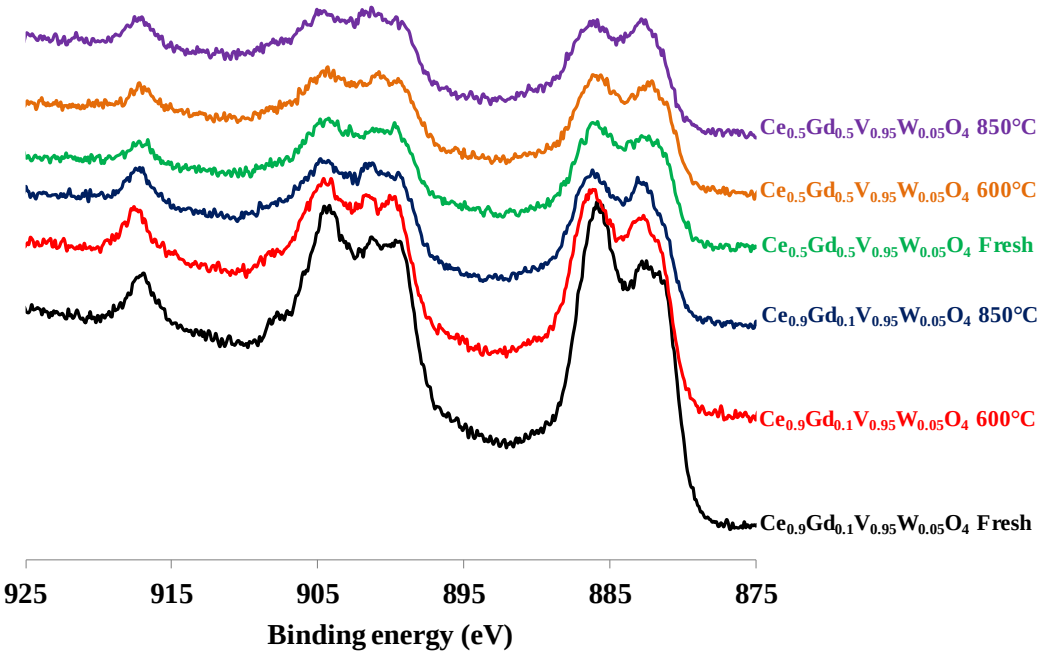

Figure 4.17 – **XPS Spectra of Ce 3d core level of the $Ce_{1-X}Gd_XV_{0.95}W_{0.05}O_4$ (X=0.1 and 0.5) catalysts**

The Pr 3d photopeak shows the characteristic multiple splitting giving rises to 4 photopeaks [19]. From Fig 4.18 two sets of signals, one centered at BE = 949.6, 953.8, and 966.2 eV are assignable to Pr $3d_{5/2}$, and the other centered at BE = 929.5 and 933.7 eV, assignable to Pr $3d_{3/2}$. Besides the intensity variation proportional to the Pr doping level, all the samples show similar spectra as the Pr_2O_3 reference sample, which indicates that Pr ions possess dominantly the +III valence state. In our XP Pr 3d spectra, satellites are rather clearly distinguishable at 985 eV [20].

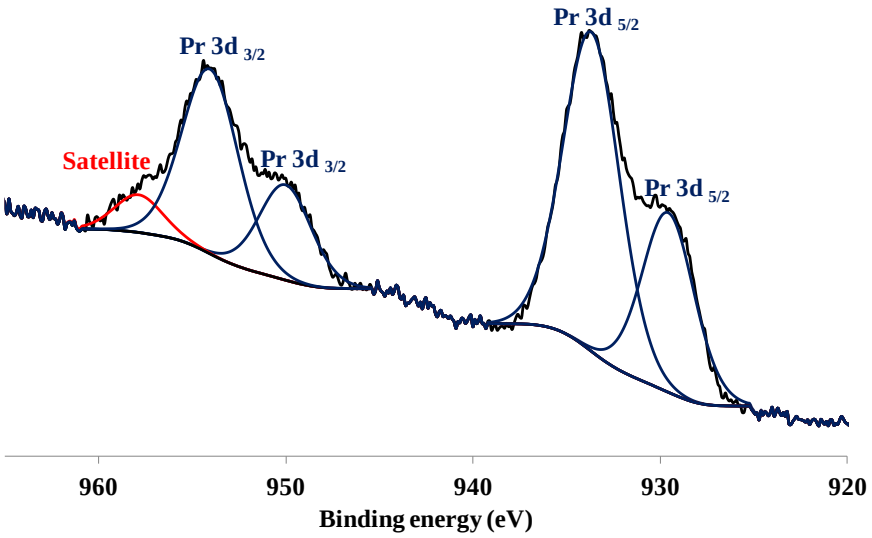

Figure 4.18 – **Fitted Pr 3d XP spectrum of fresh $Ce_{0.5}Pr_{0.5}V_{0.95}W_{0.05}O_4$ catalyst**

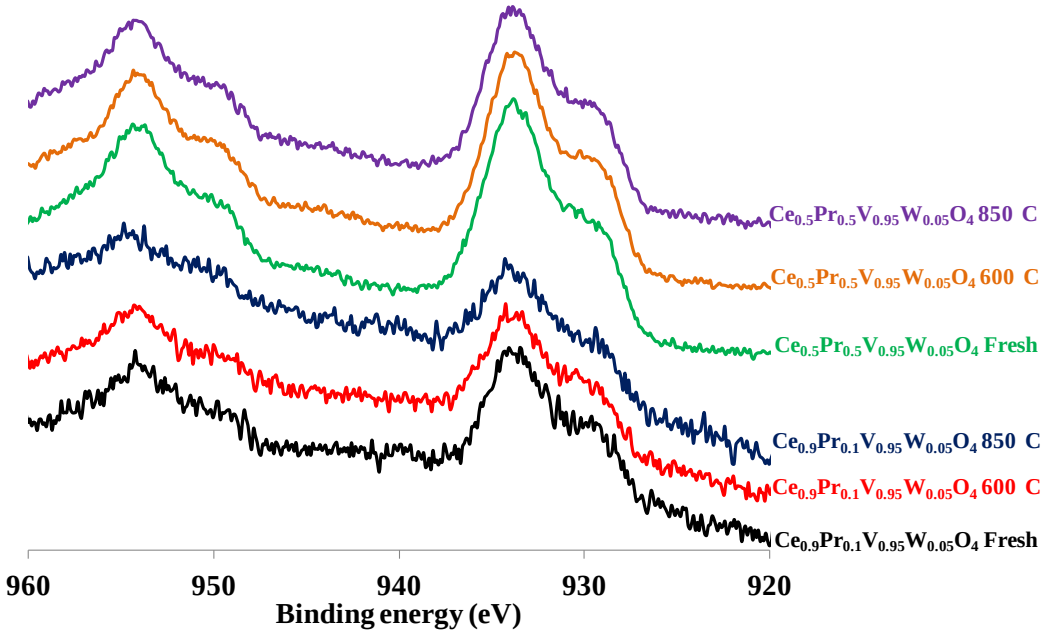

Figure 4.19 – **XPS Spectra of Pr 3d core level of the $Ce_{1-X}PrxV_{0.95}W_{0.05}O_4$ (X=0.1 and 0.5) catalysts**

The XPS spectrum of Gd 4d is shown in Fig 4.20. The two strong photopeaks at 142.5 eV and 147.8 eV corresponding to a spin-orbit splitting of 5eV refer respectively to the $4d_{5/2}$ and $4d_{3/2}$ energy levels of Gd [21]. These observations are in good agreement with reports in the literature for Gd_2O_3. Similar results were obtained for all samples. There is a clear shift toward lower binding energies of both $4d_{5/2}$ and 4 $d_{3/2}$ with the increase of Pr content, from 142.5eV to 142

eV and respectively from 147.8 eV to 147.4 eV. Along with increasing the degree of cerium substitution by gadolinium the Gd 4d peak intensity obviously increases.

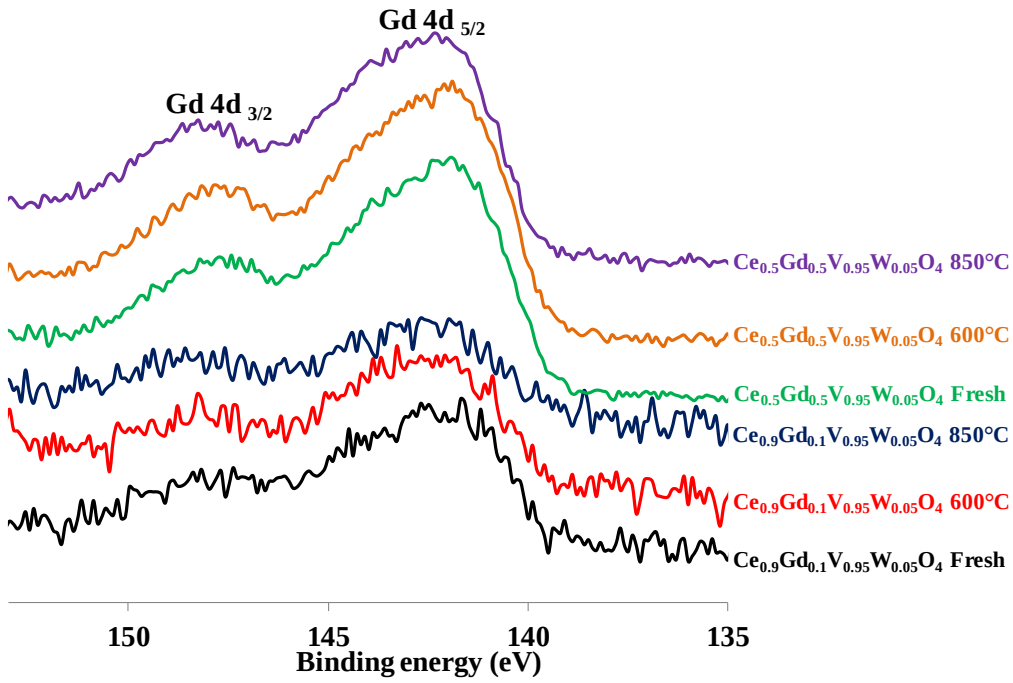

Figure 4.20 – **XPS Spectra of Gd 4d core level of the $Ce_{1-x}Gd_xV_{0.95}W_{0.05}O_4$ (X=0.1 and 0.5) catalysts**

The binding energies for the photopeak V $2p_{3/2}$ remain almost unchanged at 517.7 eV close to the values currently attributed to V^{5+} in the V_2O_5 phase [22]. It can be noted, the low sensitivity of binding energies of V $2p_{3/2}$ photopeaks to the increase of RE concentration during hydrothermal synthesis and hydrothermal aging. The chemical shift observed on the photopeak V $2p_{3/2}$ can be sometimes useful in order to distinguish the V^{4+} and V^{5+} species when the vanadium is found in two distinct phases and two different degrees of oxidation. On the other hand, the difference in energy between the O 1s and V $2p_{3/2}$ core levels may provide additional information for determining the oxidation state of vanadium. The differences between the O 1s and V $2p_{3/2}$ binding energies are close to 12.9 eV on all the samples, confirming the presence of V^{5+} oxidation state in all catalysts [23]. The relative concentrations of elements Ce, RE, V and W for $Ce_{1-X}RE_XV_{0.95}W_{0.05}O_4$ catalysts aged at different temperatures are reported in Table

4.5. It can be seen that the Ce/O atomic ratio is close to 0.3 and 0.14 and is stable for the substituted $Ce_{0.9}RE_{0.1}V_{0.95}W_{0.05}O_4$ and $Ce_{0.5}RE_{0.5}V_{0.95}W_{0.05}O_4$ catalysts respectively. V/Ce ratios decrease significantly for all the catalysts, in particular after aging at 850°C. This relative enrichment in cerium is mainly due to the fluctuations observed on the V/O ratio. The atomic ratios RE/Ce, W/V, V/(Ce+Pr), W/(Ce+Pr) and (V+W)/(Ce+Pr) are close to the theoretical value, the difference remains less than 10%, which suggests a homogeneous distribution of the elements in the catalyst. An important excess of tungsten is observed at the surface of all investigated catalysts after aging at 850°C. Tungsten enrichment on the surface can have a detrimental effect on the catalytic properties lowering the accessibility of the active V-sites.

According to the recent nomenclature of Piumetti *et al*. [24], the two peaks located at 530.92 and 529.07 eV were referred to as O_α and O_β, respectively. The abundance of labile oxygen identified as the O_α species is another property often related to SCR activity. In the case of photoemission from oxygen, the O 1s signal clearly shows two different surface oxygen species. The low binding energy peak is ascribed to lattice oxygen of $CeVO_4$ or CeO_2 (O_β: 529.0-530.5 eV) whereas the high binding energy peak (O_α: 531.0-532.8 eV) corresponds to adsorbed oxygen, hydroxyl and/or carbonate groups which reflects the presence of anionic vacancies. It is recognized that those anionic vacancies can improve oxygen adsorption and accelerate SCR through a greater NO_2 formation from NO oxidation. Despite this, the XPS O_α/O_β ratio is a common way to roughly assess the number of oxygen vacancies in the different sample (Table 4.5). The O_α/O_β ratio can also be disturbed by the presence of an increasing concentration of vanadium on the surface. For example, Huang *et al*. [25] observe an increase in this ratio as the vanadium density increases and associate this evolution with an increase in the surface concentration of anionic vacancies. The comparison of the values of the O_α/O_β and Ce^{4+}/Ce^{3+} ratios after aging shows an overall increase in Ce^{3+} concentration accompanied by a decrease in the O_α/O_β. The significant variation on the O_α/O_β ratio is discernible on unaged (as-prepared)

samples with changing rare earth concentration and nature. On the other hand, more significant changes seem to occur on aged samples.

A slight decrease of O_α/O_β ratio is observed on $Ce_{0.5}Pr_{0.5}V_{0.95}W_{0.05}O_4$ and $Ce_{0.5}Gd_{0.5}V_{0.95}W_{0.05}O_4$ catalysts whereas the concentration of O_α significantly increases on $Ce_{0.9}Pr_{0.1}V_{0.95}W_{0.05}O_4$ and $Ce_{0.9}Gd_{0.1}V_{0.95}W_{0.05}O_4$ catalyst after thermal aging. The changes observed in the ratio might reflect the creation of new oxygen vacancies in connection to an increase in Ce^{3+} concentration on CeO_2 or surface defects on $CeVO_4$ as suggested by Huang *et al* [25].

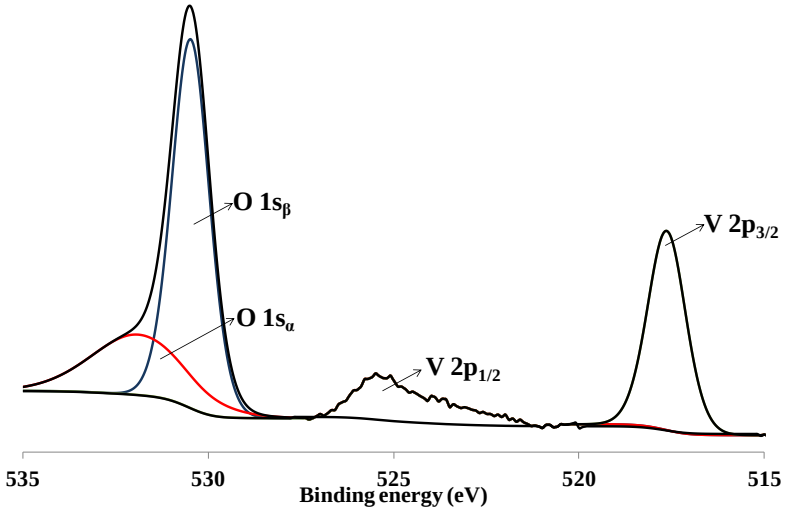

Figure 4.21 – **Fitted Spectra of V 2p and O 1s core level of the unaged $Ce_{0.5}Pr_{0.5}V_{0.95}W_{0.05}O_4$**

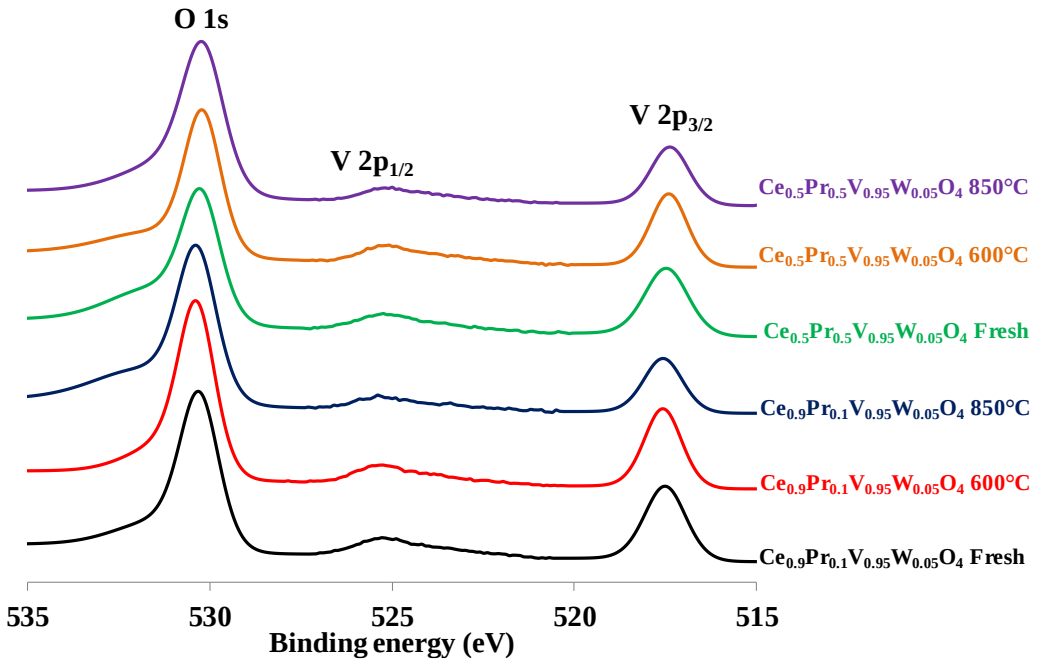

Figure 4.22 – **XPS Spectra of V 2p and O 1s core level of the $Ce_{1-X}Pr_XV_{0.95}W_{0.05}O_4$ (X=0.1 and 0.5) catalysts**

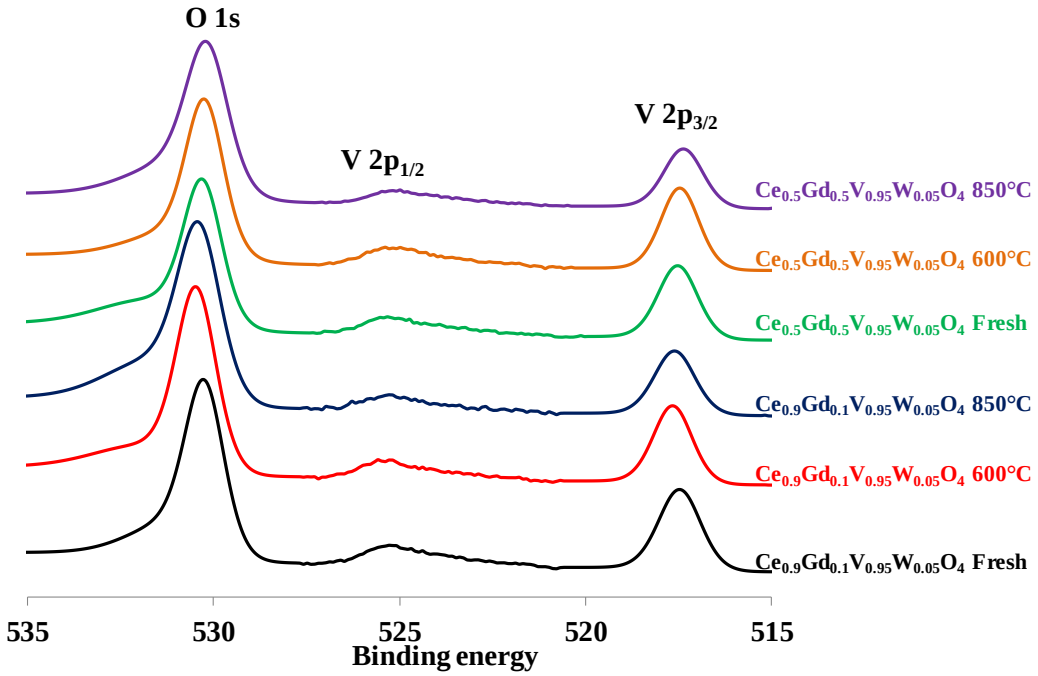

Figure 4.23 – **XPS Spectra of V 2p and O 1s core level of the $Ce_{1-X}Gd_XV_{0.95}W_{0.05}O_4$ (X=0.1 and 0.5) catalysts**

The photopeaks corresponding to the characteristic of tungsten $4d_{5/2}$ and $4d_{3/2}$ recorded on the substituted catalysts before and after aging at 600°C and 850°C are shown in Fig 4.24 and 25.

There is no significant change in the binding energies. In addition, no shoulder or line broadening is identified, so tungsten would be stabilized at the +6 oxidation state [12–14]. The formation of V^{5+} species is confirmed by the V 3p peak observed at the binding energy (V 3p) = 42.2 eV [22]. Regarding the surface compositions obtained by XPS, carbon is detected and quantified in addition to the elements characteristic of the $Ce_{1-X}RE_XV_{0.95}W_{0.05}O_4$ (X=0.1 and 0.5, RE= Pr and Gd) structure. As illustrated in Table 4.5 thermal aging induces changes in surface composition. Indeed, an increase in the atomic W/V and W/Ce+RE ratio with a rise in aging temperature suggest a surface tungsten enrichment especially when samples are aged at 850°C. On the other hand, no clear tendency characterizes the vanadium concentration. The presence of carbon on solid surfaces is always evidenced and used as an internal reference to calibrate the binding energy (B.E.) values.

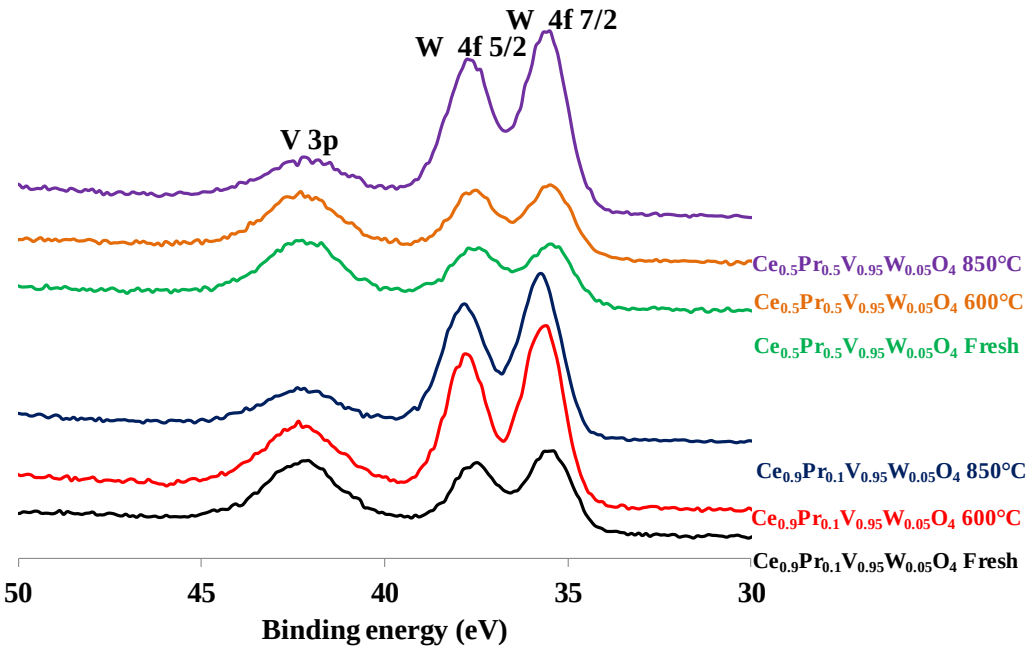

Figure 4.24 – **XPS Spectra of V 3p and W 4f core level of the $Ce_{1-X}Pr_XV_{0.95}W_{0.05}O_4$ (X=0.1 and 0.5) catalysts**

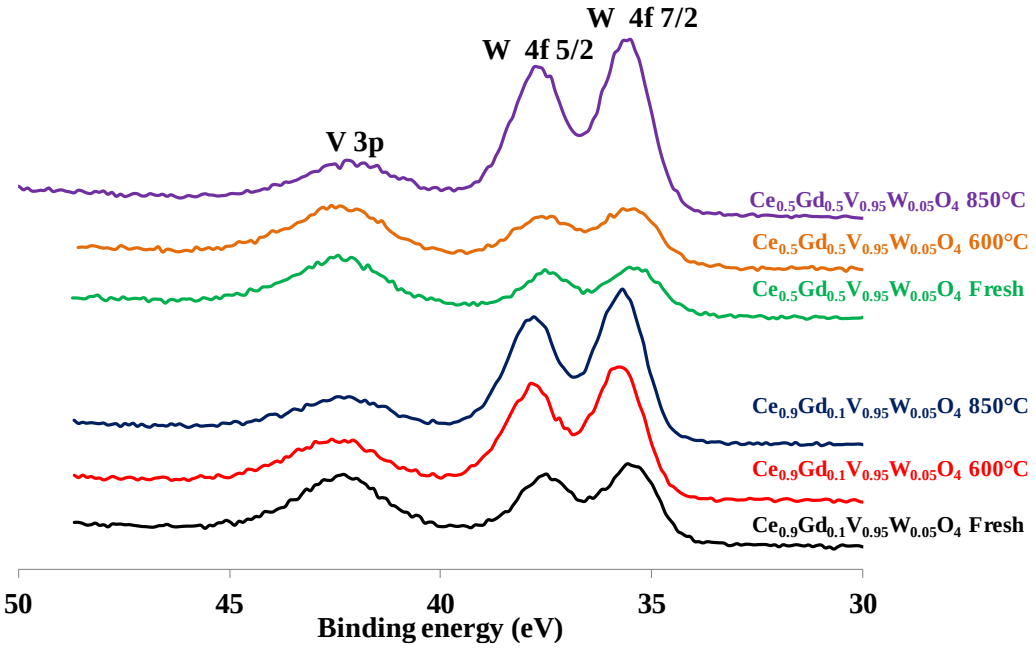

Figure 4.25 – **XPS Spectra of V 3p and W 4f core level of the $Ce_{1-X}Gd_XV_{0.95}W_{0.05}O_4$ (X=0.1 and 0.9) catalysts**

Table 4.5 – **Surface Composition of $Ce_{1-X}RE_XV_{0.95}W_{0.05}O_4$ (RE=Pr and Gd, X=0.1 and 0.5) catalysts**

Catalyst	Aging temperature (°C)	Ce/O	V/O	V/Ce	W/Ce	RE/Ce
$CeV_{0.95}W_{0.05}O_4$	unaged	0.23	0.21	0.89	0.13	-
	600	0.17	0.17	0.96	0.32	-
	850	0.21	0.15	0.72	0.33	-
$Ce_{0.9}Pr_{0.1}V_{0.95}W_{0.05}O_4$	unaged	0.27	0.22	0.82	0.08	0.13
	600	0.25	0.21	0.85	0.17	0.14
	850	0.20	0.14	0.70	0.28	0.15
$Ce_{0.5}Pr_{0.5}V_{0.95}W_{0.05}O_4$	unaged	0.13	0.39	2.91	0.14	1.30
	600	0.14	0.27	1.50	0.17	1.20
	850	0.14	0.21	1.92	0.45	1.00
$Ce_{0.9}Gd_{0.1}V_{0.95}W_{0.05}O_4$	unaged	0.30	0.22	0.70	0.08	0.10
	600	0.25	0.18	0.80	0.18	0.10
	850	0.20	0.13	0.65	0.30	0.16
$Ce_{0.5}Gd_{0.5}V_{0.95}W_{0.05}O_4$	unaged	0.14	0.20	1.50	0.12	1.00
	600	0.14	0.20	1.67	0.17	1.20
	850	0.13	0.16	1.00	0.48	0.90

Catalyst	Aging temperature (°C)	W/V	V/ (Ce+Pr)	W/ (Ce+RE)	(V+W)/ (Ce+RE)	Ce^{4+}/Ce^{3+}	O_α/O_β	B.E. (eV) V 2p
	unaged	**0.14**	**-**	**-**	**-**	**0.22**	**0.37**	**517.5**
$CeV_{0.95}W_{0.05}O_4$	**600**	**0.33**	**-**	**-**	**-**	**0.31**	**0.35**	**517.5**
	850	**0.46**	**-**	**-**	**-**	**0.31**	**0.38**	**517.5**
	unaged	**0.09**	**0.80**	**0.07**	**0.80**	**0.40**	**0.35**	**517.5**
$Ce_{0.9}Pr_{0.1}V_{0.95}W_{0.05}O_4$	**600**	**0.20**	**0.83**	**0.07**	**0.90**	**0.30**	**0.35**	**517.6**
	850	**0.40**	**0.60**	**0.20**	**0.85**	**0.50**	**0.56**	**517.6**
	unaged	**0.05**	**1.20**	**0.05**	**1.20**	**0.44**	**0.70**	**517.5**
$Ce_{0.5}Pr_{0.5}V_{0.95}W_{0.05}O_4$	**600**	**0.10**	**0.70**	**0.07**	**0.80**	**0.60**	**0.50**	**517.5**
	850	**0.20**	**0.95**	**0.20**	**1.00**	**0.71**	**0.40**	**517.5**
	unaged	**0.10**	**0.70**	**0.70**	**0.75**	**0.26**	**0.40**	**517.5**
$Ce_{0.9}Gd_{0.1}V_{0.95}W_{0.05}O_4$	**600**	**0.20**	**0.70**	**0.15**	**0.85**	**0.40**	**0.30**	**517.6**
	850	**0.40**	**0.50**	**0.20**	**0.80**	**0.60**	**0.50**	**517.6**
	unaged	**0.08**	**0.75**	**0.06**	**0.80**	**0.58**	**0.50**	**517.6**
$Ce_{0.5}Gd_{0.5}V_{0.95}W_{0.05}O_4$	**600**	**0.10**	**0.75**	**0.07**	**0.84**	**0.60**	**0.39**	**517.6**
	850	**0.50**	**0.50**	**0.30**	**0.80**	**0.70**	**0.37**	**517.6**

1.4 Catalytic activity of $Ce_{1-X}RE_XV_{0.95}W_{0.05}O_4$ (RE=Pr and Gd, X=0.1 and 0.5) catalysts after hydrothermal aging at 600°C

According to the NO/NO_x ratios different reactions can be performed on the surface of the catalysts. The main ones are the selective catalytic reduction of NO_x into N_2 under standard conditions-SCR (Eq 4.2), fast-SCR (Eq 4.3) and NO_2-SCR (Eq 4.4).

$$2NH_3 + 2NO + 1/2O_2 = 2N_2 + 3H_2O \quad \text{(Equation 4.2)}$$

$$2NH_3 + NO + NO_2 = 2N_2 + 3H_2O \quad \text{(Equation 4.3)}$$

$$4NH_3 + 2NO_2 = 6N_2 + 4H_2O \quad \text{(Equation 4.4)}$$

Other reactions can occur, particularly those leading to the incomplete reduction of NO_x to N_2O and preferential oxidation of ammonia which can also lead to the production of NO, N_2O and N_2.

$$2NH_3 + 2NO + O_2 = 2N_2O + 3H_2O \quad \text{(Equation 4.5)}$$

$$2NH_3 + NO + NO_2 + O_2 = 2N_2O + 3H_2O \quad \text{(Equation 4.6)}$$

$$2NH_3 + NO_2 + 5/4O_2 = 3/2N_2O + 3H_2O \quad \text{(Equation 4.7)}$$

$$2NH_3 + 3/2O_2 = N_2 + 3H_2O \quad \text{(Equation 4.8)}$$

$$2NH_3 + 2O_2 = N_2O + 3H_2O \quad \text{(Equation 4.9)}$$

$$2NH_3 + 5/2O_2 = 2NO + 3H_2O \quad \text{(Equation 4.10)}$$

One of the undesirable reactions is NH_3 oxidation. These reactions are correlated with temperature and are responsible for the sharp efficiency drop of NH_3-SCR catalysts at very high temperatures.

1.4.1 Ammonia-selective catalytic reduction of NO_x to nitrogen in "Standard" condition: NO/NO_x =1

For a mixture comprising an exclusively nitric oxide, the removal of NO proceeds via standard-SCR reaction, the main reaction of SCR with ammonia with NO/NO_x ratio equal to 1 so-called standard SCR will be:

$$4NH_3+4NO+O_2 = 4N_2+6H_2O \text{ (Standard-SCR)} \quad \text{(Equation 4.11)}$$

The NO_x conversion versus temperature on the aged catalyst at 600°C during standard-SCR condition is collected in Fig 4.26. All the catalysts showed the high N_2 selectivity (100%) in the whole temperature range. Therefore, the optimal catalyst could contribute to improving the NO_x conversion. For all catalysts, the NO_x conversion increased with temperature at the low-temperature range (200–350°C). The $Ce_{0.5}RE_{0.5}V_{0.95}W_{0.05}O_4$ (Pr and Gd) catalysts show a higher NO_x conversion compared to $Ce_{0.9}RE_{0.1}V_{0.95}W_{0.05}O_4$ (Pr and Gd) catalysts. $Ce_{0.5}RE_{0.5}V_{0.95}W_{0.05}O_4$ is also more active than the reference $CeV_{0.95}W_{0.05}O_4$ at low temperature (50% versus 30% of NO_x converted at 200°C). It is possible to deduce the following sequence of the NO_x conversion measured at 350°C: $CeV_{0.95}W_{0.05}O_4$ (74%) < $Ce_{0.9}Gd_{0.1}V_{0.95}W_{0.05}O_4$ =~ $Ce_{0.9}Pr_{0.1}V_{0.95}W_{0.05}O_4$ (76%) < $Ce_{0.5}Gd_{0.5}V_{0.95}W_{0.05}O_4$ (88%) < $Ce_{0.5}Pr_{0.5}V_{0.95}W_{0.05}O_4$ (90%). The specific surface area of $Ce_{0.5}Pr_{0.5}V_{0.95}W_{0.05}O_4$ and $Ce_{0.5}Gd_{0.5}V_{0.95}W_{0.05}O_4$ catalysts is two times higher than that of $CeV_{0.95}W_{0.05}O_4$ or $Ce_{0.9}Gd_{0.1}V_{0.95}W_{0.05}O_4$ or $Ce_{0.9}Pr_{0.1}V_{0.95}W_{0.05}O_4$ catalysts. At high temperature, the decline of conversion occurs when the oxidation of ammonia becomes predominant according to Eq. 4.12.

$$2NH_3 + 5/2O_2 = 2NO+3H_2O \text{ (Ammonia oxidation)} \qquad \text{(Equation 4.12)}$$

However, at high temperature, the effect of degree of cerium substitution by the rare earth has a more significant effect on NO conversion. Above 450 °C, the SCR conversion on the parent $CeV_{0.95}W_{0.05}O_4$ remains high (79% NO conversion to N_2) while a drastic loss of the selective reduction of NO to nitrogen is discernible on the doped samples affecting more severely low loaded Gd and Pr samples. Such trend cannot be easily explained at this stage because this behavior can be the conjunction of several parameters, i.e. the nature of acid sites (Brönsted vs. Lewis sites), the redox behavior of vanadates species depending on their degree of dispersion (monomeric vs. polymeric species) and the surface concentration of reactive oxygen species. According to our experimental conditions with O_2 higher than 1-2 vol. % and T>280°C, the kinetic behavior of $Ce_{1-x}RE_xV_{0.95}W_{0.05}O_4$ above 350°C could match with a standard-SCR rate given by Eq. 4.11. A higher coverage of ammonia involved in the SCR could partly explain the highest conversion observed on the aged $CeV_{0.95}W_{0.05}O_4$ samples at 500°C. This explanation seems in relatively good agreement with the atomic W/Ce+RE ratio suggesting a greater formation of strong acid sites $CeV_{0.95}W_{0.05}O_4$ induced by a higher surface tungsten concentration. Regarding the surface concentration of vanadates, only slight variations are discernible on the V/Ce+RE atomic ratio which could not be significant. However, the highest ratio obtained on $CeV_{0.95}W_{0.05}O_4$ could a priori suggests a greater vanadates dispersion. Nevertheless, some limitations are discernible because XPS seems to be not enough sense to explain the difference observed on the selective reduction according to the content of doping RE element. Finally, the ratio Ce^{4+}/Ce^{3+} could originate from the low selectivity through ammonia oxidation thanks to a greater stabilization of Ce^{4+}.

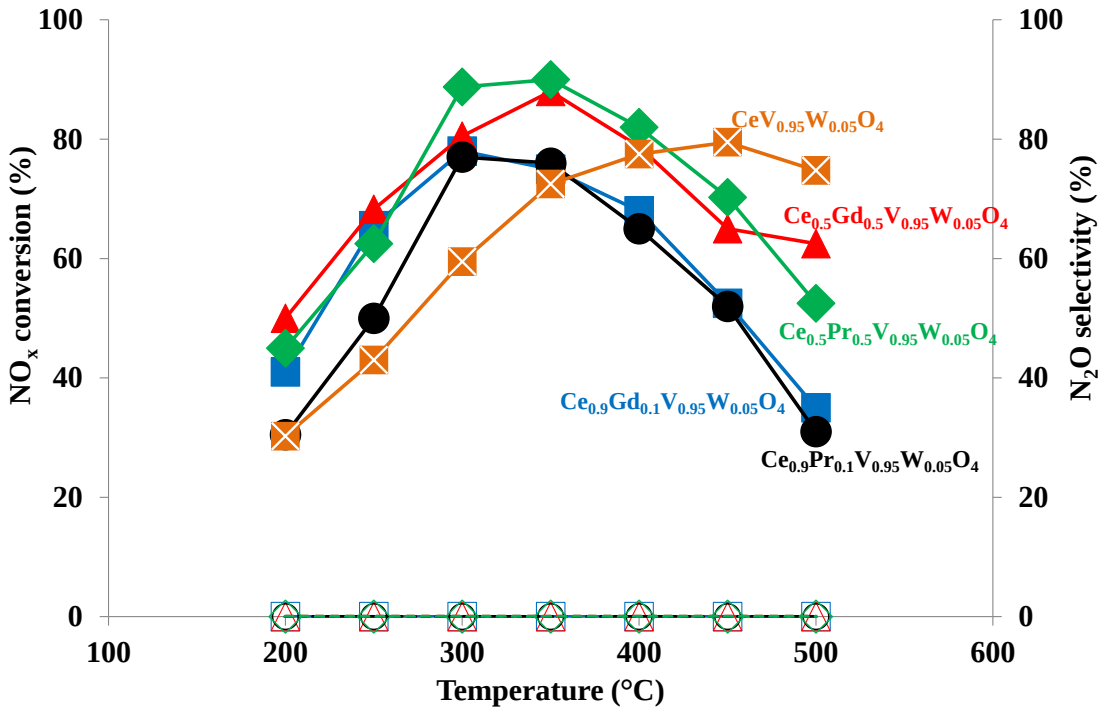

Figure 4.26 – **NO_x conversion (solid lines) and N_2O selectivity (dotted lines) of $Ce_{1-x}RE_xV_{0.95}W_{0.05}O_4$ catalysts in Standard-SCR condition aged at 600°C**

1.4.2 Ammonia-selective catalytic reduction of NO_x to nitrogen in "Fast" condition: $NO/NO_x = 0.5$

The catalytic activity of $Ce_{1-X}RE_XV_{0.95}W_{0.05}O_4$ (X=0.1 and 0.5) samples prepared by hydrothermal method and was tested according to a procedure presented in the previous section. The evolution of Fast-SCR NO_x conversions and N_2O selectivity during the temperature-programmed reaction illustrates the influence of the degree of cerium substitution by rare earth on the NO_x conversion and is presented in Fig 4.27. Under Fast-SCR conditions, an equimolar mixture of NO and NO_2 is introduced into the reactor (Equation 4.13). As expected a sharp enhancement in the SCR performances is noticeable at low temperature with conversion level above 80% in the temperature range 200-400°C. A low formation of N_2O is detected which suggest different reaction pathways involving the formation of nitrates. Accordingly, the weak production of N_2O could be reasonably explained by a partial decomposition of those adsorbed species instead of their reduction.

$$2NH_3+NO+NO_2 = 2N_2+3H_2O \text{ (Fast-SCR)} \qquad \text{(Equation 4.13)}$$

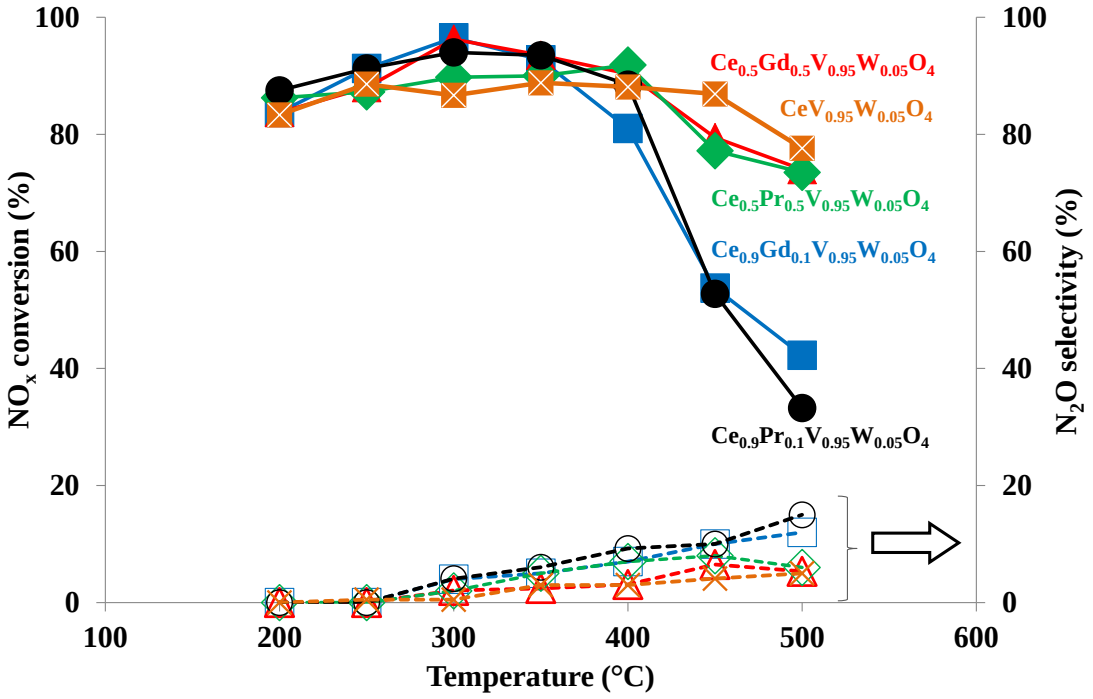

Figure 4.27 – **NO_x conversion (solid lines) and N_2O selectivity (dotted lines) of $Ce_{1-x}RE_xV_{0.95}W_{0.05}O_4$ catalysts in Fast-SCR condition aged at 600°C**

The NO_x conversion of $Ce_{0.9}RE_{0.1}V_{0.95}W_{0.05}O_4$ (X= Pr and Gd) catalysts dramatically decreases between 400–500°C, with the least NO_x conversion of 42% on $Ce_{0.9}Gd_{0.1}V_{0.95}W_{0.05}$ catalyst and 35% on $Ce_{0.9}Pr_{0.1}V_{0.95}W_{0.05}O_4$ catalyst at 500°C. In contrast, $Ce_{0.5}RE_{0.5}V_{0.95}W_{0.05}O_4$ (X=Pr and Gd) catalysts give rise to remarkably higher catalytic performance at the higher temperature. The preferential oxidation of ammonia at high temperature is also delayed on $Ce_{0.5}RE_{0.5}V_{0.95}W_{0.05}O_4$ (X=Pr and Gd) catalysts. The NO_x conversions of $Ce_{0.5}RE_{0.5}V_{0.95}W_{0.05}O_4$ (X=Pr and Gd) catalysts increase from 83% at 200°C to a maximum NO_x conversion of 95% at 400°C and then start to decrease. The NO_x conversion of $Ce_{0.5}RE_{0.5}V_{0.95}W_{0.05}$ (X=Pr and Gd) catalysts decreases and reaches 73% at 500°C. The NO_x conversion of the reference $CeV_{0.95}W_{0.05}O_4$ catalyst is significantly higher than that of the substituted catalysts at high temperature (>450°C). At high temperature, the N_2 selectivity was slowly decreased on all substituted catalysts and reference $CeV_{0.95}W_{0.05}O_4$ catalyst have the

highest N_2 selectivity among the investigated catalysts at 450°C. The $Ce_{0.5}RE_{0.5}V_{0.95}W_{0.05}O_4$ (X=Pr and Gd) catalysts have the higher N_2 selectivity below 300°C comparing to $Ce_{0.9}RE_{0.1}V_{0.95}W_{0.05}O_4$ (X=Pr and Gd) catalysts. Furthermore, the lower N_2 selectivity is observed on $Ce_{0.9}RE_{0.1}V_{0.95}W_{0.05}O_4$ (X=Pr and Gd) catalysts indicating that the deactivation of the $Ce_{0.9}RE_{0.1}V_{0.95}W_{0.05}O_4$ (X=Pr and Gd) originated from the non-selective oxidation of NH_3. As a resume, the in standard-SCR condition still appear in fast-SCR condition on Gd- and Pr-doped samples showing the best performance for the low loaded dopant.

1.4.3 Ammonia-selective catalytic reduction of NO_x to nitrogen in "NO_2" condition: NO/NO_x =3/10

The conversion curves of $Ce_{1-X}RE_XV_{0.95}W_{0.05}O_4$ catalysts under NO_2-SCR conditions after hydrothermal aging at 600°C presented in Fig 4.28. In the presence of an excess of nitrogen dioxide in the reaction mixture, the NO_2-SCR reaction predominates (Eqs 4.14). Usually, this reaction is slower compared to Fast-SCR conditions, especially at low temperatures. But the rate of conversion is higher than those measured in standard-SCR conditions. As a general trend the best catalytic properties are observable on catalysts containing the highest concentration of gadolinium and praseodymium.

$$8NH_3+6NO_2 = 7N_2+12H_2O\ (NO_2\text{-SCR}) \qquad \text{(Equation 4.14)}$$

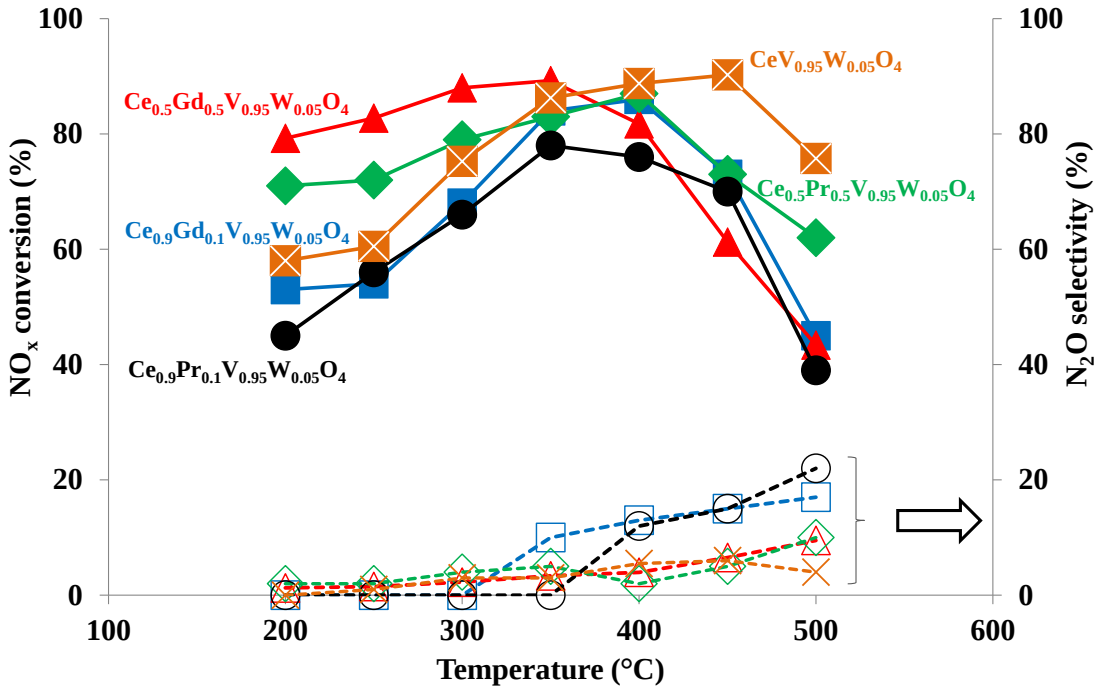

Figure 4.28 – **NO_x conversion (solid lines) and N_2O selectivity (dotted lines) of $Ce_{1-x}RE_xV_{0.95}W_{0.05}O_4$ catalysts in NO_2-SCR condition aged at 600°C**

As previously described, two conversion ranges can be distinguished. For temperatures above 400°C, the influence of the addition of rare earth elements does not appear significant; $CeV_{0.95}W_{0.05}O_4$ reference catalyst is the most active catalyst above 400°C confirming the tendency previously described in fast- and standard conditions. The higher rare earth (X=0.5) loading was advantageous for high NO_x conversion below 400°C in NO_2-SCR condition. As an example, the maximum NO_x conversion of $Ce_{0.5}Gd_{0.5}V_{0.95}W_{0.05}O_4$ at 250 and 300°C is 82% and 88%, respectively, while it is 54% (250°C) and 68% (300°C) for the $Ce_{0.9}Gd_{0.1}V_{0.95}W_{0.05}O_4$ catalyst. At high temperature, N_2 selectivity was slowly decreased for all catalysts and the reference $CeV_{0.95}W_{0.05}O_4$ catalyst has the highest N_2 selectivity among the investigated catalysts at 500°C. Whatever the nature of rare earth, substituted catalyst with X=0.5 significantly improves N_2 selectivity with a lower proportion of N_2O formed compared to $Ce_{0.9}RE_{0.1}V_{0.95}W_{0.05}O_4$ catalyst especially at high temperature.

1.5 Catalytic activity of $Ce_{1-X}RE_XV_{0.95}W_{0.05}O_4$ (RE=Pr and Gd, X=0.1 and 0.5) catalysts after hydrothermal aging at 850°C

1.5.1 Ammonia-selective catalytic reduction of NO_x to nitrogen in "fast" condition: $NO/NO_x = 0.5$

The NO_x conversion profiles as a function of temperature recorded on the $Ce_{1-X}RE_XV_{0.95}W_{0.05}O_4$ catalysts are compared in Fig 4.29. The aging temperature was chosen to simulate a high mileage such as 160000 km [29, 30].

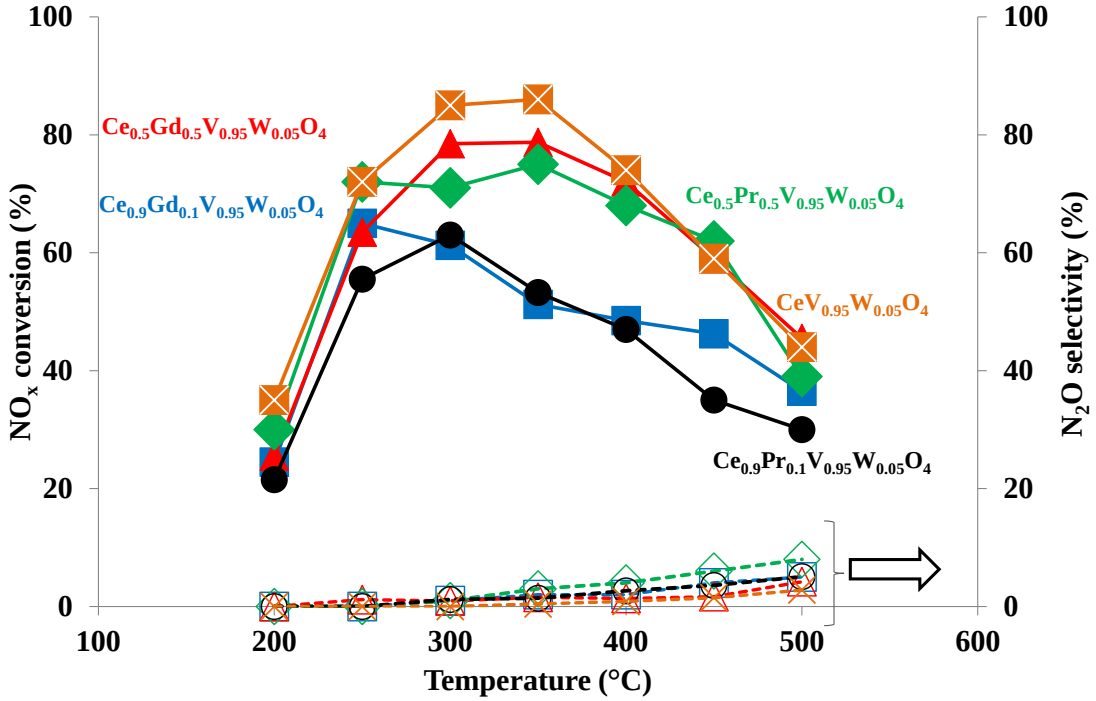

Figure 4.29 – **NO_x conversion (solid lines) and N_2O selectivity (dotted lines) of $Ce_{1-X}RE_XV_{0.95}W_{0.05}O_4$ catalysts in fast-SCR condition aged at 850°C**

As shown, this thermal aging has a strong detrimental effect on the specific surface area. Indeed, all the samples converge to the very low specific surface area in the range 2-3.5 m^2/g. Clearly, the deviations observed on the conversion above 250°C do not match with the weak changes observed on the specific surface area but more probably related to change in the surface composition and the alteration of the redox function which is responsible for the sharp loss of

SCR performances at low temperature. Indeed, at low temperatures, the slower NO to NO_2 oxidation rate can explain the decline in NO to N_2 conversion. The $Ce_{0.5}RE_{0.5}V_{0.95}W_{0.05}O_4$ catalyst aged at 850°C has a much higher NO_x conversion compared to $Ce_{0.9}RE_{0.1}V_{0.95}W_{0.05}O_4$ aged catalyst under the same temperature conditions. As can be seen, the samples aged at 600°C presents a higher performance compared to aged samples at 850°C related to the degradation of the redox function.

At high temperature, thermodynamic constraints must be taken into account. However, the decline in NO_x conversion can also be due to a faster oxidation of ammonia to NO. It can be deduce the following sequence of activity from maximum conversions measured at 300°C: $Ce_{0.9}Gd_{0.1}V_{0.95}W_{0.05}O_4$~$Ce_{0.9}Pr_{0.1}V_{0.95}W_{0.05}O_4$ (63%) < $Ce_{0.5}Pr_{0.5}V_{0.95}W_{0.05}O_4$ (71%) < $CeV_{0.95}W_{0.05}O_4$ (78.5%) < $Ce_{0.5}Gd_{0.5}V_{0.95}W_{0.05}O_4$ (85%). The higher N_2 selectivity is achieved for the substituted catalysts with a degree of substitution equal to 0.5. All samples present low N_2O production in the temperature range of 200 to about 350°C. At high temperature, N_2 selectivity is slowly decreased for all tested catalysts.

1.6 Conclusion

This section reports the behavior of bulk $Ce_{1-X}RE_XV_{0.95}W_{0.05}O_4$ (RE= Pr and Gd, X=0.1 and 0.5) catalysts for the selective reduction of NO_x by ammonia. They were prepared by hydrothermal synthesis and aged at 600°C or 850°C in air containing 10 vol. % H_2O. The series of $Ce_{1-X}RE_XV_{0.95}W_{0.05}O_4$ (RE=Pr and Gd, X=0.1 and 0.5) catalysts were characterized by means of different techniques including XRF, XRD, BET (Brunauer-Emmett-Teller), H_2-TPR, RAMAN, and XPS. This section has underlined the important impact of the rare earth nature and substitution degree on the physico-chemical properties of reference $CeV_{0.95}W_{0.05}O_4$ catalyst.

Interestingly it is found that the heat resistance and the activity of such catalyst compositions may be specifically controlled by applying defined ratios of the Ce and the RE element in the

Ce/RE vanadate, thus providing high stability catalyst with good activity. The zircon-type structure of $REVO_4$ with a segregation of cubic face-centered structure of ceria (CeO_2) is obtained after hydrothermal synthesis without additional calcination step and preserved for unaged and after aging 600°C. Hydrothermal aging at 850°C brings on a significant crystallographic change for cerium oxide that is the appearance of a minority phase attributed to rhombohedric Ce_7O_{12} for all catalysts. It is worthy to be mentioned that the loss of vanadium in the elemental analysis was not observed after aging, which suggested a stronger stabilization of V^{5+} species in $REVO_4$ structure. The studied materials need to have good properties, e.g. high surface area. Rare earth incorporation in $CeV_{0.95}W_{0.05}O_4$ structure slightly improves the texture of the unaged catalysts. After aging at 600°C, a beneficial effect of rare earth is clearly observed; the modified catalysts with a substitution degree of 0.5 possessed of a specific surface area approximately two times greater than that of the $CeV_{0.95}W_{0.05}O_4$ reference catalyst. The insertion of rare earth into the $CeV_{0.95}W_{0.05}O_4$ structure improves the sintering resistance of the $REVO_4$ particles thus limiting the loss of specific surface area. However, the change in specific surface area or surface concentration of species cannot be directly correlated with the change in NO_x conversion underlining the complexity of such a system. The studied catalysts should have high activity, stability, and selectivity in the SCR process. The evolution of vanadium species on the surface would explain the change of NO_x conversion and the N_2 selectivity. The $Ce_{0.5}RE_{0.5}V_{0.95}W_{0.05}O_4$ (Pr and Gd) catalysts have the exposure of more vanadium species on the surface, thus promoting the NH_3-SCR reactions performances. The most active SCR catalysts in activity tests were $Ce_{0.5}RE_{0.5}V_{0.95}W_{0.05}O_4$ (Pr and Gd) catalysts. However, the NO_x conversion of the $CeV_{0.95}W_{0.05}O_4$ reference catalyst is higher than that of substituted catalysts at high temperature. The contribution of the RE to the applicability of such materials to exhaust gas after-treatment relies on first the promotion of NO_x conversion towards low temperature in standard SCR condition, and secondly in its ability to promote thermal stability of the

vanadium-containing catalysts. This is due to the ability of RE to enhance the structural and textural stability of the system. According to the requests in terms of activity/stability, it is therefore possible to optimize the catalyst composition by tuning RE/Ce ratio. The mixed composition $Ce_{0.5}RE_{0.5}V_{0.95}W_{0.05}O_4$ catalysts represent a good trade-off between low-temperature activity and thermal stability required for mobile SCR applications.

2 Catalytic performances of mixed oxides $Ce_{0.5}RE_{0.5}V_{0.95}W_{0.05}O_4$ (RE= Pr, Gd, Tb, and Er) for selective catalytic reduction of NO_x by ammonia

As mentioned in section 1, the replacement of Ce by other ions with a smaller diameter, such as Pr and Gd can enhance the selective catalytic reduction of NO_x by ammonia. This section deals with the catalytic system similar to those studied in the previous section in which cerium substituted by the rare earth element. In this section, we discussed the catalytic performance of $Ce_{0.5}RE_{0.5}V_{0.95}W_{0.05}O_4$ (RE= Pr, Gd, Tb, and Er) catalysts aimed to the conversion NO_x by ammonia, it seems that their properties depend on the nature of the element and in particular on their ionic radius. A group of elements comprising Pr, Gd, Tb, and Er showed excellent resistance to deactivation and high activity after aging compared to $CeV_{0.95}W_{0.05}O_4$ reference catalyst.

2.1 Hydrothermal Synthesis of $Ce_{0.5}RE_{0.5}V_{0.95}W_{0.05}O_4$ (RE= Pr, Gd, Tb, and Er) solids

The samples were prepared by the hydrothermal method; various stages of preparation of the $Ce_{0.5}RE_{0.5}V_{0.95}W_{0.05}O_4$ (RE=Pr, Gd, Tb, and Er) are shown in Fig 4.30. In the same way as the previous part, Na_3VO_4 (99.98 wt% from Sigma-Aldrich) was added to 50 mL of distilled water

under vigorous stirring until complete dissolution. An aqueous solution of nitric acid solution (3 M) was further added drop by drop until the stabilization to pH = 1.8.

Once stabilized, Ce $(NO_3)_3 \cdot 6H_2O$, $(NH_4)_6H_2W_{12}O_{40}.xH_2O$ (meta) 99.99%, RE $(NO_3)_3$. $5H_2O$ (RE=Pr, Gd, Tb, and Er) precursors were precursors were added and dissolved into the vanadium solution. A sodium hydroxide solution (1M) was added dropwise in order to precipitate cerium and vanadium precursors into $Ce_{0.5}RE_{0.5}V_{0.95}W_{0.05}O_4$. The suspension was subsequently treated in a Teflon-lined hydrothermal synthesis autoclave at 180°C for 24 h. $Ce_{0.5}RE_{0.5}V_{0.95}W_{0.05}O_4$ was separated from the aqueous solution by centrifugation, washed abundantly with distilled water and finally with ethanol. $Ce_{0.5}RE_{0.5}V_{0.95}W_{0.05}O_4$ was then dried in air at 80°C for 24 h and catalysts were denoted as unaged solids. The solids were aged in wet atmosphere (10vol% H_2O in air) at 600 or 850°C and are denoted as aged samples.

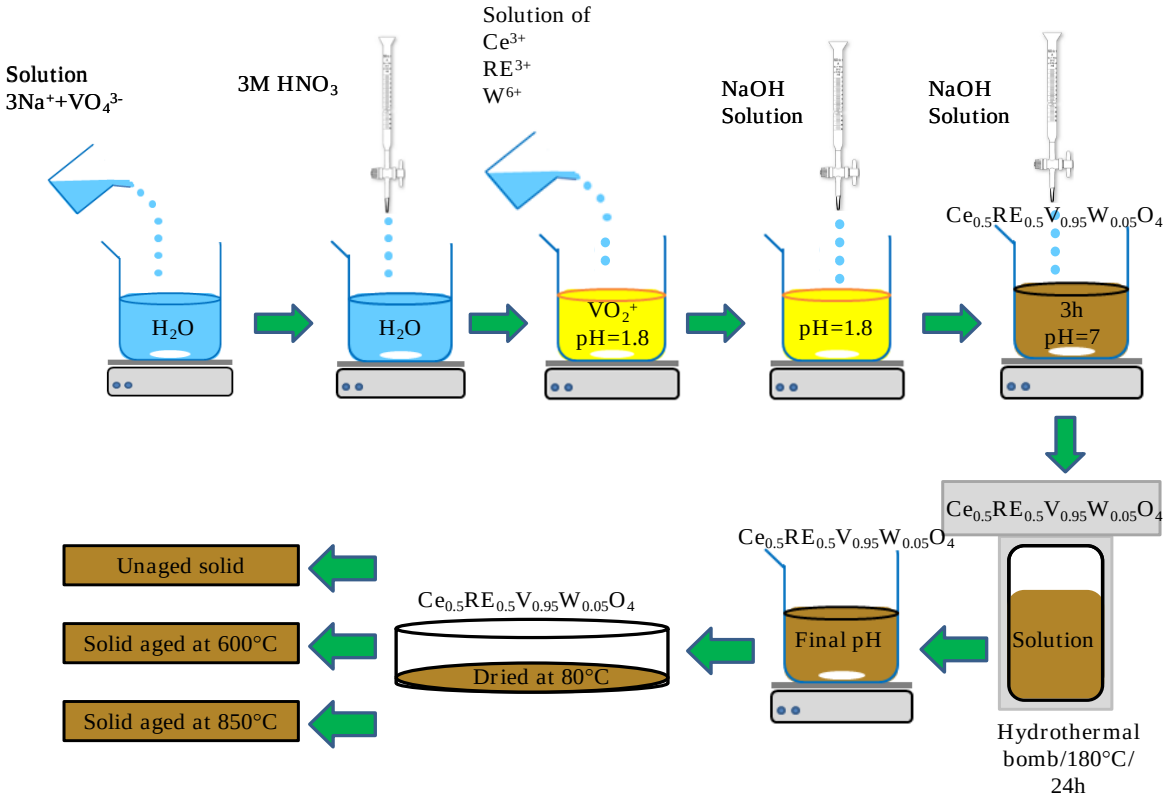

Figure 4.30 – **Steps involved during the hydrothermal synthesis of $Ce_{0.5}RE_{0.5}V_{0.95}W_{0.05}O_4$ (RE= Pr, Gd, Tb, and Er) catalysts**

The bulk chemical compositions of $Ce_{0.5}RE_{0.5}V_{0.95}W_{0.05}O_4$ (RE= Pr, Gd, Tb, and Er) catalysts were assessed by X-ray fluorescence spectrometry (XRF). The value presented in the brackets corresponds to the expected values. The content is expressed as the oxide form for each element so the sum can exceed 100% due to the different oxidation state of some element. However, all samples exhibit an excess of cerium and tungsten. The obtained values likewise confirm vanadium and erbium deficiency. These results also confirm that no loss of elements occurs during aging.

Table 4.6 – **Elemental analysis of $Ce_{0.5}RE_{0.5}V_{0.95}W_{0.05}O_4$ (RE=Pr, Gd, Tb, and Er) catalysts by X-ray fluorescence**

Catalyst	Aging Temperature (°C)	Chemical composition expressed as oxide			
		V_2O_5 (wt. %)	Ce_2O_3 (wt. %)	WO_3 (wt. %)	RE_2O_3 (wt. %)
$Ce_{0.5}Pr_{0.5}V_{0.95}W_{0.05}O_4$	unaged	32.00 (32.20)	34.10 (30.70)	4.90 (2.23)	30.20 (35)
	600	32.00 (32.20)	34.20 (30.70)	5.00 (2.23)	30.00 (35)
	850	32.00 (32.20)	34.40 (30.70)	5.30 (2.23)	30.70 (35)
$Ce_{0.5}Gd_{0.5}V_{0.95}W_{0.05}O_4$	unaged	29.90 (32.20)	33.00 (30.70)	4.50 (2.23)	32.70 (35)
	600	29.90 (32.20)	33.10 (30.70)	4.50 (2.23)	32.60 (35)
	850	29.80 (32.20)	33.40 (30.70)	4.60 (2.23)	32.10 (35)
$Ce_{0.9}Tb_{0.5}V_{0.95}W_{0.05}O_4$	unaged	31.00 (32.20)	31.00 (30.70)	4.30 (2.23)	33.00 (35)
	600	31.00 (32.20)	31.60 (30.70)	4.40 (2.23)	32.50 (35)
	850	30.50 (32.20)	32.00 (30.70)	4.50 (2.23)	32.00 (35)
$Ce_{0.5}Er_{0.5}V_{0.95}W_{0.05}O_4$	unaged	30.30 (32.20)	31.00 (30.70)	4.30 (2.23)	34.50 (35)
	600	30.50 (32.20)	31.10 (30.70)	4.30 (2.23)	34.10 (35)
	850	30.10 (32.20)	31.30 (30.70)	4.00 (2.23)	34.50 (35)

2.2 Bulk/Structural properties

2.2.1 X-ray diffraction

2.2.1.1 Unaged solids

The XRD diffractograms of the unaged $Ce_{0.5}RE_{0.5}V_{0.95}W_{0.05}O_4$ (RE=Pr, Gd, Tb, and Er) samples are shown in Fig 4.31, in which the relevant reflections are assigned to crystalline phases.

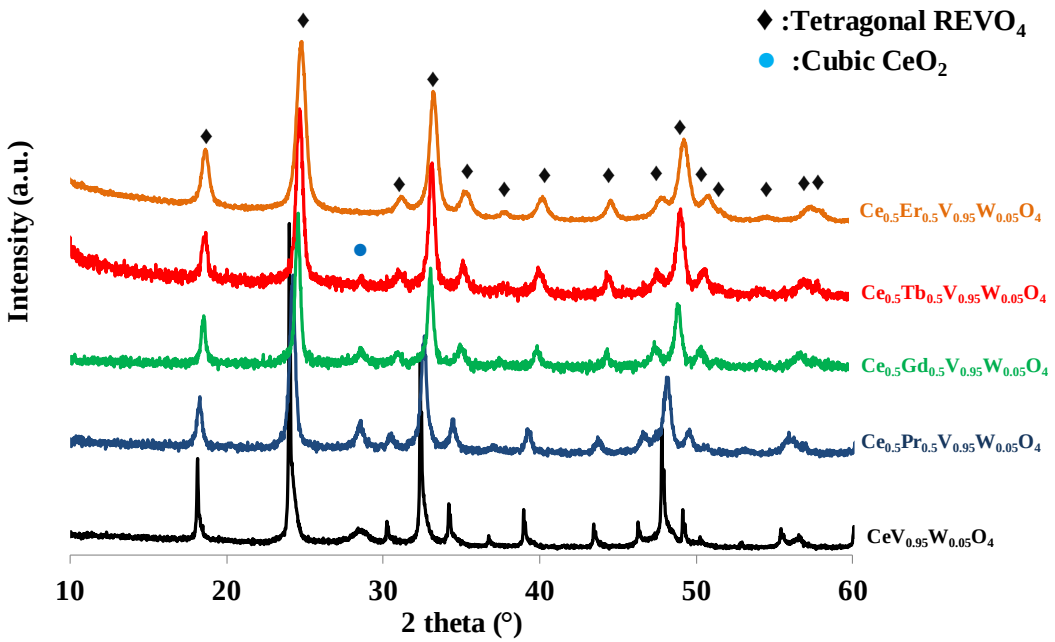

Figure 4.31 – **Crystallographic structure of unaged $Ce_{0.5}RE_{0.5}V_{0.95}W_{0.05}O_4$ (RE=Pr, Gd, Tb, and Er) catalysts**

The tetragonal $REVO_4$ (RE=Pr, Gd, Tb, and Er) crystallographic phase predominates over all samples. The diffraction lines characteristic of the cubic CeO_2 phase is also distinguished except for $Ce_{0.5}Er_{0.5}V_{0.95}W_{0.05}O_4$ catalyst. A correlation can be established between the 2θ values and the position of the rare earth in the periodic table (Fig 4.32). This displacement could reflect the insertion of Rare Earth (RE) in the $CeV_{0.95}W_{0.05}O_4$ structure. Along with decreasing ionic radius from Pr^{3+} to Er^{3+}, 2θ values increase for unaged and aged catalysts. In fact, the processes involved during aging could be more complex as underlined by the absence of displacement of the lines at values 2θ = 24.00° for aged $Ce_{0.5}Pr_{0.5}V_{0.95}W_{0.05}O_4$ and $Ce_{0.5}Gd_{0.5}V_{0.95}W_{0.05}O_4$ catalysts at 850°C. The absence of displacement on catalysts aged at 850°C could, therefore, be associated with the rare earth extraction from the structure.

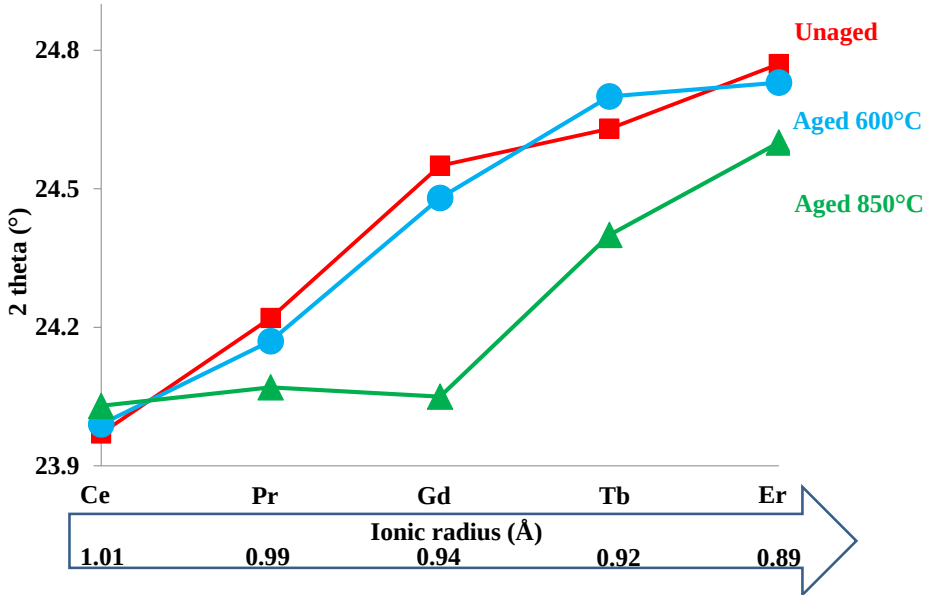

Figure 4.32 – **2 theta (°) according to the RE (RE=Pr, Gd, Tb, and Er) nature after synthesis and aging**

2.2.1.2 Solids Aged at 600°C

The powder diffractograms recorded on the catalysts obtained after aging at 600°C in a wet atmosphere (10% H_2O diluted in air) of selected and reference samples reported in Fig 4.33. $Ce_{0.5}RE_{0.5}V_{0.95}W_{0.05}O_4$ catalysts retain the tetragonal $REVO_4$ structure and the relative intensities of the diffraction peaks as for CeO_2. Minor crystalline phase segregation in the form of cubic CeO_2 is observed for the $Ce_{0.5}Er_{0.5}V_{0.95}W_{0.05}O_4$ catalyst at $2\theta = 28.62°$ that it did not appear for unaged $Ce_{0.5}Er_{0.5}V_{0.95}W_{0.05}O_4$ catalyst. Displacement of XRD peaks for the catalysts aged at 600°C (Fig 4.32) still confirms that decreasing rare earth ionic radius from Pr^{3+} to Er^{3+} may reflect cerium substitution by rare earth in the $REVO_4$ tetragonal lattice. In other words, it seems obvious, that no structural destabilization is induced by thermal aging related to signification phase segregation.

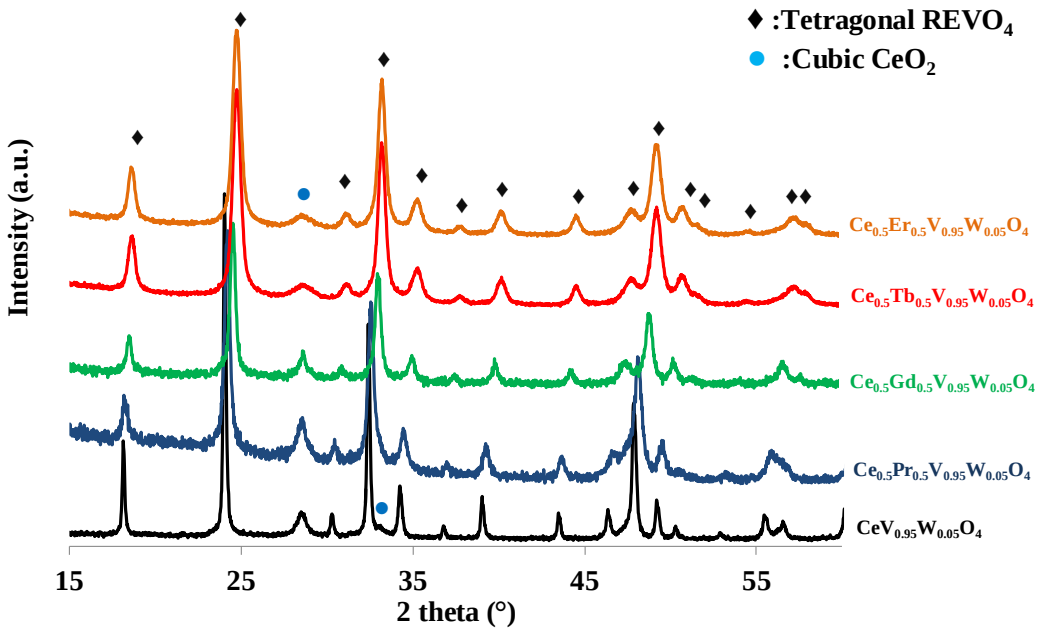

Figure 4.33 – **Crystallographic structure of catalysts aged 600°C $Ce_{0.5}RE_{0.5}V_{0.95}W_{0.05}O_4$ (RE=Pr, Gd, Tb and Er) catalysts**

2.2.1.3 Solids Aged at 850°C

Hydrothermal aging at 850°C brings on the significant crystallographic change that is the appearance of a minority phase attributed to rhombeodric Ce_7O_{12} (Fig 4.34). As mentioned previously, the segregation of Ce_7O_{12} phase is not necessarily helpful in NH_3-SCR, Ce_7O_{12} possess pairs of anionic oxygen vacancies on the axis (Fig 4.6). Aged catalysts at 850°C present the sharp and narrow peaks indicative of the highly crystalline material. In addition, one can observe significant deviations on the plot 2θ vs. ionic radius compared to unaged at aged samples at moderate temperature (600°C) which suggests that extraction of praseodymium and gadolinium would occur more extensively such behavior being less pronounced on erbium having the lowest ionic radius and then being more stabilized inside the zircon-type structure.

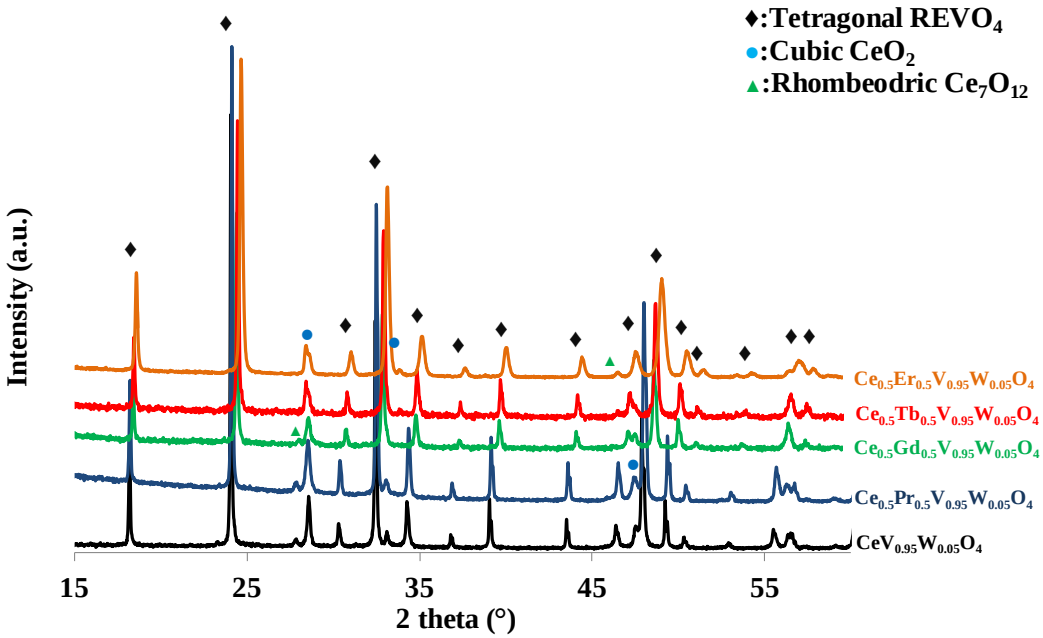

Figure 4.34 – **Crystallographic structure of catalysts aged 850°C $Ce_{0.5}RE_{0.5}V_{0.95}W_{0.05}O_4$ (RE=Pr, Gd, Tb, and Er) catalysts**

The influence of cerium substitution by the rare earth on crystallite diameter presents in Table 4.6. The crystallite diameter decrease with decreasing the ionic radius from Pr^{3+} to Er^{3+} for catalysts after synthesis and hydrothermal aging. Er-containing catalyst has the lowest crystallite size (11 nm) which is in accordance with the highest specific surface area (Table 4.8). After aging, the increase in the crystallite size of $REVO_4$ is delayed by 2 times compared to the unsubstituted $CeV_{0.95}W_{0.05}O_4$ catalyst. The impact of the substitution of Ce by RE on the crystallite diameter is visible for unaged and aged catalysts. The more ionic radius decreases from Pr^{3+} to Er^{3+}, the smaller the crystallite size is. By attaining the maximum aging temperature of 850°C, it has been shown that the presence of rare earth inhibits the sintering process of CeO_2 and $REVO_4$ crystallites. It is generally accepted that lower aging temperature allows the lower crystallite size and the higher specific surface areas and thereby may improve the catalytic activity of the catalyst.

Table 4.6 – **Influence of RE substitution and hydrothermal aging on the crystallite diameter of $REVO_4$ and CeO_2**

$Ce_{0.5}RE_{0.5}V_{0.95}W_{0.05}O_4$	Ionic radius (Å)	Aging temperature (°C)	$REVO_4$ crystallite diameter (nm)	CeO_2 crystallite diameter (nm)
RE = Ce^{3+}	1.01	Unaged	22	10
		600	54	14
		850	112	40
RE = Pr^{3+}	0.99	Unaged	20	19
		600	21	17
		850	50	36
RE = Gd^{3+}	0.94	Unaged	18	20
		600	20	22
		850	40	37
RE = Tb^{3+}	0.92	Unaged	16	33
		600	19	27
		850	43	29
RE = Er^{3+}	0.89	Unaged	11	-
		600	14	10
		850	43	25

2.2.2 Raman spectroscopy

Figs.4 (35)–(37) correspond to Raman spectra recorded on fresh and then aged at 600°C and 850°C. Raman scattering studies have made a number of important contributions to interpreting and understanding some of the results of the various studies noted previously. As previously discussed, the bands at 774 and 847 cm^{-1} coincide with the anti-symmetric (B_{1g}) and symmetric (A_{1g}) stretching of VO_4^{3-} tetrahedrons, while B_{1g} and A_{1g} bending modes are presented at 460 and 367 cm^{-1}, respectively. The peak at 254 cm^{-1} corresponds to the B_{2g} bending mode of the VO_3^{4-} tetrahedrons. The external mode of $REVO_4$ vibration appears below 250 cm^{-1}. The absence of the Raman band in the region 800–1000 cm^{-1} characterizing V_2O_5 is remarkable emphasizing the structural stability of $REVO_4$. The Raman band at 460 cm^{-1} corresponding to the stretching vibration of the Ce-O bond in CeO_2 is also observable. After aging, $Ce_{0.5}Er_{0.5}V_{0.95}W_{0.05}O_4$ catalyst shows a segregation of a phase corresponding to Er^{3+} at 700cm^{-1}.

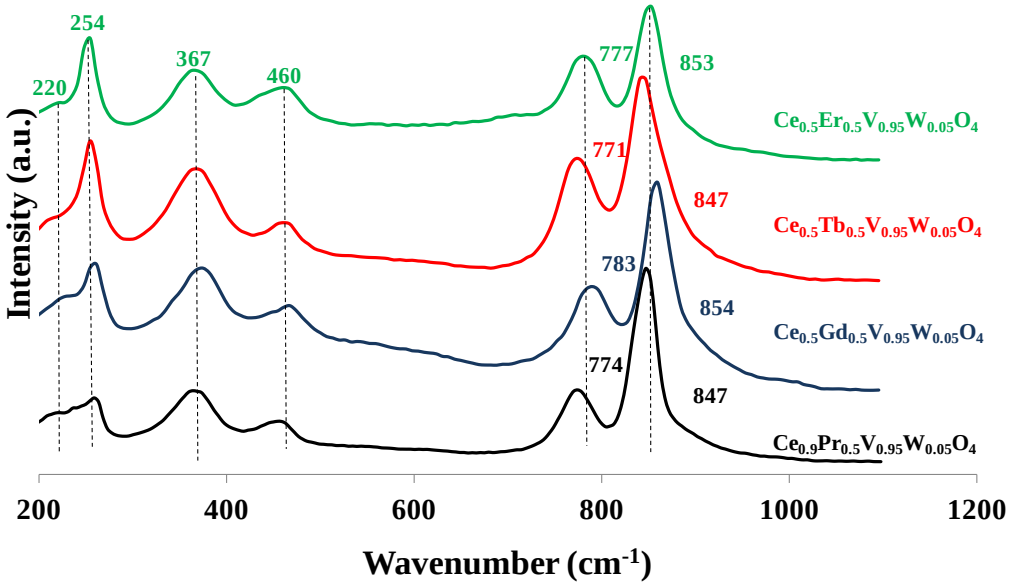

Figure 4.35 – **Raman structure of unaged $Ce_{0.5}RE_{0.5}V_{0.95}W_{0.05}O_4$ (RE=Pr, Gd, Tb and Er) catalysts**

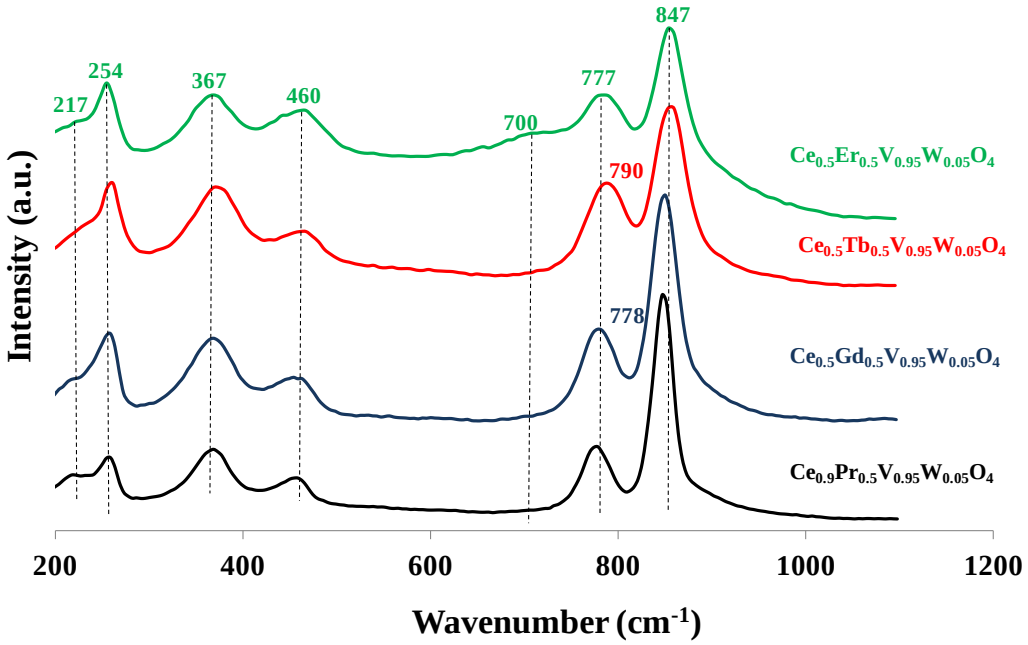

Figure 4.36 – **Raman structure of $Ce_{0.5}RE_{0.5}V_{0.95}W_{0.05}O_4$ (RE=Pr, Gd, Tb and Er) catalysts aged at 600°C**

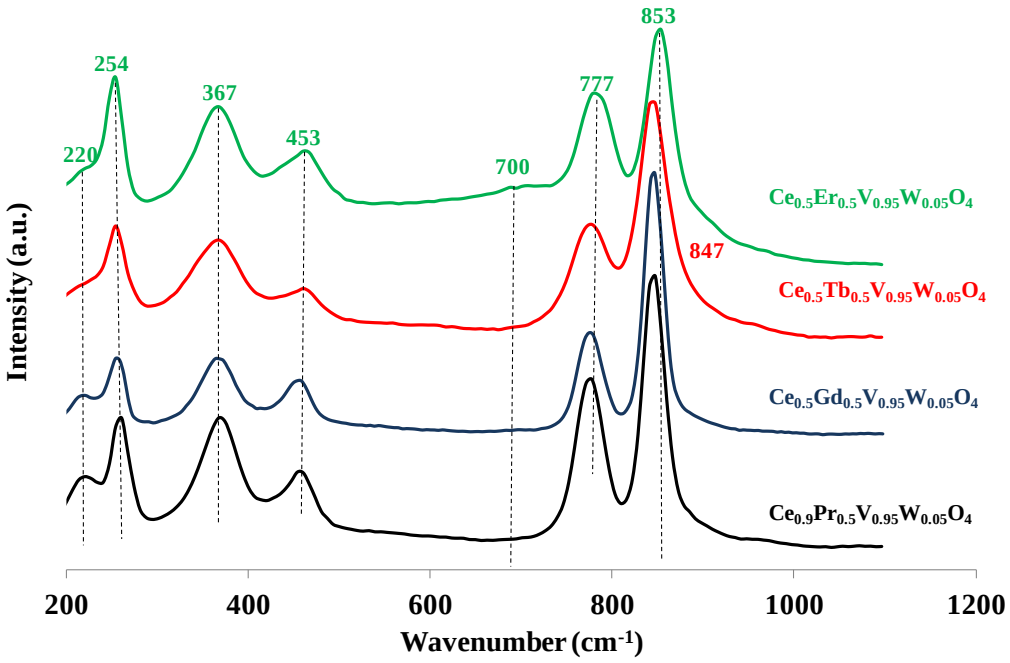

Figure 4.37 – **Raman structure of $Ce_{0.5}RE_{0.5}V_{0.95}W_{0.05}O_4$ (RE=Pr, Gd, Tb and Er) catalysts aged at 850°C**

2.2.3 Temperature-programmed reduction (H_2-TPR)

2.2.3.1 Unaged

The reducibility of the $Ce_{0.5}RE_{0.5}V_{0.95}W_{0.05}O_4$ (RE= Pr, Gd, Tb, and Er) catalysts has been investigated by H_2-TPR (Fig 4.38). The TPR reduction profiles are characterized by 2 step processes. Strong peak positioned within the range of 785–821°C, in accordance with the previous studies, can be attributed to the reduction of V^{5+} in vanadate to V^{3+}. The theoretical atomic ratio of H/V is equal to 2 (Table 4.7). This has been confirmed by a comparison between the theoretical and measured H_2 consumption, as reported in Table 4.7. By decreasing ionic radius from praseodymium to erbium, the main reduction peak shifts to the higher temperatures. This trend does not seem to be related to crystallite size, which steadily decreases by decreasing the ionic radius from praseodymium to erbium. As shown in Table 4.7 the H_2 consumption (integrated in the temperature range of 700-1000°C) of the $Ce_{0.5}Er_{0.5}V_{0.95}W_{0.05}O_4$ catalyst is lower than the other substituted catalysts. Regarding the H_2-consumption, Tb-containing

catalyst presents a higher reducibility. The small TPR signal which can be detected at 520–596°C might likely be attributed to the reduction of traces of surface vanadium species. On the other hand, this broad and weak contribution could reflect the reduction of surface Ce^{4+} species to Ce^{3+}, which is difficult to be distinguished due to the similar reduction temperature. Unaged catalysts show a low hydrogen consumption at low temperature (T<600°C). Additionally, over the Tb-containing catalyst reduction peak, is possible to observe a shoulder at the higher temperature, which can be associated with the surface heterogeneity of the sample [31]. Furthermore, this small shoulder peak appeared on the high-temperature side of the dominant reduction peak, which may be attributed to the reduction of terbium species (Tb^{4+} to Tb^{3+}) [19, 31].

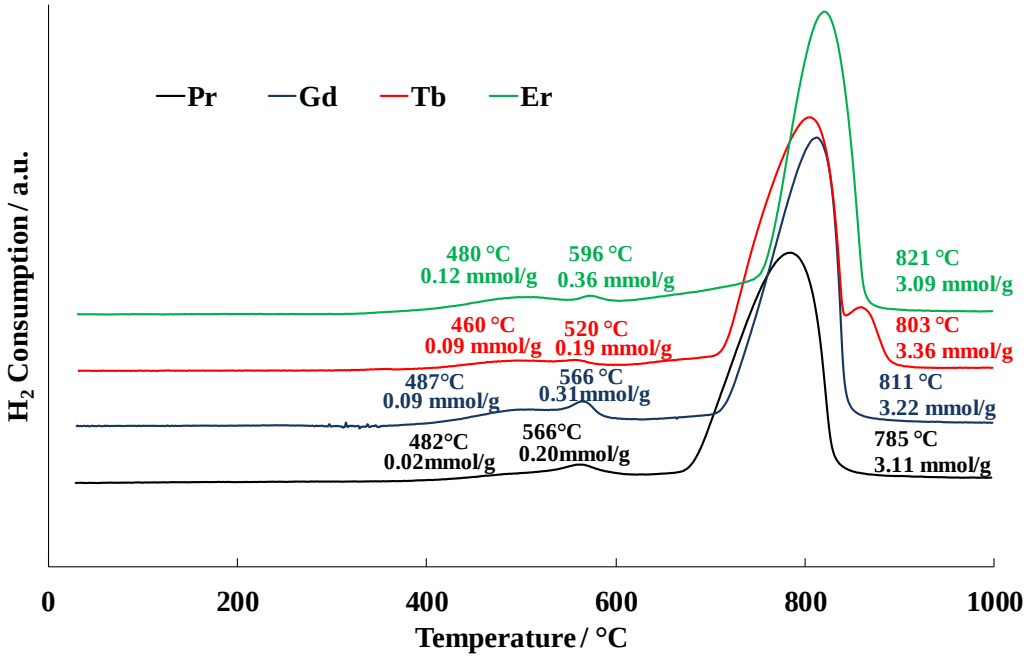

Figure 4.38 – **H_2-TPR of unaged $Ce_{0.5}RE_{0.5}V_{0.95}W_{0.05}O_4$ (RE=Pr, Gd, Tb, and Er) catalysts**

2.2.3.2 Solids Aged at 600°C

As previously observed for unaged catalysts, hydrogen is mainly consumed above 600°C corresponding to the reduction of V^{5+} to V^{3+}. The values of the H/V atomic ratios calculated from the quantities of consumed hydrogen equal to 1.9 and 2.0 (Table 4.7) are in agreement

with the reduction of $CeVO_4$ to $CeVO_3$. After aging at 600°C, the $Ce_{0.5}Tb_{0.5}V_{0.95}W_{0.05}O_4$ shoulder disappeared at the higher temperature. This feature can be related to the structural modifications induced by aging. This main peak shifts to high temperature while the ionic radius decreases, implying that the $Ce_{0.5}Pr_{0.5}V_{0.95}W_{0.05}O_4$ catalyst has the best redox properties. The reducibility (H_2-consumption) of the substituted catalyst is enhanced only for Pr-containing catalyst compared to $CeV_{0.95}W_{0.05}O_4$ catalyst. By decreasing ionic radius, H_2-TPR curves reveals a decrease in H_2-consumption. The peaks with a low intensity in the temperature range of 574–594°C previously attributed to the reduction of surface species V^{5+}. The surface V^{5+} reduction peak of the catalysts was very weak indicating that the number of surface vanadium species was very small but more reducible than V^{5+} in $CeVO_4$ structure. The evolution of vanadium species on the surface would lead to a change of NO_x conversion and possibly of N_2 selectivity. The Er-containing catalyst causes the exposure of more vanadium species on the surface, thus promoting the NH_3-SCR reactions performances based on H_2-TPR measurements. This catalyst possessed the highest quantity of surface species V^{5+} with the lowest crystallite diameter of the support $REVO_4$.

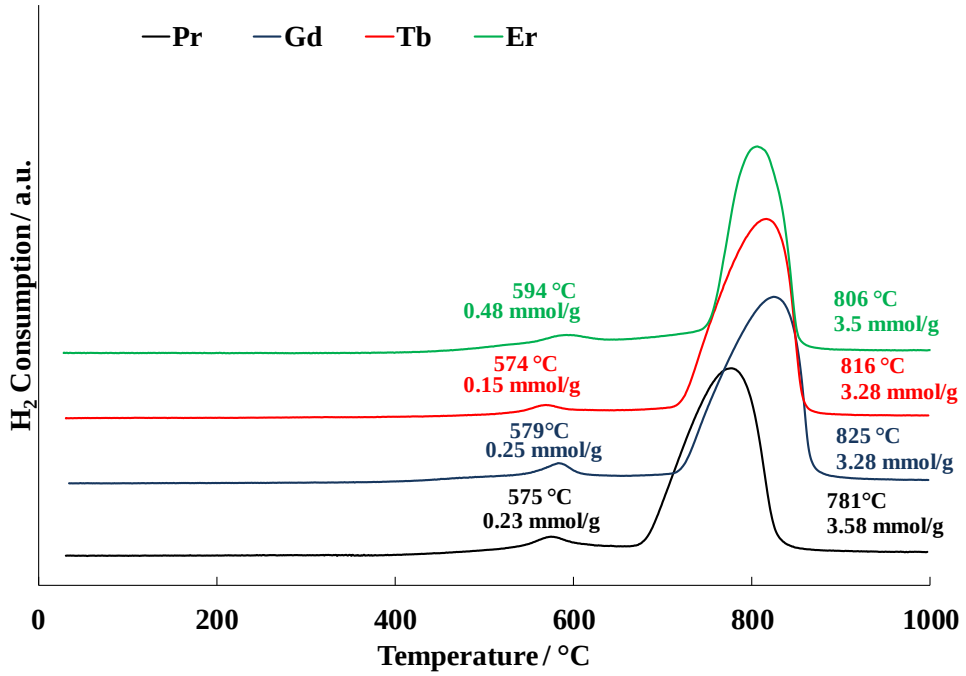

Figure 4.39 – **H_2-TPR of $Ce_{0.5}RE_{0.5}V_{0.95}W_{0.05}O_4$ (RE=Pr, Gd, Tb, and Er) catalysts aged at 600°C**

2.2.3.3 Solids Aged at 850°C

The H_2-TPR profiles obtained for the aged $Ce_{0.5}RE_{0.5}V_{0.95}W_{0.05}O_4$ (RE= Pr, Gd, Tb, and Er) catalysts are presented in Fig 4.40. Aged $Ce_{0.5}RE_{0.5}V_{0.95}W_{0.05}O_4$ (RE=Pr, Gd, Tb, and Er) catalyst showed only a single reduction peak at around 866–902°C. The reduction peaks correspond to the reduction of V^{5+} from $ReVO_4$. The V^{5+} species previously observed at low temperature completely disappeared after aging at 850°C. The lack of observation of this reduction peak for aged catalysts at 850°C could be associated with the conjunction of several factors. It can be due to the low specific surface area (<4m^2 / g) of catalysts after aging, the agglomeration of monomeric vanadium species by getting large V_2O_5 clusters or a loss of active element by volatilization at high temperature. H/V atomic ratio, calculated from the quantities of hydrogen consumed (Table 4.7) that confirmed the large peak around 850°C correspond to V^{5+} to V^{3+} reduction of the bulk oxide. As observed, the highest H_2 consumption occurs only for the Tb-containing catalyst and is associated with the lowest reduction temperature.

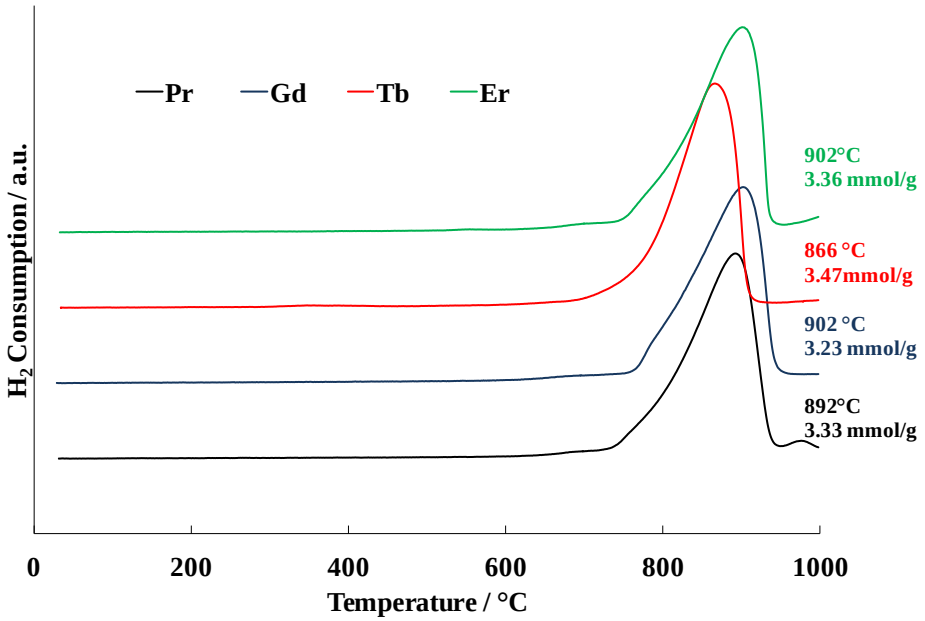

Figure 4.40 – **H_2-TPR of $Ce_{0.5}RE_{0.5}V_{0.95}W_{0.05}O_4$ (RE=Pr, Gd, Tb and Er) catalysts aged at 850°C**

Table 4.7 – **H_2-TPR results of $Ce_{1-x}RE_xV_{0.95}W_{0.05}O_4$ (X=0.1 and 0.5; RE=Pr and Gd); (70mg, 50ml min^{-1})**

Catalyst	Aging temperature (°C)	H_2 consumption [a] (mmol g^{-1})	H/V	T_{max} reduction peaks (°C)
$CeV_{0.95}W_{0.05}O_4$	unaged	3.32	2.00	809
	600	3.54	2.00	845
	850	3.78	2.10	890
$Ce_{0.5}Pr_{0.5}V_{0.95}W_{0.05}O_4$	unaged	3.11	1.90	785
	600	3.58	2.10	781
	850	3.33	2.00	892
$Ce_{0.5}Gd_{0.5}V_{0.95}W_{0.05}O_4$	unaged	3.22	1.90	811
	600	3.28	1.90	825
	850	3.23	1.90	902
$Ce_{0.9}Tb_{0.5}V_{0.95}W_{0.05}O_4$	unaged	3.36	2.00	803
	600	3.28	2.00	816
	850	3.47	2.10	866
$Ce_{0.5}Er_{0.5}V_{0.95}W_{0.05}O_4$	unaged	3.09	1.90	821
	600	3.50	2.10	806
	850	3.36	2.00	902

[a] Consumption integrated in the temperature range of 700-1000°C

2.3 Surface characterizations

2.3.1 Specific surface area

The experimental and theoretical values of the specific surface area calculated from the crystallite diameter of $REVO_4$ from XRD analysis and experimental specific surface area are presented in Table 4.8. The experimental specific surface area is determined by physical adsorption of nitrogen on the surface of the catalysts and by calculating the amount of adsorbate gas corresponding to a monomolecular layer on the surface.

Along with decreasing ionic radius from Pr^{3+} to Er^{3+}, high specific surface area (61-118 m^2/g) was obtained for the series of unaged $Ce_{0.5}RE_{0.5}V_{0.95}W_{0.05}O_4$ catalysts. Aging at 600°C induces a surface area loss for all catalysts. After aging at 600°C, the insertion of rare earth to the catalyst structure has prevented the decrease of the surface area compared to the reference $CeV_{0.95}W_{0.05}O_4$ catalyst. It is therefore obvious that the insertion of rare earth to the $CeV_{0.95}W_{0.05}O_4$ structure improves the sintering resistance of the $REVO_4$ particles (XRD) thus limiting the specific surface area loss. The observed difference between the experimental and theoretical surface can be explained by the increase of $REVO_4$ crystallite size and due to the agglomeration of catalysts aged at 600°C. Further aging at 850°C causes a major surface area loss for all catalysts owing to the thermal sintering. At 850°C, aging causes the strong divergences between experimental and theoretical surface area.

Table 4.8 – **Influence of cerium substitution by rare earth and hydrothermal aging on the specific surface area**

$Ce_{0.5}RE_{0.5}V_{0.95}W_{0.05}O_4$	Ionic radius (Å)	Aging temperature (°C)	Experimental specific surface area S_{exp} ($m^2.g^{-1}$)	Theoretical specific surface area S_{th} ($m^2.g^{-1}$)
RE = Ce^{3+}	1.01	Unaged	55	60
		600	18	23
		850	2	12
RE = Pr^{3+}	0.99	Unaged	64	63
		600	38	60
		850	3	25
RE = Gd^{3+}	0.94	Unaged	61	70
		600	41	63
		850	3.5	32
RE = Tb^{3+}	0.92	Unaged	72	76
		600	49	66
		850	4.5	28
RE = Er^{3+}	0.89	Unaged	118	106
		600	58	86
		850	4.5	28

S_{th} specific surface area calculated from the size of cubic crystallites $S_{th}=6/\rho D_\rho$

2.3.2 X-ray photoelectron spectroscopy (XPS)

X-ray photoelectron spectroscopy (XPS) is a powerful method, capable of determining the surface chemical composition of a substrate. Furthermore, XPS can distinguish the oxidation states of a sample and quantify its atomic content. The atomic percentage determined by XPS is exposed in Table 4.9. Ce 3d XPS region contains up to 10 peaks originated from different Ce oxidation states as previously illustrated in Figure 4.15. From the integration of the different components, it is therefore possible to estimate the Ce^{4+}/Ce^{3+} ratio (Table 4.9). The appearance of the photopeak and the values obtained for the Ce^{4+}/Ce^{3+} ratio show the predominance of Ce^{+3} for all catalysts, which corroborates the presence of the $REVO_4$ phase after hydrothermal synthesis. On the other hand, the hydrothermal aging causes an increase in the relative concentration of Ce^{4+}, for $Ce_{0.9}RE_{0.5}V_{0.95}W_{0.05}O_4$ catalysts (RE= Pr, Gd, Tb, and Er) except for $Ce_{0.9}Tb_{0.5}V_{0.95}W_{0.05}O_4$ for which Ce^{+3} predominates after aging.

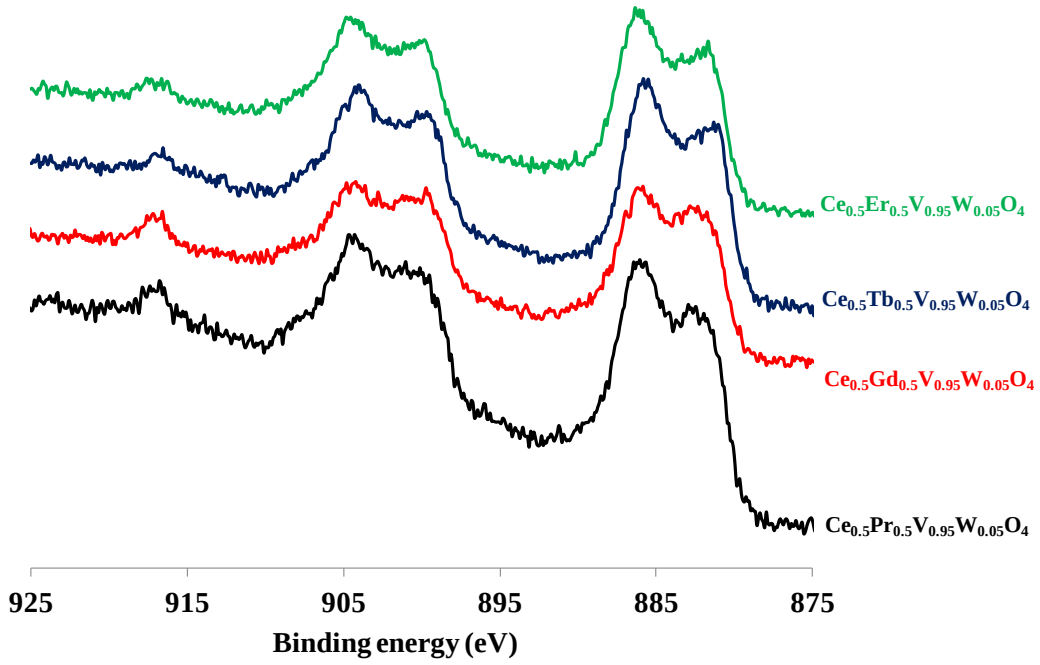

Figure 4.41 – **XPS Spectra of Ce 3d core level of the unaged $Ce_{0.5}RE_{0.5}V_{0.95}W_{0.05}O_4$ (RE=Pr, Gd, Tb, and Er) catalysts**

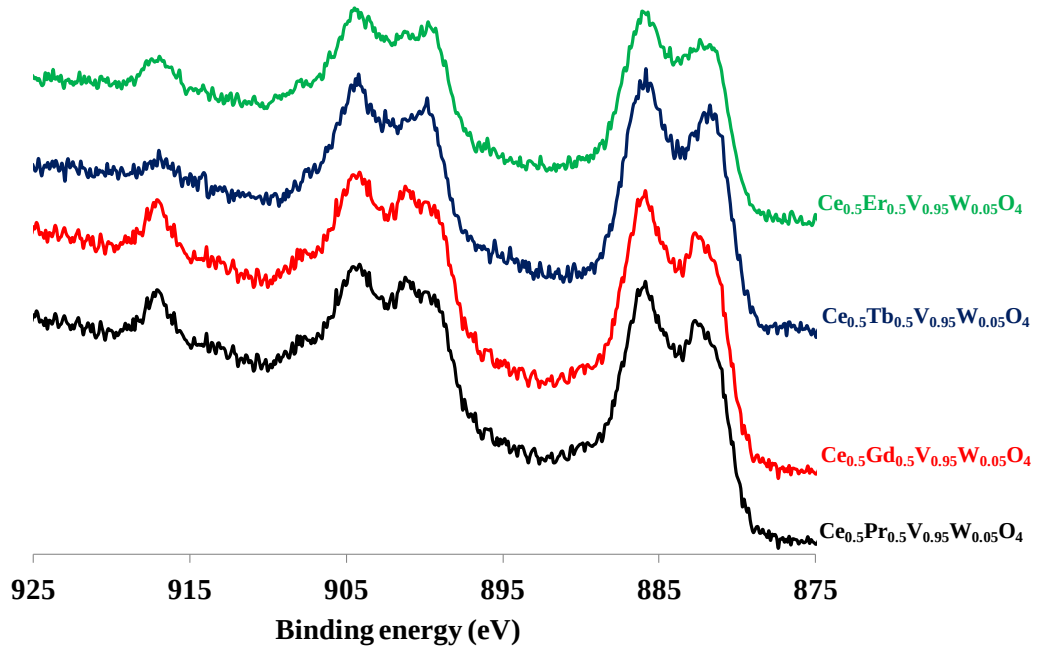

Figure 4.42 – **XPS Spectra of Ce 3d core level of the $Ce_{0.5}RE_{0.5}V_{0.95}W_{0.05}O_4$ (RE=Pr, Gd, Tb, and Er) catalysts aged at 600°C**

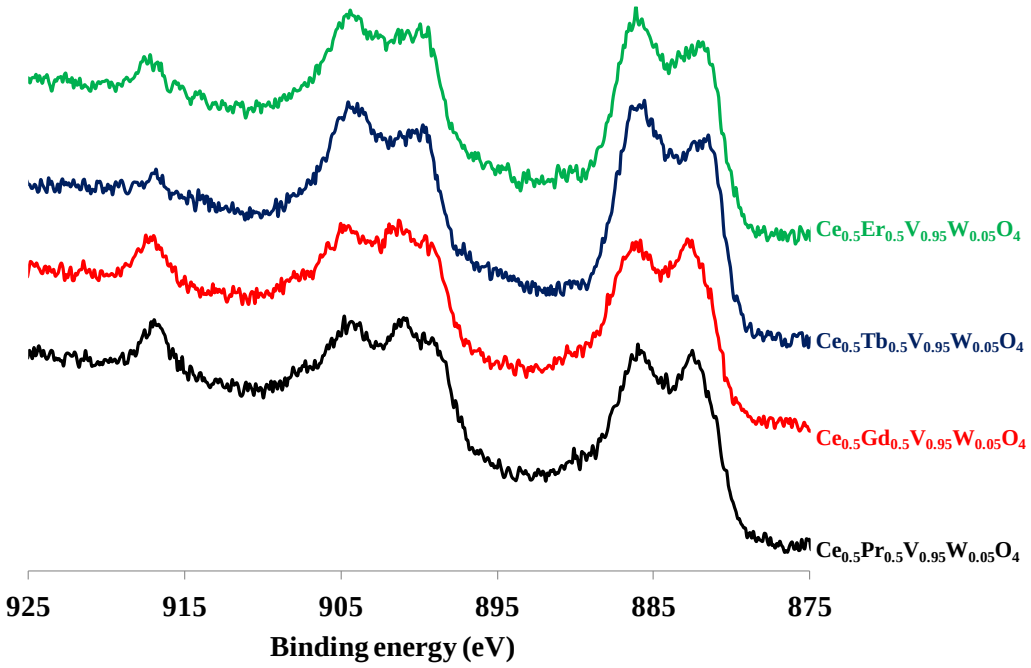

Figure 4.43 – **XPS Spectra of Ce 3d core level of the $Ce_{0.5}RE_{0.5}V_{0.95}W_{0.05}O_4$ (RE=Pr, Gd, Tb, and Er) catalysts aged at 850°C**

The Tb 4d spectra for Tb-containing catalysts are presented in Fig 4.44 and 45. The observed spectrum comprised of a very broad photopeak indicating the multiple splitting in the 4d band [18,19]. The comparison of XPS data with the corresponding data reported in the literature [7–11], revealed that terbium Tb exists in the mixed oxidation state. The spectral lines in the range 145.4 eV to 148.3 eV arises from Tb^{3+} while those in the range 151.7 eV to 154.8 eV from Tb^{4+}. The ratio of Tb^{4+}/Tb^{3+} for unaged, aged at 600°C and aged at 850°C is equal to 1.66, 1.67 and 1.66 respectively. The Tb^{4+}/Tb^{3+} ratio shows the predominance of Tb^{4+} and this ratio is approximately the same for unaged and aged catalysts.

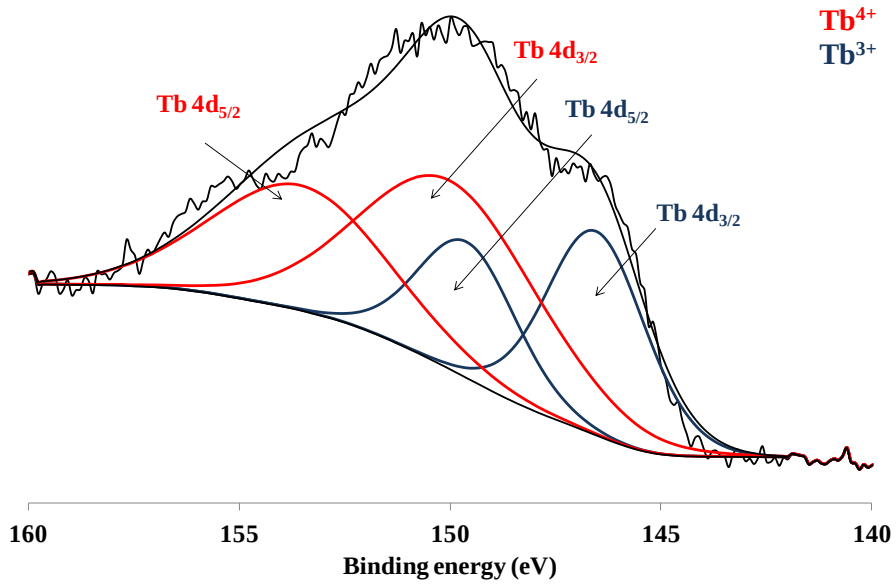

Figure 4.44 – **Fitted XPS Spectra of Tb 4d core level of the unaged $Ce_{0.5}Tb_{0.5}V_{0.95}W_{0.05}O_4$**

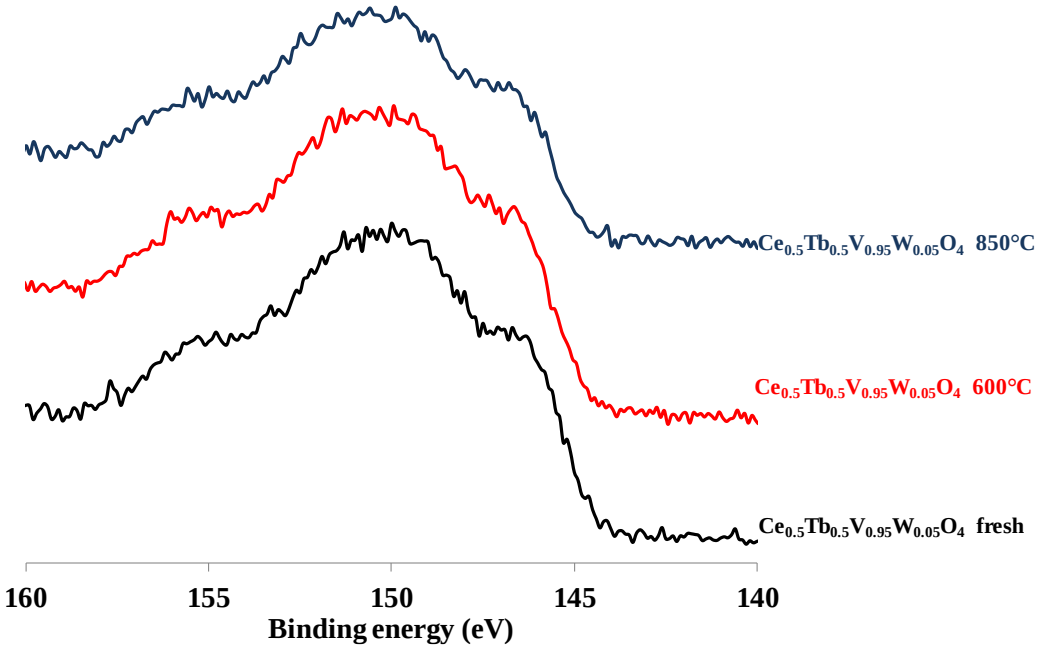

Figure 4.45 – **XPS Spectra of Tb 4d core level of the $Ce_{0.5}Tb_{0.5}V_{0.95}W_{0.05}O_4$ catalysts**

XPS analyses of Pr 3d and Gd 4d already presented in Fig 4.19 and 4.20 in the last section. The Er 4d spectra show a doublet peak which appears at binding energy 168.34 and 170.54 eV corresponding to Er $4d_{5/2}$ and Er $4d_{5/2}$ respectively along with satellite peaks (at binding energy

174, 176.45 and 182.25 eV), which is similar to pure Er_2O_3 in shape and peak position [12–16]. Evolution of the Er 4d core-level spectra as a function of aging temperatures is shown in Fig 4.46. All the samples show similar spectra as the Er_2O_3 reference sample, which indicates that Er ions possess dominantly the +3 valence state.

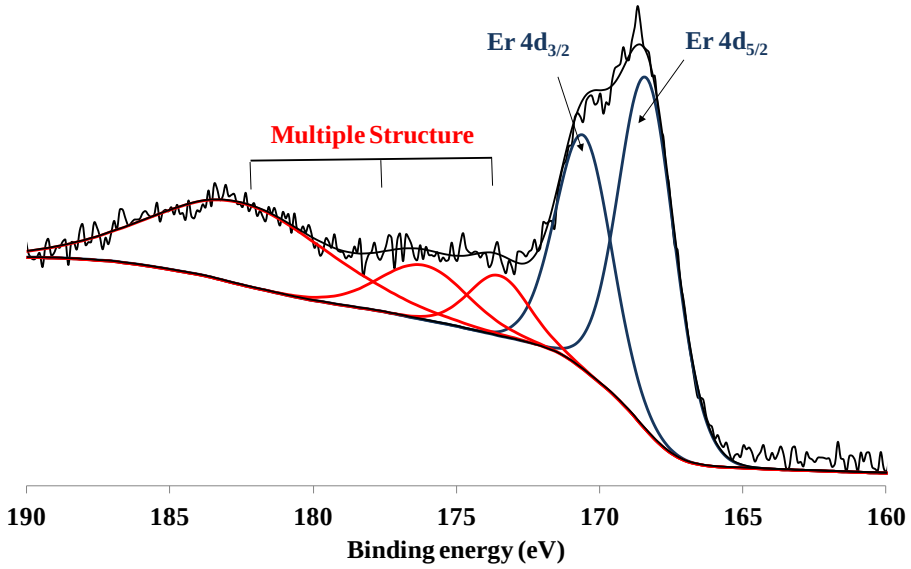

Figure 4.46 – **Fitted XPS Spectra of Er 4d core level of the unaged $Ce_{0.5}Er_{0.5}V_{0.95}W_{0.05}O_4$**

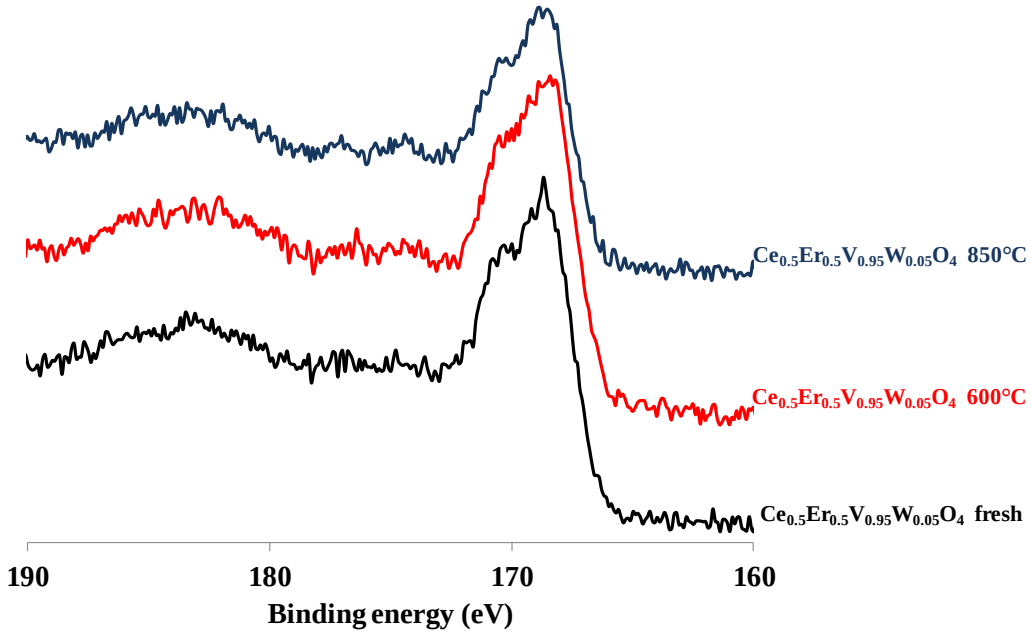

Figure 4.47 – **XPS Spectra of Er 4d core level of the $Ce_{0.5}Er_{0.5}V_{0.95}W_{0.05}O_4$ catalysts**

The binding energies for the photopeak V $2p_{3/2}$ remain almost unchanged at 517.7 eV close to the values currently attributed to V^{5+} further confirmed by the difference in energies between O 1s and V $2p_{3/2}$ photopeaks. The relative concentrations of elements Ce, RE (Pr, Gd, Tb, and Er) V and W for $Ce_{0.5}RE_{0.5}V_{0.95}W_{0.05}O_4$ catalysts aged at different temperatures are reported in Table 4.9. It can be seen that the Ce/O atomic ratio is close to 0.14 [0.12 – 0.16] for all substituted-catalysts. These values are stable for all catalysts after aging at 600°C and 850°C. The V/Ce ratio increases after aging at 600°C and then decrease after aging at 850°C except for Pr-substituted catalyst. This is influenced by the change of crystalline size as well as the disappearance of surface vanadate species dispersed at the surface after 850°C revealed by H_2-TPR measurements. Therefore, the decrease of NO_x conversion after aging at 850°C can be expected due to the loss of surface vanadium species. The atomic ratios RE/Ce, W/V, V/(Ce+RE), W/(Ce+RE) and (V+W)/(Ce+RE) are close for the catalysts to the theoretical value, the difference remains less than 10%, which is acceptable given the uncertainty of the XPS spectroscopy. Indeed, the relative concentration of W at the surface increases drastically after aging at 850°C compared to unaged catalyst and catalyst aged at 600°C.

The abundance of labile oxygen identified as the O_α species is another property that influences SCR activity. In the case of photo-emission from oxygen, the O 1s signal clearly shows two different surface oxygen species previously discussed in the section 1.3.2: O_β ascribed to lattice oxygen (binding energy peak: 529.0-530.5 eV) and O_α ascribed to oxygen vacancies or surface adsorbed oxygen, hydroxyl, or carbonate groups (binding energy peak: 531.0-532.8 eV). The O_α/O_β ratio is a common way to roughly assess the number of oxygen vacancies in the different sample as can be seen in Table 4.9. The O_α/O_β ratio can also be disturbed by the presence of an increasing concentration of vanadium on the surface. By increasing the aging temperature, the comparison of the values of the O_α/O_β and Ce^{4+}/Ce^{3+} ratios shows the overall increase in Ce^{4+} concentration accompanied by a decrease in the O_α/O_β. The higher amount of adsorbed oxygen

species (O_α) is occurring with decreasing ionic radius with the higher value for $Ce_{0.5}Pr_{0.5}V_{0.95}W_{0.05}O_4$ catalyst [25].

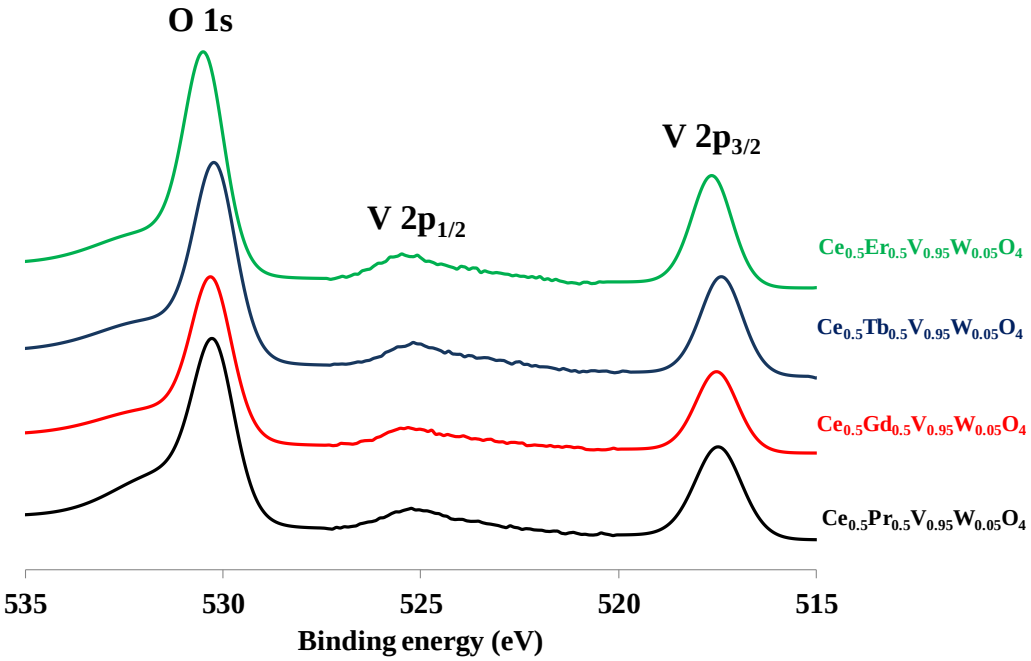

Figure 4.48 – **XPS Spectra of V 2p and O 1s core level of the unaged $Ce_{0.5}RE_{0.5}V_{0.95}W_{0.05}O_4$ (RE=Pr, Gd, Tb, and Er) catalysts**

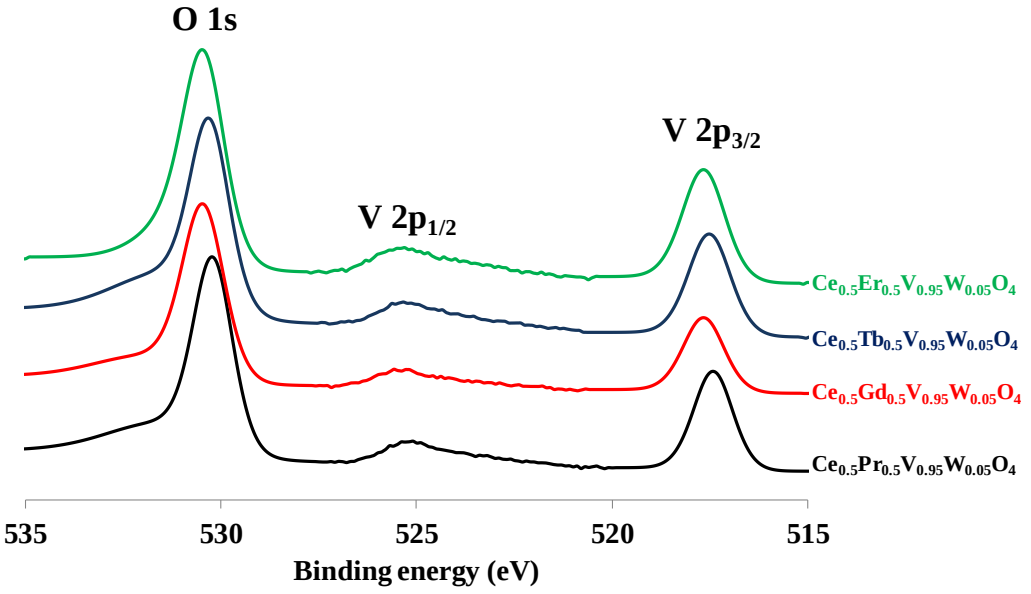

Figure 4.49 – **XPS Spectra of V 2p and O 1s core level of the $Ce_{0.5}RE_{0.5}V_{0.95}W_{0.05}O_4$ (RE=Pr, Gd, Tb, and Er) catalysts aged at 600°C**

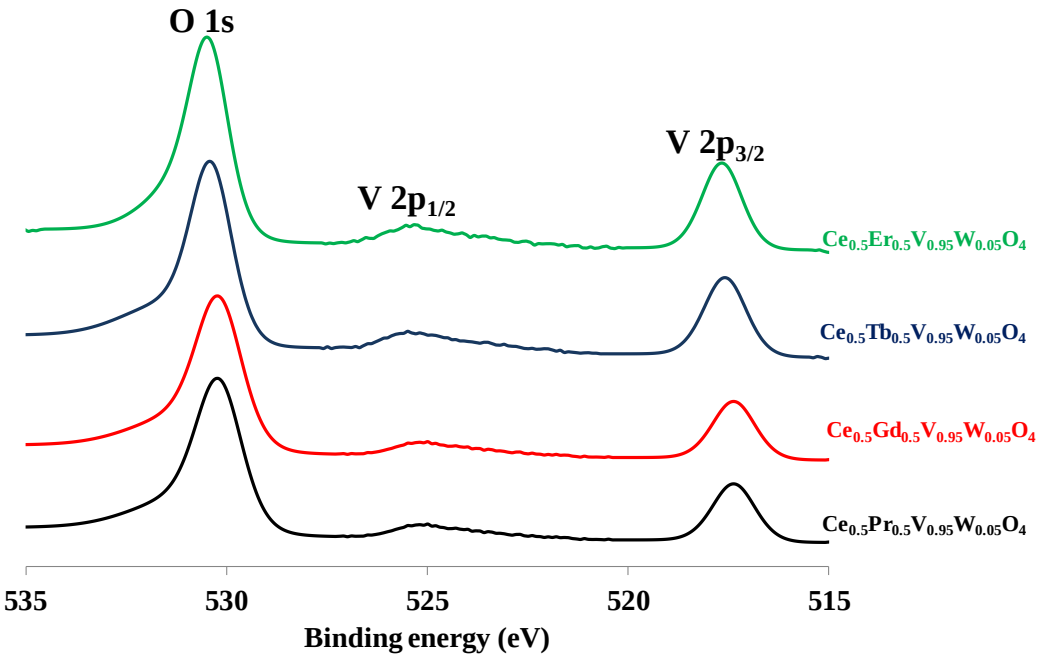

Figure 4.50 – **XPS Spectra of V 2p and O 1s core level of the $Ce_{0.5}RE_{0.5}V_{0.95}W_{0.05}O_4$ (RE=Pr, Gd, Tb, and Er) catalysts aged at 850°C**

The photopeak corresponding to the characteristic of tungsten $4d_{5/2}$ and $4d_{3/2}$ recorded on the substituted catalysts $Ce_{0.5}RE_{0.5}V_{0.95}W_{0.05}O_4$ (RE =Pr, Gd, Tb, and Er) unaged (Fig 4.51) and after aging at 600°C (Fig 4.52) and 850°C (Fig 4.53) are presented. There is no change in the binding energies despite the change of tungsten concentration previously discussed due to aging. In addition, no shoulder or line broadening is identified, so tungsten would be stabilized at the +6 oxidation state. The formation of a well-defined V_2O_5 is confirmed by the V 3p peak observed at a binding energy (V 3p) = 42.2 eV which corresponds to V^{5+} [22]. The broad peak at 32 eV for $Ce_{0.5}Er_{0.5}V_{0.95}W_{0.05}O_4$ catalysts is representative of Er $2p_{1/2}$.

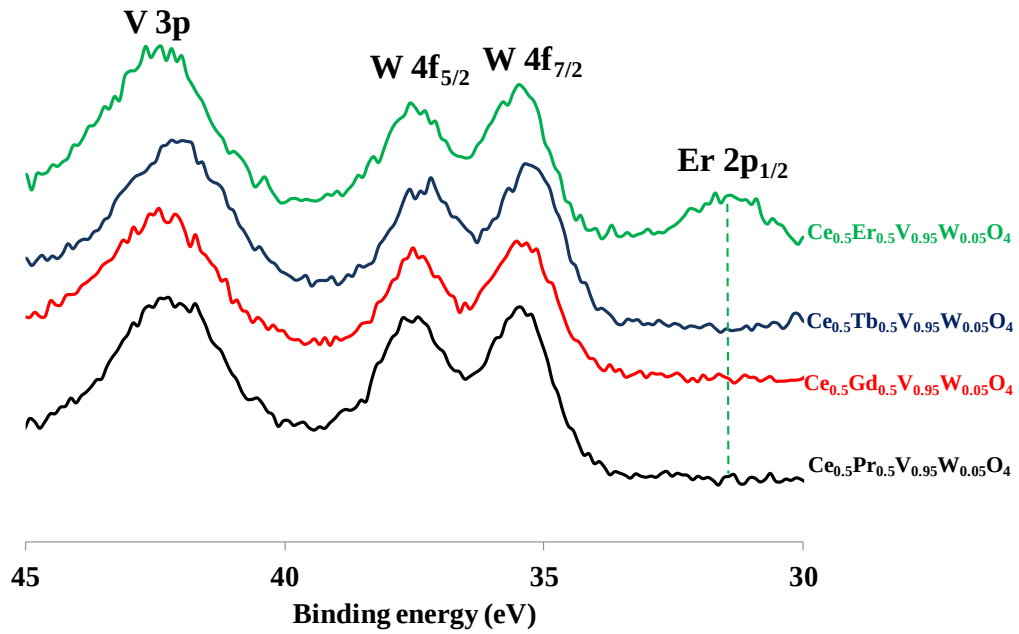

Figure 4.51 – **XPS Spectra of V 3p, W 4f and Er $2p_{1/2}$ core level of the unaged $Ce_{0.5}RE_{0.5}V_{0.95}W_{0.05}O_4$ (RE =Pr, Gd, Tb, and Er) catalysts**

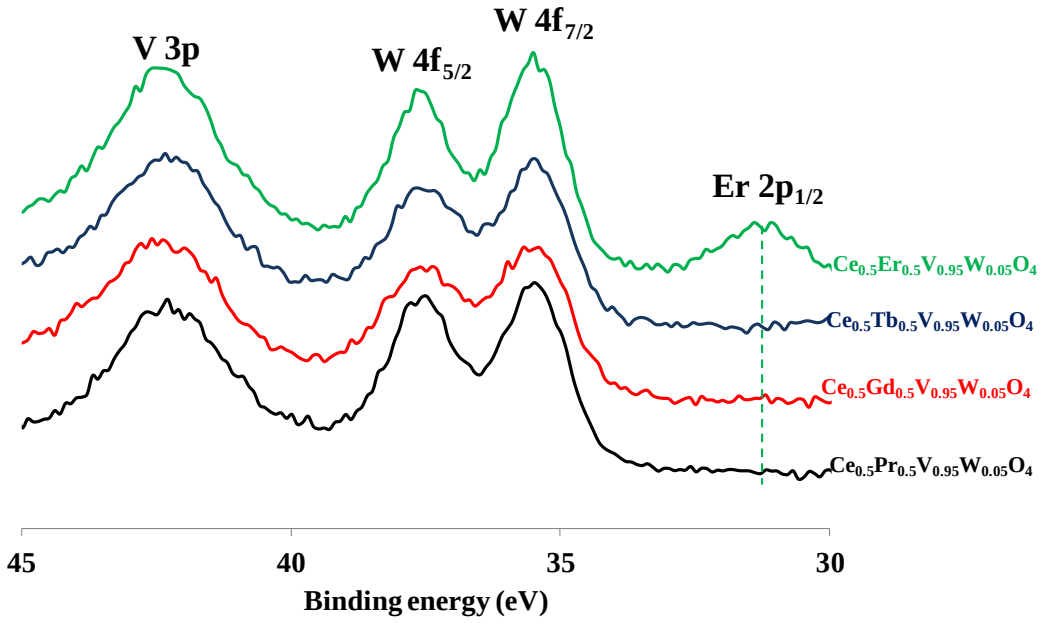

Figure 4.52 – **XPS Spectra of V 3p, W 4f and Er 2p core level of the $Ce_{0.5}RE_{0.5}V_{0.95}W_{0.05}O_4$ (RE =Pr, Gd, Tb, and Er) catalysts aged at 600°C**

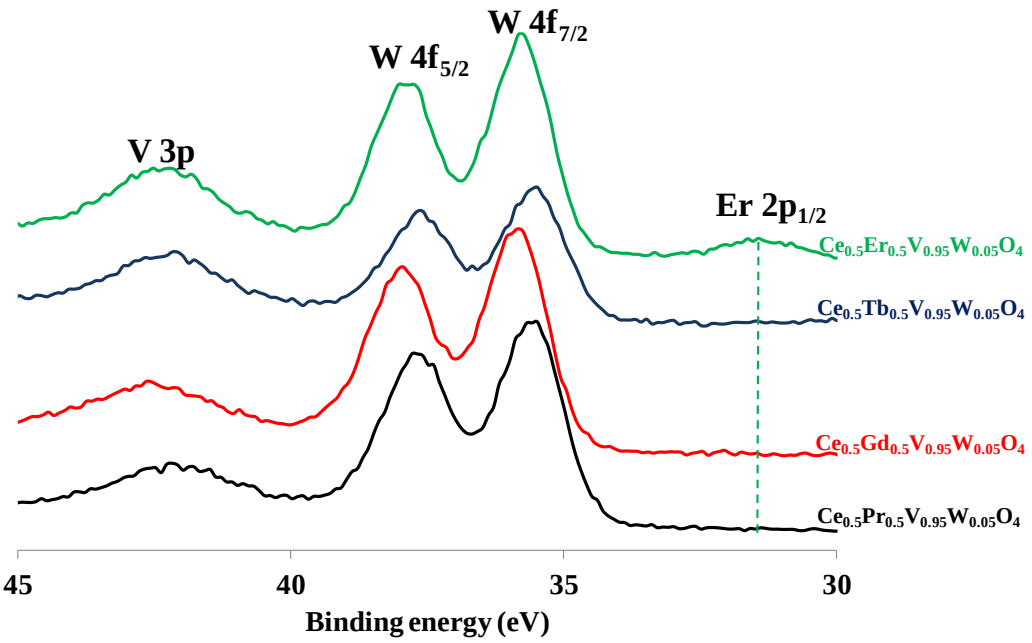

Figure 4.53 – **XPS Spectra of V 3p, W 4f and Er 2p core level of the $Ce_{0.5}RE_{0.5}V_{0.95}W_{0.05}O_4$ (RE =Pr, Gd, Tb, and Er) catalysts aged at 850°C**

Table 4.9 – **Surface Composition of $Ce_{1-x}RE_xV_{0.95}W_{0.05}O_4$ (RE=Pr, Gd, Tb, and Er) catalysts**

Catalyst	Aging temperature (°C)	W/V	V/ (Ce+RE)	W/ (Ce+RE)	(V+W)/ (Ce+RE)	Ce^{4+}/Ce^{3+}	O_α/O_β	B.E.(eV) V 2p
$CeV_{0.95}W_{0.05}O_4$	unaged	0.14	-	-	-	0.22	0.37	517.5
	600	0.33	-	-	-	0.31	0.35	517.5
	850	0.46	-	-	-	0.31	0.38	517.5
$Ce_{0.5}Pr_{0.5}V_{0.95}W_{0.05}O_4$	unaged	0.05	1.20	0.05	1.20	0.44	0.70	517.5
	600	0.10	0.70	0.07	0.80	0.60	0.50	517.5
	850	0.20	0.95	0.20	1.00	0.71	0.40	517.5
$Ce_{0.5}Gd_{0.5}V_{0.95}W_{0.05}O_4$	unaged	0.08	0.75	0.06	0.80	0.58	0.50	517.6
	600	0.10	0.75	0.07	0.84	0.60	0.39	517.6
	850	0.50	0.50	0.30	0.80	0.70	0.37	517.6
$Ce_{0.5}Tb_{0.5}V_{0.95}W_{0.05}O_4$	unaged	0.08	0.80	0.06	0.90	0.36	0.65	517.5
	600	0.08	0.90	0.07	1.00	0.48	0.57	517.5
	850	0.19	0.70	0.13	0.85	0.50	0.50	517.5
$Ce_{0.5}Er_{0.5}V_{0.95}W_{0.05}O_4$	unaged	0.06	0.80	0.05	0.90	0.36	0.60	517.5
	600	0.08	0.90	0.08	1.00	0.45	0.50	517.5
	850	0.30	0.80	0.20	1.00	0.80	0.40	517.5

Catalyst	Aging temperature (°C)	Ce/O	V/O	V/Ce	W/Ce	RE/Ce
$CeV_{0.95}W_{0.05}O_4$	unaged	0.23	0.21	0.89	0.13	-
	600	0.17	0.17	0.96	0.32	-
	850	0.21	0.15	0.72	0.33	-
$Ce_{0.9}Pr_{0.5}V_{0.95}W_{0.05}O_4$	unaged	0.13	0.39	2.91	0.14	1.30
	600	0.14	0.27	1.50	0.17	1.20
	850	0.14	0.21	1.92	0.45	1.00
$Ce_{0.5}Gd_{0.5}V_{0.95}W_{0.05}O_4$	unaged	0.14	0.20	1.50	0.12	1.00
	600	0.14	0.20	1.67	0.17	1.20
	850	0.13	0.16	1.00	0.48	0.90
$Ce_{0.9}Tb_{0.5}V_{0.95}W_{0.05}O_4$	unaged	0.15	0.20	1.30	0.09	0.80
	600	0.15	0.25	1.70	0.15	0.80
	850	0.15	0.20	1.30	0.30	0.60
$Ce_{0.5}Er_{0.5}V_{0.95}W_{0.05}O_4$	unaged	0.12	0.20	1.40	0.05	0.80
	600	0.14	0.22	1.60	0.14	0.80
	850	0.16	0.20	1.20	0.21	0.65

2.4 Catalytic activity of $Ce_{0.5}RE_{0.5}V_{0.95}W_{0.05}O_4$ (RE= Pr, Gd, Tb, and Er) catalysts after hydrothermal aging at 600°C

2.4.1 Ammonia-selective catalytic reduction of NO_x to nitrogen in "Standard" condition: NO/NO_x =1

The NO_x conversion during standard-SCR condition versus temperature is collected in Figure 4.54 on the catalysts aged in the presence of steam in the air at 600°C. All catalysts show the high N_2 selectivity (100%) in the whole temperature range. Therefore, the optimal catalyst could contribute to improving the NO_x conversion. Under the standard-SCR condition, the NO_x conversion profile of both $CeV_{0.95}W_{0.05}O_4$ and substituted catalysts possessed of a typical volcano-type shape which highlights kinetic and thermodynamic limitation as earlier discussed. At low temperatures, the slower reaction rate of NO oxidation to NO_2 could explain the decrease in catalytic activity. At high temperatures, NO oxidation to NO_2 is thermodynamically undesirable. However, the decrease in activity is probably due to preferential oxidation of ammonia to NO. Let us note that similar to previous observations this undesired reaction is not accompanied by N_2O formation. For the temperatures below 400°C, higher NO_x conversion and

broader operating temperature window were obtained on substituted catalysts compared to reference $CeV_{0.95}W_{0.05}O_4$ catalyst. Above 400°C, $Ce_{0.5}RE_{0.5}V_{0.95}W_{0.05}O_4$ (RE= Pr, Gd) catalysts lead to the lower NO_x conversion compared to $CeV_{0.95}W_{0.05}O_4$ catalyst. Up to 300°C, terbium-substituted catalyst is the most (highly) active catalyst owning to its oxidizing property. Over $Ce_{0.5}Tb_{0.5}V_{0.95}W_{0.05}O_4$ catalyst, NO_x conversion steadily increases with temperature; from 55% at 200°C, conversion reaches a maximum of 94% at 350°C. The NO_x conversion over Er-containing catalyst reaches 95% between 300 and 450°C. At 250°C over $Ce_{0.5}Er_{0.5}V_{0.95}W_{0.05}O_4$ catalyst, the standard-SCR condition leads to 71% conversion compared to total conversion at the fast-SCR condition. However, at the higher temperatures, SCR conditions no longer influence NO_x conversion. Kobel *et al*. [43] found that the reaction involving an equimolar NO and NO_2 feed mixture (Fast-SCR), is significantly faster than the Standard-SCR reaction. They recommended, in Fast-SCR condition gaseous NO_2 replace oxygen as a more effective oxidizing agent, hence allowing faster re-oxidation of the vanadium sites. In the same way, Topsoe et al. suggested that the rate determining step in NH_3-SCR reaction over vanadium-containing catalysts is re-oxidation of V^{4+}–OH to V^{5+}=O species.

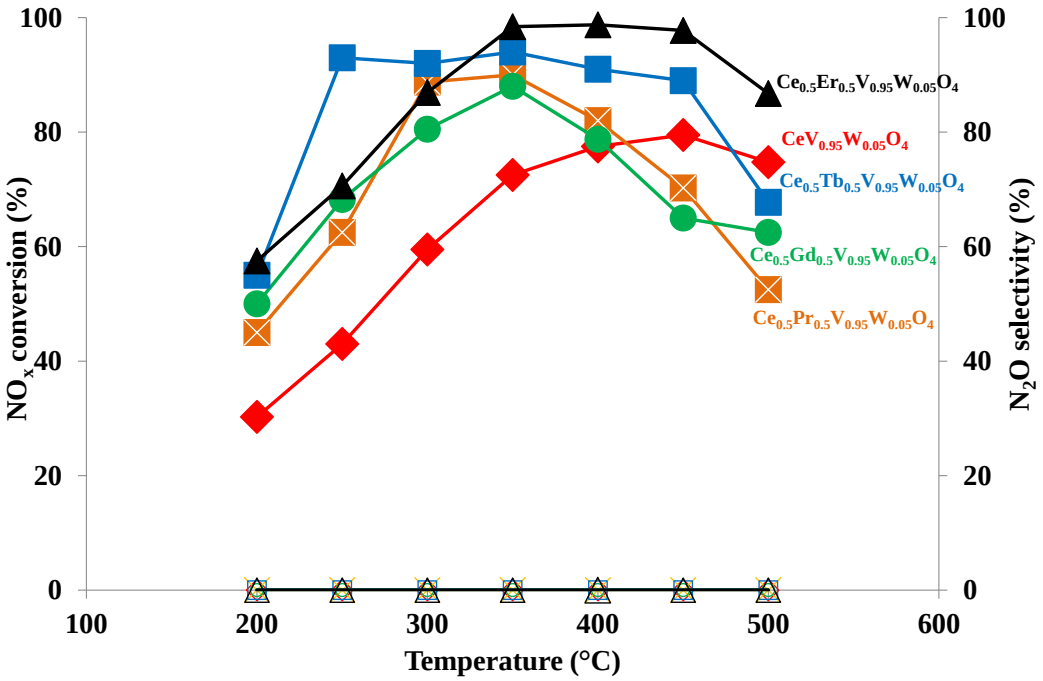

Figure 4.54 – **NO_x conversion and N_2O selectivity of $Ce_{0.5}RE_{0.5}V_{0.95}W_{0.05}O_4$ (RE=Pr, Gd, Tb, and Er) catalysts in Standard-SCR condition aged at 600°C**

2.4.2 Ammonia-selective catalytic reduction of NO_x to nitrogen in "fast" condition: $NO/NO_x = 0.5$

Under Fast-SCR conditions, a much faster rate of NO reduction to nitrogen is observable at low temperature whereas quite similar behaviors are distinguishable at high temperature. The NO_x conversion and selectivity towards N_2O of the $Ce_{0.5}RE_{0.5}V_{0.95}W_{0.05}O_4$ (RE=Pr, Gd, Tb, and Er) catalysts as a function of reaction temperature are exposed in Fig 4.55. For this series of catalyst, the NO_x conversion is stable up to 400°C and above 400°C starts to decrease. The NO_x conversion of the corresponding Tb- and Er-containing catalysts is significantly higher than that of the reference $CeV_{0.95}W_{0.05}O_4$ catalyst. The substituted catalysts by Pr and Gd have the same catalytic behavior in the whole temperature range. Above 400°C NO_x conversion decreases that can be the result of competitive oxidation of ammonia to NO which is prevailing over its reaction to N_2. The NO_x conversion of Er-containing catalyst reaches almost 95% in the wide range of temperature (200–450°C). The NO_x conversion of $Ce_{0.5}Er_{0.5}V_{0.95}W_{0.05}O_4$ catalyst decreases to 64% at 500°C. For this class of catalysts, it is even more evident the role

of the ionic radius on activity. The Er-containing catalyst with the lowest ionic radius possessed the highest Fast-SCR NO_x conversion in the whole temperature range. The ammonia oxidation is especially delayed at high temperature on $Ce_{0.5}Tb_{0.5}V_{0.95}W_{0.05}O_4$ catalyst. A high N_2 selectivity of 99% with the least amount of produced N_2O achieved for Tb-containing catalyst. However, for all catalysts, a small quantity of N_2O is observed. The N_2 selectivity decreases slightly while the temperature increases. The faster re-oxidation of the SCR function by NO_2 explains the gain in activity in Fast-SCR condition compared to the standard and NO_2-SCR conditions. As an example, catalytic measurements in standard SCR conditions on $Ce_{0.5}Er_{0.5}V_{0.95}W_{0.05}O_4$ leads to a lower NO_x conversion of approximately 62 versus 95% for Fast-SCR conditions at 250°C.

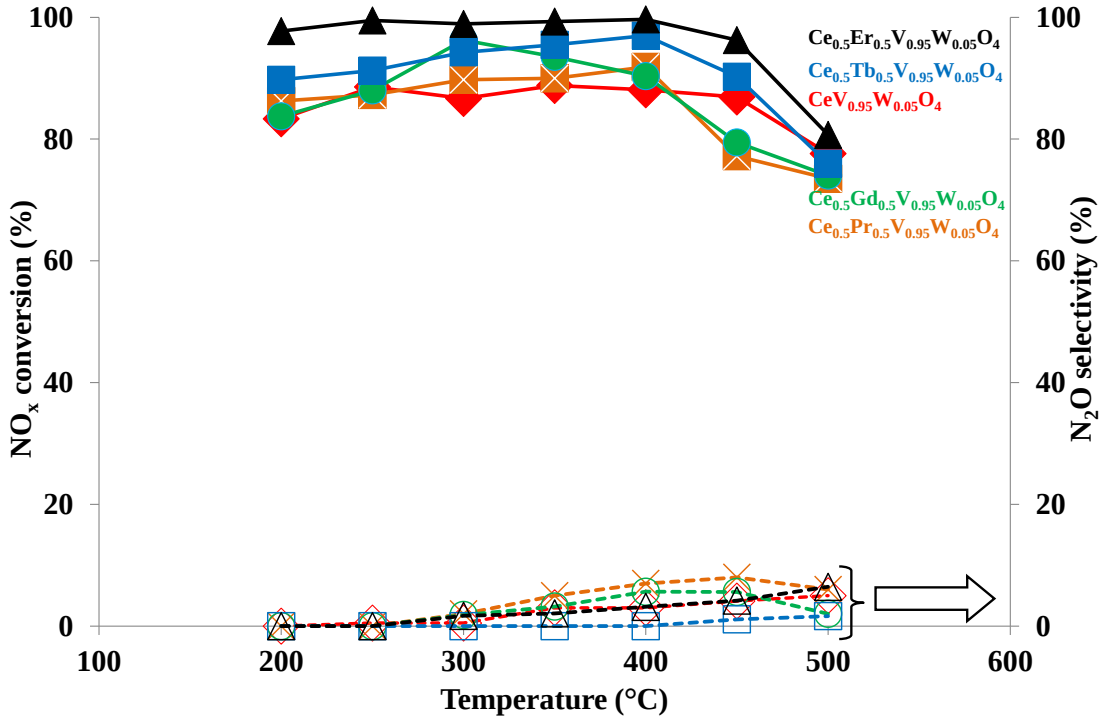

Figure 4.55 – **NO_x conversion and N_2O selectivity of $Ce_{0.5}RE_{0.5}V_{0.95}W_{0.05}O_4$ (RE=Pr, Gd, Tb and Er) catalysts in Fast-SCR condition aged at 600°C**

2.4.3 Ammonia-selective catalytic reduction of NO_x to nitrogen in "NO_2" condition: NO/NO_x =3/10

In this section, we analyze the effect of an excess of nitrogen dioxide in the reaction mixture (NO_2-SCR). Usually, this reaction is slower compared to Fast-SCR conditions, especially at low temperatures. The formation of unwanted N_2O was also observed. In particular, a group of catalysts comprising Pr, Gd, Tb, and Er does not suffer deactivation and shows an increase of activity after aging in the temperature range of 200–350°C. Below 350°C, cerium substitution by Gd and Pr has a small positive effect on the NO_x conversion compared to reference $CeV_{0.95}W_{0.05}O_4$ catalyst. However, the NO_x conversion over the reference $CeV_{0.95}W_{0.05}O_4$ catalyst is higher than the Gd- and Pr-containing at the temperatures above 350°C. The $Ce_{0.5}Tb_{0.5}V_{0.95}W_{0.05}O_4$ catalyst has a moderate activity in NO_x reduction and the maximum of 98% NO_x conversion was achieved at 300-350°C. At higher temperatures, the NO_x conversion of $Ce_{0.5}Tb_{0.5}V_{0.95}W_{0.05}O_4$ catalyst decreases. The NO_x conversion decreases to 40% at 500°C due to the competitive oxidation of NH_3 with oxygen that leads to lower NO_x conversion. From the results, it can be seen that the aged $Ce_{0.5}Er_{0.5}V_{0.95}W_{0.05}O_4$ catalyst achieved 98% and 90% NO_x conversion at 350 and 500°C, respectively. Other substituted catalysts are less active than reference $CeV_{0.95}W_{0.05}O_4$ catalyst at 500°C. These results suggest that the incorporation of rare earth is more beneficial in NO_2-SCR condition at low and moderate temperature. The $Ce_{0.5}RE_{0.5}V_{0.95}W_{0.05}O_4$ (RE= Pr and Gd) catalysts show limited N_2 selectivity in the tested condition at high temperature. When the $Ce_{0.5}RE_{0.5}V_{0.95}W_{0.05}O_4$ catalyst was substituted with erbium and terbium, N_2 selectivity was improved significantly in the whole temperature range especially at high temperature. The most active and selective catalyst is the $Ce_{0.5}Er_{0.5}V_{0.95}W_{0.05}O_4$ catalyst that possessed of the lowest ionic radius for the rare earth element.

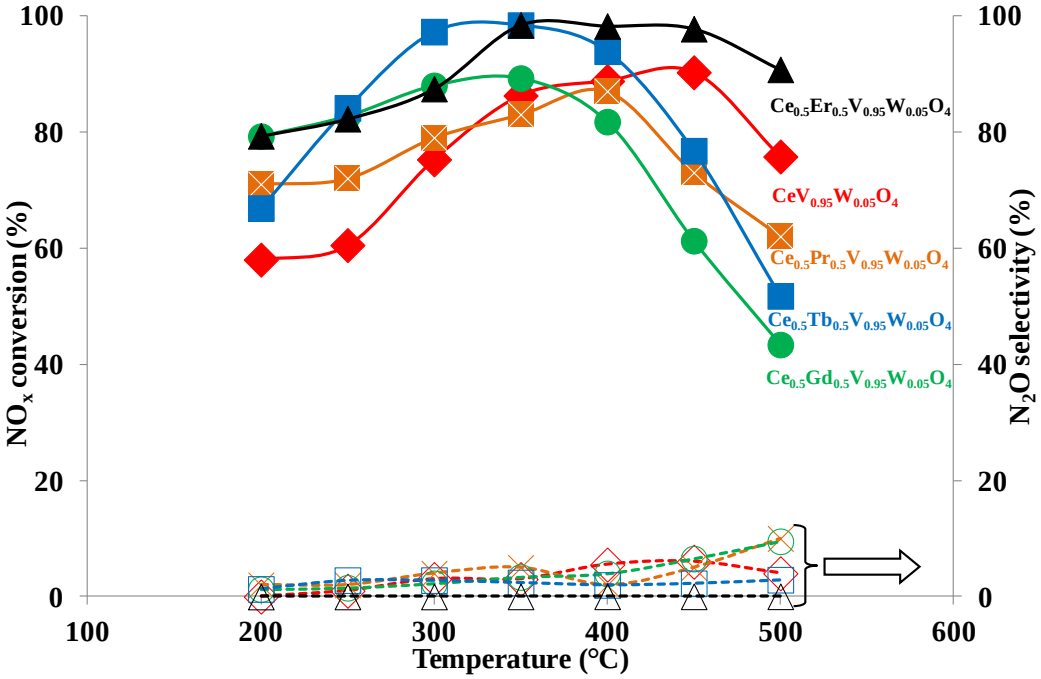

Figure 4.56 – **NO_x conversion and N_2O selectivity of $Ce_{0.5}RE_{0.5}V_{0.95}W_{0.05}O_4$ (RE=Pr, Gd, Tb and Er) catalysts in NO_2-SCR condition aged at 600°C**

2.5 Catalytic activity of $Ce_{0.5}RE_{0.5}V_{0.95}W_{0.05}O_4$ (RE= Pr, Gd, Tb and Er) catalysts after hydrothermal aging at 850°C

2.5.1 Ammonia-selective catalytic reduction of NO_x to nitrogen in "Standard" condition: NO/NO_x =1

Previous studies have already revealed that the insertion of rare earth (RE=Pr, Gd, Tb, and Er) to the $CeV_{0.95}W_{0.05}O_4$ structure is very important for the enhancement of NO_x conversion of mixed oxides, especially in standard SCR. The catalytic efficiency of the $Ce_{0.5}RE_{0.5}V_{0.95}W_{0.05}O_4$ catalysts, aged at 850°C, is shown in Fig 4.57. By erbium insertion into the solid structure, the operation temperature window of $Ce_{0.5}Er_{0.5}V_{0.95}W_{0.05}O_4$ catalyst was greatly broadened, with 40% NO_x conversion from 250 to 450°C. For the $Ce_{0.5}RE_{0.5}V_{0.95}W_{0.05}O_4$ (RE=Pr, Gd, and Er) catalysts, both the low and the high-temperature NO_x conversion were further improved to a certain extent compared to the reference $CeV_{0.95}W_{0.05}O_4$ catalyst. Insertion of terbium into the $CeV_{0.95}W_{0.05}O_4$ catalyst structure leads to a severe decline of NO_x conversion especially at the high temperature. At low temperatures

(200–250°C), the apparent SCR activity followed the particular sequence: $CeV_{0.95}W_{0.05}O_4$ <$Ce_{0.5}Tb_{0.5}V_{0.95}W_{0.05}O_4$ <$Ce_{0.5}Gd_{0.5}V_{0.95}W_{0.05}O_4$ <$Ce_{0.5}Pr_{0.5}V_{0.95}W_{0.05}O_4$ ≈ $Ce_{0.5}Er_{0.5}V_{0.95}W_{0.05}O_4$.

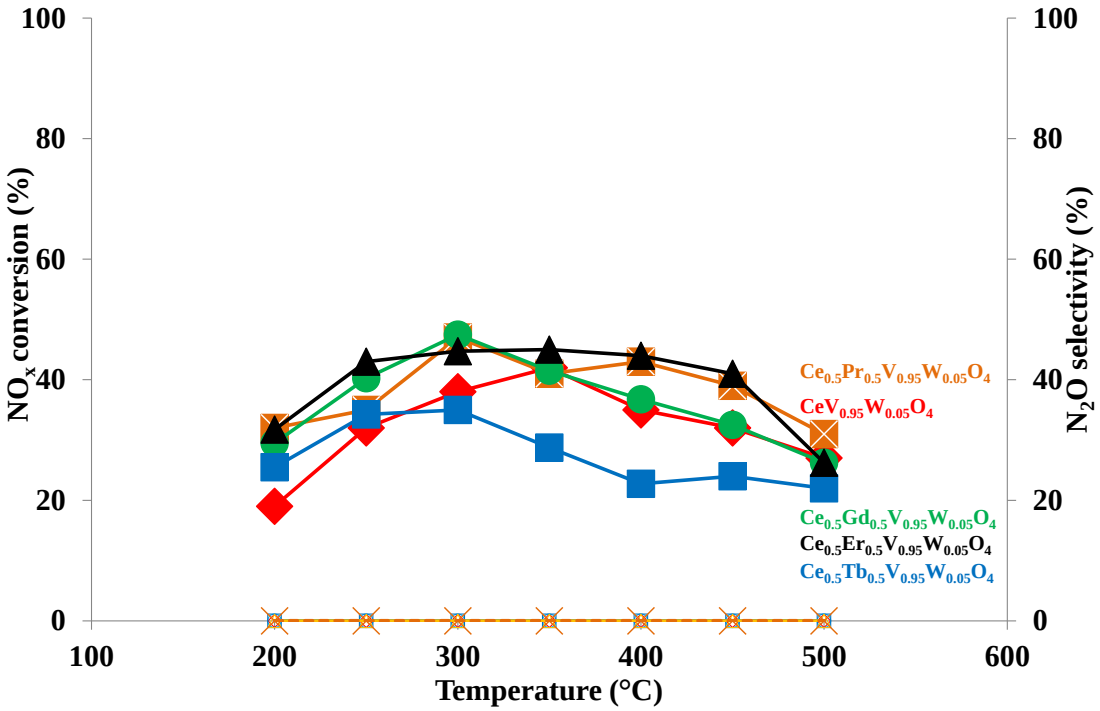

Figure 4.57 – **NO_x conversion and N_2O selectivity of $Ce_{0.5}RE_{0.5}V_{0.95}W_{0.05}O_4$ (RE=Pr, Gd, Tb and Er) catalysts in Standard-SCR condition aged at 850°C**

2.5.2 Ammonia-selective catalytic reduction of NO_x to nitrogen in "fast" condition: $NO/NO_x = 0.5$

Resistance against hydrothermal aging is related to the type of substituted rare earth. Fig 4.58 compares the NO_x conversion efficiencies and N_2O selectivity of $Ce_{0.5}RE_{0.5}V_{0.95}W_{0.05}O_4$ catalysts (RE=Pr, Gd, Tb and Er) aged at 850°C in the 200–500°C temperature range. An important effect is observed by measuring activity after aging at 850°C that all catalysts suffer a major conversion drop. The NO_x conversion profile of all catalysts in the so-called aged state resembles those observed in SCR reaction with a typical volcano-type shape. The catalytic activity increases with increasing reaction temperature up to 330–380°C where a maximum NO_x conversion is observed; at this point, the activity starts to decrease due to ammonia

oxidation reaction to NO, which is prevailing over its reaction to N_2. The activity of $Ce_{0.5}RE_{0.5}V_{0.95}W_{0.05}O_4$ (RE= Tb and Er) aged at 850°C is noticeably higher than that observed on $Ce_{0.5}RE_{0.5}V_{0.95}W_{0.05}O_4$ (RE= Pr and Gd). At the high temperature (500°C), Tb-containing catalyst seems to better maintain NO_x conversion. N_2 selectivity decreases above 400°C over all catalysts. $Ce_{0.5}Er_{0.5}V_{0.95}W_{0.05}O_4$ catalyst highlights the best compromise the selectivity toward N_2 (100%) and NO_x conversion. On the other hand, $Ce_{0.5}Pr_{0.5}V_{0.95}W_{0.05}O_4$ has the lowest NO_x conversion and N_2 selectivity.

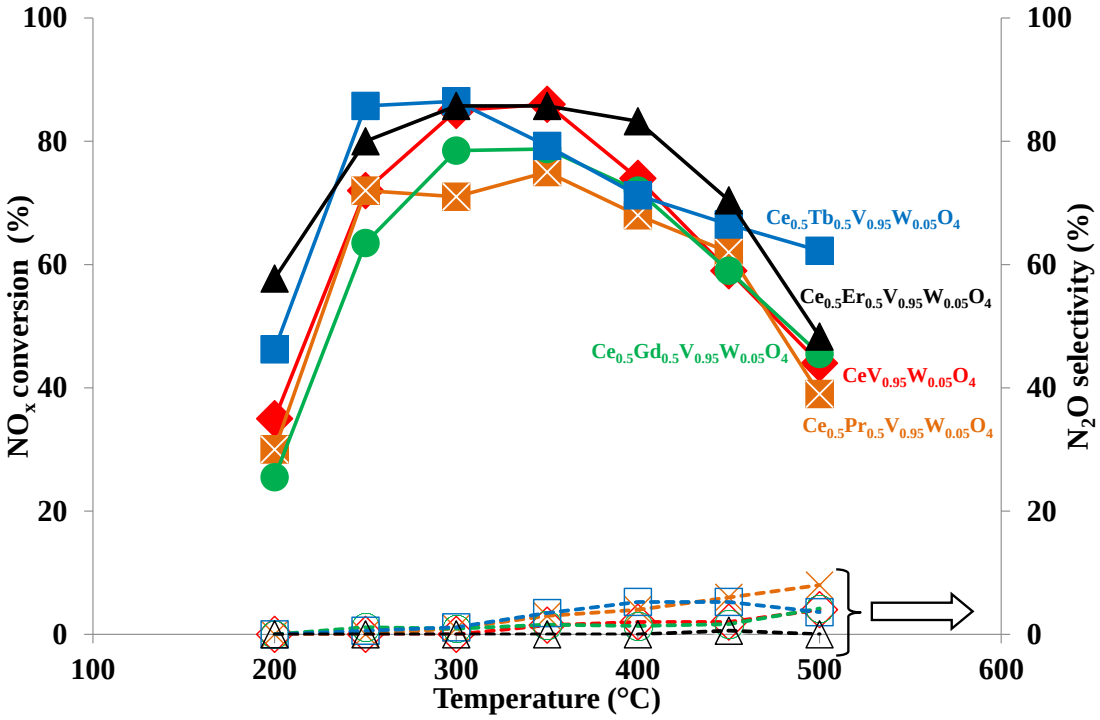

Figure 4.58 – **NO_x conversion and N_2O selectivity of $Ce_{0.5}RE_{0.5}V_{0.95}W_{0.05}O_4$ (RE=Pr, Gd, Tb, and Er) catalysts in Fast-SCR condition aged at 850°C**

2.5.3 Ammonia-selective catalytic reduction of NO_x to nitrogen in "NO_2" condition: NO/NO_x =3/10

De-NO_x activity was also investigated using an excess of nitrogen dioxide in the reaction mixture in the so-called NO_2-SCR condition (Fig 4.59). Catalytic activity in the low-temperature range is enhanced by the insertion of rare earth in $CeV_{0.95}W_{0.05}O_4$ structure, and the results confirm the same behavior which was highlighted in the Fast-SCR reaction. After

aging at 850°C, a progressive decrease of activity is observed for all substituted samples, while $CeV_{0.95}W_{0.05}O_4$ catalyst show a slight increase in conversion between 350-450°C. With the rise in temperature, the N_2 selectivity of catalysts decreased above 300°C, whereas the N_2 selectivity of $CeV_{0.95}W_{0.05}O_4$ catalyst was much higher than other catalysts. Notably, both $CeV_{0.95}W_{0.05}O_4$ and $Ce_{0.5}Er_{0.5}V_{0.95}W_{0.05}O_4$ catalysts illustrate an excellent N_2 selectivity between 200°C and 450°C and the highest N_2 selectivities reach 97% and 93% respectively at 500°C. The results demonstrated that, after partial substitution of Ce^{3+} with Pr^{3+} and Gd^{3+}, N_2 selectivity decreased significantly.

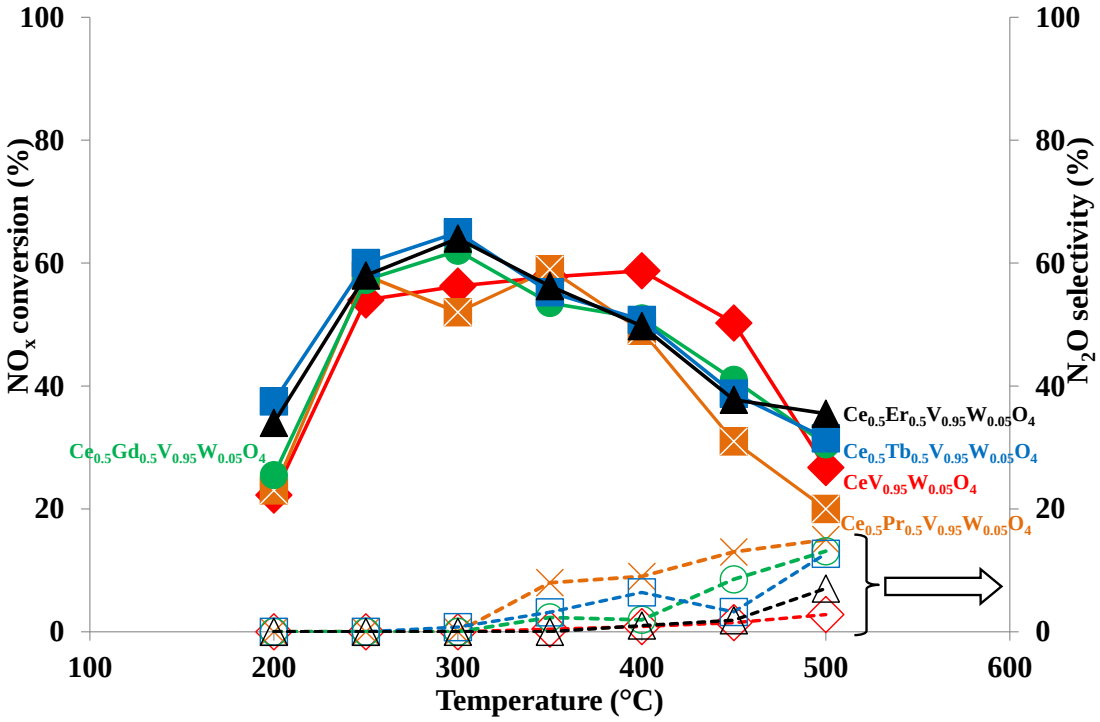

Figure 4.59 – **NO_x conversion and N_2O selectivity of $Ce_{0.5}RE_{0.5}V_{0.95}W_{0.05}O_4$ (RE=Pr, Gd, Tb and Er) catalysts in Standard-SCR condition aged at 850°C**

2.6 Conclusion of section

When applied to mobile sources the NH_3-SCR technology has to fulfill some specific requirements to meet the restrictive emission limits imposed by developing environmental legislation. The SCR catalyst has to show a high thermal stability and high catalytic activity at low temperature. Moreover, its composition has to be "environmentally friendly" in order to avoid any hazardous interactions with the environment and creatures. The catalytic activity of unsupported $Ce_{1-X}RE_XV_{0.95}W_{0.05}O_4$ (RE=Pr, Gd, Tb, and Er) catalysts were investigated in ammonia-SCR at various NO/NO_x ratio. Catalysts were obtained from a hydrothermal synthesis route under the mild condition and then stabilized after aging in the wet atmosphere at 600 or 850°C. A particular attention was paid to the role of the ionic radius of the rare earth element on catalytic activity. The catalysts textural, structural and morphological properties were characterized by temperature programmed reduction, X-ray powder diffraction, Raman, and B.E.T. methods. All samples were characterized by the same structural features related to the predominance of the tetragonal $REVO_4$ structure in agreement with the insertion of Rare Earth (RE) in the $CeVO_4$ crystalline structure. Along with decreasing ionic radius from Pr^{3+} to Er^{3+}, high specific surface area (between 61 up to 118 m^2/g) for the series of $Ce_{1-X}RE_XV_{0.95}W_{0.05}O_4$ catalysts was obtained. The insertion of the rare earth element in the catalyst structure has prevented the decrease in the specific surface area after aging at 600°C. Therefore, it can be concluded that the thermal stability of the substituted catalyst is significantly higher than that observed in the reference $CeV_{0.95}W_{0.05}O_4$ catalyst. The SCR catalytic activity was investigated in a fixed bed reactor with GHSV of 250 000 $mL.h^{-1}.g^{-1}$. The realistic gas mixture consisted of 400 ppm NO_x+400 ppm NH_3+8% O_2+10% CO_2+10% H_2O in Helium. Under the Fast-SCR condition, substitution of Ce by rare earth has increased the NO_x conversion in low and medium temperature. The substituted catalysts by Pr^{3+} and Gd^{3+} have similar catalytic behavior in the whole temperature range. Above 400°C NO_x conversion decreases that it can be the result of

competitive oxidation of ammonia to NO, which is prevailing over its reaction to N_2. The NO_x conversion of Er-containing catalyst reached almost 95% in the wide range of 200–450°C. The standard-SCR condition is the least favorable, with conversion levels lower than those recorded in fast-SCR in the range of 200–450°C. Under the standard-SCR condition, the NO conversion profile of both $CeV_{0.95}W_{0.05}O_4$ and substituted catalysts has a typical volcano-type shape. At low temperatures, the slower reaction rate of NO oxidation to NO_2 could explain the decrease in catalytic activity. At high temperature, thermodynamic constraints must be taken into consideration for the NO/NO_2 reaction. However, the decrease in activity is probably due to the fast oxidation of ammonia to NO. From 350°C to 450°C, both catalysts substituted by Pr^{3+} and Gd^{3+} convert NO_x up to 85%; above 450°C they partly lose their SCR activities due to the preferential oxidation of ammonia. At low temperature, substituted catalyst by Tb is the most active catalyst until 300°C, owing to the oxidizing property of catalyst. Beyond this temperature, the NO_x conversion of Er-containing reaches a value close to 95% between 300 and 450°C. It was found that the catalytic activity of catalysts is remarkably dependent on the nature of the rare earth element and their position in the periodic table by comparing their activity in NH_3-SCR. Elements characterized by an ionic radius larger than 1Å show a diminished NO removal efficiency after aging, while for a smaller ionic radius NO_x conversion significantly improves. This behavior might be correlated with the characteristics of RE^{3+}–O–V^{5+} bond and to their ability to alter the characteristics of the V–O bond and the acid/base surface properties. It is likely that RE elements with the smaller radius (like Tb and Er) exert a stronger electron withdrawing effect to the vanadium sites, thus increasing their acidity compared to RE elements with large ionic radius (like Ce and La). The interplay of redox and acid/base properties of rare earth vanadates can therefore explain their mutual behavior in SCR reaction and discriminate the more and less active elements.

3 References

[1] M. Casanova, E. Rocchini, A. Trovarelli, K. Schermanz, and I. Begsteiger, "High-temperature stability of V_2O_5/TiO_2-WO_3-SiO_2 SCR catalysts modified with rare-earths," J. Alloys Compd., vol. 408–412, no. x, pp. 1108–1112, 2006.

[2] N. Bion, J. Saussey, M. Haneda, and M. Daturi, "Study by in situ FTIR spectroscopy of the SCR of NO_x by ethanol on Ag/Al_2O_3 — Evidence of the role of isocyanate species," J. Catal., vol. 217, no. x, pp. 47–58, 2003.

[3] M. Casanova, J. Llorca, A. Sagar, K. Schermanz, and A. Trovarelli, "Mixed iron-erbium vanadate NH_3-SCR catalysts," Catal. Today, vol. 241, no. PA, pp. 159–168, 2015.

[4] J. Chen, F. Guo, N. Zhuang, J. Lan, X. Hu, and S. Gao, "A study on the growth of Yb : YVO_4 single crystal," vol. 243, pp. 450–455, 2002.

[5] M. A. L. Vargas, M. Casanova, A. Trovarelli, and G. Busca, "An IR study of thermally stable V_2O_5-WO_3-TiO_2 SCR catalysts modified with silica and rare-earths (Ce, Tb, Er)," Appl. Catal. B Environ., vol. 75, no. 3–4, pp. 303–311, 2007.

[6] L. Chen, J. Li, and M. Ge, "Promotional Effect of Ce-doped V_2O_5-WO_3/TiO_2 with Low Vanadium Loadings for Selective Catalytic Reduction of NO_x by NH_3," J. Phys. Chem. C, vol. 113, no. x, pp. 21177–21184, 2009.

[7] R. C. Ropp and B. Carroll, "Precipitation of rare earth vanadates from aqueous solution," J. Inorg. Nucl. Chem., vol. 39, no. 8, pp. 1303–1307, 1977.

[8] L. Chen, "Hydrothermal synthesis and ethanol sensing properties of $CeVO_4$ and $CeVO_4$-CeO_2 powders," Mater. Lett., vol. 60, no. 15, pp. 1859–1862, 2006.

[9] C. Yang, "Spectroscopic Studies of Surface Chemistry on Cerium Oxide," 2016.

[10] A. Trovarelli, F. Zamar, J. Llorca, C. De Leitenburg, G. Dolcetti, and J. T. Kiss, "Nanophase Fluorite-Structured CeO_2 – ZrO_2 Catalysts Prepared by High-Energy Mechanical Milling Analysis of Low-Temperature Redox Activity and Oxygen Storage Capacity," J Catal, vol. 169, pp. 490–502, 1997.

[11] K. M. Ryan, J. P. McGrath, R. A. Farrell, W. M. O'Neill, C. J. Barnes, and M. A. Morris, "Measurements of the lattice constant of ceria when doped with lanthana and praseodymia - The possibility of local defect ordering and the observation of extensive phase separation," J. Phys. Condens. Matter, vol. 15, no. 2, 2003.

[12] E. Shoko, M. F. Smith, and R. H. McKenzie, "A Consistent Picture of Charge Distribution in Reduced Ceria Phases," Condens. Matter, vol. 5, no. 1, pp. 1–28, 2009.

[13] E. Shoko, M. F. Smith, and R. H. McKenzie, "Charge distribution near bulk oxygen vacancies in cerium oxides," J. Phys. Condens. Matter, vol. 22, no. 22, p. 223201, 2010.

[14] H. Chen, A. Sayari, and A. Adnot, "Composition – activity effects of Mn – Ce – O composites on phenol catalytic wet oxidation," Appl. Catal. B Environ., vol. 32, pp. 195–204, 2001.

[15] Z. Wu, R. Jin, Y. Liu, and H. Wang, "Ceria modified MnO_x/TiO_2 as a superior catalyst

for NO reduction with NH_3 at low-temperature," Catal. Commun., vol. 9, no. 13, pp. 2217–2220, 2008.

[16] R. Afrikaans and S. Africa, "The Preparation of WO_3/TiO_2 and $WO_3/A1_2O_3$ and Characterization Reduction," vol. 317, no. 1989, pp. 309–317, 2000.

[17] E. S. Sankar, G. Venkata, R. Babu, C. R. Reddy, B. D. Raju, K. Seetha, and R. Rao, Clean synthesis of alkyl levulinates from levulinic acid over one pot synthesized WO_3-SBA-16 catalyst. Elsevier B.V., 2016.

[18] J. M. Sánchez-Amaya, G. Blanco, F. J. Garcia-Garcia, M. Bethencourt, and F. J. Botana, "XPS and AES analyses of cerium conversion coatings generated on by thermal activation," Surf. Coatings Technol., vol. 213, pp. 105–116, 2012.

[19] Y. Zhang, J. Deng, H. Zhang, Y. Liu, and H. Dai, "Three-dimensionally ordered macroporous $Pr_6O_{11}$and Tb_4O_7 with mesoporous walls: Preparation, characterization, and catalytic activity for CO oxidation," Catal. Today, vol. 245, pp. 28–36, 2015.

[20] J. Gurgul, M. T. Rinke, I. Schellenberg, and R. Pöttgen, "The antimonide oxides RE ZnSbO and RE MnSbO (RE ¼ Ce , Pr) e An XPS study," vol. 17, pp. 122–127, 2013.

[21] X. Jiang, L. Yu, C. Yao, F. Zhang, J. Zhang, and C. Li, "Synthesis and Characterization of Gd_2O_3 Hollow Microspheres Using a Template-Directed Method," Materials (Basel)., vol. 9, no. 12, p. 323, 2016.

[22] J. Świątowska-Mrowiecka, V. Maurice, S. Zanna, L. Klein, and P. Marcus, "XPS study of Li ion intercalation in V_2O_5 thin films prepared by thermal oxidation of vanadium metal," Electrochim. Acta, vol. 52, no. 18, pp. 5644–5653, 2007.

[23] S. Surnev, M. G. Ramsey, and F. P. Netzer, "Vanadium oxide surface studies," Prog. Surf. Sci., vol. 73, no. 4–8, pp. 117–165, 2003.

[24] M. Piumetti, D. Fino, and N. Russo, "Mesoporous manganese oxides prepared by solution combustion synthesis as catalysts for the total oxidation of VOCs," Appl. Catal. B Environ., vol. 163, pp. 277–287, 2015.

[25] H. Huang, Y. Gu, J. Zhao, and X. Wang, "Catalytic combustion of chlorobenzene over VO_x/CeO_2 catalysts," J. Catal., vol. 326, no. 3, pp. 54–68, 2015.

[26] W. Lisowski, A. H. J. van den Berg, G. A. M. Kip, and L. J. Hanekamp, "Characterization of tungsten tips for STM by SEM/AES/XPS," Fresenius. J. Anal. Chem., vol. 341, no. 3–4, pp. 196–199, 1991.

[27] R. Pavlíková, K. Mašek, N. Tsud, J. Polášek, and V. Matolín, "Methanol Dehydrogenation over Tungsten Oxide One Dimensional Structures," WDS'14 Proc. Contrib. Pap. - Phys., pp. 159 – 164, 2014.

[28] J. N. Fiedor, A. Proctor, M. Houalla, and D. M. Hercules, "Study of the Reduction Behavior of W / Ti02 Catalysts by XPS using Curve Fitting , Deconvolution and Factor Analysis," Surf. Interface Anal., vol. 23, no. November 1994, pp. 204–212, 1995.

[29] D. Ignatov, C. Küpper, S. Pischinger, M. Bahn, W. Betton, O. Rütten, and R. Weinowski, "Catalyst Aging Method for Future Emissions Standard Requirements," pp. 1–19, 2010.

[30] G. Madia, M. Elsener, M. Koebel, F. Raimondi, and A. Wokaun, “Thermal stability of vanadia-tungsta-titania catalysts in the SCR process,” Appl. Catal. B Environ., vol. 39, no. 2, pp. 181–190, 2002.

[31] W. Y. Hernández, O. H. Laguna, M. A. Centeno, and J. A. Odriozola, “Structural and catalytic properties of lanthanide (La, Eu, Gd) doped ceria,” J. Solid State Chem., vol. 184, no. 11, pp. 3014–3020, 2011.

[32] B. M. Reddy, P. Saikia, P. Bharali, Y. Yamada, T. Kobayashi, M. Muhler, and W. Gru, “Structural Characterization and Catalytic Activity of Nanosized Ceria - Terbia Solid Solutions,” pp. 16393–16399, 2008.

[33] S. S. Pitale, V. Kumar, I. M. Nagpure, O. M. Ntwaeaborwa, E. Coetsee, and H. C. Swart, “Cathodoluminescent properties and surface characterization of bluish-white $LiAl_5O_8$:Tb phosphor,” J. Appl. Phys., vol. 109, no. 1, 2011.

[34] S. V. Belaya, V. V. Bakovets, A. I. Boronin, S. V. Koshcheev, M. N. Lobzareva, I. V. Korolkov, and P. A. Stabnikov, “Terbium oxide films grown by chemical vapor deposition from terbium(III) dipivaloylmethanate,” Inorg. Mater., vol. 50, no. 4, pp. 379–386, 2014.

[35] S. Saini, H. S. Yaddanapudi, K. Tian, Y. Yin, D. Magginetti, and A. Tiwari, “Terbium Ion Doping in $Ca_3Co_4O_9$: A Step towards High-Performance Thermoelectric Materials,” Sci. Rep., vol. 7, no. November 2016, p. 44621, 2017.

[36] T.-M. Pan, C.-W. Wang, W.-H. Weng, and S.-T. Pang, “Impact of titanium content and postdeposition annealing on the structural and sensing properties of $TbTi_xO_y$ sensing membranes,” J. Mater. Chem. C, vol. 2, no. 36, pp. 7575–7582, 2014.

[37] N. S. Arul, D. Mangalaraj, and T. W. Kim, “Photocatalytic degradation mechanisms of CeO_2/Tb_2O_3 nanotubes,” Appl. Surf. Sci., vol. 349, pp. 459–464, 2015.

[38] N. Guerfi, O. Bourbia, and S. Achour, “Study of Erbium Oxidation by XPS and UPS,” Mater. Sci. Forum, vol. 480–481, pp. 193–196, 2005.

[39] H. H. Shen, S. M. Peng, X. G. Long, X. S. Zhou, L. Yang, and X. T. Zu, “The effect of substrate temperature on the oxidation behavior of erbium thick films,” Vacuum, vol. 86, no. 8, pp. 1097–1101, 2012.

[40] N. Prakash, R. Karthikeyan, D. Thangaraju, M. Navaneethan, M. Arivanandhan, T. Koyama, and Y. Hayakawa, “Effect of Erbium on the Photocatalytic Activity of TiO_2 /Ag Nanocomposites under Visible Light Irradiation,” ChemPhysChem, vol. 16, no. 14, pp. 3084–3092, 2015.

[41] S. Kaya and E. Yilmaz, “Modifications of structural, chemical, and electrical characteristics of Er_2O_3/Si interface under Co-60 gamma irradiation,” Nucl. Instruments Methods Phys. Res. Sect. B Beam Interact. with Mater. Atoms, vol. 418, no. January, pp. 74–79, 2018.

[42] B. M. Abu-Zied, M. A. Hussein, and A. M. Asiri, “Synthesis, characterization and electrical conductivity of nano-crystalline erbium sesquioxide by the precipitation method and subsequent calcination,” Int. J. Electrochem. Sci., vol. 11, no. 8, pp. 7182–7197, 2016.

[43] M. Koebel, G. Madia, F. Raimondi, and A. Wokaun, “Enhanced reoxidation of vanadia by NO_2 in the fast SCR reaction,” J. Catal., vol. 209, no. 1, pp. 159–165, 2002.

Chapter V

Catalytic performances of $Ce_{1-X}Er_XV_{0.95}W_{0.05}O_4$ mixed oxides (X=0, 0.2, 0.5, and 0.8)

Summary

1 Catalytic performances of $Ce_{1-X}Er_XV_{0.95}W_{0.05}O_4$ (X= 0.2, 0.5, and 0.8) catalysts for the selective reduction of NO_x by ammonia 207

1.1 Hydrothermal synthesis of $Ce_{1-X}Er_XV_{0.95}W_{0.05}O_4$ (X= 0.2, 0.5 and 0.8) solids 207

1.2 Bulk/Structural properties 209

1.2.1 X-ray fluorescence spectrometry 209

1.2.2 X-ray diffraction 210

1.2.2.1 Unaged solids 210

1.2.2.2 Solids aged at 600°C 212

1.2.2.3 Solids aged at 850°C 212

1.2.3 Raman spectroscopy 214

1.2.3.1 Unaged solids 214

1.2.3.2 Aged solids 216

1.2.4 Temperature-programmed reduction (H_2-TPR) 218

1.2.4.1 Reducibility of unaged solids 218

1.2.4.2 Reducibility of aged samples 219

1.2.4.3 Determination of kinetic parameters for the low and high reduction process from H_2-temperature-programmed reduction experiments 222

1.3 Surface characterizations 226

1.3.1 Specific surface area 226

1.3.2 X-ray photoelectron spectroscopy (XPS) 227

1.4 Surface acidity from pyridine adsorption-desorption experiments 233

1.5 Catalytic activity of $Ce_{1-X}Er_XV_{0.95}W_{0.05}O_4$ (X=0, 0.2, 0.5, and 0.8) catalysts after hydrothermal aging at 600°C..... 235

1.5.1 Ammonia-selective catalytic reduction of NO_x to nitrogen in "Standard" condition: NO/NO_x=1 235

1.5.2 Ammonia-selective catalytic reduction of NO_x to nitrogen in "fast" condition: NO/NO_x = 0.5 236

1.5.3 Ammonia-selective catalytic reduction of NO_x to nitrogen in "NO_2" condition: NO/NO_x =3/10 238

1.6 Catalytic activity of $Ce_{1-X}Er_XV_{0.95}W_{0.05}O_4$ (X=0, 0.2, 0.5, and 0.8) catalysts after hydrothermal aging at 850°C..... 239

1.6.1 Ammonia-selective catalytic reduction of NO_x to nitrogen in "Standard" condition: NO/NO_x =1 239

1.6.2 Ammonia-selective catalytic reduction of NO_x to nitrogen in "fast" condition: NO/NO_x= 0.5 240

1.6.3 Ammonia-selective catalytic reduction of NO_x to nitrogen in "NO_2" condition: NO/NO_x =3/10 242

1.7 Tentative comparison between physicochemical and catalytic properties 243

2 Conclusion 245

3 References 247

1 Catalytic performances of $Ce_{1-X}Er_XV_{0.95}W_{0.05}O_4$ (X= 0.2, 0.5, and 0.8) catalysts for the selective reduction of NO_x by ammonia

Partial substitution of cerium by erbium was implemented in this chapter. As previously shown in the previous chapter, the Er species were found to be crucial for enhancing the NO_x conversion. The substitution of cerium by erbium increases NO conversion to nitrogen regardless of the operating conditions. Accordingly, bulk $Ce_{1-X}Er_XV_{0.95}W_{0.05}O_4$ catalysts with different composition with X=0.2, 0.5, and 0.8 were prepared with the aim to optimize the composition especially for the ammonia-selective catalytic reduction of NO_x to nitrogen. In order to choose the optimal catalyst, $Ce_{1-X}Er_XV_{0.95}W_{0.05}O_4$ (X= 0.2, 0.5, and 0.8) catalysts are elucidated by comparing their physical-chemical properties and the catalytic activity. The catalytic properties were evaluated in standard-, fast- and NO_2-SCR conditions for stationary and mobile applications. Aged $Ce_{0.5}Er_{0.5}V_{0.95}W_{0.05}O_4$ catalyst exhibits better catalytic properties in terms of NO conversion and N_2 selectivity thus providing an alternative to less stable supported vanadia-based catalysts towards high temperature. All these changes can be rationalized based on the surface modifications of redox and acidic properties of vanadium species due to a slight extraction and stabilization of VO_x species. The fact that activity is influenced by the erbium indicates that an alteration of the V-O bond characteristic in $REVO_4$ can be responsible for the difference in SCR activity [1, 2].

1.1 Hydrothermal synthesis of $Ce_{1-X}Er_XV_{0.95}W_{0.05}O_4$ (X= 0.2, 0.5 and 0.8) solids

$Ce_{1-X}Er_XV_{0.95}W_{0.05}O_4$ (X= 0.2, 0.5 and 0.8) catalysts were synthesized via a hydrothermal route as described previously. Hydrothermal synthesis generally involves crystal germination and crystal growth under high temperature and high-pressure water conditions. Na_3VO_4 (99.98% Sigma-Aldrich) was dissolved in 50 mL of deionized water under vigorous stirring. The pH value was adjusted to 1.8 by adding dropwise an aqueous solution of nitric acid (3M). In those operating

conditions VO_2^+ cations were likely stabilized in an aqueous phase. In a second step, an aqueous solution was prepared after the dissolution of the precursors $Ce(NO_3)_3 \cdot 6H_2O$, $(NH_4)_6H_2W_{12}O_{40}.xH_2O$ (meta) 99.99wt%, $Er(NO_3)_3.5H_2O$. This second solution was added to the former one containing VO_2^+ cations. Afterward, a progressive addition dropwise of an aqueous solution of sodium hydroxide (1M) until the stabilization of the pH value to 7 induced the precipitation. pH values during precipitation decrease sharply. At the end of the hydrothermal treatment, a significant shift of the pH value from 7 to 3.5 occurred in accordance with earlier observations. The resulting suspension was transferred into a 50 ml Teflon-lined stainless steel autoclave and sealed tightly. Hydrothermal synthesis was carried out at 180°C for 24h in an oven without shaking or stirring. After cooling to room temperature, the precipitates were collected, washed with distilled water and absolute ethanol several times, and then dried at 80°C for 24h. The aging has a significant influence on the structure and activity of the catalytic material and is therefore always addressed accordingly. Two aging temperature procedures were applied to 600 or 850°C. The samples were hydrothermally aged with flowing gas containing 90vol% air and 10vol% water vapor with a GHSV of 41666 $mL.h^{-1}.g^{-1}$ and a temperature rise of 5°C for 5h.

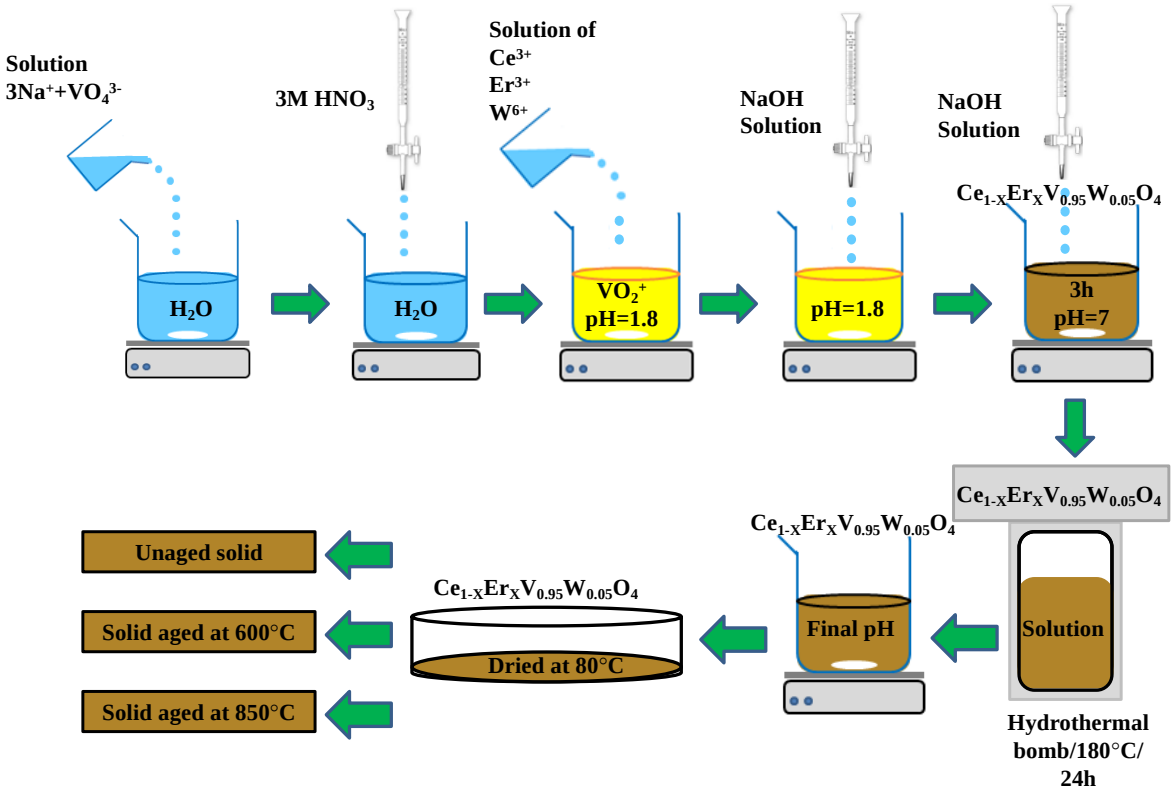

Figure 5.1 – **Steps involved during the hydrothermal synthesis of $Ce_{1-X}Er_XV_{0.95}W_{0.05}O_4$ (X= 0.2, 0.5 and 0.8) catalysts**

1.2 Bulk/Structural properties

1.2.1 X-ray fluorescence spectrometry

The elemental analysis allows determining the weight composition of each element present in the solid. The chemical analysis was performed using X-ray fluorescence spectrometry method to determine the bulk composition of selected $Ce_{1-X}Er_XV_{0.95}W_{0.05}O_4$ catalysts (Table 5.1). The value presented in the brackets corresponds to the expected values. A large excess of tungsten is discernable while a slight deviation is observed with an excess of cerium and slight deficiencies for V and Er. The composition of these samples is not affected intensely by hydrothermal aging with measured values close to the theoretical values. The main variations concern tungsten which could be due to the non-homogeneous distribution of tungsten on the solid or a matrix effect during XRF analysis. More importantly, no loss of vanadium during aging treatment is detected due to sublimation of vanadium oxide.

Table 5.1 – **Elemental analysis of $Ce_{1-X}Er_XV_{0.95}W_{0.05}O_4$ (X= 0.2, 0.5 and 0.8) catalysts by X-ray fluorescence**

Catalyst	Aging temperature (°C)	Chemical composition expressed as oxide			
		V_2O_5 (wt. %)	Ce_2O_3 (wt. %)	WO_3 (wt. %)	Er_2O_3 (wt. %)
$Ce_{0.8}Er_{0.2}V_{0.95}W_{0.05}O_4$	Unaged	30.00 (33.00)	51.00 (50.60)	4.40 (2.23)	14.60 (14.70)
	600	30.50 (33.00)	50.60 (50.60)	4.40 (2.23)	14.50 (14.70)
	850	31.00 (33.00)	50.20 (50.60)	4.30 (2.23)	14.40 (14.70)
$Ce_{0.5}Er_{0.5}V_{0.95}W_{0.05}O_4$	Unaged	30.30 (32.20)	31.00 (30.70)	4.30 (2.23)	34.50 (35.00)
	600	30.50 (32.20)	31.10 (30.70)	4.30 (2.23)	34.10 (35.00)
	850	30.10 (32.20)	31.30 (30.70)	4.00 (2.23)	34.50 (35.00)
$Ce_{0.2}Er_{0.8}V_{0.95}W_{0.05}O_4$	Unaged	29.00 (31.00)	12.00 (12.00)	4.00 (2.23)	53.50 (55.00)
	600	29.10 (31.00)	13.00 (12.00)	4.60 (2.23)	53.00 (55.00)
	850	30.20 (31.00)	13.00 (12.00)	4.70 (2.23)	53.00 (55.00)

1.2.2 X-ray diffraction

X-ray diffraction (XRD) was verified the stabilization of the expected zircon-type structure of the solid and possible bulk segregation. In addition to phase determination, powder XRD patterns can be used to estimate the crystal size in a powder material.

1.2.2.1 Unaged solids

Over $Ce_{1-X}Er_XV_{0.95}W_{0.05}O_4$ (X=0.2, 0.5, and 0.8) catalysts the predominance crystallographic phase is tetragonal $REVO_4$ (RE=Ce and Er). For this structure, the most intense line is located at around $2\theta = 24.0°$. $REVO_4$ crystallizes in the zircon phase (SG: $I4_1/amd$, Z = 4). The zircon type structure can be described by CeO_8 dodecahedrons with eight similar Ce-O distances and isolated VO_4 tetrahedrons. Additional lines of low intensity appear at the values around 2θ =28.5° attributed to the cubic face-centered structure of ceria (CeO_2) for $Ce_{1-X}Er_XV_{0.95}W_{0.05}O_4$ catalysts (X= 0.2 and 0.8). Interestingly, no crystalline cubic CeO_2 phase is detected over the unaged $Ce_{0.5}Er_{0.5}V_{0.95}W_{0.05}O_4$ catalyst.

As earlier illustrated a correlation can be established between 2θ value of the most intense (200) reflection of $REVO_4$ phase and the erbium substitution degree (Fig 5.3). This displacement

becomes more significant for the catalyst with the higher substitution degree (X=0.8) in agreement with a greater insertion of Erbium in the catalyst structure. However, all reflections of these mixed oxides were gradually shifted to the higher 2θ angles with rising the substitution degree. These results indicate the progressive and homogeneous substitution of cerium Ce^{3+} by erbium Er^{3+}.

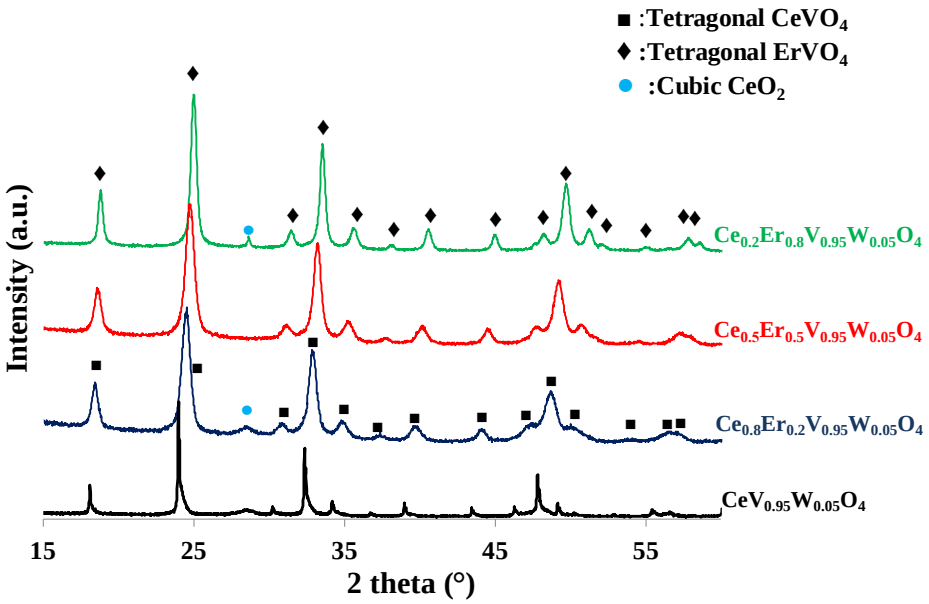

Figure 5.2 – **Crystallographic structure of unaged catalysts $Ce_{1-x}Er_xV_{0.95}W_{0.05}O_4$ (X= 0, 0.2, 0.5 and 0.8) catalysts**

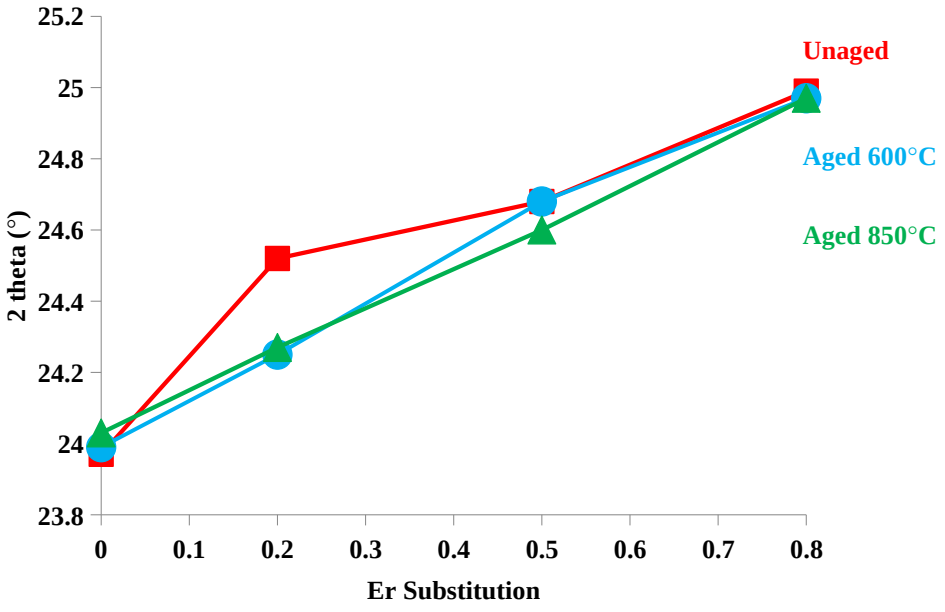

Figure 5.3 – **2theta according to the substitution degree of Erbium after synthesis and aging**

1.2.2.2 Solids aged at 600°C

XRD patterns recorded on powder samples are after aging at 600°C reported in Fig 5.4. The most intense signals at 2θ = 24.0°, 32.3 and 47.8° can be assigned to the characteristic (200), (112) and (312) reflections of the tetragonal structure of $REVO_4$ (JCPDS 00-012-0757) on aged samples. Additional reflections appear notably the most intense at 2θ= 28.5° characterizing the cubic structure of CeO_2 (JCPDS 01-081-0792).

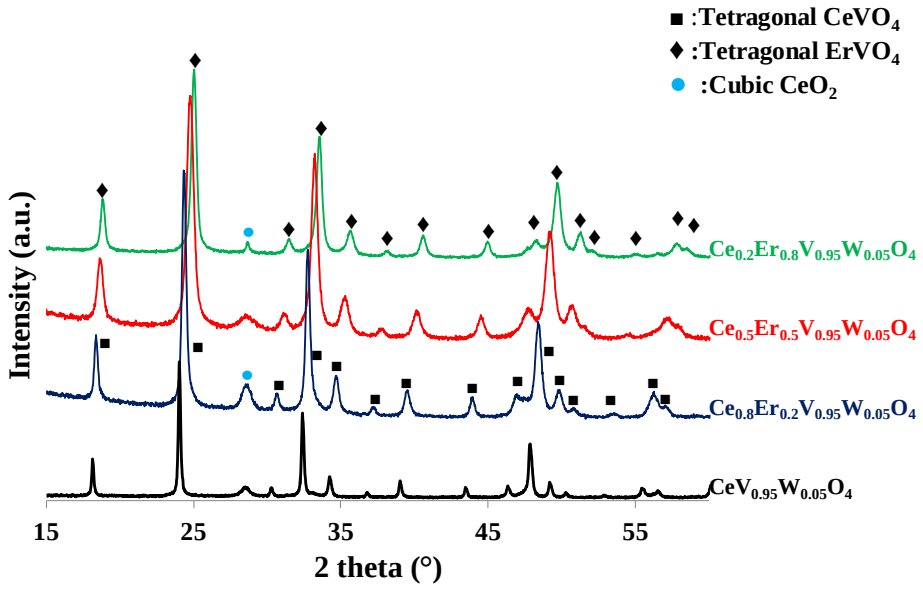

Figure 5.4 – **Crystallographic structure of $Ce_{1-x}Er_xV_{0.95}W_{0.05}O_4$ (X= 0, 0.2, 0.5 and 0.8) catalysts aged at 600°C**

1.2.2.3 Solids aged at 850°C

Hydrothermal aging at 850°C induces significant crystallographic changes. The patterns recorded after aging at 850°C show mainly the tetragonal structure of $REVO_4$ and the segregation of a phase corresponding to the cubic structure of ceria. For all substituted catalysts appearance of a segregated phase attributed to rhombohedric Ce_7O_{12} detected after aging at 850°C. The segregation of Ce_7O_{12} phase is not necessarily helpful in NH_3-SCR since Ce_7O_{12} possess pairs as previously discussed in the previous chapter. It can be noted that tungsten oxides WO_x are not detected by XRD. However, the amorphous form and/or very small

quantities does not allow their identification. The characteristic diffraction lines of Er_2O_3 and V_2O_5 do not appear on the spectra recorded on unaged and after hydrothermal.

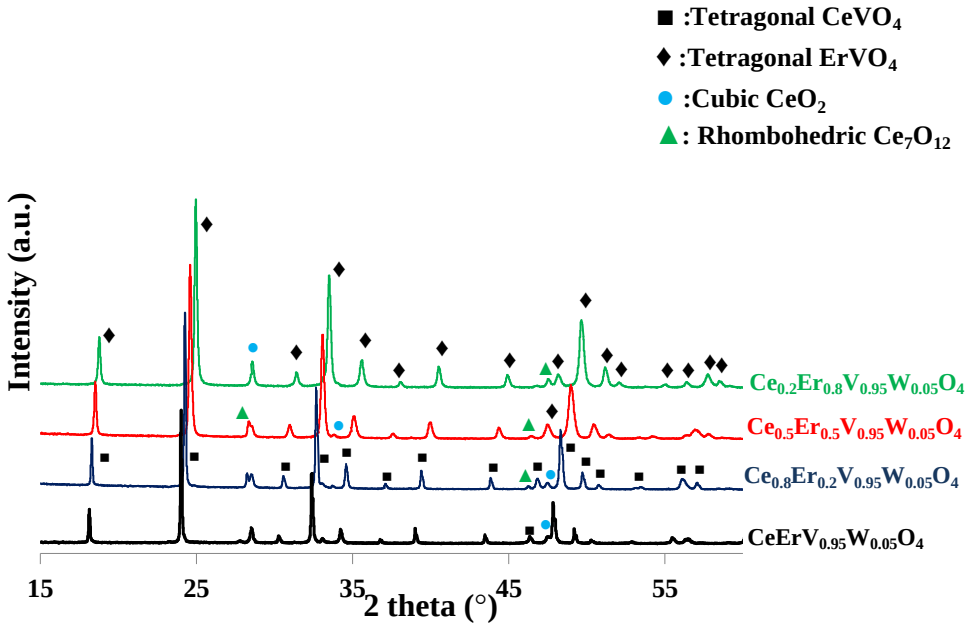

Figure 5.5 – **Crystallographic structure of $Ce_{1-X}Er_XV_{0.95}W_{0.05}O_4$ (X= 0, 0.2, 0.5 and 0.8) catalysts aged at 850°C**

The crystallite diameters calculated from the Debye-Scherrer relationship are reported in Table 5.2. The unaged catalysts generally have the similar $REVO_4$ crystallite diameter 11 to 18 nm. However, $Ce_{0.5}Er_{0.5}V_{0.95}W_{0.05}O_4$ catalyst possessed of the smallest crystallite diameter. The impact of cerium substitution by erbium on the crystallite diameter is more visible after aging. The more cerium substituted by erbium (from 0.2 to 0.5), the smaller the crystallite size is, and by further increasing the substitution degree to 0.8 the crystallite diameter increases again. The comparison of the crystallite diameter before and after aging shows that the $REVO_4$ phase is more sensitive to sintering than CeO_2 with crystallite sizes between 10 to 19 nm after aging at 600°C and between 25 to 40 nm after aging at 850°C. The sintering after aging concerns more readily the $Ce_{0.8}Er_{0.2}V_{0.95}W_{0.05}O_4$ catalyst than the $Ce_{0.5}Er_{0.5}V_{0.95}W_{0.05}O_4$ and $Ce_{0.2}Er_{0.8}V_{0.95}W_{0.05}O_4$ catalysts with the larger substitution degree. The XRD results also show that CeO_2 crystallites have a good sintering resistance after aging at 600°C. The crystallites of the $REVO_4$ phase become larger than those of the CeO_2 after catalyst aging. It can be noticed

that the partial substitution of Ce^{3+} by Er^{3+} has no influence on the sintering of CeO_2. As a resume, it is obvious that erbium improves the thermal stability at increasing substitution. However, slight segregations of mixed oxides, undetectable from XRD analysis, could be hypothesized especially for the high degree of substitution, i.e. X = 0.8.

Table 5.2 – **Influence of cerium substitution by rare earth on the average crystallite size of $REVO_4$ and CeO_2**

Catalyst	Aging temperature (°C)	$REVO_4$ Crystallite diameter (nm)	CeO_2 Crystallite diameter (nm)
$CeV_{0.95}W_{0.05}O_4$	unaged	22	10
	600	54	14
	850	112	40
$Ce_{0.8}Er_{0.2}V_{0.95}W_{0.05}O_4$	unaged	13	17
	600	23	19
	850	64	40
$Ce_{0.5}Er_{0.5}V_{0.95}W_{0.05}O_4$	unaged	11	-
	600	14	10
	850	43	25
$Ce_{0.2}Er_{0.8}V_{0.95}W_{0.05}O_4$	unaged	18	14
	600	29	15
	850	44	36

1.2.3 Raman spectroscopy

1.2.3.1 Unaged solids

As XRD is limited in its sensitivity towards detection of crystalline species, Raman spectroscopy was used as an additional method for structure characterization. This complementary technique allows detecting amorphous compounds which are not detectable by XRD. By increasing the degree of cerium substitution with erbium, some characteristic peaks of Er^{3+} ions transitions corresponding to Er_2O_3 phase are clearly observed over $Ce_{0.2}Er_{0.8}V_{0.95}W_{0.05}O_4$ catalyst as shown in Figure 5.6. Those contributions were previously found to gradually increases with the rise in Er content [1–3]. This growing intensity could be related with the progressive appearance of the $ErVO_4$ tetragonal structure. The transition at 705cm^{-1} is due to the electronic transition from $^4F_{9/2} \rightarrow {}^4I_{15/2}$. Similarly, the emission observed

at 603cm^{-1} expected to result from relaxation and emission from a higher energy level excited state $^4S_{3/2} \rightarrow {}^4I_{15/2}$ [4]. Strong Raman peaks detect above 800cm^{-1} which are assigned to the asymmetrical A_{1g} optical modes of tetrahedral VO_4^{3-} ions. The Raman peaks at around 778 cm^{-1} are assigned to the asymmetric stretching modes (ν_3) of E_g and B_{1g} of $REVO_4$. The bending modes of ν_4 (B_{1g}) and ν_2 (A_{1g}) were detected at 460 and 367 cm^{-1}, respectively. The Raman peak at 264 cm^{-1} was specified as the ν_2 (B_{2g}) bending mode of the VO_4 tetrahedrons. The proximity of the CeO_2 mainline (F_{2g} mode to 460 cm^{-1}) and the line $E_g + B_{2g}$ of VO_4^{3-} to 460 cm^{-1} (corresponding to $REVO_4$) prevents the identification of the CeO_2 phase [1–3].

Cerium Oxide (CeO_2) has the fluorite-type cubic crystal structure that exhibits only one allowed Raman mode, T_{2g}. It emanates from the Ce-O-Ce symmetric vibration at around 460 cm^{-1} [6]. The wavenumber of this line varied from 460 cm^{-1} to 507 cm^{-1} by increasing erbium substitution degree. Denning and Ross proposed that a number of factors contribute to changes of the Raman band position including phonon confinement, strain, particle size effect, and defects [7]. Raman band shifts caused by differences in particle sizes have been reported by a number of authors [6–8]. Therefore, the length of the V-O and Ce-O bonds in the $REVO_4$ matrix is thus modified by the substitution of cerium by erbium. The V-O elongation line characteristic of V_2O_5 located at 998 cm^{-1} is not visible on the Raman spectra. The line corresponding to the vibrational mode of elongation (O-W^{6+}-O) to 715 cm^{-1} characteristics of WO_3 is not detected. As a conclusion, it appears that Ce^{3+} is predominantly substituted by Er^{3+} for $X \leq 0.5$ leading to a homogeneous $REVO_4$ mixed oxide. Regarding high erbium content, the structural features are more complex because the formation of $ErVO_4$ takes place coexisting with $REVO_4$ leading to much stronger in homogeneities.

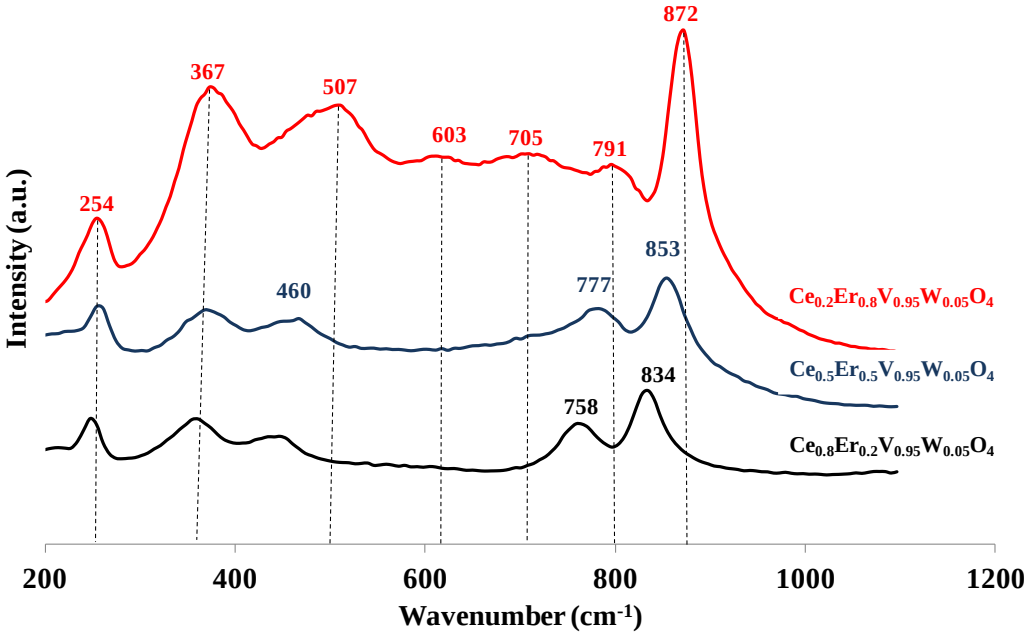

Figure 5.6 – **Raman structure of unaged $Ce_{1-x}Er_xV_{0.95}W_{0.05}O_4$ (X= 0.2, 0.5 and 0.8) catalysts**

1.2.3.2 Aged solids

The Raman spectrum of substituted catalysts after aging at 600°C and 850°C present in Figure 5.7 and 5.8, respectively. Tetragonal $REVO_4$ (RE = Ce and Er) with a point group of D4h has two molecular formula per unit cell with Raman active modes of A_{1g}, B_{1g}, and E_g. The main Raman bands of $REVO_4$ can be observed at around 254, 361, 460, 777, and 853 cm^{-1}. The Raman peak at 853 cm^{-1} (ν_1) is assigned to the A_{1g} symmetric stretching mode of VO_4^{3-}, whereas the Raman peaks observed at 779 cm^{-1} are attributed B_{1g} antisymmetric stretching modes of the vanadates (ν_3), The Raman peaks observed at 460 and 361 cm^{-1} are associated with the B_{1g} and A_{1g} deformations (ν_4 and ν_2), respectively. Similar to the XRD data of $REVO_4$, the hydrothermally synthesized also showed the predominance phase corresponding to $REVO_4$. The B_{2g} bending mode of the VO_4^{3-} tetrahedral can be identified at 254 cm^{-1}. No impurity phase of CeO_2 was detected because pure CeO_2 exhibits an intense Raman band at 460cm^{-1} and less intense Raman bands at 239, 590, and 1174 cm^{-1}, and none of these peaks were observed in the

Raman spectra. The proximity of the CeO_2 mainline (460cm^{-1}) prevents the identification of the CeO_2 phase. It can be seen that all modes undergo noticeable changes in wavenumber, line width, and intensity by erbium content and aging. After aging, $Ce_{0.5}Er_{0.5}V_{0.95}W_{0.05}O_4$ catalyst shows the characteristic line (=~ 700cm^{-1}) associated with Er^{3+} electronic transition.

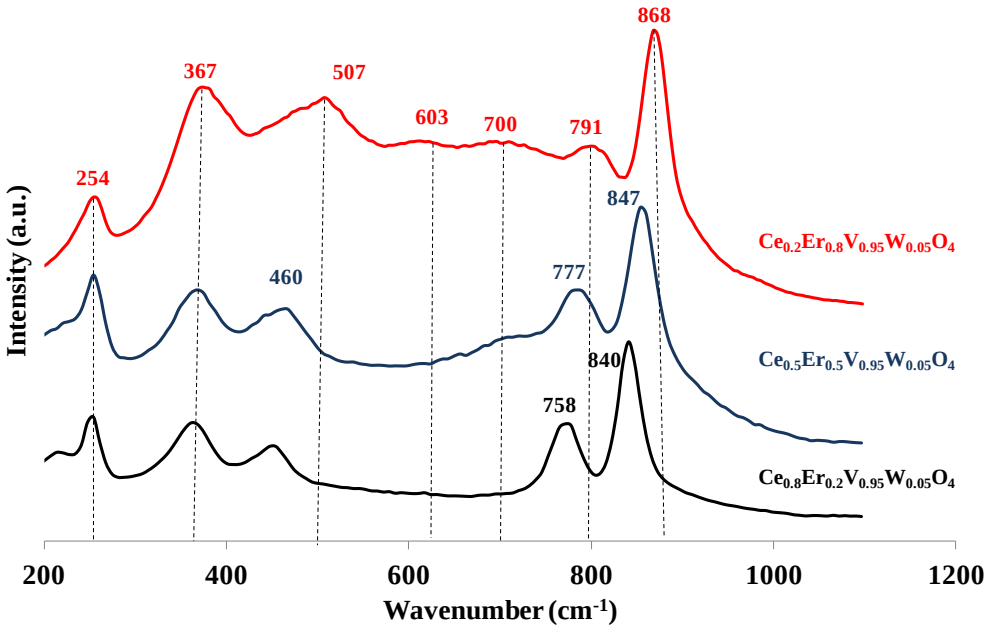

Figure 5.7 – **Raman structure of $Ce_{1-x}Er_xV_{0.95}W_{0.05}O_4$ (X= 0.2, 0.5 and 0.8) catalysts aged at 600°C**

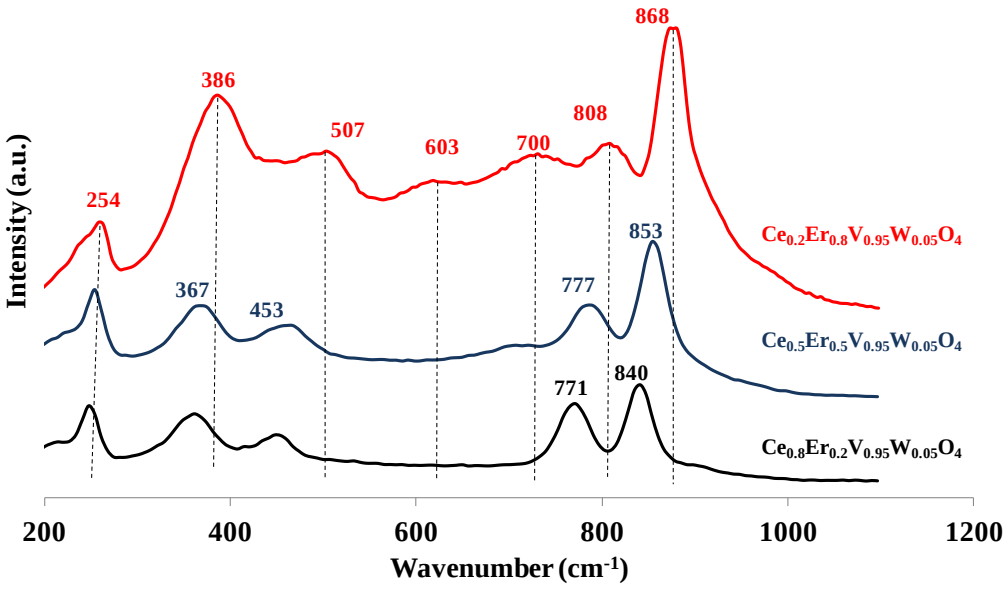

Figure 5.8 – **Raman structure of $Ce_{1-x}Er_xV_{0.95}W_{0.05}O_4$ (X= 0.2, 0.5 and 0.8) catalysts aged at 850°C**

1.2.4 Temperature-programmed reduction (H_2-TPR)

1.2.4.1 Reducibility of unaged solids

H_2-TPR is a very convenient technique for studying the reducibility of the catalysts. The H_2-TPR profiles of $Ce_{1-X}Er_XV_{0.95}W_{0.05}O_4$ (X= 0.2, 0.5 and 0.8) catalysts before aging in the temperature range of 0–1000°C is compared in Figure 5.9. They mimic those earlier discussed with a prominent H_2 uptake above 700°C corresponding to the bulk reduction process of $REV^{+5}O_4 \rightarrow REV^{+3}O_3$ according to Eq. 5.1. Below 700°C, weak and broad signals are discernible. As previously discussed this could reflect equally the reduction of Ce^{4+} to Ce^{3+} and/or segregated $V^{5+}O_x$ to $V^{4+}O_x$.

$$REVO_4 + H_2 = REVO_3 + H_2O \text{ (RE= Ce, and Er) (Equation 5.1)}$$

The estimated values of the H/V atomic ratios from the quantities of consumed hydrogen are equal to 1.9 and 2.0 (Table 5.3), in agreement with the reduction of $REVO_4$ to $REVO_3$. Regarding the maximum reduction temperature, a discontinuity is observable at increasing erbium content with a minimum temperature observed for X = 0.5. By increasing erbium content from 0.2 to 0.5 the H_2 consumption decrease. $Ce_{0.2}Er_{0.8}V_{0.95}W_{0.05}O_4$ catalyst has the highest number of the H_2-consumption compared to other catalysts. The less intense reduction peak observed at low temperature could reflect the reduction of surface Ce^{4+} species to Ce^{3+}. Those observations could also contribute to the reduction of surface V^{5+} species, which is difficult to be distinguished due to the similar reduction temperature.

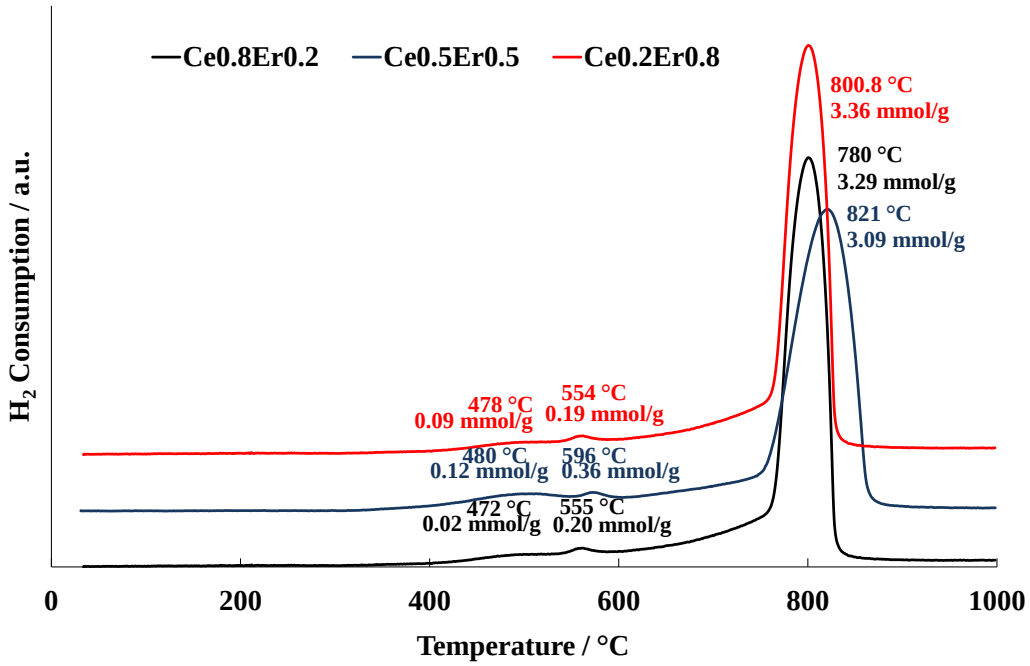

Figure 5.9 – **H_2-TPR of unaged $Ce_{1-x}Er_xV_{0.95}W_{0.05}O_4$ (X= 0.2, 0.5 and 0.8) catalysts**

1.2.4.2 Reducibility of aged samples

The H_2-TPR profiles of the catalysts aged at 600°C and 850°C are presented in Figure 5.10. and 5.11. Obviously, the aging process has a strong detrimental effect on the reducibility. Indeed, a sharp shift of the bulk reduction to the higher temperature is noticeable with a rise in the aging temperature. Such a tendency is more accentuated over $Ce_{0.5}Er_{0.5}V_{0.95}W_{0.05}O_4$ catalyst. However, no deviation of the H/V atomic ratio is discernible. Regarding the weak reduction process, the H_2 uptake slightly increases after aging at 600°C compared to freshly-prepared samples but completely disappears when this thermal treatment proceeds more severely at 850°C. Those observations are not trivial and could reflect complex structural modifications that could alter the surface composition especially if extraction and surface segregation is enhanced at increasing aging temperature. An agglomeration of monomeric vanadium species by getting large V_2O_5 clusters could explain their disappearance through volatilization. However, the absence of significant deviation of vanadium content from

elemental analysis emphasizes the fact that this chemical process is marginal. As a matter of fact, structural recombination could occur then explaining those observations.

Finally, the most prominent observation is likely related to the appearance of a second bulk reduction process on $Ce_{0.2}Er_{0.8}V_{0.95}W_{0.05}O_4$ catalysts near 800°C. This result is interesting because there is no significant structural observation which translates of such change on the reducibility of the catalyst. The remaining shoulder over $Ce_{0.2}Er_{0.8}V_{0.95}W_{0.05}O_4$ catalyst could be related to the reduction of the species in solid solution through a two-step reduction process involving the reduction of vanadium species at grain boundaries and in the bulk of large particles formed after high aging temperature (850°C).

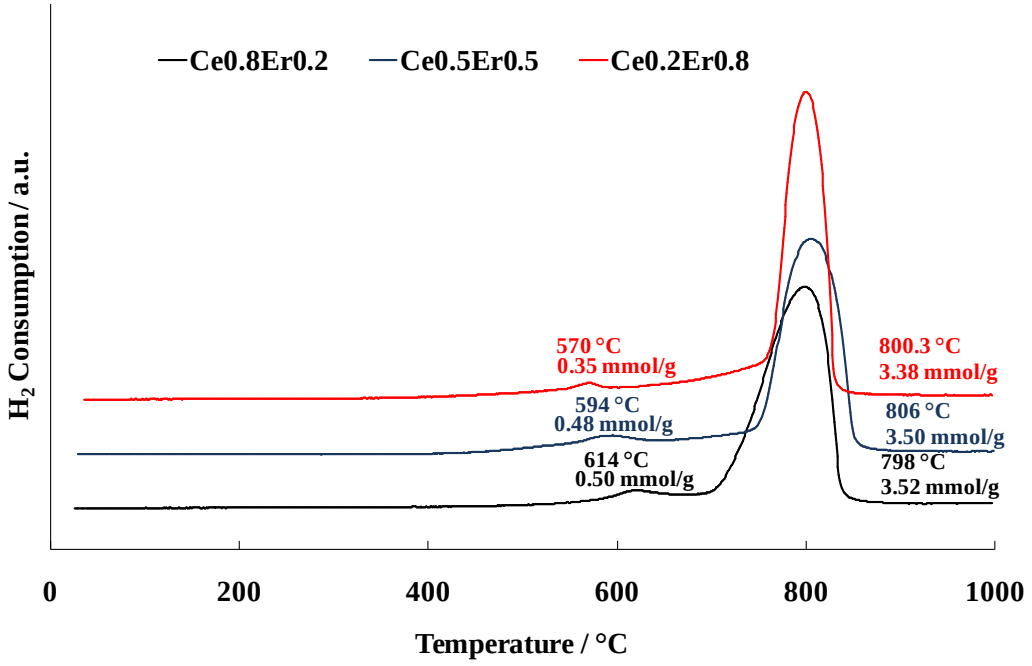

Figure 5.10 – **H_2-TPR of $Ce_{1-X}Er_XV_{0.95}W_{0.05}O_4$ (X= 0.2, 0.5 and 0.8) catalysts aged at 600°C**

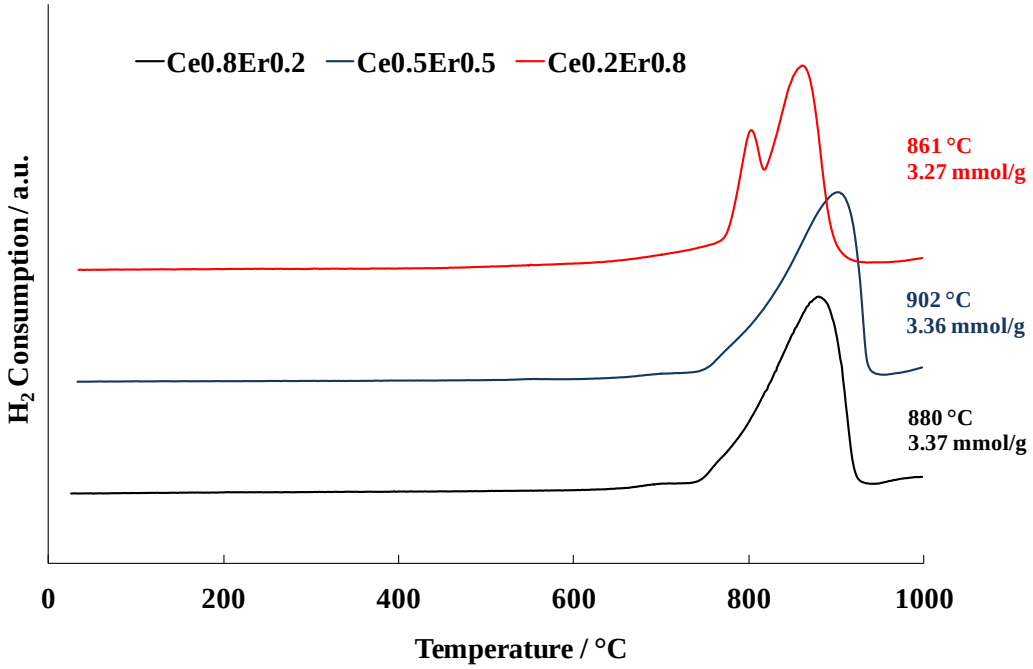

Figure 5.11 – **H_2-TPR of $Ce_{1-x}Er_xV_{0.95}W_{0.05}O_4$ (X= 0.2, 0.5 and 0.8) catalysts aged at 850°C**

Table 5.3 – **H_2-TPR results of $Ce_{1-x}Er_xV_{0.95}W_{0.05}O_4$ (X=0, 0.2, 0.5, 0.8); (70mg, 50ml min^{-1})**

Catalyst	Aging temperature (°C)	H_2 consumption [a] (mmol g^{-1})	H/V	T_{max} reduction peaks
$CeV_{0.95}W_{0.05}O_4$	unaged	3.32	2.00	809.0
	600	3.54	2.10	845.0
	850	3.78	2.10	890.0
$Ce_{0.8}Er_{0.2}V_{0.95}W_{0.05}O_4$	unaged	3.29	2.00	780.0
	600	3.52	2.10	798.0
	850	3.37	2.00	880.0
$Ce_{0.5}Er_{0.5}V_{0.95}W_{0.05}O_4$	unaged	3.09	1.90	821.0
	600	3.50	2.10	806.0
	850	3.36	2.00	902.0
$Ce_{0.2}Er_{0.8}V_{0.95}W_{0.05}O_4$	unaged	3.36	2.00	801.0
	600	3.38	2.00	800.0
	850	3.27	2.00	861.0

[a] Consumption integrated in the temperature range of 700-1000°C

1.2.4.3 Determination of kinetic parameters for the low and high reduction process from H_2-temperature-programmed reduction experiments

In this part, particular attention was paid to the calculation of kinetic parameters corresponding to the low and high reduction temperature processes. In practice, the Kissinger method was used to determine the apparent activation energy as described elsewhere [13, 14]. This method does not need a precise knowledge of the reaction mechanism for the reduction processes. From H_2-TPR profiles, recorded at different heating rates (5°C/min, 10°C/min, 15°C/min, 20°C/min) one can observe a shift of the maxima to the higher temperature at increasing heating rates. Eq. 5.2 can be established suggesting a linear relationship between β/T_{max}^2 vs $1/T_{max}$. Then, the pre-exponential factor and the activation energy can be estimated from the intercept and the slope ($-E_a/R$ with R = 8.31 $J.mol^{-1}.K^{-1}$) respectively of the straight lines.

$$\ln\frac{\beta}{T_{max}^2} = \ln\frac{AR}{E_a} - \frac{E_a}{RT_{max}} \quad \text{(Equation 5.2)}$$

In this formula, β is the heating rate, T_{max} is the absolute temperature (in Kelvin), A is the pre-exponential factor R is the universal gas constant and E_a is the activation energy. The different H_2 uptake profiles vs temperatures are reported in Figs 5.13-18 showing similar tendencies on the low and high-temperature process. The plot $\ln \beta/T^2_{max}$ vs $1/T_{max}$ verifies a linear relationship without significant dispersion allowing a precise estimation of the activation energy values. Regarding the high temperature reduction process corresponding to the bulk reduction of V^{5+} to V^{3+} species stabilized in the zircon-type structure, E_a values for $Ce_{0.8}Er_{0.2}V_{0.95}W_{0.05}O_4$, $Ce_{0.5}Er_{0.5}V_{0.95}W_{0.05}O_4$ and $Ce_{0.2}Er_{0.8}V_{0.95}W_{0.05}O_4$ are respectively 110, 136 and 184 kJ/mol at increasing erbium loading which suggests that the addition of Er in $Ce_{1-X}Er_XV_{0.95}W_{0.05}O_4$ restrained the reduction of $CeVO_4$ to $CeVO_3$. Let us now examine the impact of erbium on the low reduction process. Interestingly, the reverse dependency is discernible with a decrease from 124 to 84 kJ/mol respectively at increasing erbium loading.

Such evolution is consistent with Fig 5.12 showing a surface reduction occurring more readily at the lower temperature.

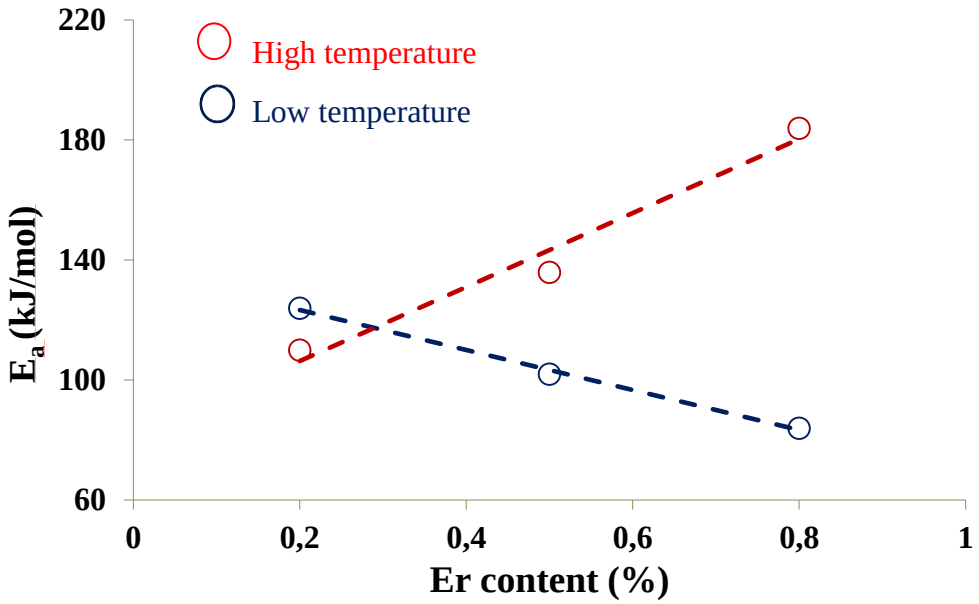

Figure 5.12 – **Activation energy vs the substitution degree of Erbium after aging at 600°C**

The significance of this change is not obvious but could distinguish reduction processes taking place in the bulk and at the surface. Previous tentative assignments ascribed the low process equally to the reduction process of Ce^{4+} to Ce^{3+} or more reducible vanadate species which could segregate at the surface.

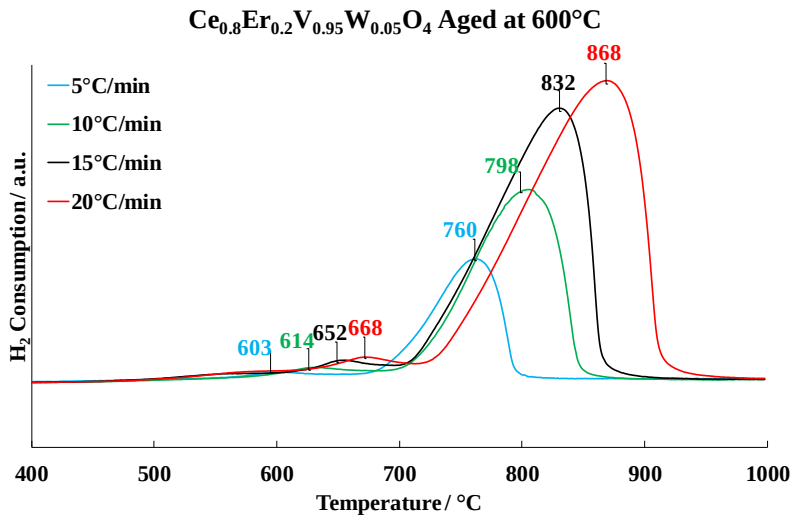

Figure 5.13 – **H_2-TPR profiles of $Ce_{0.8}Er_{0.2}V_{0.95}W_{0.05}O_4$ at different heating rates**

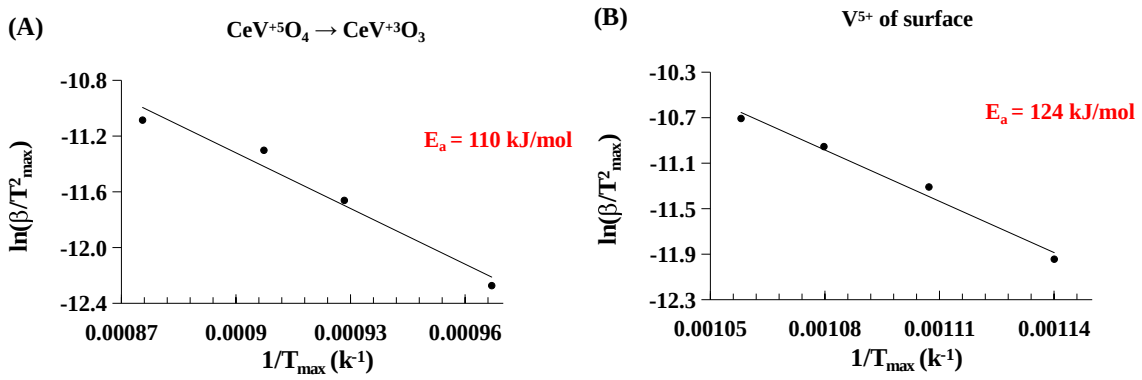

Figure 5.14 – **Kissinger plots for the reduction of $Ce_{0.8}Er_{0.2}V_{0.95}W_{0.05}O_4$, $CeV^{+5}O_4 \rightarrow CeV^{+3}O_3$ (A) and V^{5+} of the surface (B) in a hydrogen atmosphere. Corresponding apparent activation energy (E_a) is given in the profile**

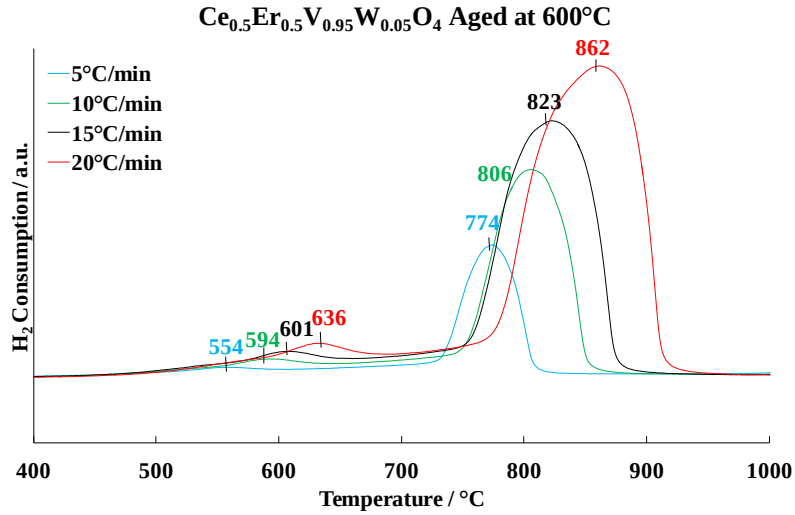

Figure 5.15 – **H_2-TPR profiles of $Ce_{0.5}Er_{0.5}V_{0.95}W_{0.05}O_4$ at different heating rates**

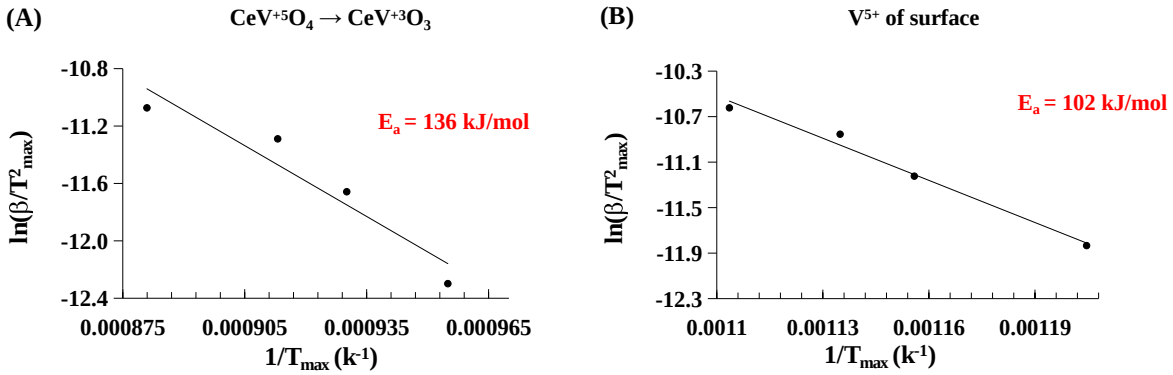

Figure 5.16 – **Kissinger plots for the reduction of $Ce_{0.5}Er_{0.5}V_{0.95}W_{0.05}O_4$, $CeV^{+5}O_4 \rightarrow CeV^{+3}O_3$ (A) and V^{5+} of surface (B) in a hydrogen atmosphere. Corresponding apparent activation energy (E_a) is given in the profiles**

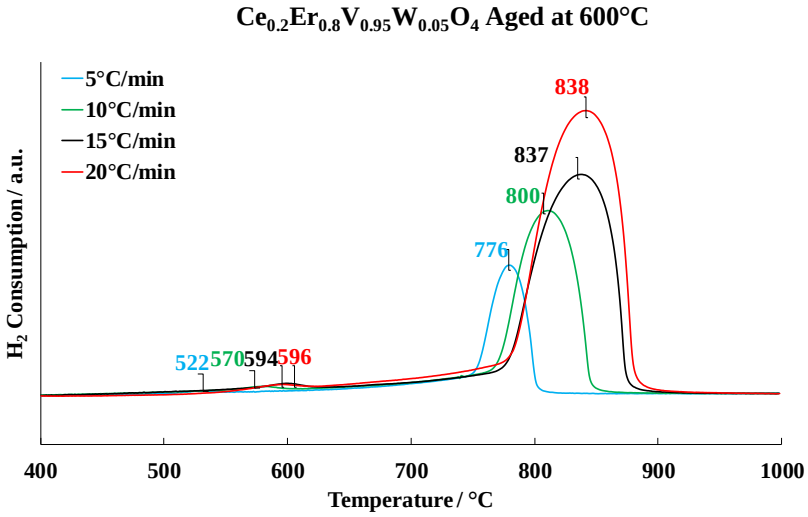

Figure 5.17 – **H_2-TPR profiles of $Ce_{0.2}Er_{0.8}V_{0.95}W_{0.05}O_4$ at different heating rates**

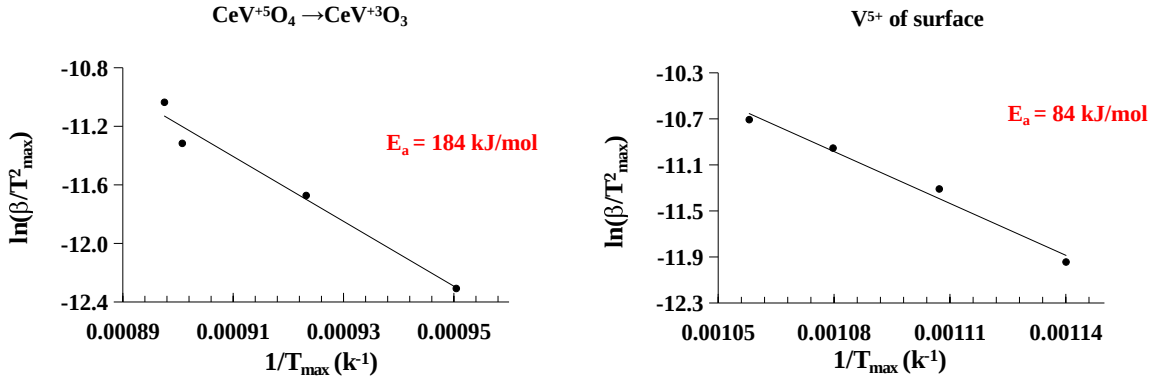

Figure 5.18 – **Kissinger plots for the reduction of $Ce_{0.2}Er_{0.8}V_{0.95}W_{0.05}O_4$, $CeV^{+5}O_4 \rightarrow CeV^{+3}O_3$ (A) and V^{5+} of surface (B) in a hydrogen atmosphere. Corresponding apparent activation energy (E_a) is given in the profile**

1.3 Surface characterizations

1.3.1 Specific surface area

The specific surface area (SSA) of $Ce_{1-X}Er_XV_{0.95}W_{0.05}O_4$ (X=0, 0.2, 0.5, and 0.8) catalysts before and after aging can be seen in Table 5.4. The experimental surface S_{exp} ($m^2.g^{-1}$) is determined by physical adsorption of nitrogen on the surface of the solid and theoretical surface S_{th} ($m^2.g^{-1}$) is calculated from the size of cubic crystallites $S_{th}=6/\rho D_\rho$ by XRD. As summarized in Table 5.4, the incorporation of Er into $CeV_{0.95}W_{0.05}O_4$ catalyst enhanced the BET surface area, reaching a maximum for the composition $Ce_{0.5}Er_{0.5}V_{0.95}W_{0.05}O_4$ (118 $m^2.g^{-1}$). The specific surface area for the unaged $Ce_{0.5}Er_{0.5}V_{0.95}W_{0.05}O_4$ sample was quite high before aging, but it decreased greatly after aging at 600°C. The unaged $Ce_{0.2}Er_{0.8}V_{0.95}W_{0.05}O_4$ catalyst has a lower specific surface area compared to the other samples but the impact of aging at 600°C was less severe than for the other catalysts. All three samples end up with roughly the same specific surface area after aging at 850°C. The difference between S_{exp} values and S_{th} values can be explained by the increase in $REVO_4$ crystallite size due to agglomeration of crystallites after aging. The aging at 600°C mainly leads to a crystal growth since the S_{exp} values and S_{th} values remain very close. When the aging is performed at 850°C, there are strong differences between S_{exp} values and S_{th} values, owing to the thermal sintering through both growth and agglomeration of crystallites. The results above show that the incorporation of a certain amount of Er into the zircon-type structure can increase the specific surface area, which should be beneficial for enhancing the catalytic performance of these catalysts as shown in section 1.4 and 1.5.

Table 5.4 – **Influence of cerium substitution by rare earth element and hydrothermal aging on the specific surface area**

Catalyst	Aging temperature (°C)	Experimental specific surface area S_{exp} ($m^2.g^{-1}$)	Theoretical specific surface area S_{th} ($m^2.g^{-1}$)
$CeV_{0.95}W_{0.05}O_4$	Unaged	56	60
	600	18	23
	850	2	12
$Ce_{0.8}Er_{0.2}V_{0.95}W_{0.05}O_4$	Unaged	105	97
	600	43	54
	850	4	20
$Ce_{0.5}Er_{0.5}V_{0.95}W_{0.05}O_4$	Unaged	118	106
	600	58	86
	850	4.5	28
$Ce_{0.2}Er_{0.8}V_{0.95}W_{0.05}O_4$	Unaged	68	70
	600	40	43
	850	4.5	28

1.3.2 X-ray photoelectron spectroscopy (XPS)

XPS measurements were performed to obtain information about the surface elemental compositions and valence states of the catalysts. Binding energy values were calibrated using the C 1s core level at 284.8 eV as the reference to eliminating the possible charging effect that may occur because of surface contamination. Fig 5.19 displays the Ce 3d XPS spectrum of the $Ce_{1-X}Er_XV_{0.95}W_{0.05}O_4$ (X= 0.2, 0.5 and 0.8) catalysts. The Ce 3d spectra are complicated and can be individually deconvoluted into $3d_{5/2}$ and $3d_{3/2}$ spin-orbit components (labeled as v and u, respectively) describing the $Ce^{4+}\leftrightarrow Ce^{3+}$ electronic transitions as previously illustrated in Figure 4.15. No obvious difference was observed from the Ce 3d XPS spectra of samples.

The Ce^{4+}/Ce^{3+} ratio was calculated, and the results are summarized in Table 5.5. The Ce^{4+}/Ce^{3+} ratio of unaged catalysts is equal to 0.24 for $Ce_{0.8}Er_{0.2}V_{0.95}W_{0.05}O_4$ catalyst, but a bit higher, about 0.36 for $Ce_{0.5}Er_{0.5}V_{0.95}W_{0.05}O_4$ catalyst and is equal to 0.42 over $Ce_{0.2}Er_{0.8}V_{0.95}W_{0.05}O_4$ catalyst. The Ce^{4+}/Ce^{3+} ratio increased for all catalysts by increasing the aging temperature. The

Ce^{4+}/Ce^{3+} atomic ratio is influenced by the change in the crystalline size of $CeVO_4$ and CeO_2 particles during the aging procedure.

On the other hand, the higher Ce^{4+}/Ce^{3+} ratio may result in the higher SCR activity due to the intensified oxygen storage between Ce^{4+} and Ce^{3+} via the following equations $2CeO_2 \rightarrow Ce_2O_3 + O^*$ and $Ce_2O_3 + 1/2\ O_2 \rightarrow 2CeO_2$, which can promote the oxidation of NO to NO_2 [11]. Besides, a slight shift in the Ce 3d spectra towards higher binding energies can be observed over all samples. These results indicate that erbium has a strong interaction with cerium species.

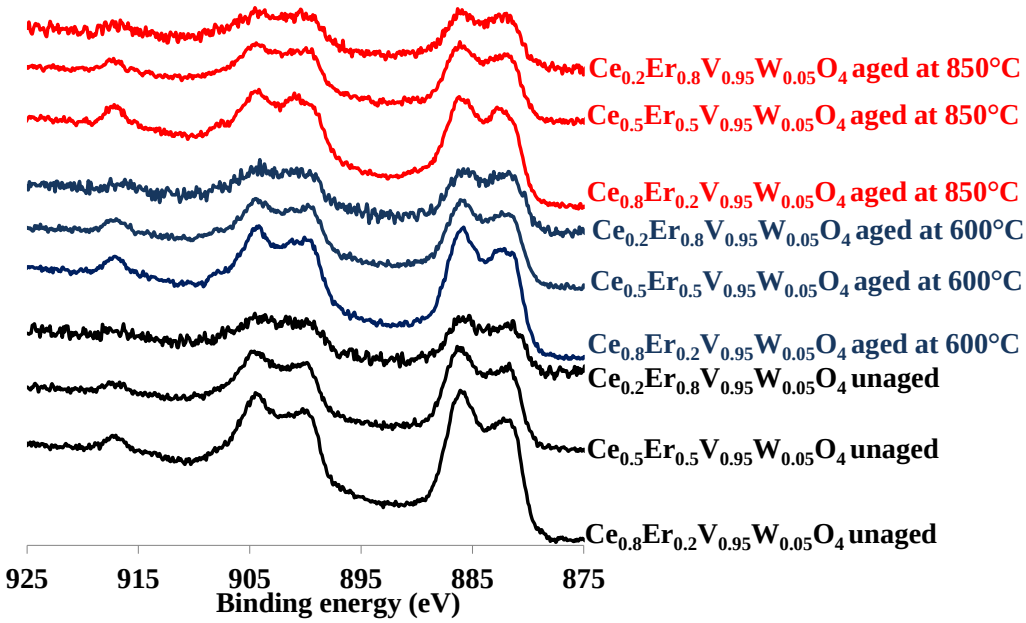

Figure 5.19 – **XPS Spectra of Ce 3d core level of the $Ce_{1-x}Er_xV_{0.95}W_{0.05}O_4$ (X=0.2, 0.5, 0.8) catalysts**

The XPS core level spectra of erbium (Er) 4d obtained before and after aging at 600°C and 850°C illustrated in Fig 5.20. The Er 4d spectra show a doublet peak appears at binding energy 168.3 and 170.5 eV corresponding to Er $4d_{5/2}$ and Er $4d_{5/2}$ respectively along with satellite peaks (at binding energy 174, 176.4 and 182.2 eV) as previously described in chapter 4 and which is characteristic of Er^{3+}. This is in agreement with the partial substitution of Ce^{3+} by Er^{3+} in the

zircon-type structure. No additional peak can be observed by increasing the degree of cerium substitution by erbium.

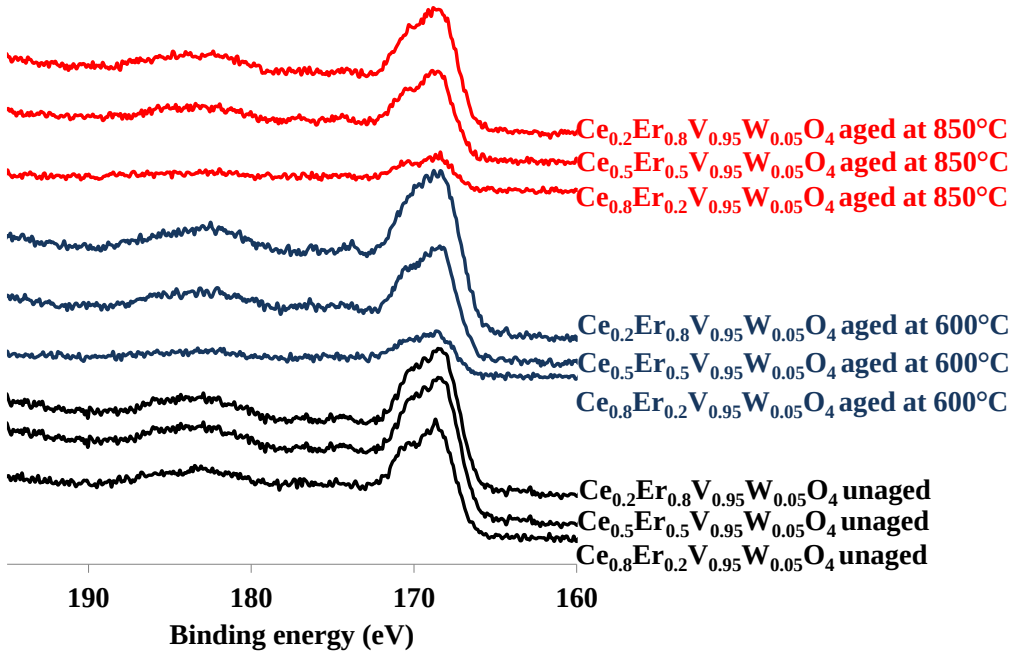

Figure 5.20 – **XPS Spectra of Er 4d core level of the $Ce_{1-x}Er_xV_{0.95}W_{0.05}O_4$ (X=0.2, 0.5, 0.2) catalysts**

As previously discussed, the surface concentration of O_α could be the important parameters because of its inherent activity to oxidize NO to NO_2 recognized as a key intermediate in the overall SCR process.

For the V 2p spectrum, the binding energy separation between core levels V $2p_{1/2}$ (524.9 eV) and V $2p_{3/2}$ (517.6 eV) is ~7.3 eV, corresponding well to the electronic states of V^{5+} in V_2O_5 or zircon-type structure as previously discussed. The binding energies for the photopeak V $2p_{3/2}$ remain almost unchanged that revealed low sensitivity to the amount of erbium and hydrothermal aging.

The relative concentrations of elements Ce, Er, V and W for $Ce_{1-x}Er_xV_{0.95}W_{0.05}O_4$ catalysts aged at different temperatures are reported in Table 5.5. It can be seen that the Ce/O atomic

ratio values progressively decrease when the degree of substitution increases and also this ratio is stable for each catalyst after aging at 600°C and 850°C. The RE/Ce, W/V, V/(Ce+RE), W/(Ce+RE) and (V+W)/(Ce+RE) ratios are close to the theoretical value for all unaged catalysts, the difference remains less than 10%, which is acceptable given the uncertainty of the XPS spectroscopy. Furthermore, the relative concentration of W on the surface of catalysts increases by aging.

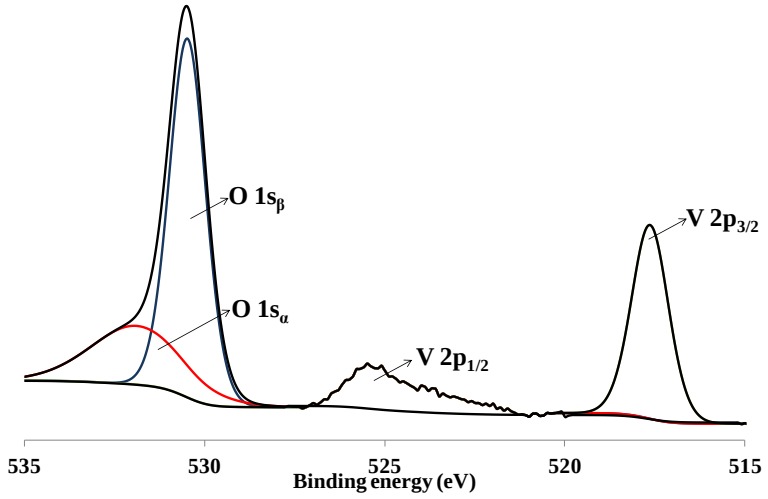

Figure 5.21 – **Fitted Spectra of V 2p and O 1s core level of the unaged $Ce_{0.5}Er_{0.5}V_{0.95}W_{0.05}O_4$**

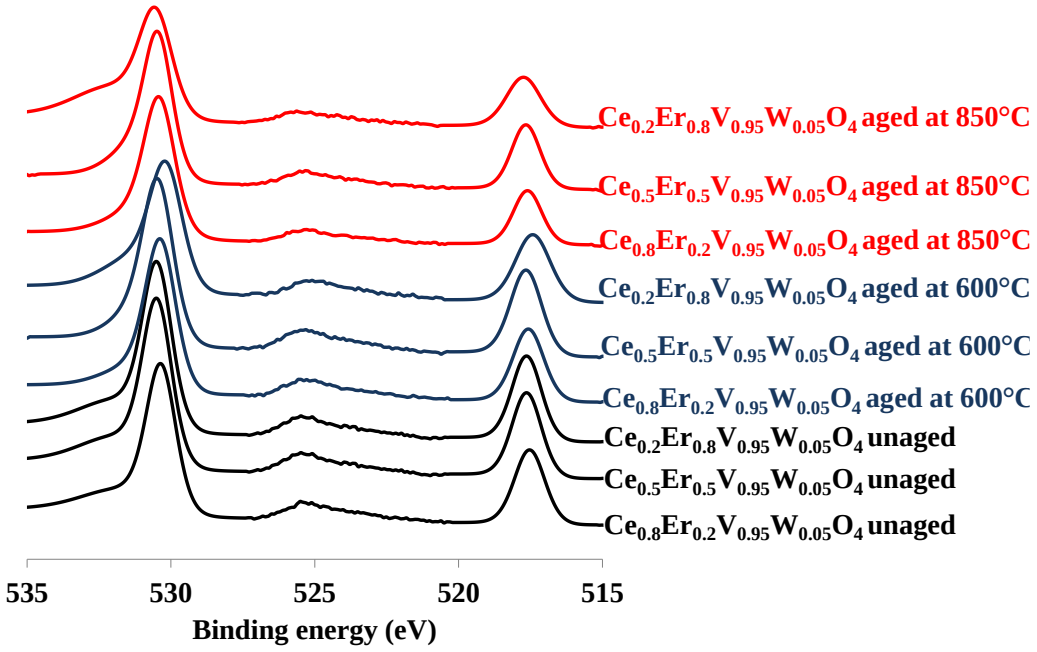

Figure 5.22 – **XPS Spectra of V 2p and O 1s core level of the $Ce_{1-X}Er_XV_{0.95}W_{0.05}O_4$ (X=0.2, 0.5, and 0.8) catalysts**

The 4f energy level of tungsten splits into two energy levels of $4f_{7/2}$ and $4f_{5/2}$ with energy splitting of 2.15 eV due to the spin-orbit coupling. Fig 5.23 illustrates the XPS photopeaks of W (4f) of $Ce_{1-X}Er_XV_{0.95}W_{0.05}O_4$ catalysts, with different aging temperatures. The 4f profile can be fitted by two peaks centered at 37.7 and 35.5 eV which are, respectively, the binding energy of electrons in the $4f_{5/2}$ and $4f_{7/2}$ levels of tungsten in the W^{+6} oxidation state, indicating that all catalysts are composed of tungstate species. The amount of W on the surface of catalysts increases as the aging temperature increases.

The broad peak at 32 eV for $Ce_{0.5}Er_{0.5}V_{0.95}W_{0.05}O_4$ catalysts is representative of Er $2p_{1/2}$. By increasing the erbium percentages, the intensity of this peak increases consequently as well as surface concentration.

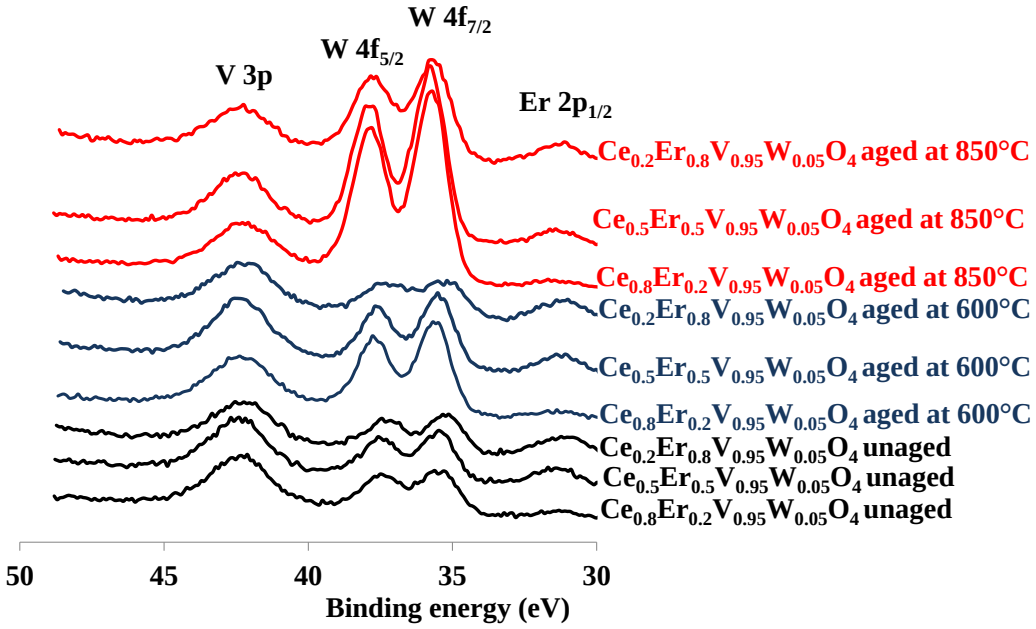

Figure 5.23 – **XPS Spectra of V 3p, W 4f, and Er$2p_{1/2}$ core level of the $Ce_{1-X}Er_XV_{0.95}W_{0.05}O_4$ (X=0.2, 0.5, and 0.8) catalysts**

The semi-quantitative analysis shows rather the same trends as those earlier discussed in chapter 4. The atomic ratios for vanadium and tungsten clearly indicate a preferential tungsten enrichment which impacts the W/V ratio. The decrease observed on the atomic O_α/O_β ratio

seems also consistent with a lowering of Ce^{3+} corresponding to an increase of the Ce^{4+}/Ce^{3+} ratio.

Table 5.5 – **Surface atomic composition of $Ce_{1-x}Er_xV_{0.95}W_{0.05}O_4$ (Er=0.2, 0.5 and0.8) catalysts**

Catalyst	Aging temperature (°C)	W/V	V/ (Ce+Er)	W/ (Ce+Er)	(V+W)/ (Ce+Er)	Ce^{4+}/Ce^{3+}	O_α/O_β	B.E.(eV) V 2p
	unaged	0.14	-	-	-	0.22	0.37	517.5
$CeV_{0.95}W_{0.05}O_4$	600	0.33	-	-	-	0.31	0.35	517.5
	850	0.46	-	-	-	0.31	0.38	517.5
	unaged	0.07	0.81	0.05	0.90	0.24	0.54	517.5
$Ce_{0.8}Er_{0.2}V_{0.95}W_{0.05}O_4$	600	0.13	0.82	0.11	0.95	0.32	0.30	517.6
	850	0.40	0.70	0.25	1	0.36	0.40	517.6
	unaged	0.06	0.08	0.05	1.00	0.36	0.60	517.5
$Ce_{0.5}Er_{0.5}V_{0.95}W_{0.05}O_4$	600	0.08	0.90	0.08	1.00	0.45	0.50	517.5
	850	0.30	0.80	0.20	1.00	0.80	0.40	517.5
	unaged	0.05	0.95	0.06	1.19	0.42	0.75	517.4
$Ce_{0.2}Er_{0.8}V_{0.95}W_{0.05}O_4$	600	0.06	1.00	0.07	1.12	0.46	0.70	517.4
	850	0.19	0.90	0.17	1.06	0.65	0.50	517.7

Catalyst	Aging temperature (°C)	Ce/O	V/O	V/Ce	W/Ce	Er/Ce
	unaged	0.23	0.21	0.89	0.13	-
$CeV_{0.95}W_{0.05}O_4$	600	0.17	0.17	0.96	0.32	-
	850	0.21	0.15	0.72	0.33	-
	unaged	0.25	0.22	0.90	0.06	0.19
$Ce_{0.8}Er_{0.2}V_{0.95}W_{0.05}O_4$	600	0.23	0.23	1.00	0.14	0.20
	850	0.22	0.17	0.80	0.3	0.22
	unaged	0.12	0.20	1.40	0.05	0.80
$Ce_{0.5}Er_{0.5}V_{0.95}W_{0.05}O_4$	600	0.14	0.22	1.60	0.14	0.80
	850	0.16	0.20	1.20	0.21	0.65
	unaged	0.05	0.24	4.20	0.25	3.00
$Ce_{0.2}Er_{0.8}V_{0.95}W_{0.05}O_4$	600	0.05	0.18	4.00	0.26	3.00
	850	0.05	0.18	3.00	0.60	3.20

1.4 Surface acidity from pyridine adsorption-desorption experiments

As one of the most important surface properties for SCR reaction, the number of acid sites was critical to the adsorption of NH_3 and the followed SCR reaction cycles. Pyridine is one of the most largely used basic probe molecule to characterize the surface acidity of catalysts. In the present case, infrared spectroscopy of adsorbed pyridine was used to determine the influence of the ceria/Erbium ratio on the nature of the acid sites of the catalysts. The IR spectra of pyridine adsorbed onto catalyst at 25°C and desorbed at various temperatures are shown in Fig. 5.24. IR bands ascribed to the ring deformation of pyridine appear in the range 1400–1700 cm^{-1} and allow the discrimination of Brönsted and Lewis sites. Infrared bands at 1603 cm^{-1} (ν_{8a}), 1574 (ν_{8b}), 1490 (ν_{19a}), 1443 cm^{-1} (ν_{19b}) were previously ascribed to the vibrational modes of pyridine adsorbed on Lewis acid sites whereas IR bands located at 1640 cm^{-1} (ν_{8a}), 1540 (ν_{19b}), are currently ascribed to pyridinium ion formed after coordination with Brönsted acid sites [12,13]. Let us note that Brönsted acid sites were not detected on this series of catalysts. Lewis acid sites (LAS) are evidenced by the bands at 1443 cm^{-1} and 1605 cm^{-1}. The intensity of the first one is related to the number of LAS, whereas the position of the second band characterizes the strength of LAS. Normalized pyridine uptake has been estimated from the integration of IR bands at 1603 cm^{-1} and 1443 cm^{-1} by using the absorption coefficient of Lewis acid sites as reported elsewhere [14]. The concentrations of Lewis acid sites at 150°C on the $Ce_{0.5}Er_{0.5}V_{0.95}W_{0.05}O_4$, $Ce_{0.5}Er_{0.5}V_{0.95}W_{0.05}O_4$ and $Ce_{0.2}Er_{0.8}V_{0.95}W_{0.05}O_4$ catalysts are 5.6, 34.2 and 3.5 μmol/g, respectively. Accordingly, the highest number of LAS was found on $Ce_{0.5}Er_{0.5}V_{0.95}W_{0.05}O_4$ catalyst. As expected, the ammonia storage capacity decreased with increasing temperature, showing that the strength of the acidic sites of these catalysts is rather weak. By increasing the temperature up to 450°C no more LAS can be detected over all catalysts.

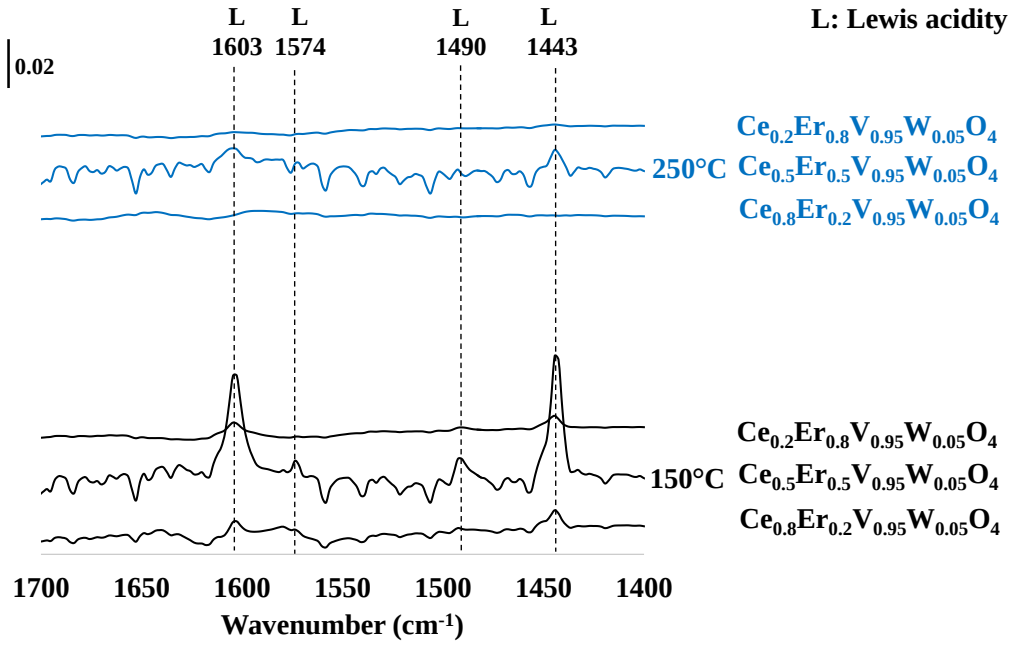

Figure 5.24 – **IR spectra of adsorbed pyridine after desorption at 150°C, 250°C, 350°C, 450°C on $Ce_{1-x}Er_xV_{0.95}W_{0.05}O_4$ (X=0, 0.2, 0.5, and 0.8) catalysts after aging in ex situ conditions in wet atmosphere (air + 10 vol.% H_2O) at 600°C**

Table 5.6 – **Normalized amount of Lewis acidity (µmol.g^{-1}) according to the desorption temperature of pyridine over $Ce_{1-x}Er_xV_{0.95}W_{0.05}O_4$ (X=0, 0.2, 0.5, and 0.8) catalysts aged at 600°C**

Catalyst	Normalized amount of Lewis acidity (µmol.g^{-1}) Desorption temperature			
	150°C	250°C	350°C	450°C
$Ce_{0.8}Er_{0.2}V_{0.95}W_{0.05}O_4$	5.60	0.00	0.00	0.00
$Ce_{0.5}Er_{0.5}V_{0.95}Wo_{0.05}O_4$	34.20	9.20	5.90	0.00
$Ce_{0.2}Er_{0.8}V_{0.95}W_{0.05}O_4$	3.50	0.90	0.60	0.00

1.5 Catalytic activity of $Ce_{1-X}Er_XV_{0.95}W_{0.05}O_4$ (X=0, 0.2, 0.5, and 0.8) catalysts after hydrothermal aging at 600°C

1.5.1 Ammonia-selective catalytic reduction of NO_x to nitrogen in "Standard" condition: $NO/NO_x=1$

In the absence of NO_2 in the inlet reaction mixture, the removal of NO proceeds via standard-SCR reaction. It is noted that these conditions are the least desirable with conversion levels lower than those recorded in fast and NO_2-SCR over the entire temperature range. The influence of the temperature on the NH_3-SCR performances of $Ce_{1-X}Er_XV_{0.95}W_{0.05}O_4$ (X=0, 0.2, 0.5, and 0.8) catalysts, aged at 600°C are presented in Figure 5.25. As discussed, two different kinetic regimes are distinguishable at low and high temperature. The conversion profiles vs. T recorded on $Ce_{0.8}Er_{0.2}V_{0.95}W_{0.05}O_4$ and $CeV_{0.95}W_{0.05}O_4$ are superimposed in the whole ranges of temperature suggesting a weak effect of Er at low concentration in the whole temperature range. At the higher erbium content, an optimal concentration is observed leading to the highest concentration over $Ce_{0.5}Er_{0.5}V_{0.95}W_{0.05}O_4$ catalyst. It seems obvious that high content of erbium has a detrimental effect on the selective conversion of NO to nitrogen with a narrower operating window likely due to ammonia oxidation that occurs more readily. However, a strong decline is observable above those temperatures leading to the worst conversion due to the competitive oxidation of NH_3 with oxygen. All catalysts possessed of the high N_2 selectivity (100%) in the whole temperature range.

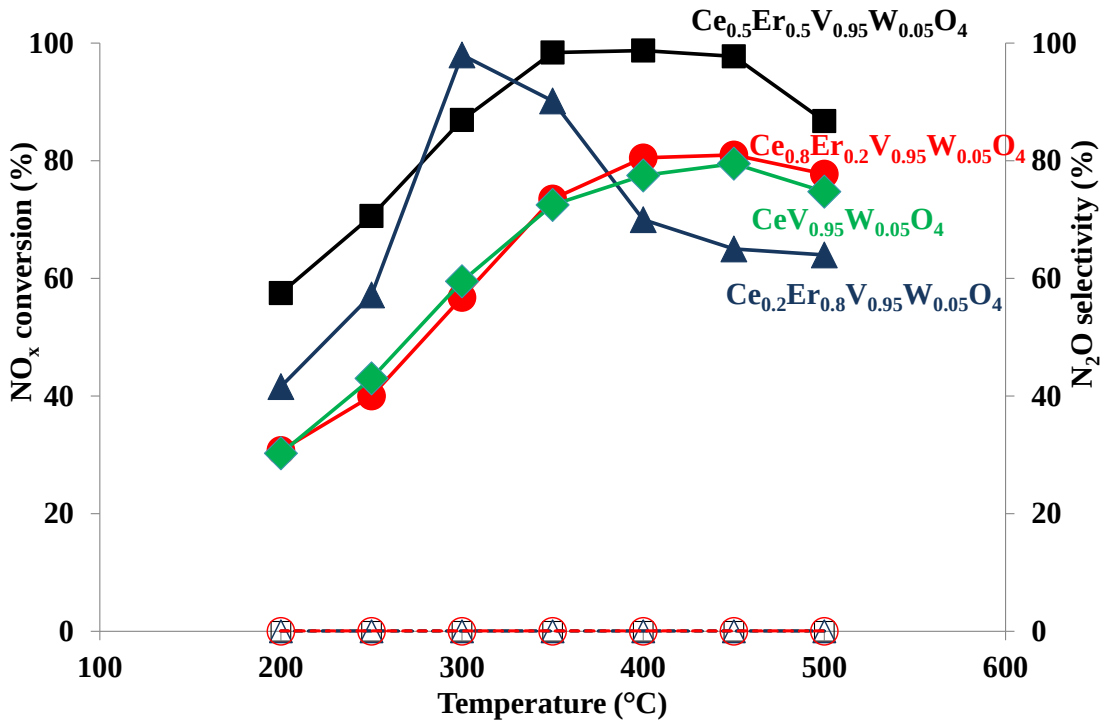

Figure 5.25 – **NO_x conversion (solid lines) and N_2O selectivity (dotted lines) of $Ce_{1-x}Er_xV_{0.95}W_{0.05}O_4$ catalysts in standard-SCR condition aged at 600°C**

1.5.2 Ammonia-selective catalytic reduction of NO_x to nitrogen in "fast" condition: $NO/NO_x = 0.5$

Under Fast-SCR conditions, an equimolar mixture of NO and NO_2 is introduced into the reactor. These conditions are obtained in a post-treatment system provided to oxidize a fraction of NO to NO_2 on DOC (Diesel Oxidative Catalyst) located upstream of the SCR catalyst. The influence of the degree of cerium substitution by erbium over the catalysts on the NO_x conversion and N_2 selectivity as a function of reaction temperatures presented in Figure 5.26. The catalytic activity of $Ce_{1-X}Er_XV_{0.95}W_{0.05}O_4$ (X=0, 0.2, and 0.5) catalysts does not affect a lot by temperature changes. The NO_x conversion of $Ce_{0.8}Er_{0.2}V_{0.95}W_{0.05}O_4$ catalyst is 85% between 200-450°C. Above 450°C, the NO_x conversion slightly decreases to 80% at 500°C. The NO_x conversion of $Ce_{0.5}Er_{0.5}V_{0.95}W_{0.05}O_4$ catalyst reaches 95% between 200 to 450°C. At 500°C, the NO_x conversion decreases and reaches 80%. The NO_x conversion of $Ce_{0.2}Er_{0.8}V_{0.95}W_{0.05}O_4$ catalyst increases from 60% to a maximum of 80% at 300°C. As a matter of fact, the worst

catalytic properties are obtained on $Ce_{0.2}Er_{0.8}V_{0.95}W_{0.05}O_4$ catalyst with a maximum conversion limited to 60%. Similarly, a significant NO_x conversion drop occurs when above 300°C. The NO_x conversion of $Ce_{0.2}Er_{0.8}V_{0.95}W_{0.05}O_4$ catalyst decreases to 40% at 500°C, which accentuates the trend observed in standard-SCR conditions. It seems obvious that the most active and selective catalyst over the entire temperature range is $Ce_{0.5}Er_{0.5}V_{0.95}W_{0.05}O_4$ catalyst. It can be concluded that the degree of erbium substitution plays an important role in the NH_3-SCR activity since the catalytic activity varies to a large extent for the different samples. As observed in both figures 5.25 and 26, the conversions recorded in fast-SCR conditions are much higher compared to standard conditions, especially at low temperature. As earlier explained, a faster re-oxidation of vanadate species by NO_2 and/or adsorbed nitrates rather than oxygen can explain these results. Traces of N_2O were detected in fast SCR condition. $CeV_{0.95}W_{0.05}O_4$ catalyst exhibits the highest selectivity towards nitrogen formation, whereas $Ce_{0.2}Er_{0.8}V_{0.95}W_{0.05}O_4$ has the least selectivity in the temperature region 200–450°C. The N_2 selectivity of the $Ce_{0.8}Er_{0.2}V_{0.95}W_{0.05}O_4$ catalyst decreases noticeably at 500°C with quite a large formation of N_2O.

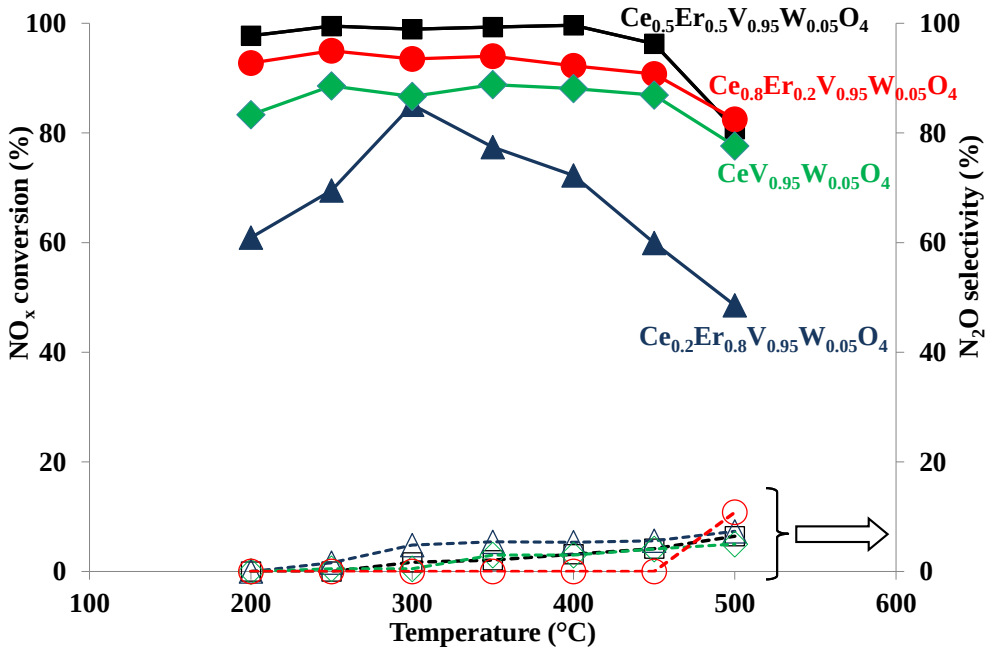

Figure 5.26 – **NO_x conversion (solid lines) and N_2O selectivity (dotted lines) of $Ce_{1-x}Er_xV_{0.95}W_{0.05}O_4$ catalysts in fast-SCR condition aged at 600°C**

1.5.3 Ammonia-selective catalytic reduction of NO_x to nitrogen in "NO_2" condition: NO/NO_x =3/10

In this subsection, the effect of an excess of nitrogen dioxide in the reaction mixture (NO_2-SCR) has been analyzed. Interestingly, significant changes in NO_x conversion are clearly observable with regards to erbium percentage. The reference catalyst ($CeV_{0.95}W_{0.05}O_4$) exhibits poor catalytic activity at the low temperature. By contrast, a significant enhancement of NO_x conversion is observed for the Er-containing samples and especially $Ce_{0.5}Er_{0.5}V_{0.95}W_{0.05}O_4$ catalyst. $Ce_{0.8}Er_{0.2}V_{0.95}W_{0.05}O_4$ catalyst exhibits a steady increase of NO_x conversion from 57% conversion at 200°C with a maximum NO_x conversion of 92% at 400°C. At high temperatures, the oxidation of NH_3 with oxygen leads to lower NO_x conversion. The NO_x conversion obviously declines when the temperature rises to 500°C. The NO_x conversion decreases to 83% at 500°C due to the oxidation of NH_3 with oxygen that leads to lower NO_x conversion. NO_x conversion over $Ce_{0.5}Er_{0.5}V_{0.95}W_{0.05}O_4$ catalyst increases from 80% at 200°C to a maximum of 95% in a temperature range of 350–450°C and afterward starts to decreases. Higher NO_x conversion capability and broader operating temperature window were obtained on $Ce_{0.5}Er_{0.5}V_{0.95}W_{0.05}O_4$ catalyst. The ammonia oxidation is especially delayed at the high temperature on $Ce_{0.5}Er_{0.5}V_{0.95}W_{0.05}O_4$ compared to other catalysts. $Ce_{0.2}Er_{0.8}V_{0.95}W_{0.05}O_4$ catalyst exhibits lower NO_x conversion with the maximum NO_x conversion of 45% at 300°C, while limited conversion enhancement achieves compared to $Ce_{0.8}Er_{0.2}V_{0.95}W_{0.05}O_4$ catalyst at 250–350°C. The NO_x conversion of $Ce_{0.2}Er_{0.8}V_{0.95}W_{0.05}O_4$ catalyst increases from 56% at 200°C to a maximum of 98% at 350°C. The NO_x conversion of $Ce_{0.2}Er_{0.8}V_{0.95}W_{0.05}O_4$ catalyst decreases from 82% to 62% from 400 to 500°C respectively. $Ce_{0.5}Er_{0.5}V_{0.95}W_{0.05}O_4$ catalyst is the most selective catalyst toward N_2. At high temperature, N_2 selectivity slightly decreased. Remarkably, the N_2 selectivity of $Ce_{0.8}Er_{0.2}V_{0.95}W_{0.05}O_4$ catalyst remains above 98% at 200–300°C while it decreases above 300°C with quite a large formation of N_2O.

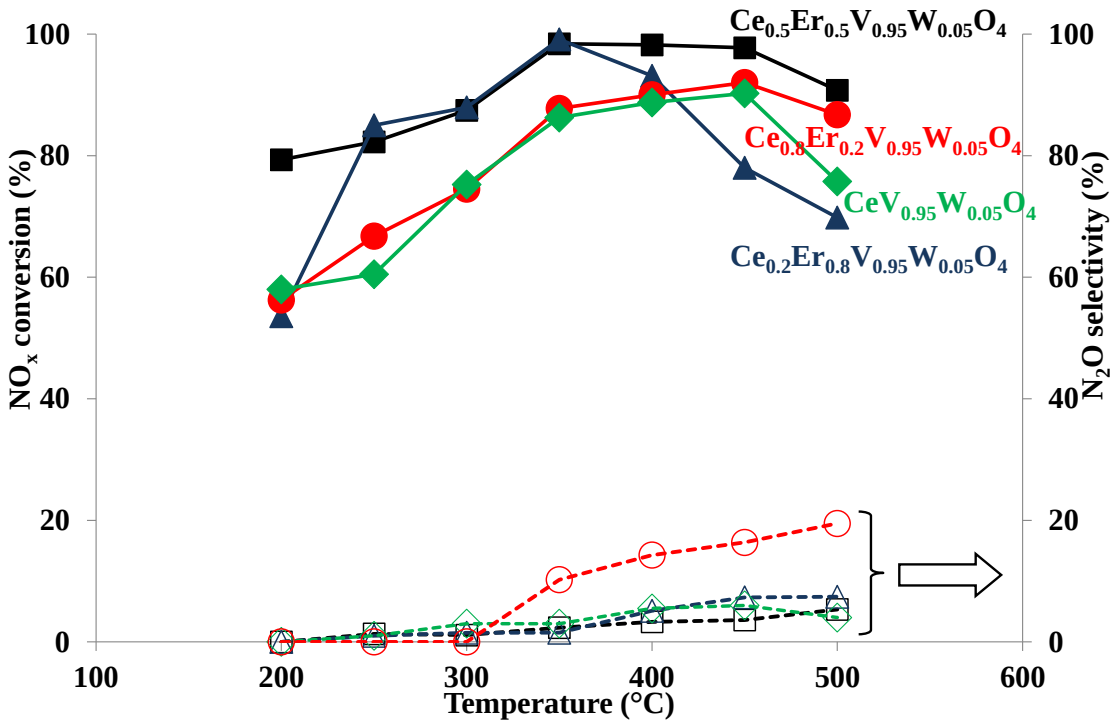

Figure 5.27 – **NO_x conversion (solid lines) and N_2O selectivity (dotted lines) of $Ce_{1-x}Er_xV_{0.95}W_{0.05}O_4$ catalysts in NO_2-SCR condition aged at 600°C**

1.6 Catalytic activity of $Ce_{1-X}Er_XV_{0.95}W_{0.05}O_4$ (X=0, 0.2, 0.5, and 0.8) catalysts after hydrothermal aging at 850°C

1.6.1 Ammonia-selective catalytic reduction of NO_x to nitrogen in "Standard" condition: NO/NO_x =1

According to Fig 5.28, the de-NO_x ability of all catalysts decreases after hydrothermal aging at 850°C which might be first due to the sintering of the active component and/or changes in surface compositions. The NO_x conversion of $Ce_{0.8}Er_{0.2}V_{0.95}W_{0.05}O_4$ reaches 15% at 200°C, a maximum of 22% is recorded near 250–400°C and NO_x conversion decreases slightly to 18% at 500°C. Regarding $Ce_{0.5}Er_{0.5}V_{0.95}W_{0.05}O_4$, the NO_x conversion is significantly enhanced with the maximum NO_x conversion of 65% at 300°C compared to other catalysts. A rise in temperature induces a significant loss of NO_x conversion from 65 to 37% at 500°C. $Ce_{0.5}Er_{0.5}V_{0.95}W_{0.05}O_4$ catalyst compared to the reference $CeV_{0.95}W_{0.05}O_4$ shows higher NO_x conversion (200–400°C). Surprisingly, temperature increase does not induce a loss of

conversion over $Ce_{0.2}Er_{0.8}V_{0.95}W_{0.05}O_4$ catalyst, the conversion becoming even better than that recorded at low temperature. The ammonia oxidation is especially delayed at high temperature on $Ce_{0.2}Er_{0.8}V_{0.95}W_{0.05}O_4$ catalyst compared to other catalysts. This observation is remarkable because the opposite observation was reported on the aged sample at 600°C characterized by a poorer selectivity than the other samples. Let us note that nitrogen is still the unique reaction product formed in those operating conditions.

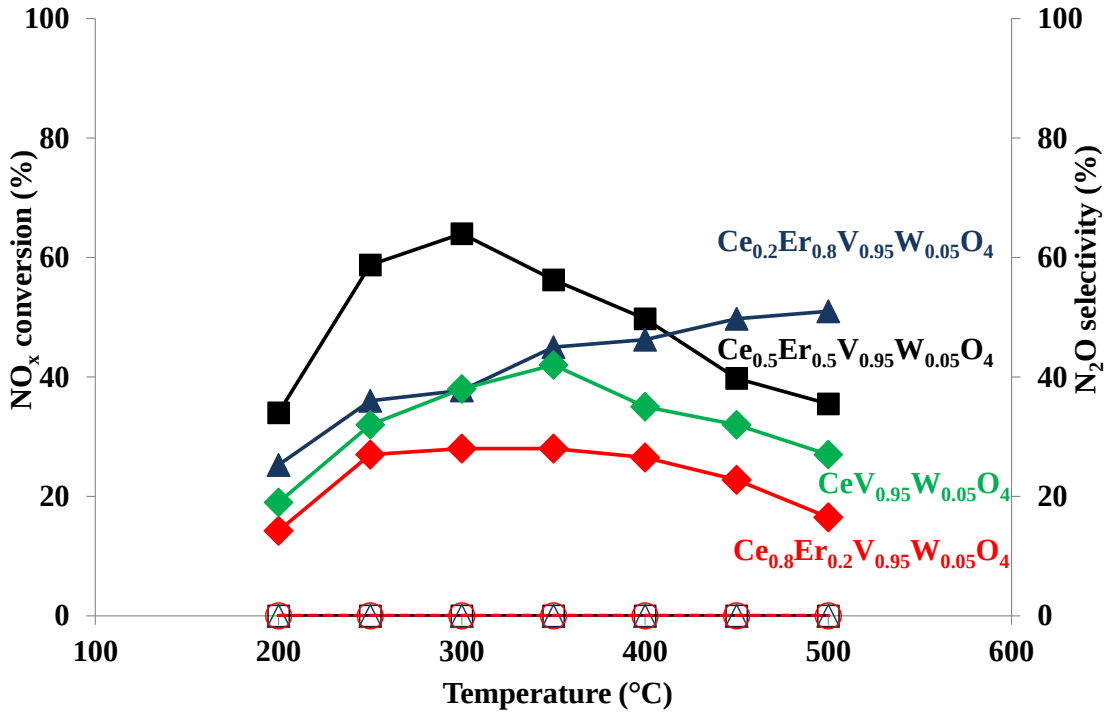

Figure 5.28 – **NO_x conversion (solid lines) and N_2O selectivity (dotted lines) of $Ce_{1-x}Er_xV_{0.95}W_{0.05}O_4$ catalysts in standard-SCR condition aged at 850°C**

1.6.2 Ammonia-selective catalytic reduction of NO_x to nitrogen in "fast" condition: $NO/NO_x = 0.5$

After aging at 850°C, a progressive decrease of activity in Fast-SCR conditions is observed for all substituted samples (see Fig 5.29). At 200°C, the NO_x conversion remains rather low: NO_x conversion of 25, 20, 60, and 25% for X equal to 0, 0.2, 0.5, and 0.8, respectively. Above 200°C, the NO_x conversion increases drastically as a function of temperature. At 300°C, NO_x

conversion of $Ce_{1-x}Er_xV_{0.95}W_{0.05}O_4$ (X=0.2 and 0.8) catalysts start to decrease, then at 500°C ended around 20 and 50% conversion over $Ce_{0.8}Er_{0.2}V_{0.95}W_{0.05}O_4$ and $Ce_{0.2}Er_{0.8}V_{0.95}W_{0.05}O_4$ catalysts, respectively. The NO_x conversion over $Ce_{0.5}Er_{0.5}V_{0.95}W_{0.05}O_4$ catalyst remains 80% at 300-400°C. Above 400°C, the NO_x conversion of $Ce_{0.5}Er_{0.5}V_{0.95}W_{0.05}O_4$ catalyst slightly decreases and reaches a minimum conversion of 45% at 500°C. The ammonia oxidation is especially supposed to be delayed at high temperature on $Ce_{0.5}Er_{0.5}V_{0.95}W_{0.05}O_4$ compared to other catalysts. $Ce_{0.5}Er_{0.5}V_{0.95}W_{0.05}O_4$ catalyst is 100% selective toward N_2 (200–450°C) in fast SCR whereas at 500°C the N_2 selectivity slightly declines to 98%. The $Ce_{0.5}Er_{0.5}V_{0.95}W_{0.05}O_4$ catalyst has the highest N_2 selectivity among the investigated catalysts in fast SCR. The N_2 selectivity of the $Ce_{0.2}Er_{0.8}V_{0.95}W_{0.05}O_4$ catalyst decreases noticeably at 450°C with a larger formation of N_2O. $CeV_{0.95}W_{0.05}O_4$ shows an excellent N_2 selectivity between 200°C and 450°C but the least N_2 selectivity of 93% at 500°C.

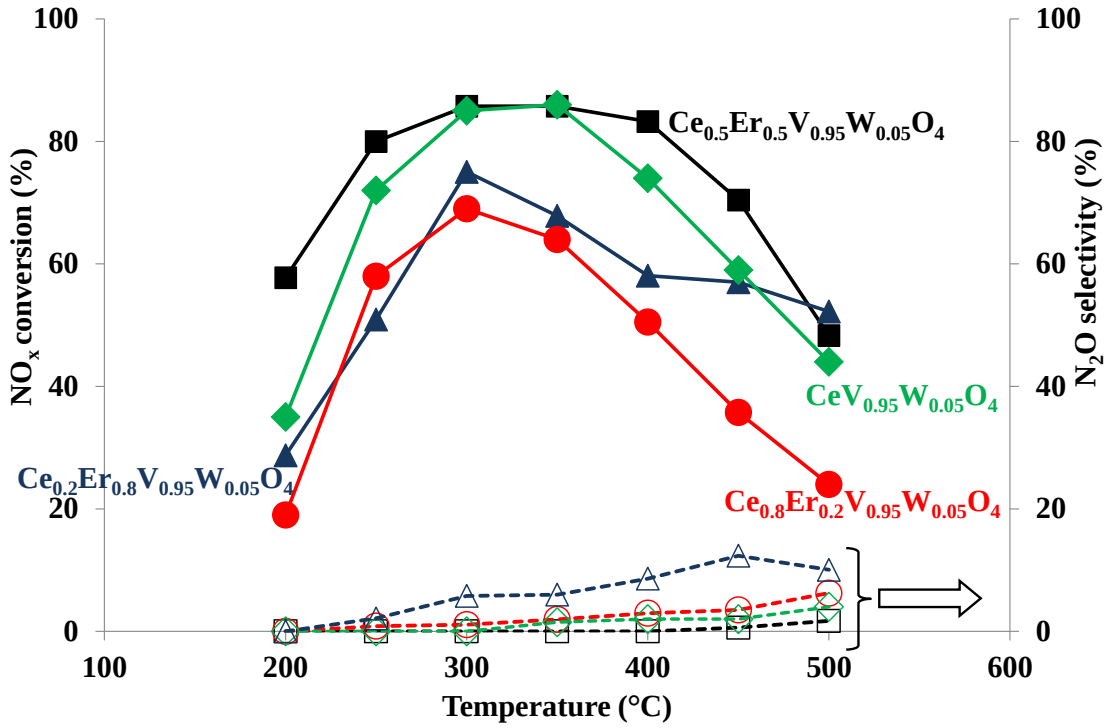

Figure 5.29 – **NO_x conversion (solid lines) and N_2O selectivity (dotted lines) of $Ce_{1-x}Er_xV_{0.95}W_{0.05}O_4$ catalysts in fast-SCR condition aged at 850°C**

1.6.3 Ammonia-selective catalytic reduction of NO_x to nitrogen in "NO_2" condition: NO/NO_x =3/10

De-NO_x activity was also investigated using an excess of nitrogen dioxide in the reaction mixture in the so-called NO_2-SCR condition (Fig 5.30). The efficiency of the catalyst is however close to that measured in Fast-SCR at low temperature. Interestingly, significant changes in NO_x conversion are clearly observable with regards to different erbium substitution degree. Accordingly, a higher NO_x conversion and broader operating temperature window were obtained on $Ce_{0.2}Er_{0.8}V_{0.95}W_{0.05}O_4$ catalyst above 250°C, with the maximum conversion of 78% at 350°C. The undesirable ammonia oxidation by oxygen should be the predominant side reaction that results in decreasing NO_x conversion above 300°C. We can deduce the following sequence of activity at 500°C: $Ce_{0.8}Er_{0.2}V_{0.95}W_{0.05}O_4$ (20%) < $CeV_{0.95}W_{0.05}O_4$ (23%) < $Ce_{0.5}Er_{0.5}V_{0.95}W_{0.05}O_4$ (40%) < $Ce_{0.2}Er_{0.8}V_{0.95}W_{0.05}O_4$ (57%). It is worthwhile to note the quantity of N_2O (up to 30 ppm) detected in NO_2-SCR condition. The N_2 selectivity decreases as a function of the temperature. Reference $CeV_{0.95}W_{0.05}O_4$ catalyst exhibits the highest selectivity towards nitrogen formation, whereas $Ce_{0.2}Er_{0.8}V_{0.95}W_{0.05}O_4$ has the least selectivity in the measured temperature region.

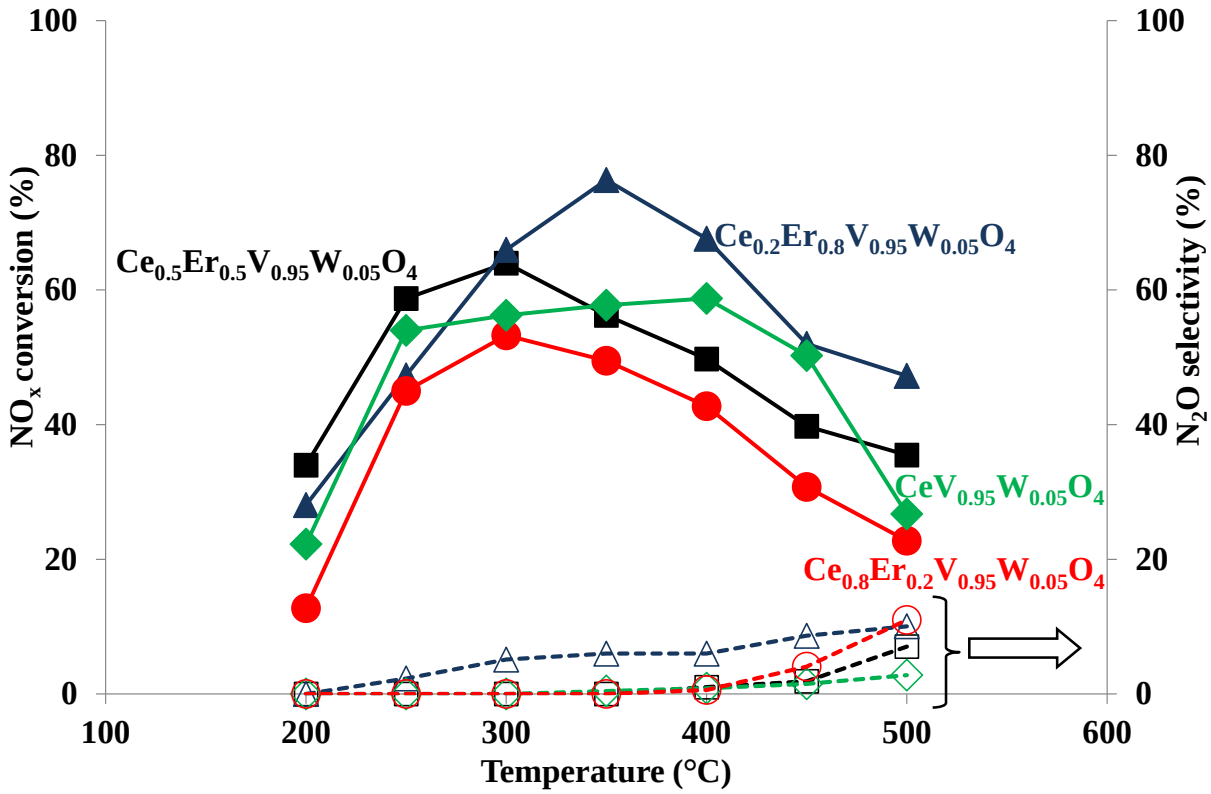

Figure 5.30 – **NO_x conversion (solid lines) and N_2O selectivity (dotted lines) of $Ce_{1-x}Er_xV_{0.95}W_{0.05}O_4$ catalysts in NO_2-SCR condition aged at 850°C**

1.7 Tentative comparison between physicochemical and catalytic properties

The substitution of cerium by erbium leads to contrasting results in term of catalytic properties. Clearly, an optimal erbium composition for X = 0.5 is observed on catalysts aged at 600°C irrespective of the operating conditions and in a wide range of temperature whereas the best SCR performance mostly appears for X = 0.8. At a first glance, crystallites sintering could partly explain changes in catalytic activity on catalysts aged at 600°C with the lowest crystallites size measured on $Ce_{0.5}Er_{0.5}V_{0.95}W_{0.05}O_4$ catalyst. However, such a comparison does not appear distinctly on catalysts aged at 850°C which emphasize the fact that changes in surface composition would be mainly responsible for the changes in catalytic performances. As a matter fact, XRD analysis and Raman spectroscopy measurements provide relevant information related to the formation of $ErVO_4$ at the highest erbium loading (X = 0.8) which

could be intrinsically more active than $Ce_{0.5}Er_{0.5}V_{0.95}W_{0.05}O_4$ and $CeV_{0.95}W_{0.05}O_4$ catalysts. Such a hypothesis seems in rather agreement with H_2-TPR analysis showing the appearance of an additional reduction process taking place at low temperature. This extra reduction process could reflect better redox properties of $ErVO_4$. As earlier discussed, we rule out the involvement of Ce_7O_{12} which has not been found relevant for SCR applications [19, 20]. Hence, the most active aged $Ce_{0.2}Er_{0.8}V_{0.95}W_{0.05}O_4$ catalyst at 850°C would be more likely related to bulk and surface reconstruction in connection with higher redox properties of $ErVO_4$. Particular attention was paid to the weak reduction process only discernible on aged samples at 600°C. Activation energy values for the reduction process have been estimated according to the Kissinger's method. A gradual decrease on the estimates from 124 to 84 $kJ.mol^{-1}$ was observed at increasing erbium content. Based on this evolution, some comparisons with surface composition from XPS analysis can be tentatively established even if weak evolutions on the composition are characterized. No discrepancy was observed between bulk and surface erbium concentration and the evolution of the activation barrier. However, more significant conclusions can be drawn by plotting the activation energy vs. the relative concentration of vanadium and tungsten. As exemplified in Fig. 5.31, changes in the activation energy are weakly dependent on the surface tungsten composition in comparison with the concentration of vanadates. Such evolution is consistent with a higher reducibility of polyvanadates which polymerize at increasing surface density, especially on $Ce_{0.2}Er_{0.8}V_{0.95}W_{0.05}O_4$. In comparison with the previous investigation [21], the diffusion of tungsten at the surface is not favored which minimized its beneficial effect earlier reported on $CeV_{0.95}W_{0.05}O_4$ acting as a spacer and then preventing the aggregation of monomeric to polymeric vanadate species.

As a matter of fact, those observations can qualitatively explain the catalytic behavior at low temperature with an optimal concentration of monovanadates for X = 0.5 whereas the greater extent of polyvanadates for X = 0.8 recognized as more active but much less selective would

be responsible of the sharp loss of SCR performances at high temperature. Another evidence that supports the superiority of $Ce_{0.5}Er_{0.5}V_{0.95}W_{0.05}O_4$ is also related to its stronger acidic properties as demonstrated in Fig. 5.24.

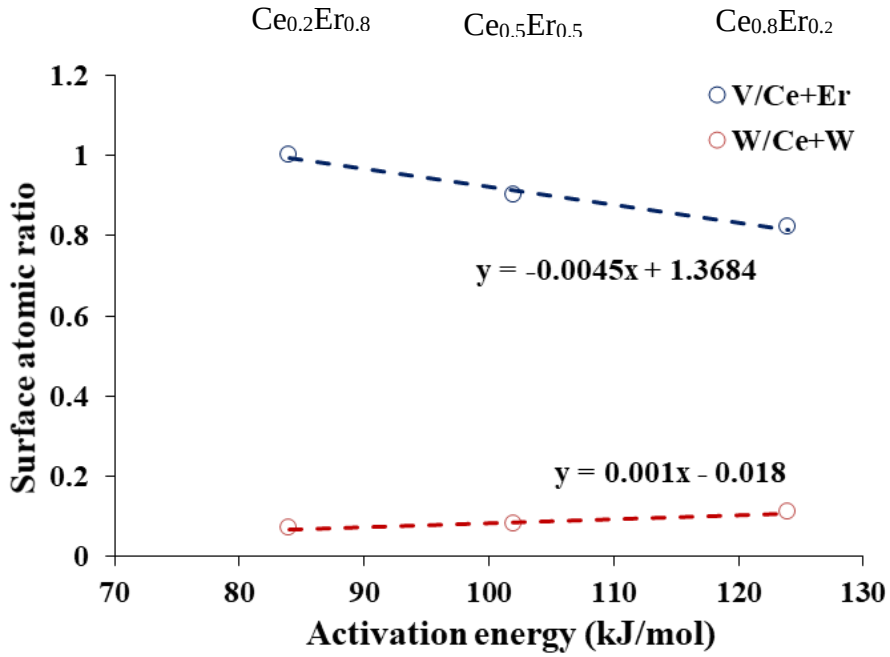

Figure 5.31 – **The activation energy at the low temperature vs. the relative concentration of vanadium and tungsten over $Ce_{1-X}Er_XV_{0.95}W_{0.05}O_4$ (X=0.2, 0.5, 0.8) catalysts**

2 Conclusion

This chapter reports the behavior of bulk $Ce_{1-X}Er_XV_{0.95}W_{0.05}O_4$ (X=0.2, 0.5, and 0.8) catalysts for the selective reduction of NO_x by ammonia. They were prepared by hydrothermal synthesis and aged at 600°C and 850°C in air containing 10 vol. % H_2O. The zircon-type structure of $REVO_4$ is obtained after hydrothermal synthesis without additional calcination step and preserved after aging. An important parameter is related to the insertion of erbium in the zircon-type structure. Subsequent thermal aging treatment in the wet atmosphere shows that $REVO_4$ is more sensitive to crystallite growth and to agglomeration than CeO_2. In fact, the thermal sintering of CeO_2 is only detectable at 850°C. Isolated vanadate (V^{5+}) species remain essentially

stabilized in tetrahedral coordination inside the zircon-type structure of $REVO_4$. It is worthwhile to note that no V_2O_5 can be detected and no loss of vanadium due to sublimation of V_2O_5 was characterized on aged samples from elemental analysis. The insertion of erbium was found as a key parameter for samples with cooperative effects on NO conversion to nitrogen regardless of the operating conditions. It is confirmed by H_2-TPR that the reducibility of vanadate species increases by increasing the degree of cerium substitution by erbium. The presence of erbium (X=0.2 and 0.5) in $Ce_{1-X}Er_XV_{0.95}W_{0.05}O_4$ structure was found to promote significantly the textural properties. The best catalytic performances were obtained on $Ce_{0.5}Er_{0.5}V_{0.95}W_{0.05}O_4$ catalyst with the selective conversion of NO_x into nitrogen between 200 and 450°C whatever the conditions (standard, fast or NO_2-SCR). The loss of conversion over $Ce_{0.2}Er_{0.8}V_{0.95}W_{0.05}O_4$ catalyst can also be related to the loss of specific surface area. Reduction rate data of $Ce_{0.8}Er_{0.2}V_{0.95}W_{0.05}O_4$, $Ce_{0.5}Er_{0.5}V_{0.95}W_{0.05}O_4$, and $Ce_{0.8}Er_{0.2}V_{0.95}W_{0.05}O_4$ catalysts have been examined by Kissinger method. The addition of Er increases the activation energy of $CeVO_4$ to $CeVO_3$ reduction and decreases the activation energy of the reduction of surface vanadate V^{5+} species.

3 References

[1] M. Casanova, K. Schermanz, J. Llorca, and A. Trovarelli, "Improved high temperature stability of NH_3 -SCR catalysts based on rare earth vanadates supported on TiO_2WO_3 SiO_2," *Catal. Today*, vol. 184, no. 1, pp. 227–236, 2012.

[2] M. Casanova, J. Llorca, A. Sagar, K. Schermanz, and A. Trovarelli, "Mixed iron-erbium vanadate NH_3-SCR catalysts," *Catal. Today*, vol. 241, no. PA, pp. 159–168, 2015.

[3] S. Notes, A. M. Lejus, and D. Michel, "+ 17 + 4 + 4," vol. 105, pp. 105–108, 1977.

[4] M. R. Dousti, M. R. Sahar, R. J. Amjad, S. K. Ghoshal, and A. Awang, "Surface enhanced Raman scattering and up-conversion emission by silver nanoparticles in erbium-zinc-tellurite glass," *J. Lumin.*, vol. 143, pp. 368–373, 2013.

[5] I. Guedes, Y. Hirano, M. Grimsditch, N. Wakabayashi, C.-K. Loong, and L. A. Boatner, "Raman study of phonon modes in $ErVO_4$ single crystals," *J. Appl. Phys.*, vol. 90, no. 4, pp. 1843–1846, 2001.

[6] H. Yang, J. Zha, P. Zhang, Y. Qin, T. Chen, and F. Ye, "Fabrication of $CeVO_4$ as nanozyme for facile colorimetric discrimination of hydroquinone from resorcinol and catechol," *Sensors Actuators, B Chem.*, vol. 247, pp. 469–478, 2017.

[7] Z. Wu, A. J. Rondinone, I. N. Ivanov, and S. H. Overbury, "Structure of vanadium oxide supported on ceria by multiwavelength Raman spectroscopy," *J. Phys. Chem. C*, vol. 115, no. 51, pp. 25368–25378, 2011.

[8] Y. Lee, G. He, A. J. Akey, R. Si, M. Flytzani-Stephanopoulos, and I. P. Herman, "Raman analysis of mode softening in nanoparticle CeO_2- and Au-CeO_2- during CO oxidation," *J. Am. Chem. Soc.*, vol. 133, no. 33, pp. 12952–12955, 2011.

[9] D. Bloor, J. R. Dean, J. H. Denning, and S. D. Ross, "The vibrational spectra and structures of rare earth oxides in the A modification The vibrational spectra and structures of rare earth oxides in the A .modification," *J. Phys. J. Phys. C Solid State Phys*, vol. 5, no. 5, 1123.

[10] C. Bass, "of CeOz. Second-order scattering, lattice," vol. 48, no. 1, pp. 178–185, 1993.

[11] S. Dogra, J. Singh, N. Dilawar Sharma, K. Samanta, H. K. Poswal, S. M. Sharma, and A. K. Bandyopadhyay, "Phase progression via phonon modes in lanthanide dioxides under pressure," *Vib. Spectrosc.*, vol. 70, pp. 193–199, 2014.

[12] V. D. Araújo, W. Avansi, H. B. de Carvalho, M. L. Moreira, E. Longo, C. Ribeiro, and M. I. B. Bernardi, "CeO_2 nanoparticles synthesized by a microwave-assisted hydrothermal method: evolution from nanospheres to nanorods," *CrystEngComm*, vol. 14, no. 3, pp. 1150–1154, 2012.

[13] F. Cavani, N. Ballarini, and A. Cericola, "Oxidative dehydrogenation of ethane and propane: How far from commercial implementation?," *Catal. Today*, vol. 127, no. 1–4, pp. 113–131, 2007.

[14] B. Agula, T. Ren, X. Zhao, B. Zhaorigetu, and Z. Yuan, "Relationship between the

reducibility and selectivity of $CeMo_xV_{1-x}O_4$ catalysts by kinetic parameters of TPR," *J. Nat. Gas Chem.*, vol. 20, no. 3, pp. 232–236, 2011.

[15] F. Gao, X. Tang, H. Yi, S. Zhao, C. Li, J. Li, Y. Shi, and X. Meng, A Review on Selective Catalytic Reduction of NO_x by NH_3 over Mn–Based Catalysts at Low Temperatures: Catalysts, Mechanisms, Kinetics and DFT Calculations, vol. 7, no. 7. 2017.

[16] F. Hatayama and T. Ohno, "Structure and Acidity of Vanadium Oxide layered on Titania (Anatase and Rutile)," vol. 87, no. 16, pp. 2629–2633, 1991.

[17] T. Barzetti, E. Selli, D. Moscotti, L. Forni, C. Fisica, U. Milano, and V. C. Golgi, "Pyridine and ammonia as probes for FTIR analysis of solid acid catalysts," vol. 92, no. ii, pp. 1401–1407, 1996.

[18] J. Goscianska, M. Ziolek, E. Gibson, and M. Daturi, "Meso – macroporous zirconia modified with niobia as support for platinum — Acidic and basic properties," *Catal. Today*, vol. 152, no. 1–4, pp. 33–41, 2010.

[19] Z. Wu, R. Jin, Y. Liu, and H. Wang, "Ceria modified MnO_x/TiO_2 as a superior catalyst for NO reduction with NH_3 at low-temperature," *Catal. Commun.*, vol. 9, no. 13, pp. 2217–2220, 2008.

[20] E. Shoko, M. F. Smith, and R. H. McKenzie, "Charge distribution near bulk oxygen vacancies in cerium oxides," *J. Phys. Condens. Matter*, vol. 22, no. 22, p. 223201, 2010.

[21] S. Gillot, Development of thermally stable vanadium for SCR catalyst coupling with DPF, University of science and technology of Lille, PhD thesis, 2015.

Chapter VI

Catalytic performances of $Ce_{0.5}Er_{0.5}V_{0.95}X_{0.05}O_4$ mixed oxides (X=W, Mo, Sb, and Nb)

Summary

1 Catalytic performances of $Ce_{0.5}Er_{0.5}V_{0.95}X_{0.05}O_4$ (X=W, Mo, Sb, and Nb) catalysts for the selective reduction of NO_x by ammonia 253

1.1 Hydrothermal synthesis of $Ce_{0.5}Er_{0.5}V_{0.95}X_{0.05}O_4$ (X=W, Mo, Sb, and Nb) solids 253

1.2 Bulk/Structural properties 255

1.2.1 X-ray fluorescence spectrometry 255

1.2.2 X-ray diffraction 255

1.2.2.1 Unaged solids 255

1.2.2.2 Solids aged at 600°C 257

1.2.2.3 Solids aged at 850°C 258

1.2.3 Raman spectroscopy 260

1.2.4 Temperature-programmed reduction (H_2-TPR) 262

1.2.4.1 Solids Aged at 600°C 262

1.2.4.2 Solids Aged at 850°C 263

1.3 Surface characterizations 265

1.3.1 Specific surface area 265

1.3.2 X-ray photoelectron spectroscopy (XPS) 266

1.3.3 Surface acidity from pyridine adsorption-desorption experiments 274

1.4 Catalytic activity of $Ce_{0.5}Er_{0.5}V_{0.95}X_{0.05}O_4$ (X=W, Mo, Sb, and Nb) catalysts after hydrothermal aging at 600°C 276

1.4.1 Ammonia-selective catalytic reduction of NO_x to nitrogen in "Standard" condition: NO/NO_x=1 276

1.4.2 Ammonia-selective catalytic reduction of NO_x to nitrogen in "fast" condition: NO/NO_x= 0.5 277

1.4.3 Ammonia-selective catalytic reduction of NO_x to nitrogen in "NO_2" condition: NO/NO_x =3/10 278

1.5 Conclusion 281

2 References 281

1 Catalytic performances of $Ce_{0.5}Er_{0.5}V_{0.95}X_{0.05}O_4$ (X=W, Mo, Sb, and Nb) catalysts for the selective reduction of NO_x by ammonia

As mentioned in chapter 4 and 5, the replacement of Ce by other ions with a smaller diameter, such as Er can strongly enhance the selective catalytic reduction of NO_x. Vanadium is a well-known component of NH_3-SCR catalysts, and its modification by incorporation of tungsten is applied to improve the stability, acidity and redox properties of catalysts. The modification of acidity through tungsten incorporation promotes the catalytic activity [12]. We want to investigate the replacement of W by Mo, Sb, and Nb in $Ce_{0.5}Er_{0.5}V_{0.95}W_{0.05}O_4$ catalyst structure which is expected to be beneficial for NH_3-SCR. A series of $Ce_{0.5}Er_{0.5}V_{0.95}X_{0.05}O_4$ (X=W, Mo, Sb, and Nb) was prepared through hydrothermal synthesis and was characterized by XRF, XRD, Raman, H_2-TPR, N_2 adsorption, XPS and Pyridine adsorption. The $Ce_{0.5}Er_{0.5}V_{0.95}X_{0.05}O_4$ (X=W, Mo, Sb, and Nb) catalysts were applied to the removal of NO_x by selective catalytic reduction with ammonia (NH_3-SCR) in standard, fast and NO_2 conditions.

Hydrothermal synthesis of $Ce_{0.5}Er_{0.5}V_{0.95}X_{0.05}O_4$ (X=W, Mo, Sb, and Nb) solids

$Ce_{0.5}Er_{0.5}V_{0.95}X_{0.05}O_4$ (X=W, Mo, Nb, and Sb) catalysts were synthesized via a hydrothermal route as described before. Na_3VO_4 (99.98% Sigma-Aldrich) was dissolved in 50mL of deionized water under vigorous stirring. The pH value was adjusted to 1.8 by adding dropwise an aqueous solution of nitric acid (3M). In those operating conditions VO_2^+ cations were likely stabilized in an aqueous phase. In a second step, an aqueous solution was prepared after the dissolution of the precursors of salt $Ce(NO_3)_3 \cdot 6H_2O$ (99%, Sigma-Aldrich), $Er(NO_3)_3.5H_2O$, and $(NH_4)_6H_2W_{12}O_{40}.xH_2O$ (meta) 99.99% or $C_4H_4NNbO_9 \cdot xH_2O$ or Sb_2O_5 or $(NH_4)_6Mo_7O_{24} \cdot 4H_2O$. This second solution was added to the former one containing VO_2^+

cations. Afterward, a progressive addition dropwise of an aqueous solution of sodium hydroxide (1M) until the stabilization of the pH value to 7 induced the precipitation as hydroxide precursors. The suspension thus obtained was hydrothermally treated at 180°C for 24h. At the end of the hydrothermal treatment, a significant shift in the pH value from 7 to 3.5 occurred in accordance with earlier observations. The sample as-prepared was separated by centrifugation, then abundantly washed with deionized water and ethanol and finally dried in air at 80°C for 24 h. This sample was labeled "unaged" in the text of this manuscript. The unaged sample was further aged at 600°C and 850°C for 5h in a gas mixture composed of 10 vol.% H_2O diluted in air.

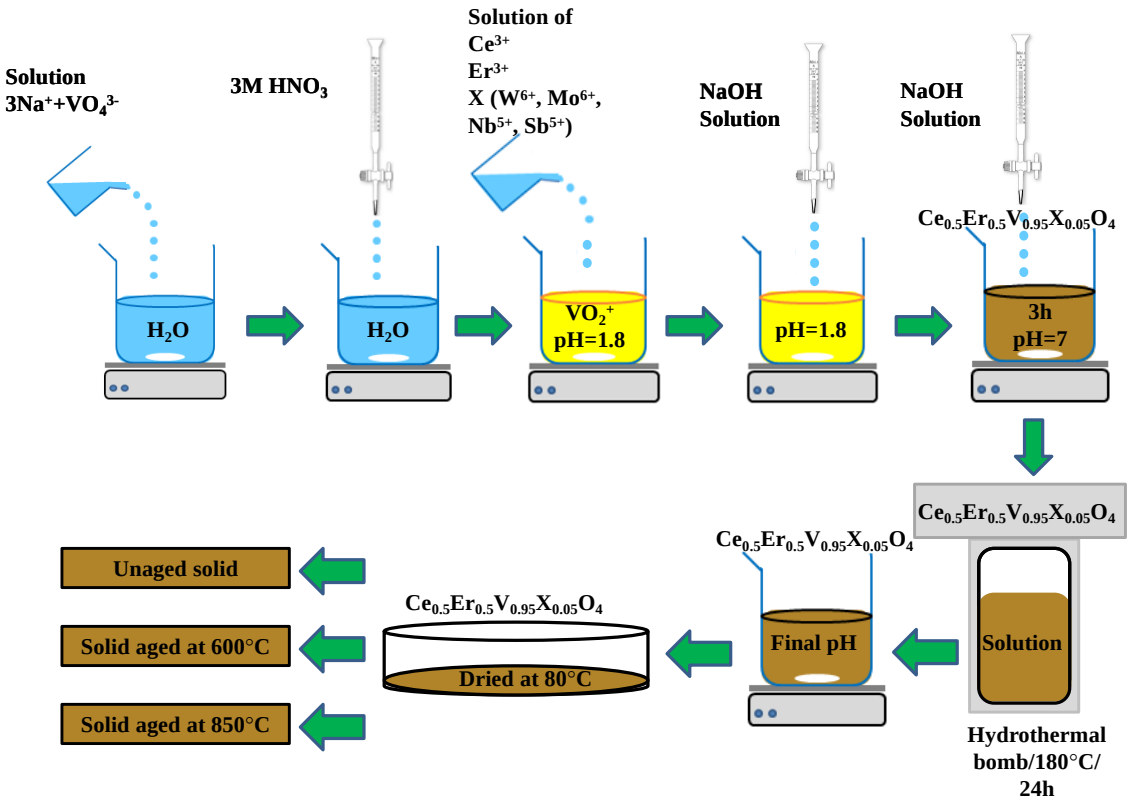

Figure 6.1 – **Steps involved in the hydrothermal synthesis of $Ce_{0.5}Er_{0.5}V_{0.95}X_{0.05}O_4$ (X=W, Mo, Sb, and Nb) catalyst**

1.1 Bulk/Structural properties

1.1.1 X-ray fluorescence spectrometry

The bulk compositions of solids were determined by X-ray fluorescence spectrometry (Table 6.1). The value presented in the brackets corresponds to the expected values. The compositions are close to the nominal composition, no more than 10% difference was observed between the reel and nominal values. However, an excess of tungsten is discernible while large antimony deficiencies are observable. The compositions of the samples are not affected by the hydrothermal aging. No loss of vanadium can be observed due to the possible sublimation of vanadium oxide.

Table 6.1 **– Elemental analysis of $Ce_{0.5}Er_{0.5}V_{0.95}X_{0.05}O_4$ (X=W, Mo, Sb, and Nb) catalysts by X-ray fluorescence spectroscopy**

Catalyst	Aging Temperature (°C)	Chemical composition expressed as oxide			
		V_2O_5 (wt.%)	Ce_2O_3 (wt.%)	WO_3, MoO_3, Sb_2O_5, Nb_2O_5 (wt.%)	Er_2O_3 (wt.%)
$Ce_{0.5}Er_{0.5}V_{0.95}W_{0.05}O_4$	unaged	30.30 (32.20)	31.00 (30.70)	4.30 (2.23)	34.50 (35.00)
	600°C	30.50 (32.20)	31.10 (30.70)	4.30 (2.23)	34.10 (35.00)
	850°C	30.10 (32.20)	31.30 (30.70)	4.00 (2.23)	34.50 (35.00)
$Ce_{0.5}Er_{0.5}V_{0.95}Mo_{0.05}O_4$	unaged	29.00 (33.00)	34.00 (31.00)	1.30 (1.30)	36.00 (35.00)
	600°C	29.00 (33.00)	34.00 (31.00)	1.30 (1.30)	36.00 (35.00)
	850°C	31.00 (33.00)	34.20 (31.00)	1.00 (1.30)	37.00 (35.00)
$Ce_{0.5}Er_{0.5}V_{0.95}Sb_{0.05}O_4$	unaged	31.00 (32.00)	32.00 (30.00)	1.17 (3.00)	36.00 (36.00)
	600°C	31.00 (32.00)	31.00 (30.00)	1.20 (3.00)	36.00 (36.00)
	850°C	31.00 (32.00)	31.00 (30.00)	1.30 (3.00)	37.00 (36.00)
$Ce_{0.5}Er_{0.5}V_{0.95}Nb_{0.05}O_4$	unaged	31.00 (32.00)	30.00 (31.00)	2.20 (2.50)	34.50 (35.00)
	600°C	31.00 (32.00)	30.00 (31.00)	2.20 (2.50)	34.50 (35.00)
	850°C	31.00 (32.00)	31.00 (31.00)	2.40 (2.50)	34.50 (35.00)

1.1.2 X-ray diffraction

1.1.2.1 Unaged solids

XRD patterns recorded on powder samples are reported in Fig 6.2. The most intense peaks at 2θ = 24.0°, 32.3 and 47.8° can be assigned to the characteristic (200), (112) and (312)

reflections of the tetragonal structure of $ErVO_4$ on unaged samples. Additional reflections appear over unaged $Ce_{0.5}Er_{0.5}V_{0.95}Mo_{0.05}O_4$ and $Ce_{0.5}Er_{0.5}V_{0.95}Sb_{0.05}O_4$ catalysts, notably the most intense at $2\theta = 28.5°$ characterizing the cubic structure of CeO_2. From the nature of species given by E-pH diagram [4], the formation of ceria can be explained by the dehydration of $Ce(OH)_4$ during the hydrothermal synthesis and subsequent oxidation with air into CeO_2 [1] according to Eqs. (6.1 and 6.2).

$$4Ce^{3+}(aq) + O_2(g) + 14H_2O(l) = 4Ce(OH)_4(s) + 12H^+(aq) \quad \text{(Equation 6.1)}$$

$$Ce(OH)_4(s) \xrightarrow{600°C} CeO_2 + H_2O \quad \text{(Equation 6.2)}$$

On the other hand, the absence of CeO_2 phase on $Ce_{0.5}Er_{0.5}V_{0.95}W_{0.05}O_4$ and $Ce_{0.5}Er_{0.5}V_{0.95}Nb_{0.05}O_4$ catalysts is likely due to the highest solubility of $Ce(OH)_4$ ($Ks=2*10^{-48}$) in the strong acidic medium [2].

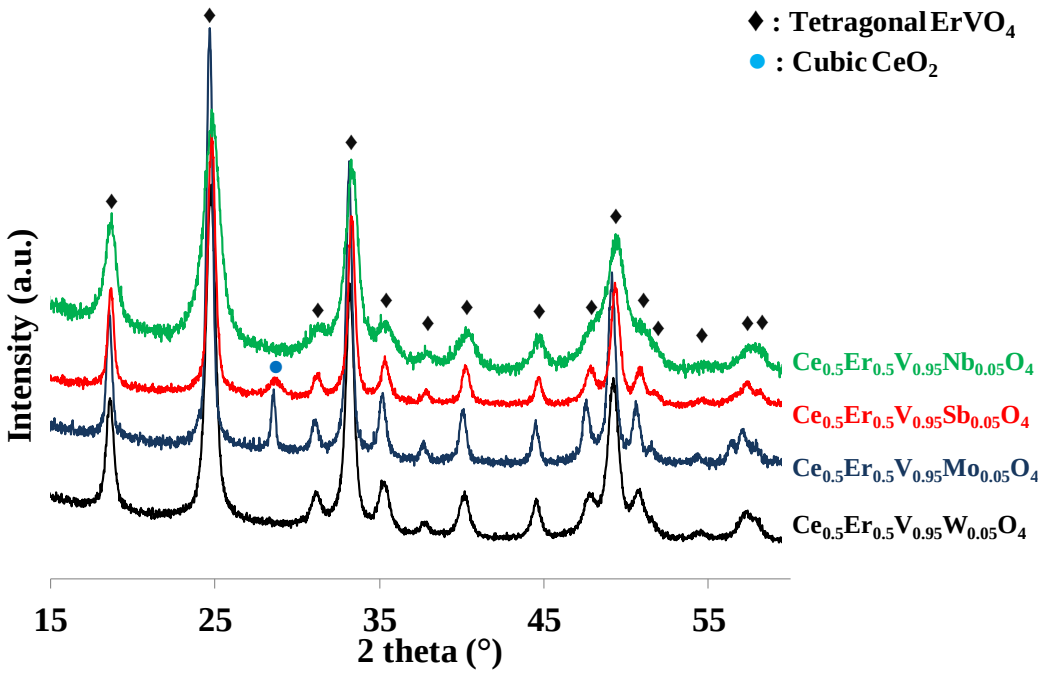

Figure 6.2 – **Crystallographic structure of unaged $Ce_{0.5}Er_{0.5}V_{0.95}X_{0.05}O_4$ (X=W, Mo, Sb, and Nb) solids**

Figure 6.3 presents the relation between the 2θ values and the ionic radius of W^{6+}, Mo^{5+}, Sb^{5+}, and Nb^{5+}. This displacement could be the result of the partial substitution of vanadium by W, Mo, Nb, and Sb. The displacement is more significant for the Nb-containing catalyst with the highest ionic radius. A discontinuity is observed for either molybdenum or tungsten. The difference in oxidation state between W^{6+} or Mo^{6+}/Mo^{5+} can explain an incomplete insertion of these elements in the zircon-type structure.

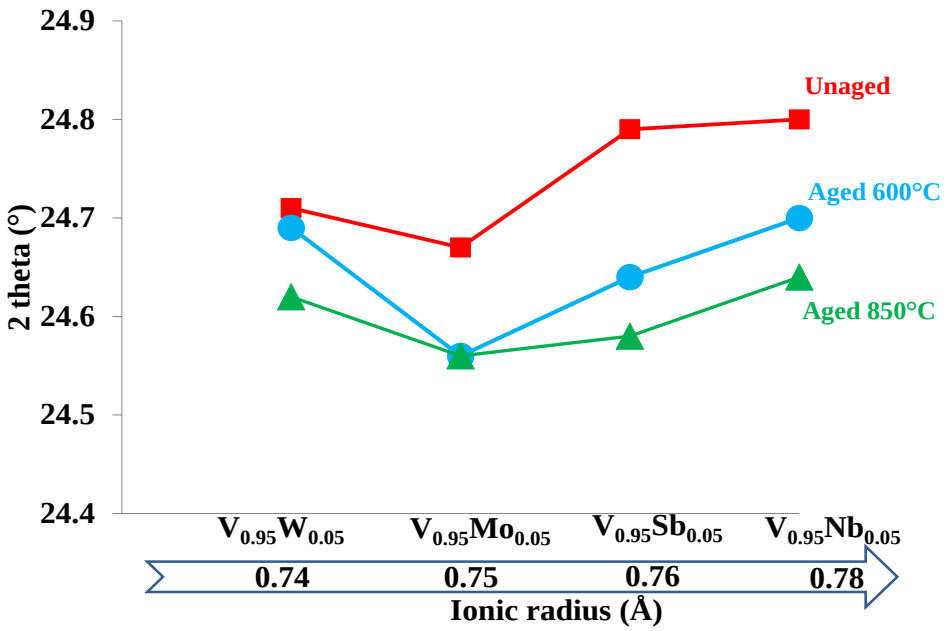

Figure 6.3 – **2 theta(°) according to the substitution nature (X= W, Mo, Sb, and Nb) after synthesis and aging** [3]

1.1.2.2 Solids aged at 600°C

XRD patterns recorded on samples aged at 600°C are dominated by the characteristic reflections of the tetragonal $ErVO_4$ phase (zircon-type structure) with the most intense one at 2θ= 24.0° (Fig. 6.4). Additional X-ray lines appear at 2θ = 28.5°, 33.1° and 47.5° previously ascribed to the face-centered fluorite structure of CeO_2 for all samples. The evolution of 2θ values and the ionic radius of the substituting element on the solid aged at 600°C reveals similar trends than for unaged solids. The discontinuity observed for Mo or W is even more intense.

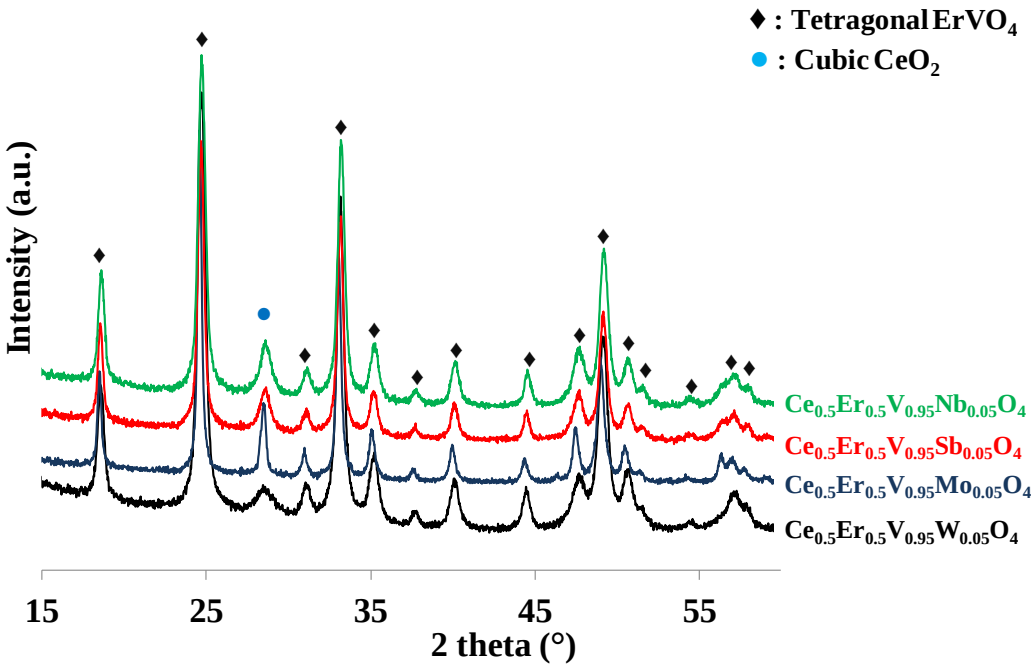

Figure 6.4 – **Crystallographic structure of $Ce_{0.5}Er_{0.5}V_{0.95}X_{0.05}O_4$ (X=W, Mo, Sb, and Nb) solids aged at 600°C**

1.1.2.3 Solids aged at 850°C

All the catalysts mainly display a tetragonal structure (zircon structure). XRD patterns of the tetragonal $ErVO_4$ are characterized by the three main diffraction lines located, respectively, in the 2θ regions around 18, 25, and 33°. A segregated phase corresponding to cubic CeO_2 phase is observed on the solids $Ce_{0.5}Er_{0.5}V_{0.95}X_{0.05}O_4$ (X=Sb, Nb). The homogeneity in the intensity of the diffraction patterns suggests a similar degree of crystallization for all the samples. Hydrothermal aging at 850°C induces significant crystallographic change. For $Ce_{0.5}Er_{0.5}V_{0.95}X_{0.05}O_4$ (X=W, Mo) substituted catalysts, the appearance of a segregated phase attributed to rhombohedric Ce_7O_{12} is detected after aging at 850°C (Fig 6.5).

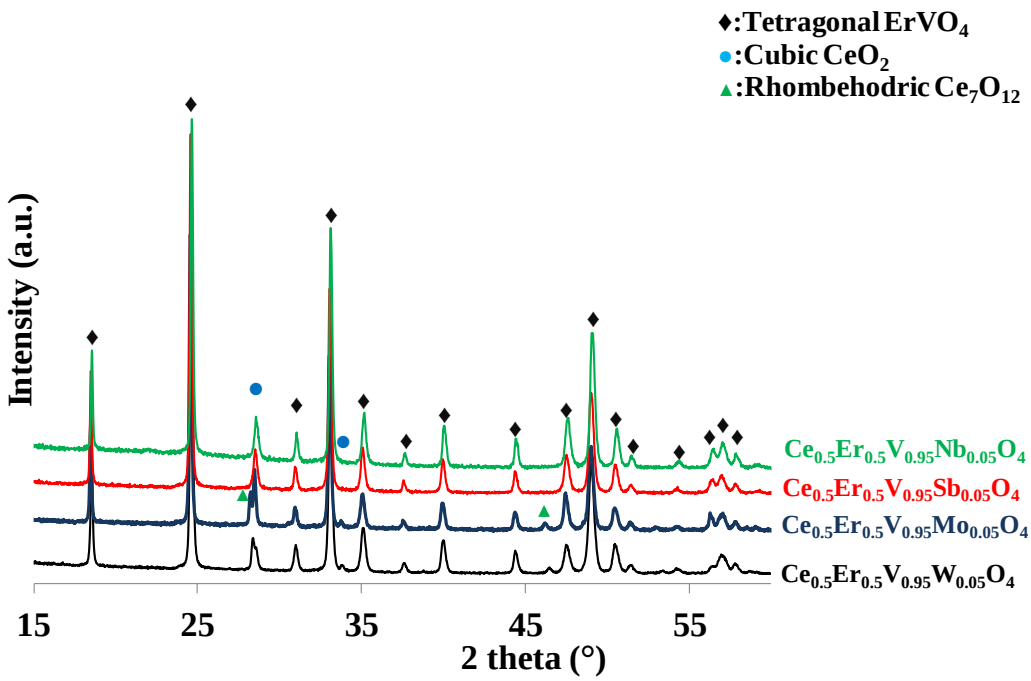

Figure 6.5 – **Crystallographic structure of $Ce_{0.5}Er_{0.5}V_{0.95}X_{0.05}O_4$ (X=W, Mo, Sb, and Nb) solids aged at 850°C**

Average crystallite sizes have been estimated by using the Scherrer-equation and considering the most intense reflections for $ErVO_4$ and CeO_2 (Table 6.2). The lowest crystallite size of $ErVO_4$ phase obtained over an unaged $Ce_{0.5}Er_{0.5}V_{0.95}Nb_{0.05}O_4$ catalyst (8nm) is in agreement with the highest specific surface area (Table 6.4). However after aging at 600°C $Ce_{0.5}Er_{0.5}V_{0.95}W_{0.05}O_4$ catalyst possessed of lowest crystallite size. It is revealed that with increasing the aging temperature the crystallite size increases. In agreement with the similar broadness of the diffraction peaks, the crystallite size of approximately 55nm is obtained over $Ce_{0.5}Er_{0.5}V_{0.95}X_{0.05}O_4$ (X= Mo, Nb, and Sb) catalysts after aging at 850°C. The aging treatment impacts more significantly on the crystallite size of zircon-type phase which exhibits a greater sensibility to sintering with respect to CeO_2.

Table 6.2 – **Influence of vanadium substitution by W, Mo, Sb, and Nb on the average crystallite size of $ErVO_4$ and CeO_2 estimated from XRD patterns**

Catalyst	Aging temperature (°C)	$ErVO_4$ crystallite diameter (nm)	CeO_2 crystallite diameter (nm)
$Ce_{0.5}Er_{0.5}V_{0.95}W_{0.05}O_4$	Unaged	11	-
	600	14	10
	850	43	25
$Ce_{0.5}Er_{0.5}V_{0.95}Mo_{0.05}O_4$	Unaged	20	23
	600	30	28
	850	56	70
$Ce_{0.5}Er_{0.5}V_{0.95}Sb_{0.05}O_4$	Unaged	17	11
	600	20	13
	850	59	34
$Ce_{0.5}Er_{0.5}V_{0.95}Nb_{0.05}O_4$	Unaged	8	-
	600	17	13
	850	52	32

1.1.3 Raman spectroscopy

Raman spectra recorded on unaged catalysts are presented in Fig. 6.6. As seen, CeO_2 exhibits an intense and narrow band at 460cm^{-1} previously ascribed to the F_{2g} vibration of the characteristic cubic fluorite structure of CeO_2. Figs 6. (6) – (8) correspond to Raman spectra recorded on fresh and then aged at 600°C or 850°C. Regarding V_2O_5, numerous Raman lines exhibit V–O–V bridging modes whereas the terminal V=O bond of vanadium species should be detected at 995 cm^{-1} It is worthy to note that these Raman lines ascribed to VO_x species from V_2O_5 are not observed in the spectra recorded on samples even after aging at 850°C. The most intense Raman lines observed at 220, 254, 367, 460, 783, and 854 cm^{-1} are characteristic of $ErVO_4$ phase. Earlier investigations assigned the 854cm^{-1} Raman lines to A_{1g} vanadate symmetric stretching, the 783 signal to the Eg and antisymmetric stretching mode of vanadates and the 367 and 460 cm^{-1} signals to the B_{2g} and B_{1g} deformations [6]. After aging, all catalysts show the characteristic lines corresponding to an electronic transition of Er^{3+} at 708cm^{-1}.

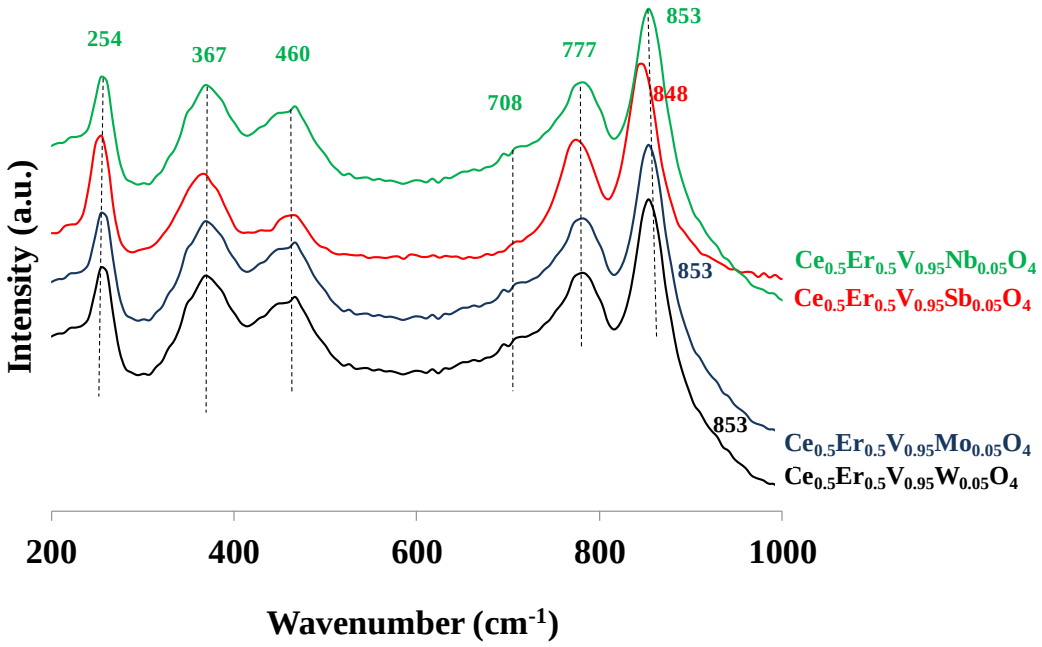

Figure 6.6 – **Raman spectra of unaged $Ce_{0.5}Er_{0.5}V_{0.95}X_{0.05}O_4$ (X=W, Mo, Sb, and Nb) solids**

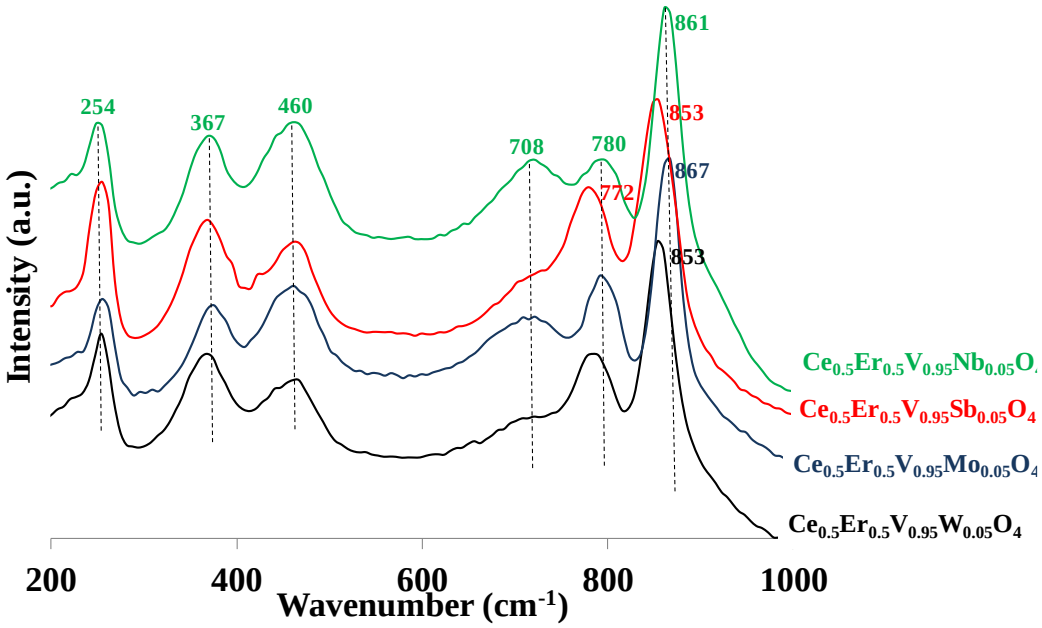

Figure 6.7 – **Raman spectra of $Ce_{0.5}Er_{0.5}V_{0.95}X_{0.05}O_4$ (X=W, Mo, Sb, and Nb) solids aged at 600°C**

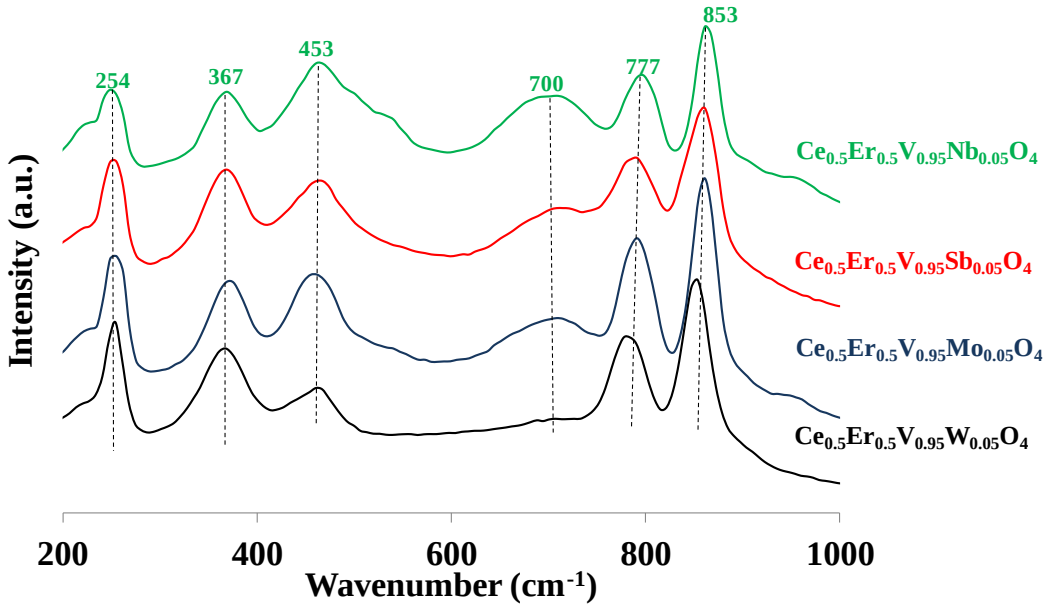

Figure 6.8 – **Raman spectra of $Ce_{0.5}Er_{0.5}V_{0.95}X_{0.05}O_4$ (X=W, Mo, Sb, and Nb) solids aged at 850°C**

1.1.4 Temperature-programmed reduction (H_2-TPR)

1.1.4.1 Solids Aged at 600°C

The series of catalysts have been characterized by H_2 temperature-programmed reduction experiments (Fig. 6.9). The H_2-TPR reduction profiles are characterized by two steps process with an intense peak positioned with a maximum in the range of 750–806°C. As discussed in the previous chapter, this can be attributed to the reduction of V^{5+} in zircon-type structure to V^{3+} [7]. The H_2 consumption profile is shifted to the high temperature from niobium to tungsten. Integration of this peak yielded an H/V molar ratio of 2.1, 1.9, 2.1, and 2 for X=W, Mo, Sb, and Nb respectively (Table 6.3), which is the value, required for the reduction of $CeVO_4$ to $CeVO_3$. It was found that under the same conditions, $Ce_{0.5}Er_{0.5}V_{0.95}W_{0.05}O_4$ catalyst resulted in smaller crystallite size (14nm) than other catalysts (Table 6.2). This catalyst possessed of the highest reduction temperature of V^{5+} to V^{3+}. Similarly, the reduction temperature (T_{max}) over $Ce_{0.5}Er_{0.5}V_{0.95}Mo_{0.05}O_4$ (30nm), $Ce_{0.5}Er_{0.5}V_{0.95}Sb_{0.05}O_4$ (20nm), and $Ce_{0.5}Er_{0.5}V_{0.95}Nb_{0.05}O_4$

(17nm) catalysts decreases by decreasing the crystallite diameter. Therefore, the reducibility of the solid can be related to the crystallites size. In the H_2-TPR profiles of catalyst (aged at 600°C), an additional reduction peak appeared in the temperature range of 560-692°C. This less intense reduction peak observed at low temperature can reflect the reduction of surface Ce^{4+} species to Ce^{3+} or can also contribute to the reduction of dispersed entities at the surface of the solid like mono or poly-vanadate or tungstate species which is difficult to be distinguished due to the similar reduction temperature.

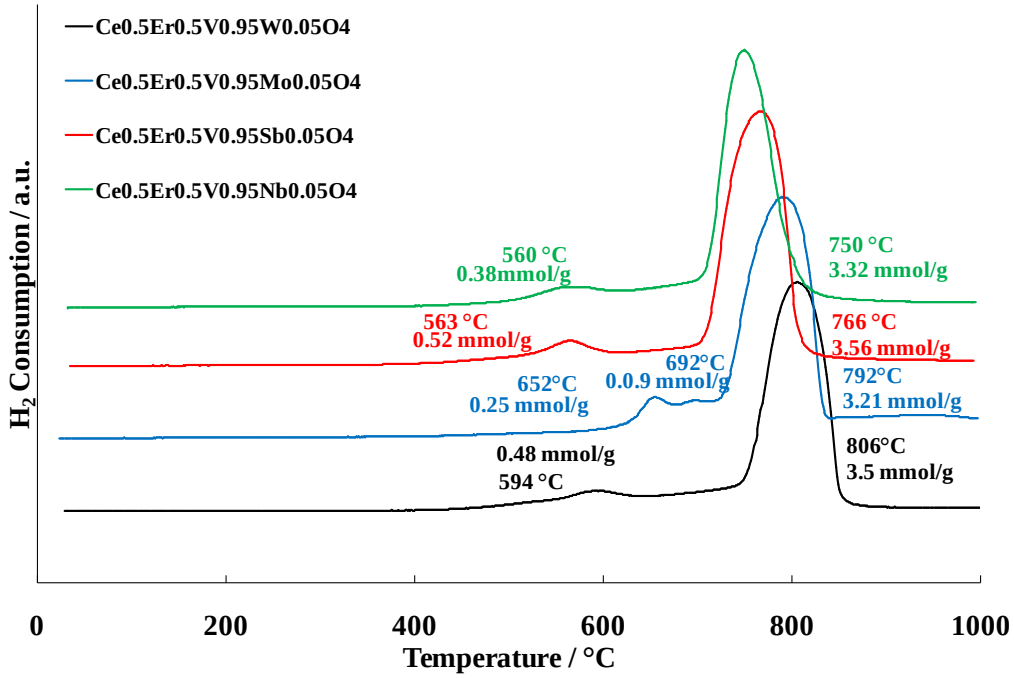

Figure 6.9 – **H_2 consumption during H_2-TPR of $Ce_{0.5}Er_{0.5}V_{0.95}X_{0.05}O_4$ (X=W, Mo, Sb, and Nb) solids aged at 600°C**

1.1.4.2 Solids Aged at 850°C

Figure 6.10 presents the H_2-TPR profiles of the $Ce_{0.5}Er_{0.5}V_{0.95}X_{0.05}O_4$ (X=W, Mo, Sb, Nb) catalysts after aging at 850°C. The high-temperature reduction peak is assigned to the reduction of vanadium species from V^{5+} to V^{3+} with H_2 consumption close to the theoretical value (H/V=2). The modifications of the particle size can be related to the significant alteration of reducibility. By increasing the aging temperature, the crystallite diameter (Table 6.2) increases

and accordingly reduction peaks shift to the higher temperature for all catalysts. On the other hand, the reduction peaks observed at low temperature completely disappeared over $Ce_{0.5}Er_{0.5}V_{0.95}Mo_{0.05}O_4$ and$Ce_{0.5}Er_{0.5}V_{0.95}Sb_{0.05}O_4$ catalysts after aging at 850°C. The lack of observation of this reduction peak over $Ce_{0.5}Er_{0.5}V_{0.95}Mo_{0.05}O_4$ and $Ce_{0.5}Er_{0.5}V_{0.95}Sb_{0.05}O_4$ solids aged at 850°C can be due to the low specific surface area (<4m^2/g) of solids after aging and the agglomeration of monomeric vanadium species leading to the formation of large V_2O_5 clusters at high temperature.

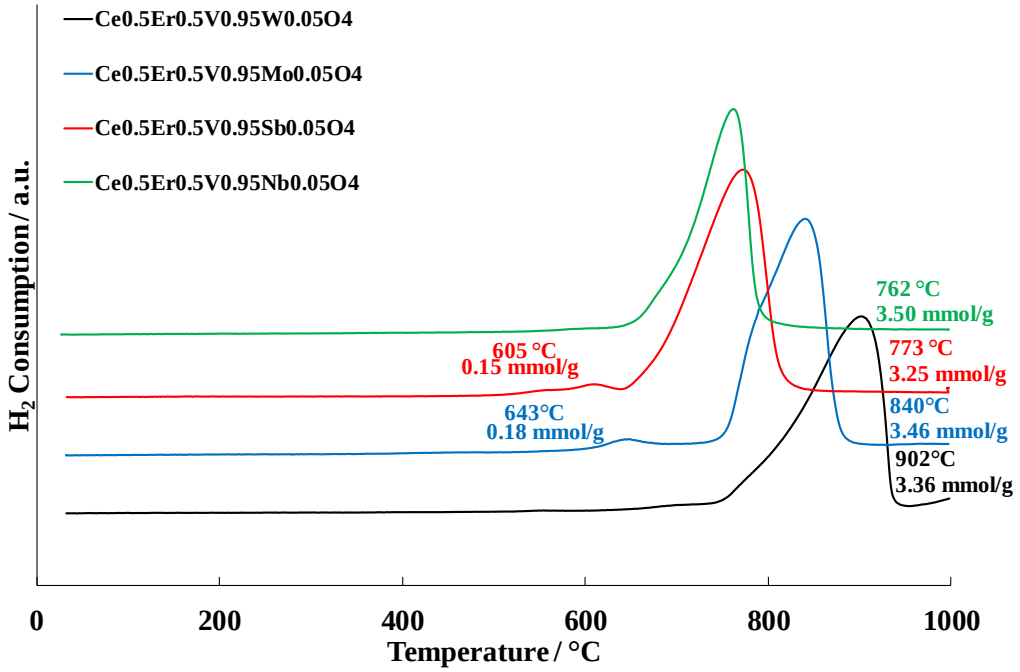

Figure 6.10 – **H_2 consumption during H_2-TPR of $Ce_{0.5}Er_{0.5}V_{0.95}X_{0.05}O_4$ solids aged at 850°C (X=W, Mo, Sb, and Nb); (70mg, 50ml min^{-1})**

Table 6.3 – **H_2-TPR results of $Ce_{0.5}Er_{0.5}V_{0.95}X_{0.05}O_4$ (X=W, Mo, Sb, and Nb); (70mg, 50ml min^{-1})**

Catalyst	Aging temperature (°C)	H_2 consumption [a] (mmol g^{-1})	H/V	T_{max} reduction peaks (°C)
$Ce_{0.5}Er_{0.5}V_{0.95}W_{0.05}O_4$	600	3.50	2.10	806
	850	3.36	2.00	902
$Ce_{0.5}Er_{0.5}V_{0.95}Mo_{0.05}O_4$	600	3.21	1.90	792
	850	3.46	2.00	840
$Ce_{0.5}Er_{0.5}V_{0.95}Sb_{0.05}O_4$	600	3.56	2.10	766
	850	3.25	1.90	773
$Ce_{0.5}Er_{0.5}V_{0.95}Nb_{0.05}O_4$	600	3.32	2.00	750
	850	3.50	2.10	762

[a] Consumption integrated in the temperature range of 700-1000°C

1.2 Surface characterizations

1.2.1 Specific surface area

The specific surface area of the samples was determined by N_2 adsorption. The specific surface area (SSA) of $Ce_{0.5}Er_{0.5}V_{0.95}X_{0.05}O_4$ (X=W, Mo, Sb, Nb) catalysts before and after aging can be seen in Table 6.4. The experimental surface S_{exp} ($m^2.g^{-1}$) is compared to the theoretical surface S_{th} ($m^2.g^{-1}$) calculated from the size of the crystalline phase assuming cubic morphology $S_{th}=6/\rho D_\rho$ by XRD. BET (Brunauer-Emmett-Teller) surface areas were significantly enhanced upon incorporation of Nb and W into catalyst structure. The highest surface of $180m^2g^{-1}$ was observed over an unaged $Ce_{0.5}Er_{0.5}V_{0.95}Nb_{0.05}O_4$ catalyst. It should be underline that the S_{BET} values are very close to the S_{th} values for the unaged solids suggesting that all external surface of nanoparticles is accessible (no significant contribution from microporosity). Aging at 600°C induces a surface area loss for all solids. The $Ce_{0.5}Er_{0.5}V_{0.95}Mo_{0.05}O_4$ possessed of a lowest initial specific surface area compared the other samples but do not sinter as severely after aging at 600°C. After aging at 600°C, $Ce_{0.5}Er_{0.5}V_{0.95}W_{0.05}O_4$ catalyst has the highest surface area.

Sintering and aggregation of nanocrystallites cause a loss of surface area and will maybe significantly affect catalytic systems. All samples end up with roughly the same specific surface area after aging at 850°C but there are strong differences between BET and theoretical surfaces, owing to the thermal sintering. This suggests the combination of agglomeration and crystal growth during aging.

Table 6.4 – **Influence of vanadium substitution by X (W, Mo, Sb, and Nb) and hydrothermal aging on the specific surface**

Catalyst	Aging temperature (°C)	Experimental specific surface area S_{exp} ($m^2.g^{-1}$)	Theoretical specific surface area S_{th} ($m^2.g^{-1}$)
$Ce_{0.5}Er_{0.5}V_{0.95}W_{0.05}O_4$	Unaged	118	106
	600°C	58	86
	850°C	4.5	28
$Ce_{0.5}Er_{0.5}V_{0.95}Mo_{0.05}O_4$	Unaged	62	70
	600°C	35	47
	850°C	2.8	25
$Ce_{0.5}Er_{0.5}V_{0.95}Sb_{0.05}O_4$	Unaged	82	82
	600°C	38	67
	850°C	3	25
$Ce_{0.5}Er_{0.5}V_{0.95}Nb_{0.05}O_4$	Unaged	180	171
	600°C	50	82
	850°C	3.5	25

1.2.2 X-ray photoelectron spectroscopy (XPS)

The decomposition of Ce 3d photopeak can be fitted into ten peaks (v^o, v', u^o and u' related to Ce^{3+} species and v, v", v"', u, u" and u"' related to Ce^{4+} species) as presented in the previous chapter [8]. The Ce 3d XPS spectra presented in Figure 6.11 for the series of $Ce_{0.5}Er_{0.5}V_{0.95}X_{0.05}O_4$ (X=W, Mo, Sb, and Nb) solids catalysts reveal the coexistence of Ce^{3+} and Ce^{4+} species.

Quantitative analyses from XPS analysis are summarized in Table 6.5. Complementary information comes from the examination of the Ce^{4+}/Ce^{3+} atomic ratio on the aged sample. The increase of Ce^{4+}/Ce^{3+} ratio after aging is observed for all catalysts. In fact, XRD analysis

previously underlined a higher increase of crystallite size after aging on $REVO_4$ phase as compared to CeO_2 phase thus leading to a relative increase of Ce^{4+} surface concentration detected by XPS. Such a trend can be compared with spectral features of the O 1s photopeak characterized by two contributions on samples at 530.5 eV and 532.0 eV reflecting the distribution at the surface of lattice oxygen O^{2-}(O_β) and adsorbed oxygen species (O_α) i.e. O_2^-, O^- or OH groups. O_α species are more active being more prone to create surface oxygen vacancies and defect sites which could have some consequences on the catalytic properties. A relatively good agreement between an increase in Ce^{4+}/Ce^{3+} parallel to a decrease in O_α/O_β values underlines lower concentrations of surface oxygen vacancies. As a matter of fact, such a tendency can be correctly explained by a higher sensitivity of $REVO_4$ to particle growth than CeO_2 with a rise in aging temperature as earlier discussed from the evolution of crystallite sizes in Table 6.2.

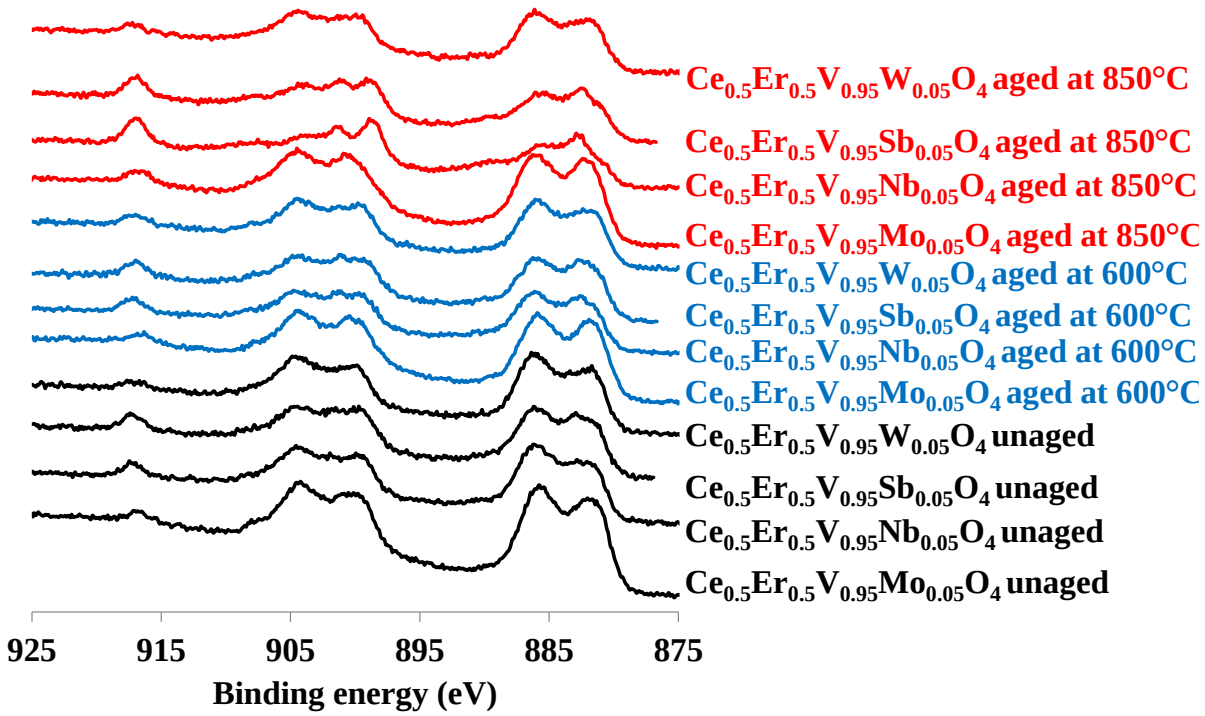

Figure 6.11 – **XPS Spectra of Ce 3d core level of $Ce_{0.5}Er_{0.5}V_{0.95}X_{0.05}O_4$ (X=W, Mo, Sb, and Nb) solids**

The XPS core level spectra of erbium (Er) 4d obtained before and after aging at 600°C and 850°C illustrated in Fig 6.12. The sub-peaks were revealed by peak deconvolution. The deconvoluted sub-peaks are also illustrated in Fig 6.13. The Er 4d spectra show a doublet peak at binding energy 168.34 and 170.54 eV corresponding to Er $4d_{5/2}$ and Er $4d_{5/2}$ respectively along with satellite peaks (at binding energy 174, 176.45 and 182.25 eV) characteristic of Er^{3+}.

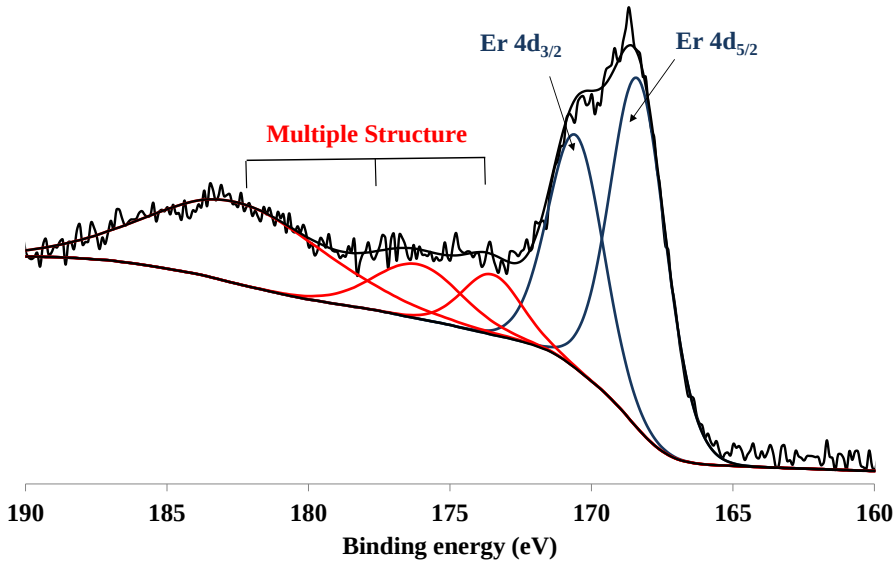

Figure 6.12 – **Fitted XPS Spectra of Er 4d core level of the unaged $Ce_{0.5}Er_{0.5}V_{0.95}W_{0.05}O_4$**

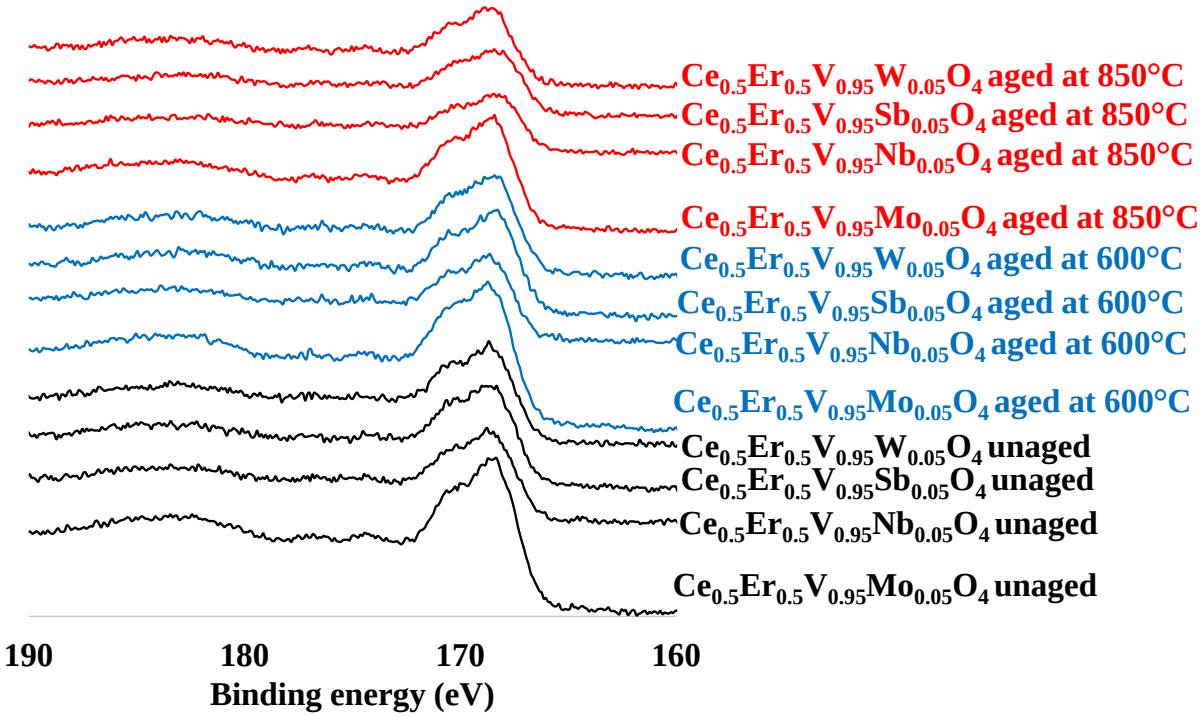

Figure 6.13 – **XPS Spectra of Er 4d core level of the $Ce_{0.5}Er_{0.5}V_{0.95}X_{0.05}O_4$ (X=W, Mo, Sb, and Nb) solids**

Fitted XPS Spectra of V 2p and O 1s already presented in chapter 4. The O 1s and V 2p XPS spectra as a function of aging and vanadium partial substitution by X (W, Mo, Sb, and Nb) are given in Fig 6.l4. For the V 2p spectrum, the binding energy separation between core levels V $2p_{1/2}$ (524.9 eV) and V $2p_{3/2}$ (517.6 eV) is ~7.3 eV, corresponds to the electronic states of V^{5+}. The binding energies for the photopeak V $2p_{3/2}$ remain almost unchanged that revealed low sensitivity to the vanadium substitution. The relative concentrations of elements Ce, Er, V and X (W, Mo, Sb, Nb) for $Ce_{0.5}Er_{0.5}V_{0.95}W_{0.05}O_4$ solids aged at different temperatures are reported in Table 6.5. It can be seen that the Ce/O atomic ratio values are stable for solids substituted with Sb, Nb and Mo, and also this ratio remains stable even after aging at 600°C and 850°C. The Er/Ce, X/V, V/(Ce+RE), X/(Ce+RE) and (V+X)/(Ce+RE) ratios on unaged solids are close to the theoretical value, the difference remains less than 10%, which is acceptable given the uncertainty of the XPS spectroscopy. Furthermore, the relative concentration of X (W, Mo, Sb,

Nb) on the surface of catalysts increases after aging. In Table 6.5, the ratio of O_α/O_β after aging at 600°C on $Ce_{0.5}Er_{0.5}V_{0.95}Sb_{0.05}O_4$ catalyst was calculated as 0.37 while that of $Ce_{0.5}Er_{0.5}V_{0.95}Nb_{0.05}O_4$, $Ce_{0.5}Er_{0.5}V_{0.95}Mo_{0.05}O_4$ and $Ce_{0.5}Er_{0.5}V_{0.95}W_{0.05}O_4$ catalysts increased to 0.40, 0.50 and 0.50, respectively.

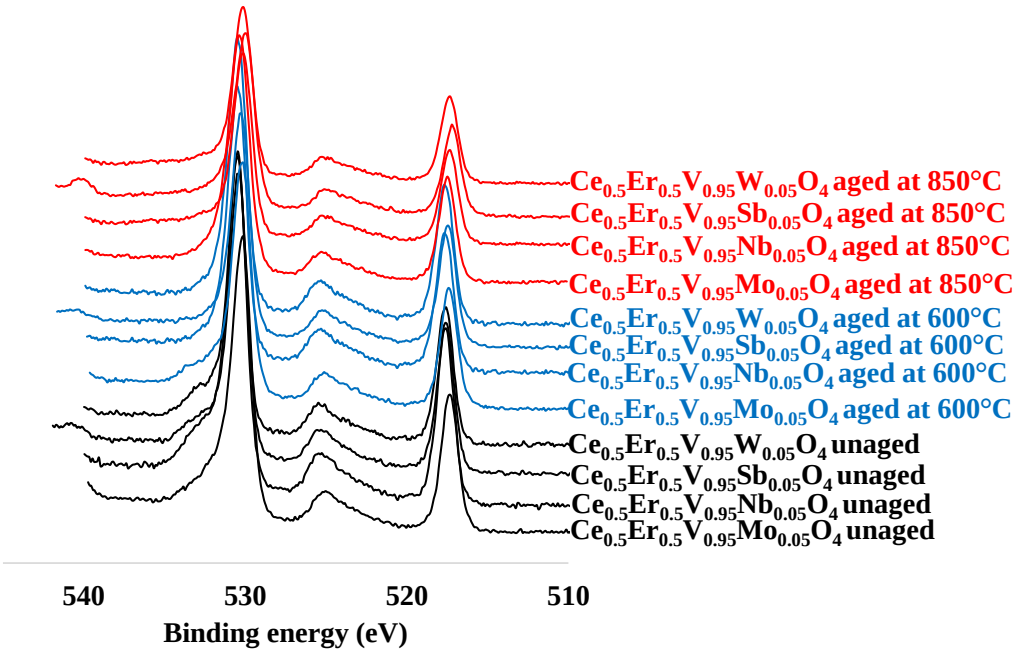

Figure 6.14 – **XPS Spectra of V 2p, O 1s and Sb 3d core level of the $Ce_{0.5}Er_{0.5}V_{0.95}X_{0.05}O_4$ (X=W, Mo, Sb, and Nb) solids**

The chemical state and composition of the antimony oxide were obtained from XPS measurements. The spectra deconvolution corresponding to Sb 3d photo-emission lines was performed fixing the Sb $3d_{3/2}$ and Sb $3d_{5/2}$ area ratio in 2:3 and the Sb 3d doublet splitting energy in 9.6 eV. The deconvoluted peaks were observed in the Sb 3d region at 540.2, and 530.6 confirming the Sb valence states as Sb^{5+} [9].

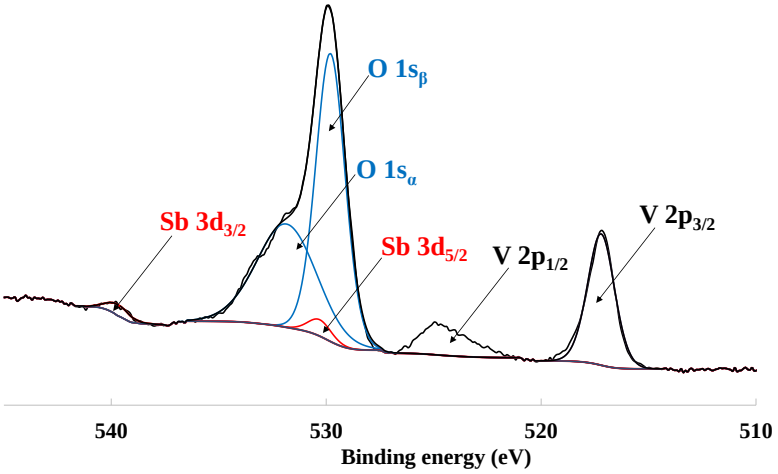

Figure 6.15 – **Fitted Spectra of V 2p, O 1s and Sb 3d core level of the unaged $Ce_{0.5}Er_{0.5}V_{0.95}Sb_{0.05}O_4$**

The electronic structures of Mo oxides have been examined using XPS before and after aging. Before aging, the spectrum for the unaged $Ce_{0.5}Er_{0.5}V_{0.95}Mo_{0.05}O_4$ in the Mo 3d region showed the presence of two well-resolved photopeaks at 232.5 and 235.6 eV (FWHM = 1.6 eV). These photopeaks were assigned to the Mo $3d_{5/2}$ and Mo $3d_{3/2}$ spin-orbit components, respectively (Fig 6.16). Firment and Ferretti [10] indicated a binding energy of 232.6 ± 0.3 eV for single crystal MoO_3 (010). The Mo 3d spectra show no evidence of splitting or broadening within the resolution of the instrument, indicating that Mo was present in a single environment in the surface region (6+).

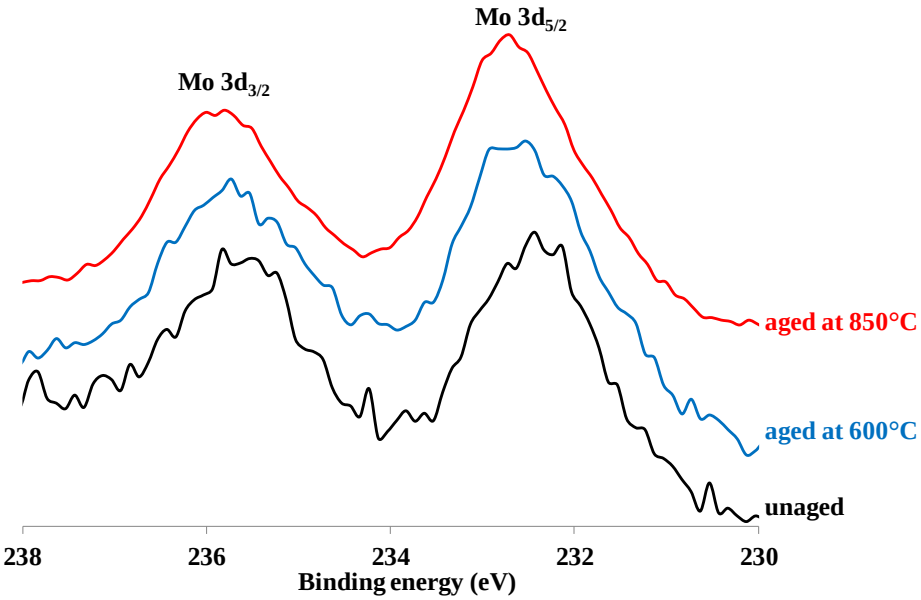

Figure 6.16 – **XPS Spectra of Mo 3d core level of $Ce_{0.5}Er_{0.5}V_{0.95}Mo_{0.05}O_4$ solids**

In order to determine the oxidation state of niobium over the catalysts, the XPS spectra were recorded over unaged, aged at 600 or 850°C samples. The results are presented in Figure 6.17. Two peaks at 206.80 and 209.66 eV were detected on the solid aged at 850°C. The energy of spin-orbit separation of 2.8 eV agrees with the existence of Nb^{5+} ions in the lattices or as Nb_2O_5 [10]. The segregation of Nb_2O_5 at high temperature cannot be ruled out. On the unaged solid and the solid aged at 600°C, the intensity of the photopeaks is too low to lead to a conclusion. XPS Spectra of tungsten were already discussed in chapters 4 and 5.

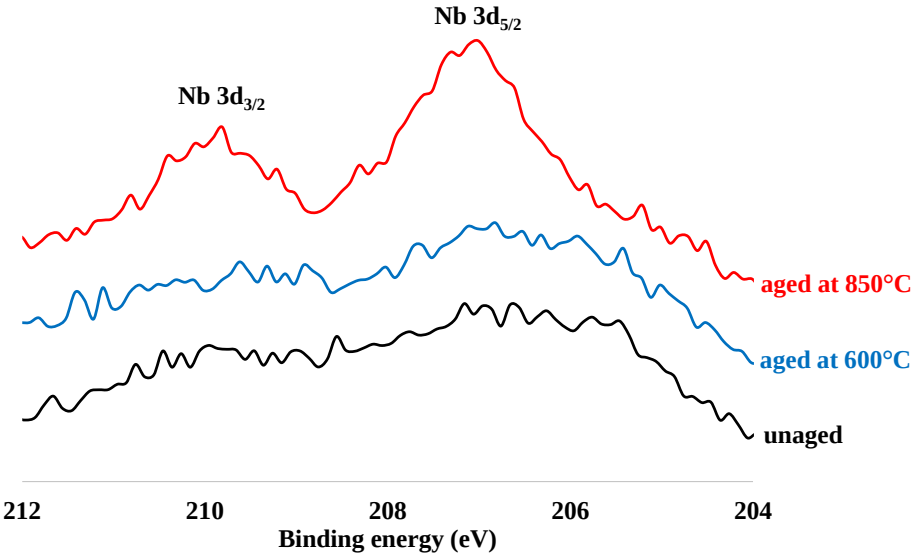

Figure 6.17 – **XPS Spectra of Nb 3d core level of $Ce_{0.5}Er_{0.5}V_{0.95}Nb_{0.05}O_4$ solids**

Table 6.5 – **Surface Composition of $Ce_{0.5}Er_{0.5}V_{0.95}X_{0.05}O_4$ (X=W, Mo, Sb, and Nb) solids**

Catalyst	Aging temperature (°C)	X/V	V/ (Ce+Er)	X/ (Ce+Er)	(V+X)/ (Ce+Er)	Ce^{4+}/Ce^{3+}	O_α/O_β	B.E.(eV) V 2p
$Ce_{0.5}Er_{0.5}V_{0.95}W_{0.05}O_4$	unaged	0.06	0.80	0.05	0.90	0.36	0.60	517.5
	600°C	0.08	0.90	0.08	1.00	0.45	0.50	517.5
	850°C	0.30	0.80	0.20	1.00	0.80	0.40	517.5
$Ce_{0.5}Er_{0.5}V_{0.95}Mo_{0.05}O_4$	unaged	0.05	0.83	0.04	0.90	0.22	0.52	517.5
	600°C	0.10	0.75	0.08	0.80	0.35	0.50	517.5
	850°C	0.36	0.67	0.22	0.90	0.70	0.48	517.5
$Ce_{0.5}Er_{0.5}V_{0.95}Sb_{0.05}O_4$	unaged	0.03	0.93	0.04	0.96	0.52	0.34	517.6
	600°C	0.03	0.93	0.04	1.00	0.75	0.37	517.5
	850°C	0.04	1.03	0.05	1.08	0.90	0.30	517.5
$Ce_{0.5}Er_{0.5}V_{0.95}Nb_{0.05}O_4$	unaged	0.10	0.82	0.10	0.93	0.42	0.50	517.6
	600°C	0.11	0.97	0.09	1.08	0.60	0.40	517.6
	850°C	0.14	0.92	0.12	1.02	0.98	0.22	517.7

Catalyst	Aging temperature (°C)	Ce/O	V/O	V/Ce	X/Ce	Er/Ce
	unaged	**0.12**	**0.20**	**1.40**	**0.05**	**0.80**
$Ce_{0.5}Er_{0.5}V_{0.95}W_{0.05}O_4$	**600°C**	**0.14**	**0.22**	**1.60**	**0.14**	**0.80**
	850°C	**0.16**	**0.20**	**1.20**	**0.21**	**0.65**
	unaged	**0.13**	**0.20**	**1.57**	**0.07**	**0.91**
$Ce_{0.5}Er_{0.5}V_{0.95}Mo_{0.05}O_4$	**600°C**	**0.13**	**0.21**	**1.69**	**0.19**	**1.30**
	850°C	**0.15**	**0.19**	**1.25**	**0.45**	**0.90**
	unaged	**0.14**	**0.23**	**1.64**	**0.05**	**0.80**
$Ce_{0.9}Er_{0.5}V_{0.95}Sb_{0.05}O_4$	**600°C**	**0.15**	**0.30**	**1.93**	**0.05**	**0.85**
	850°C	**0.15**	**0.25**	**1.7**	**0.07**	**0.70**
	unaged	**0.15**	**0.21**	**1.45**	**0.15**	**0.80**
$Ce_{0.5}Er_{0.5}V_{0.95}Nb_{0.05}O_4$	**600°C**	**0.15**	**0.26**	**1.60**	**0.17**	**0.95**
	850°C	**0.15**	**0.25**	**1.63**	**0.20**	**0.81**

1.2.3 Surface acidity from pyridine adsorption-desorption experiments

The acid sites on the surface of the catalyst are classified as Brönsted and Lewis acid sites. Brönsted acid sites are due to acidic hydroxyls in the structure and Lewis acid sites are the cations exposed to the reactants. Pyridine as a weak base often binds to these sites and gives characteristic IR absorption peak. Even if at low temperature, the redox properties of the catalyst, rather than its acidity, is the factor that seems to control the reactivity of the catalyst, at high temperature the surface acidity plays a crucial role in the adsorption and activation of ammonia and thus governs the activity of the catalyst (with the redox properties of the solid). The IR spectra of pyridine adsorbed the samples is shown in the Figure 6.18. Infrared bands at 1603 cm^{-1} (ν_{8a}), 1574 (ν_{8b}), 1490 (ν_{19a}), 1443 cm^{-1} (ν_{19b}) were previously ascribed to the vibrational modes of pyridine adsorbed on Lewis acid sites whereas IR bands located at 1640 cm^{-1} (ν_{8a}), 1540 (ν_{19b}), are currently ascribed to pyridinium ion coordinated to Brönsted acid sites. Let us note that Brönsted acid sites were not detected on all catalysts except perhaps for $Ce_{0.5}Er_{0.5}V_{0.95}Mo_{0.05}O_4$ with a very low intensity signal. The amount of Lewis acidity ($\mu mol.g^{-1}$) according to the desorption temperature of pyridine over $Ce_{0.5}Er_{0.5}V_{0.95}X_{0.05}O_4$ (X=W, Mo, Sb, and Nb) catalysts aged at 600°C are detailed in Table 6.6. It is thus observed that these

samples show Lewis acid sites of various acid strengths (different wavenumbers). The results demonstrated the low acidity of the $Ce_{0.5}Er_{0.5}V_{0.95}Nb_{0.05}O_4$ solid, as well as the moderate density of acidic sites over $Ce_{0.5}Er_{0.5}V_{0.95}X_{0.05}O_4$ (X=W, Mo, and Sb) catalysts at 150°C. $Ce_{0.5}Er_{0.5}V_{0.95}W_{0.05}O_4$ catalyst possessed of the highest amount of Lewis acidity (Table 6.6). It is therefore expected that the incorporation of W induces a gain in acidity, both in density and strength of acid sites to improve the catalytic properties, especially at the high reaction temperature. By increasing the desorption temperature to 450°C all solids lose their acidity.

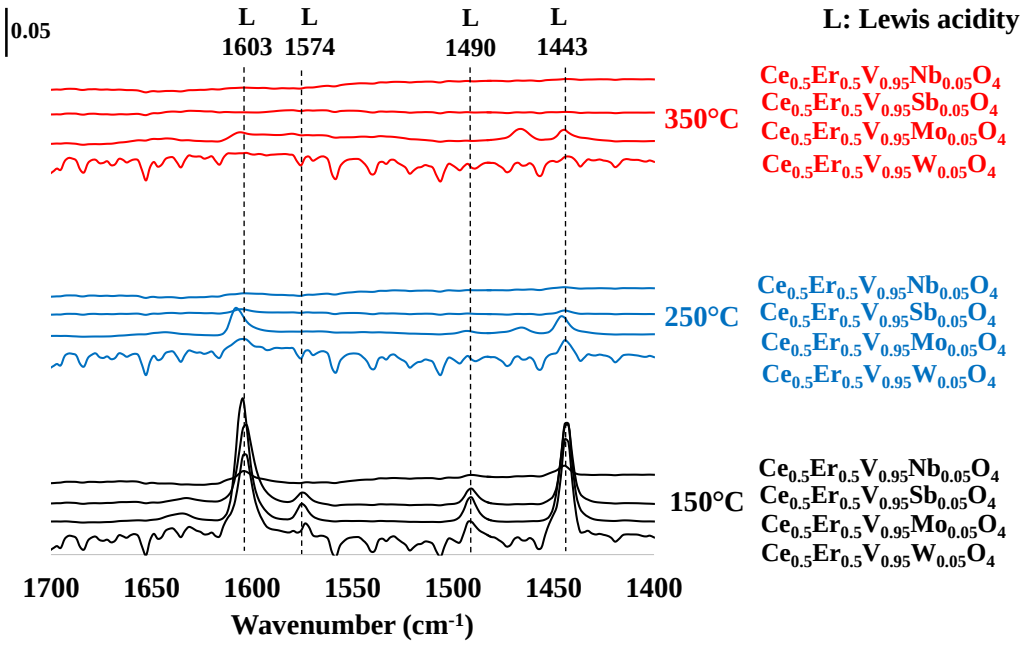

Figure 6.18 – **IR spectra of adsorbed pyridine at 150°C, 250°C, 350°C, 450°C on $Ce_{1-0.5}Er_{0.5}V_{0.95}X_{0.05}O_4$ (X=W, Mo, Sb, Nb) catalysts after aging in ex-situ conditions in wet atmosphere (air + 10 vol.% H_2O) at 600°C**

Table 6.6 – **Quantification of Lewis acid sites (µmol.g^{-1}) according to the desorption temperature of pyridine over $Ce_{0.5}Er_{0.5}V_{0.95}X_{0.05}O_4$ (X=W, Mo, Sb, and Nb) catalysts aged at 600°C**

Catalyst	Normalized amount of Lewis acidity (µmol.g^{-1})			
	Desorption temperature			
	150°C	250°C	350°C	450°C
$Ce_{0.5}Er_{0.5}V_{0.95}W_{0.05}O_4$	34.20	9.20	5.90	0.00
$Ce_{0.5}Er_{0.5}V_{0.95}Mo_{0.05}O_4$	33.60	6.60	4.60	0.00
$Ce_{0.5}Er_{0.5}V_{0.95}Sb_{0.05}O_4$	25.50	1.4	0.10	0.00
$Ce_{0.5}Er_{0.5}V_{0.95}Nb_{0.05}O_4$	1.80	0.20	0.20	0.00

1.3 Catalytic activity of $Ce_{0.5}Er_{0.5}V_{0.95}X_{0.05}O_4$ (X=W, Mo, Sb, and Nb) catalysts after hydrothermal aging at 600°C

1.3.1 Ammonia-selective catalytic reduction of NO_x to nitrogen in "Standard" condition: $NO/NO_x=1$

Overall NO_x conversion profiles versus temperature on aged solids at 600°C in the standard-SCR conditions ($NO/NO_x=1$) are collected in Fig. 6.19. The NO_x conversion increases on $Ce_{0.5}Er_{0.5}V_{0.95}W_{0.05}O_4$ catalyst from 55% conversion at 200°C to a maximum NO_x conversion of 95% at 250–350°C. The NO_x conversion declines when the temperature rises to 500°C due to the competitive oxidation of NH_3 with oxygen leading to lower NO_x conversion. The substitution of vanadium with Mo, Sb, and Nb leads to an overall decrease of NO_x conversion in the whole temperature range. Nevertheless, the addition of Nb resulted in an enhancement of NO_x conversion comparing to Sb- and Mo-containing catalysts. The NO_x conversion on $Ce_{0.5}Er_{0.5}V_{0.95}X_{0.05}O_4$ (X=Mo, Sb, and Nb) catalysts increases with temperature at the low-temperature range (200–300°C). The $Ce_{0.5}Er_{0.5}V_{0.95}X_{0.05}O_4$ (X=Mo, Sb, and Nb) catalysts lead to an increase of NO_x conversion from 45% conversion at 200°C with a maximum NO_x conversion at 400°C. The highest NO_x conversion at 400°C over $Ce_{0.5}Er_{0.5}V_{0.95}Nb_{0.05}O_4$, $Ce_{0.5}Er_{0.5}V_{0.95}Mo_{0.05}O_4$ and $Ce_{0.5}Er_{0.5}V_{0.95}Sb_{0.05}O_4$ catalysts is 90%, 87%, and 77%, respectively and decreases to 50% at 500°C due to the competitive oxidation of NH_3 with oxygen. All

catalysts possessed of the high N_2 selectivity (100%) in the whole temperature range in Standard SCR conditions.

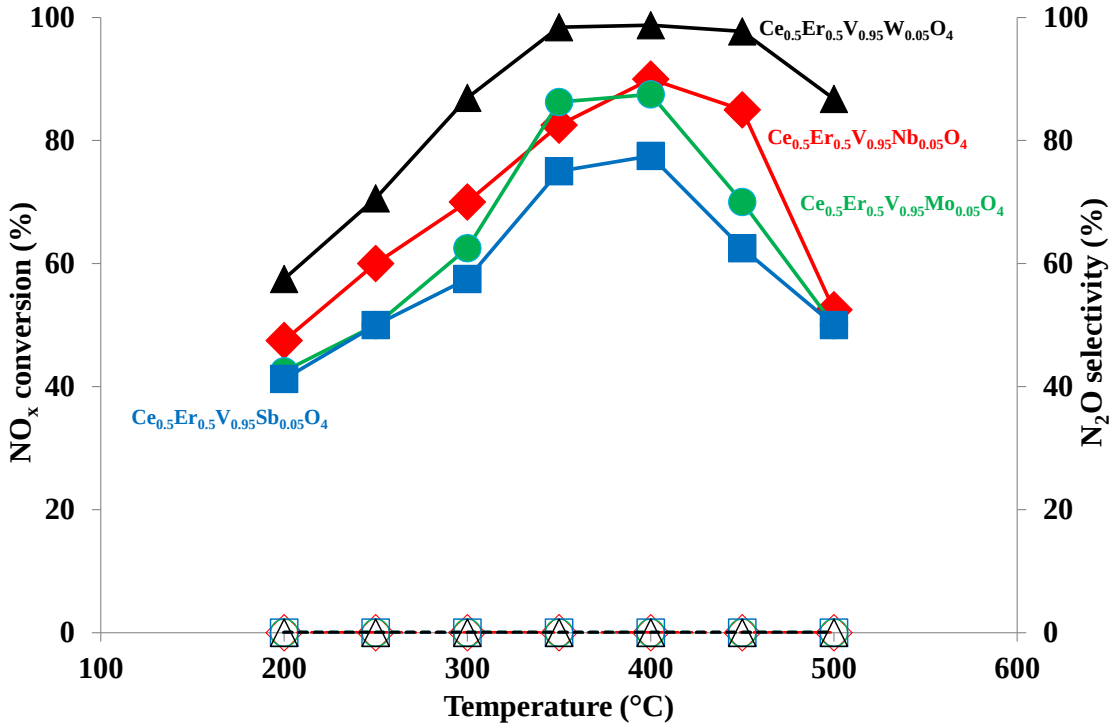

Figure 6.19 – **NO_x conversion (solid lines) and N_2O selectivity (dotted line) during the standard-SCR reaction after aged at 600°C**

1.3.2 Ammonia-selective catalytic reduction of NO_x to nitrogen in "fast" condition: NO/NO_x= 0.5

The fast-SCR NO conversion over catalysts aged for 5h at 600°C is illustrated in Fig. 6.20. The catalytic activity of $Ce_{0.5}Er_{0.5}V_{0.95}W_{0.05}O_4$ catalyst was clearly higher than those of the other catalysts. The NO_x conversion of $Ce_{0.5}Er_{0.5}V_{0.95}W_{0.05}O_4$ catalyst reaches 95% between 200 to 450°C. At 500°C, the NO_x conversion decreases and reaches 80%. The NO_x conversion of $Ce_{0.5}Er_{0.5}V_{0.95}Mo_{0.05}O_4$ catalyst reaches 76% at 200°C, a maximum of 87% is recorded near 400°C and NO_x conversion decreases to 58% at 500°C. The increase of NO_x conversion between 200 and 300°C is more intense on $Ce_{0.5}Er_{0.5}V_{0.95}Sb_{0.05}O_4$ catalyst than on $Ce_{0.5}Er_{0.5}V_{0.95}Mo_{0.05}O_4$ catalyst despite the lower conversion at 200°C on

$Ce_{0.5}Er_{0.5}V_{0.95}Sb_{0.05}O_4$ catalyst. The NO_x conversion on $Ce_{0.5}Er_{0.5}V_{0.95}Nb_{0.05}O_4$ catalyst exhibits a maximum of 90% (400°C) and then gradually decreases at higher temperatures to 52 % (500°C). Fig 6.20 gives the N_2 selectivity of the samples in the NH_3-SCR reaction and shows that undesired N_2O is formed above 300°C on all the four catalysts. High N_2 selectivity of 90% at 500°C was achieved over all catalysts.

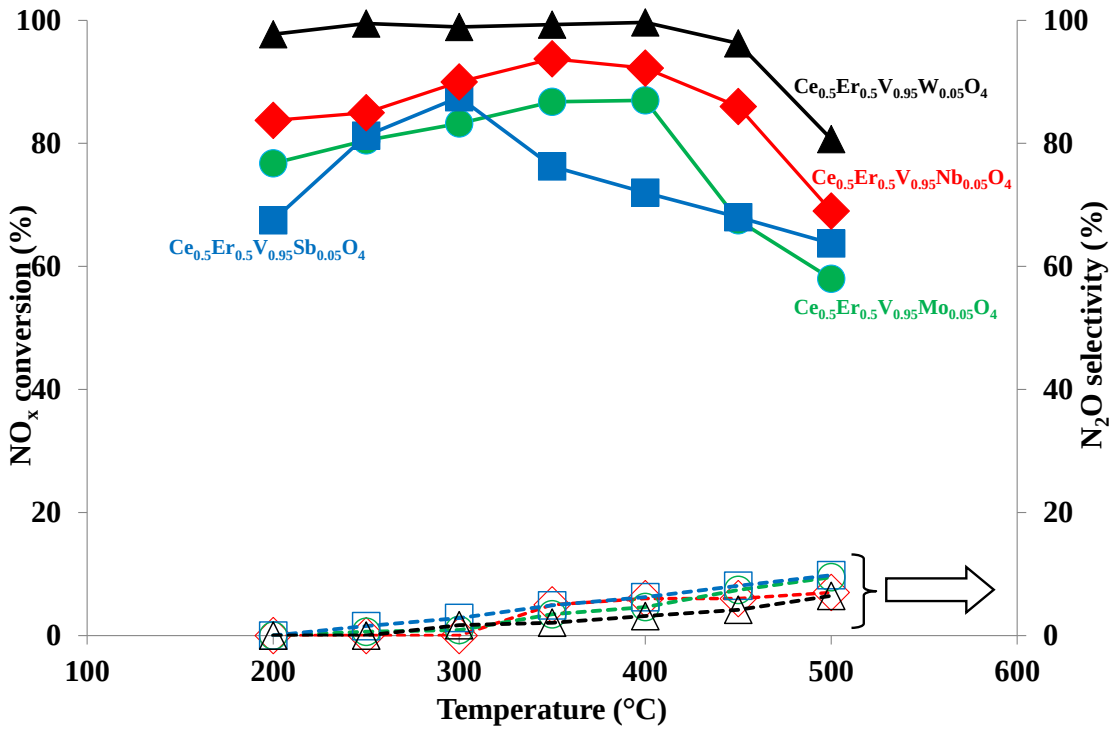

Figure 6.20 – **NO_x conversion (solid lines) and N_2O selectivity (dotted line) during the fast-SCR reaction after aged at 600°C**

1.3.3 Ammonia-selective catalytic reduction of NO_x to nitrogen in "NO_2" condition: NO/NO_x =3/10

In this section, we analyze the effect of an excess of nitrogen dioxide in the reaction mixture (NO_2-SCR). Usually, this reaction is slower compared to Fast-SCR conditions, especially at low temperatures. The formation of unwanted N_2O was also investigated. The aged $Ce_{0.5}Er_{0.5}V_{0.95}W_{0.05}O_4$ catalyst achieves 98% and 90% NO_x conversion at 350 and 500°C, respectively. NO_x conversion over $Ce_{0.5}Er_{0.5}V_{0.95}Mo_{0.05}O_4$ catalyst increases from 58% at

200°C to a maximum of 84% at 400°C and then starts to decreases. Furthermore, the observed decrease in the activity at temperatures above 400°C seen for $Ce_{0.5}Er_{0.5}V_{0.95}Mo_{0.05}O_4$ catalyst can be attributed to ammonia oxidation over this catalyst. The NO_x conversion of $Ce_{0.5}Er_{0.5}V_{0.95}Sb_{0.05}O_4$ catalyst reaches 63% at 200°C, a maximum of 82% is recorded near 350°C and NO_x conversion decreases slightly to 70% at 500°C. $Ce_{0.5}Er_{0.5}V_{0.95}Nb_{0.05}O_4$ catalyst has a moderate activity in NO_x reduction and the maximum of 88% NO_x conversion was achieved at 350–450°C. The NO_x conversion decreases to 75% at 500°C. $Ce_{0.5}Er_{0.5}V_{0.95}W_{0.05}O_4$ catalyst exhibits a higher selectivity towards N_2 compared to other solids (Figure 6.21). Consequently, at the lower temperatures, the N_2O formation is completely avoided over the catalyst, whilst $Ce_{0.5}Er_{0.5}V_{0.95}Sb_{0.05}O_4$ catalyst forms slight amounts of N_2O (<5ppm at 300°C). All N_2 selectivities decrease monotonically as a function of the temperature. The N_2 selectivity of the $Ce_{0.5}Er_{0.5}V_{0.95}Sb_{0.05}O_4$ catalyst decreases noticeably 500°C with quite a large amount of N_2O being formed. The most active and selective catalyst is the $Ce_{0.5}Er_{0.5}V_{0.95}W_{0.05}O_4$ catalyst in NO_2-SCR after aging at 600°C.

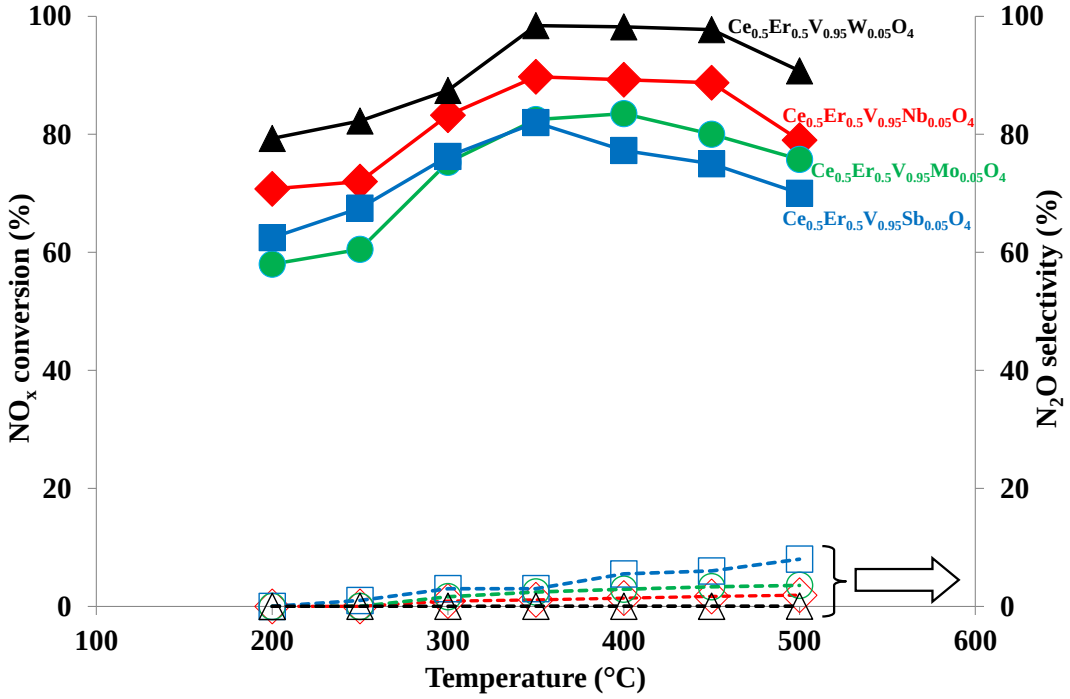

Figure 6.21 – **NO_x conversion (solid lines) and N_2O selectivity (dotted line) during the NO_2-SCR reaction after aging at aged at 600°C**

Table 6.7 summarizes previous results from characterization section. The comparison of catalytic activity in standard and fast-SCR underlines the higher performances of $Ce_{0.5}Er_{0.5}V_{0.95}W_{0.05}O_4$ and $Ce_{0.5}Er_{0.5}V_{0.95}Nb_{0.05}O_4$ catalysts whereas $Ce_{0.5}Er_{0.5}V_{0.95}Mo_{0.05}O_4$ and $Ce_{0.5}Er_{0.5}V_{0.95}Sb_{0.05}O_4$ catalysts are less actives. The specific surface area follows the same evolution. An additional parameter is the content of X element in the solid (X= W, Mo, Sb or Nb). The loading also follows the same sequence: W 4.3 wt. %; Nb 2.2 wt. %; Mo 1.3 wt. % and Sb 1.2wt%. The mechanism of NH_3-SCR involves several parameters including acidity, reducibility and promotion of NO oxidation. Then a direct correlation between catalytic performances and physico-chemical parameters is not obvious. The chapter 3 underlines the crucial role played by the segregation of CeO_2 and detected through the evolution of Ce^{4+}/Ce^{3+} atomic ratio. An enhancement in the NO_x reduction to nitrogen over $Ce_{0.5}Er_{0.5}V_{0.95}W_{0.05}O_4$ aged at 600°C is observed. Such enhancement can be related to an increased density of sites provided by CeO_2 for oxidizing more readily NO to NO_2 and then ensuring a faster re-oxidation of V(+IV) to V(+V) compared to O_2 in standard conditions. Another parameter concerns the oxygen species. O_α species are generally more active than O_β species due to the higher mobility. These results support consistently that a high activity for NO oxidation to NO_2 is conducive to enhance the SCR activity with the high concentration of chemisorbed oxygen species for mobilizing at the low temperature. In this series, the higher surface concentration of O_α species is obtained on W and Mo substituted solid but the catalytic performances are quite different.

Table 6.7 – **Comparison of the SCR performance to physicochemical properties of catalysts aged at 600°C**

$Ce_{0.5}Er_{0.5}V_{0.95}X_{0.05}O_4$ catalysts aged at 600°C	**S_{BET}**	**H_2-TPR**				**IR Pyri.**	**XPS**				**NO conv at 200°C**	
	m^2/g	**T_{max}**		**H_2 consumption**		**n Lewis at. 150°C**	**Ce^{4+}/Ce^{3+}**	**X/ Ce+Er**	**O_a/O_β**	**Oxid. State of X**	**Std SCR**	**Fast SCR**
		LT*	**HT***	**LT***	**HT***							
$Ce_{0.5}Er_{0.5}V_{0.95}W_{0.05}O_4$	58	594	806	0.48	3.50	34.2	0.45	0.08	0.50	6+	57%	97%
$Ce_{0.5}Er_{0.5}V_{0.95}Mo_{0.05}O_4$	35	652/ 692	792	0.25/ 0.09	3.21	33.6	0.35	0.08	0.50	6+	43%	76%
$Ce_{0.5}Er_{0.5}V_{0.95}Sb_{0.05}O_4$	38	563	766	0.52	3.56	25.5	0.75	0.04	0.37	5+	41%	67%
$Ce_{0.5}Er_{0.5}V_{0.95}Nb_{0.05}O_4$	50	560	750	0.38	3.32	1.8	0.60	0.09	0.40	5+	47%	83%

*LT: low temperature; HT: High temperature

1.4 Conclusion

It has been shown the incorporation of W, Mo, Sb, and Nb into the $Ce_{0.5}Er_{0.5}V_{0.95}$ $X_{0.05}O_4$ structure significantly affects the resulting structure and in turn the properties and activity of the catalysts. In this chapter, a series of $Ce_{0.5}Er_{0.5}V_{0.95}X_{0.05}O_4$ (X=W, Mo, Sb, and Nb) mixed oxide catalysts were prepared with the hydrothermal method and aged at different temperatures (600 or 850°C). In conclusion of this chapter, the addition of tungsten induces a significant increase in activity and stability compared to the other solid. The stability of $Ce_{0.5}Er_{0.5}V_{0.95}W_{0.05}O_4$ solid in the selective reduction of NO_x seems rather related to a conservation of the density of sites and a high concentration of acid sites associated with high tungsten content. The results show that the aging significantly affects the structure, surface composition, redox ability and the acidity, which influence the NH_3-SCR performance of the catalysts as a consequence. The zircon-type structure of $REVO_4$ is obtained after hydrothermal synthesis and preserved after aging. An important parameter is related to the coexistence of low amount of CeO_2 with $REVO_4$. Subsequent thermal aging treatment in the wet atmosphere shows that $REVO_4$ is more sensitive to agglomeration and crystallite growth than CeO_2. Important

information is provided by surface physicochemical analysis. XPS analysis shows an increase of the surface vanadium composition on aged samples with the highest atomic V/Ce ratio after aging at 850°C. IR spectroscopic measurements showed predominantly the presence of Lewis acid sites and a higher concentration on $Ce_{0.5}Er_{0.5}V_{0.95}W_{0.05}O_4$ solid. The strength of acid sites and their composition is still a matter of discussion especially the involvement of Lewis and Brönsted sites and surface vanadia species. Our IR spectroscopic observations essentially led to the observation of Lewis acid sites (LAS) on $Ce_{0.5}Er_{0.5}V_{0.95}W_{0.05}O_4$ catalyst after aging at 600°C. $Ce_{0.5}Er_{0.5}V_{0.95}W_{0.05}O_4$ catalyst possessed of the highest specific surface area ($58 m^2/g$) and crystallite diameter (14nm) after aging at 600°C. With regards to the higher textural properties, aged $Ce_{0.5}Er_{0.5}V_{0.95}W_{0.05}O_4$ catalyst exhibits better catalytic properties in terms of NO conversion and selectivity thus providing an alternative to less stable supported vanadia-based catalysts.

2 References

[1] L. Chen, “Hydrothermal synthesis and ethanol sensing properties of $CeVO_4$ and $CeVO_4$ – CeO_2 powders,” vol. 60, no. 3, pp. 1859–1862, 2006.

[2] A. I. Y. Tok, F. Y. C. Boey, Z. Dong, and X. L. Sun, “Hydrothermal synthesis of CeO_2 nano-particles,” vol. 190, pp. 217–222, 2007.

[3] B. Y. R. D. Shannon, M. H, N. H. Baur, O. H. Gibbs, M. Eu, and V. Cu, “R. D. Shannon (1976). ‘Revised effective ionic radii and systematic studies of interatomic distances in halides and chalcogenides’. Acta Cryst A32: 751Ä767. BibcodeÅ1976AcCrA..32..751S. doi:10.1107/S0567739476001551.,” 1976.

[4] P. Yu, S. A. Hayes, T. J. O. Keefe, M. J. O. Keefe, and J. O. Stoffer, “The Phase Stability of Cerium Species in Aqueous Systems and Pourbaix Diagram Calculations,” pp. 74–79, 2006.

[5] H. Huang, Y. Gu, J. Zhao, and X. Wang, “Catalytic combustion of chlorobenzene over VO_x/CeO_2 catalysts,” *J. Catal.*, vol. 326, no. 3, pp. 54–68, 2015.

[6] I. Guedes, Y. Hirano, M. Grimsditch, N. Wakabayashi, C.-K. Loong, and L. A. Boatner, “Raman study of phonon modes in $ErVO_4$ single crystals,” *J. Appl. Phys.*, vol. 90, no. 4, pp. 1843–1846, 2001.

[7] C. Au and W. Zhang, “Oxidative dehydrogenation of propane over rare-earth orthovanadates,” vol. 93, no. 6, pp. 1195–1204, 1997.

[8] M. Romeo, K. Bak, J. El Fallah, F. Le Normand, and L. Hilaire, “XPS Study of the reduction of cerium dioxide,” *Surf. Interface Anal.*, vol. 20, no. 6, pp. 508–512, 1993.

[9] Y. Wang, J. Lu, X. Ma, Y. Niu, V. Singh, P. Ma, C. Zhang, J. Niu, and J. Wang, “Synthesis, characterization and catalytic oxidation of organosilanes with a novel multilayer polyoxomolybdate containing mixed-valence antimony,” *Mol. Catal.*, vol. 452, no. March, pp. 167–174, 2018.

[10] L. E. Firment and A. Ferretti, “Stoichiometric and oxygen deficient MoO_3(010) surfaces,” *Surf. Sci.*, vol. 129, no. 1, pp. 155–176, 1983.

[11] G. Ramis, L. Yi, and G. Busca, “Ammonia activation over catalysts for the selective catalytic reduction of NO , and the selective catalytic oxidation of NH_3 . An FT-IR study,” vol. 28, pp. 373–380, 1996.

[12] S. Gillot, Development of thermally stable vanadium for SCR catalyst coupling with DPF, University of science and technology of Lille, PhD thesis, 2015

General conclusions and outlook

General conclusions and outlook

This thesis concerns the elaboration of new oxidic active phases containing vanadium for high temperature applications. The NH_3-SCR reaction possesses an environmental interest, with regard to the reduction of NO_x emissions of the diesel engine exhaust. Among the available technologies on the market, the selective reduction of NO_x by ammonia (or urea) is one of the most effective at the low temperatures. N_2O is a very strong greenhouse gas, which can be potentially formed as a by-product of the NH_3-SCR reaction. Although not monitored in current emission regulations, the control of N_2O release is crucial towards the environment, as is expected to be highlighted in the Euro VI emission regulations. The literature review was necessary in order to understand the many parameters governing the NH_3-SCR (Chapter I). The objective of this study was the development of alternative catalysts for the exhaust gas treatment of diesel vehicles. These catalysts were supposed to meet the criteria of NH_3-SCR, in particular

- High performance on NO_x removal according to the Euro VI regulation for the diesel engine
- High selectivity toward nitrogen
- High resistance toward hydrothermal aging

And additionally, of being constituted of available, non-toxic and low-cost materials. The main strategies that were followed during this study to improve the catalytic performances of the catalysts, namely the control of the textural properties and the optimization of the catalysts composition.

The enhancement of the ammonia SCR activity of Ce-CeV reference solid was achieved by adding of CeO_2 excess (Chapter III). It was found that the thermal stability of catalysts is remarkably depending on the NO/NO_x ratio and the quantity of CeO_2 in excess in the samples. 11Ce-CeV (*i.e.* 11 wt% $CeO_2/CeVO_4$) at medium temperature was found as the most active catalyst.

Bulk $Ce_{0.5}RE_{0.5}V_{0.95}W_{0.05}O_4$ (RE= Pr, Gd, Tb, and Er) catalysts have revealed promising performances for NH_3-SCR (Chapter IV). These solids have smaller crystallite size than $CeV_{0.95}W_{0.05}O_4$ solid and higher specific surface area. These properties might improve oxygen mobility and redox capability leading to the enhanced catalytic performance of catalysts. The gain in catalytic activity increased in the same order as ionic radius decreases $Ce_{0.5}Pr_{0.5}V_{0.95}W_{0.05}O_4$ < $Ce_{0.5}Gd_{0.5}V_{0.95}W_{0.05}O_4$ < $Ce_{0.5}Tb_{0.5}V_{0.95}W_{0.05}O_4$ < $Ce_{0.5}Er_{0.5}V_{0.95}W_{0.05}O_4$. The ionic radius are seen as the key factor determining the deNO_x activity of catalysts. Incorporation of erbium into zircon-type structure results in the highest NO_x conversion.

On the other hand, composition optimization of the Er-containing catalyst was conducted (Chapter V). Accordingly, bulk $Ce_{1-X}Er_XV_{0.95}W_{0.05}O_4$ (X=0.2, 0.5, and 0.8) catalysts prepared by hydrothermal synthesis have been developed for the ammonia-selective catalytic reduction of NO_x to nitrogen. In order to choose the optimal $Ce_{1-X}Er_XV_{0.95}W_{0.05}O_4$ (X= 0.2, 0.5, and 0.8) catalysts is investigated by comparing physical-chemical properties and the catalytic activity. Characterization techniques (XRF, XRD, BET, RAMAN, H_2-TPR, and XPS) have been performed and discussed trying to correlate the catalytic performances of the samples. The catalytic properties were evaluated in standard-, fast- and NO_2-SCR conditions for stationary and mobile applications. Aged $Ce_{0.5}Er_{0.5}V_{0.95}W_{0.05}O_4$ catalyst exhibits better catalytic properties in terms of NO conversion and selectivity thus providing an alternative to less stable supported vanadia-based catalysts.

The most promising catalyst obtained by the partial substitution of cerium by erbium were finally $Ce_{0.5}Er_{0.5}V_{0.95}W_{0.05}O_4$ catalyst. In view of the foregoing, we investigated the replacement of W by Mo, Sb, and Nb in $Ce_{0.5}Er_{0.5}V_{0.95}W_{0.05}O_4$ catalyst structure which can be beneficial for NH_3-SCR (Chapter VI). A series of $Ce_{0.5}Er_{0.5}V_{0.95}X_{0.05}O_4$ (X=W, Mo, Sb, and Nb) was prepared by hydrothermal approach and was characterized by XRF, XRD, Raman, H_2-TPR,

N_2 adsorption, XPS and Pyridine adsorption. The $Ce_{0.5}Er_{0.5}V_{0.95}X_{0.05}O_4$ (X=W, Mo, Sb, and Nb) catalysts aged at 600°C were applied to the removal of NO_x by selective catalytic reduction with ammonia (NH_3-SCR).

The most promising catalyst obtained by the composition optimization approaches was finally $Ce_{0.5}Er_{0.5}V_{0.95}W_{0.05}O_4$ catalyst.

The contribution of the Er to the applicability of such materials to exhaust gas after-treatment relies in its ability to promote thermal stability of the vanadium-containing catalysts. This is due to the ability of Er to enhance the structural and textural stability. According to the requests in terms of activity/stability it is therefore possible to optimize the catalyst composition by tuning Ce/Er ratio. The mixed composition $Ce_{0.5}Er_{0.5}V_{0.95}W_{0.05}O_4$ represents a good trade-off between low-temperature activity and thermal stability required for mobile SCR applications.

The reaction mechanism can be further investigated on this system and compared to conventional V_2O_5-WO_3-TiO_2 catalyst. Additional experiments such as NO oxidation to NO_2 and NH_3 oxidation to $NO/N_2O/N_2$ can complete this study for a better characterization of catalytic functions of $Ce_{0.5}RE_{0.5}V_{0.95}X_{0.05}O_4$ (RE= Pr, Gd, Tb, and Er ; X=W, Mo, Sb, and Nb) –based catalysts. The direct synthesis of this oxidic phase onto the particulate filter is an interesting issue for an easier deposition of the active phase. Such solution can simplify the procedure and expose a relatively high specific surface area compared to conventional washcoat method. Moreover, the influence of these metal ions on structure-reactivity relationships and the mechanism of the NH_3-SCR reaction should be investigated by a combination of different in-situ/operando spectroscopies. Further work should design the experimental activity tests in the presence of SO_2.

Improved resistance to deactivation of coupled NH_3-SCR/ DPF catalyst for diesel exhaust emissions control

Abstract

Diesel engines have been extensively implemented because they emit lesser CO_2 than gasoline engine of equivalent power, since they work in lean condition, *i.e.* in excess of oxygen. Recently, Selective Catalytic Reduction (SCR) catalysts coated on Diesel Particulate Filters (DPF) have been introduced for automotive applications due to capability of reducing NO_x and PM simultaneously. However, such implementation requires improved thermal resistance of the SCR catalyst due to the exotherms related to the periodic regeneration of DPF. The point of this manuscript is to propose a catalyst active in NO_x reduction by NH_3 after aging at high temperature. The first part of this manuscript details the modifications of $CeV_{0.95}W_{0.05}O_4$ catalyst by adding of rare earths elements (Pr^{3+}, Gd^{3+}, Tb^{3+}, and Er^{3+}). The most promising catalyst obtained by the partial substitution of cerium by rare earths was finally $Ce_{0.5}Er_{0.5}V_{0.95}W_{0.05}O_4$ catalyst. A partial substitution of the cerium by the erbium allows obtaining an increase of the activity after an aging at 600°C and 850°C attributed to the ability of erbium to promote thermal stability of the vanadium-containing catalysts. This behavior might be also correlated with the characteristics of Er^{3+}–O–V^{5+} bond and to their ability to alter the characteristics of the V–O bond and the acid/base surface properties. $Ce_{0.5}Er_{0.5}V_{0.95}W_{0.05}O_4$ catalyst, an optimized formulation, is able to get a NO_x conversion superior to 80% between 250 and 400°C in Fast-SCR condition after an aging at 850°C.

Amélioration de la résistance à la désactivation d'un système catalytique couplé NH_3-SCR/ DPF pour le contrôle des émissions de gaz d'échappement des moteurs diesel

Résumé

Les moteurs Diesels connaissent un intérêt récent tout particulier car ils rejettent moins de CO_2 que les moteurs essences à puissance égale, du fait qu'ils travaillent en mélange pauvre (en excès d'oxygène). Récemment, des catalyseurs de réduction catalytique sélective (SCR) déposés sur des filtres à particules diesel (FAP) ont été développés pour les applications automobiles en raison de leur capacité à réduire simultanément les émissions de NO_x et de particules. Une telle mise en œuvre nécessite une résistance thermique améliorée du catalyseur SCR du fait des exothermes liés à la régénération périodique du FAP. Le but de ce travail est de proposer un catalyseur pour la réduction des NO_x par NH_3 actif après vieillissement à haute température. La première partie de ce manuscrit détaille les modifications du catalyseur $CeV_{0.95}W_{0.05}O_4$ en ajoutant des éléments de terres rares (Pr^{3+}, Gd^{3+}, Tb^{3+}, Er^{3+}). Le catalyseur le plus prometteur obtenu par la substitution partielle du cérium par des terres rares était finalement le catalyseur $Ce_{0.5}Er_{0.5}V_{0.95}W_{0.05}O_4$. Une substitution partielle du cérium par de l'erbium permet d'obtenir un gain d'activité après vieillissement à 600 et 850°C attribué à la capacité de l'erbium à favoriser la stabilité thermique des catalyseurs contenant du vanadium. Ce comportement pourrait également être corrélé aux caractéristiques de la liaison Er^{3+}–O–V^{5+} et à leur capacité à modifier les caractéristiques de la liaison V–O et les propriétés acide/base de surface. Le catalyseur $Ce_{0.5}Er_{0.5}V_{0.95}W_{0.05}O_4$, la formulation optimisée, permet d'obtenir une conversion de NO_x supérieure à 80% entre 250 et 400°C en condition Fast-SCR après un vieillissement à 850°C.